CZECH TECHNICAL UNIVERSITY IN PRAGUE
Faculty of Nuclear Sciences and Physical Engineering
Department of Physics

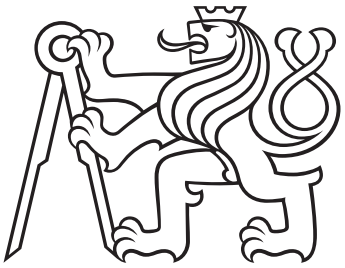

MASTER'S THESIS

Efficiency and accuracy of time-of-flight detector measurements in the ATLAS experiment and di-photon vertex reconstruction for the search for an axion-like particle in data from LHC Run-3

Viktoriia Lysenko
Supervisor: doc. Dr. André Sopczak
Prague, 2023

ČESKÉ VYSOKÉ UČENÍ TECHNICKÉ V PRAZE

Fakulta Jaderná a Fyzikálně Inženýrská

Katedra fyziky

DIPLOMOVÁ PRÁCE

Účinnost a přesnost měření detektoru doby letu v experimentu ATLAS a rekonstrukce di-fotónového vertexu pro pátrání po axionu podobné částici v datech z LHC Run-3

Viktoriia Lysenko

Vedoucí práce: doc. Dr. André Sopczak

Praha, 2023

FACULTY OF NUCLEAR SCIENCES
AND PHYSICAL ENGINEERING
DEPARTMENT OF PHYSICS

DIPLOMA THESIS ASSIGNMENT

Academic year: 2022/2023

Student:	Viktoriia Lysenko
Study programme:	***Nuclear and particle physics***
Thesis title: (in Czech)	Účinnost a přesnost měření detektoru doby letu v experimentu ATLAS a rekonstrukce di-fotónového vertexu pro pátrání po axionu podobné částici v datech z LHC Run-3
Thesis title: (in English)	Efficiency and accuracy of time-of-flight detector measurements in the ATLAS experiment and di-photon vertex reconstruction for the search for an axion-like particle in data from LHC Run-3
Language of the Thesis:	English

Instructions:

1) Familiarise yourself with the ATLAS software for data analysis, including grid processing
2) Study the vertex recontruction for di-photons events
3) Demonstrate that the background rejection for an Axion-Like-Particle search will increase with an improved vertex reconstruction, assuming the ToF detector resolution
4) Study the ToF detector performance with first LHC Run-3 data
5) Use the ToF data and demonstrate an improved vertex reconstruction for di-photon events
6) Discuss your results regarding the search for Axion-Like-Particles with LHC Run-3 data

Recommended literature:

[1] ATLAS Collaboration, Phys. Rev. Lett. 125 (2020) 261801 [2009.14537]

[2] CMS Collaboration, J. High Energy Phys. 2018, 153.

[3] ATLAS Collaboration, ATL-COM-FWD-2021-013 [https://cds.cern.ch/record/2749821]

[4] A. Sopczak, et al., ATL-COM-PHYS-2020-238 [https://cds.cern.ch/record/2714416]

[5] L. Adamczyk, et al., ATLAS-TDR-024 [https://cds.cern.ch/record/2017378]

Name and affiliation of the supervisor:

doc. Dr. André Sopczak
Institute of Experimental and Applied Physics CTU in Prague

Date of the assignment: 20.10.2022

Due date of the thesis: 03.05.2023

The assignment is valid for two years since the date of the assignment.

.....
Guarantor of the study programme

ČESKÉ VYSOKÉ UČENÍ TECHNICKÉ V PRAZE Fakulta jaderná a fyzikálně inženýrská -3-

.....
Department head

.....
Dean

In Prague on 20.10.2022

FAKULTA JADERNÁ A FYZIKÁLNĚ INŽENÝRSKÁ

KATEDRA FYZIKY

ZADÁNÍ DIPLOMOVÉ PRÁCE

Akademický rok: 2022/2023

Student:	Viktoriia Lysenko
Studijní program:	Jaderná a částicová fyzika
Název práce: (česky)	Účinnost a přesnost měření detektoru doby letu v experimentu ATLAS a rekonstrukce di-fotónového vertexu pro pátrání po axionu podobné částici v datech z LHC Run-3
Název práce: (anglicky)	Efficiency and accuracy of time-of-flight detector measurements in the ATLAS experiment and di-photon vertex reconstruction for the search for an axion-like particle in data from LHC Run-3
Jazyk práce:	Angličtina

Pokyny pro vypracování:

1) Seznamte se s ATLAS softwarem pro analýzu dat včetně gridových výpočtů

2) Studium rekonstrukce vertexu pro di-fotónové události

3) Ukažte, že potlačení pozadí pro pátrání po axionu podobné částici se zvýší s vylepšenou rekonstrukcí vertexu vzhledem k rozlišení ToF detektoru

4) Studium výkonu ToF detektoru z prvních LHC Run-3 dat

5) Použijte ToF data a demonstrujte vylepšenou rekonstrukci vertexu pro di-fotónové události

6) Diskutujte výsledky týkající se pátrání po axionu podobné částici pomocí LHC Run-3 dat

Doporučená literatura:

[1] ATLAS Collaboration, Phys. Rev. Lett. 125 (2020) 261801 [2009.14537]

[2] CMS Collaboration, J. High Energy Phys. 2018, 153.

[3] ATLAS Collaboration, ATL-COM-FWD-2021-013 [https://cds.cern.ch/record/2749821]

[4] A. Sopczak, et al., ATL-COM-PHYS-2020-238 [https://cds.cern.ch/record/2714416]

[5] L. Adamczyk, et al., ATLAS-TDR-024 [https://cds.cern.ch/record/2017378]

Jméno a pracoviště vedoucího diplomové práce:

doc. Dr. André Sopczak
IInstitute of Experimental and Applied Physics CTU in Prague

Datum zadání diplomové práce: 20.10.2022

Termín odevzdání diplomové práce: 03.05.2023

Doba platnosti zadání je dva roky od data zadání.

.....
garant studijního programu

.....
vedoucí katedry

.....
děkan

V Praze dne 20.10.2022

ČESKÉ VYSOKÉ UČENÍ TECHNICKÉ V PRAZE
Fakulta jaderná a fyzikálně inženýrská

Břehová 7
115 19 Praha 1

P R O H L Á Š E N Í

Já, níže podepsaný

Jméno a příjmení studenta:	Viktoriia Lysenko
Osobní číslo:	514021
Název studijního programu (oboru):	Jaderná a částicová fyzika

prohlašuji, že jsem diplomovou práci s názvem:

Efficiency and accuracy of time-of-flight detector measurements in the ATLAS experiment and di-photon vertex reconstruction for the search for an axion-like particle in data from LHC Run-3

vypracoval(a) samostatně a uvedl(a) veškeré použité informační zdroje v souladu s Metodickým pokynem o dodržování etických principů při přípravě vysokoškolských závěrečných prací.

V Praze dne 23.8.2023 ……

podpis

Acknowledgements

I would like to thank my supervisor, doc. Dr. André Sopczak, for all advises and active involvement during the work. The support for this study by the AFP team, and in particular by the AFP-ToF team is gratefully acknowledged. Special thanks to Dr. Karel Černý, for the consultations during the work. I also would like to thank my family for the encouragement during my studies.

Viktoriia Lysenko

Title:

Efficiency and accuracy of time-of-flight detector measurements in the ATLAS experiment and di-photon vertex reconstruction for the search for an axion-like particle in data from LHC Run-3

Author:	Viktoriia Lysenko
Study program:	Nuclear and particle physics
Type of work:	Master's thesis
Supervisor:	doc. Dr. André Sopczak Institute of Experimental and Applied Physics CTU in Prague

---

Abstract:

In summer 2022, the first LHC Run-3 proton-proton collision data were recorded with the ATLAS central detector and the ATLAS Forward Proton (AFP) detectors. An analysis of this data was performed. Two methods were used to study the efficiency of the Time-of-Flight (ToF) detector for all 2022 data. For the determination of the ToF time resolution, first an elaborate calibration was performed. These performance studies of the ToF data included a proton-proton vertex reconstruction using the matching of ToF and central ATLAS vertex positions. After a calibration of time delays, a preliminary resolution of the vertex reconstruction was determined with a low-μ ATLAS data set. In addition, based on selected di-photon events, a vertex reconstruction study was conducted with a high-μ 2022 data set. The potential of ToF data for an improved vertex reconstruction and thus reduction of background in an Axion-Like-Particle search using AFP data has been demonstrated.

Key words: LHC Run-3, AFP, ToF, ALP, di-photon

Název práce:

Účinnost a přesnost měření detektoru doby letu v experimentu ATLAS a rekonstrukce di-fotónového vertexu pro pátrání po axionu podobné částici v datech z LHC Run-3

Autor:	Viktoriia Lysenko
Studijní program:	Jaderná a částicová fyzika
Druh práce:	Diplomová práce
Vedoucí práce:	doc. Dr. André Sopczak Ústav Technické a Experimentální Fyziky ČVUT v Praze

---

Abstrakt:

V létě 2022 byla na Velkém hadronovém urychlovači zaznamenána první data z proton-protonových srážek v rámci LHC Runu-3 pomocí centrálního detektoru ATLAS a detektorů ATLAS Forward Proton (AFP). Byla provedena analýza těchto dat. Pro studium účinnosti detektoru času průletu (ToF) byly použity dvě metody pro všechna data z roku 2022. Pro určení časového rozlišení ToF byla nejprve provedena podrobná kalibrace. Tyto studie kvality ToF dat zahrnovaly rekonstrukci proton-protonového vertexu porovnáním poloh vertexů ToF a centrálního ATLAS. Po kalibraci časových prodlev bylo určeno předběžné rozlišení vertexové rekonstrukce pomocí ATLAS sadou dat s nízkým μ. Navíc na základě vybraných di-fotonových událostí byly provedeny studie rekonstrukce vertexů s daty z roku 2022 s vysokým μ. Byl prokázán potenciál ToF dat pro vylepšení rekonstrukce vertexů, a tím i snížení pozadí při hledání Axionu podobné částice pomocí AFP dat.

Klíčová slova: LHC Run-3, AFP, ToF, ALP, di-foton

Contents

1 Introduction **1**

2 Detector design **5**
2.1 ATLAS Central Detector 5
2.2 ATLAS Forward Proton Detector 6
2.3 Time-of-Flight Detector 7

3 Analysis of the ToF detector with LHC Run-3 Data **9**
3.1 Data selection 9
3.2 Time resolution 11
3.2.1 Multi-peak structure analysis 19
3.2.2 HPTDC calibration 22
3.3 Efficiency 34
3.3.1 Background analysis 41
3.3.2 2022 efficiency summary 48

4 ToF vertex reconstruction **49**
4.1 Time delays correction 50
4.2 Vertex matching 55

5 Di-photon vertex reconstruction **59**

6 Future applications on an ALP search **61**

7 Conclusions **63**

Bibliography **65**

Appendix **69**
A Codes 69
B ToF time resolution 70
B.1 Before the HPTDC calibration 70
B.2 After the HPTDC calibration 90
B.3 After the likelihood cleanup procedure 115
C ToF efficiency 131

Acronyms **145**

List of Figures

1.1 Feynman diagram illustrating Axion-Like Particle (ALP) mediated light-by-light scattering in process of central exclusive di-photons production. 2

2.1 Cut-away view of the A Toroidal LHC ApparatuS (ATLAS) detector. 5
2.2 ATLAS Forward Proton (AFP) design. 6
2.3 Time-of-Flight (ToF) LQ-bar design. Vertical × Horizontal × Depth. 7
2.4 AFP Silicon pixel Tracker (SiT) and ToF LQ-bars. Proton beam comes from the right side. 8

3.1 Correlation of SiT versus ToF in run 429027 for C-side (top) and run 428770 for the A-side (bottom). The horizontal axis stands for the ToF trains, the vertical axis stands for the X-position in the SiT in mm. 10
3.2 Raw time distributions in run 429027 (left) and low-μ run 428770 (right) for side A, channel 0B. 11
3.3 Raw time distribution before (left) and after (right) additional cuts on time were applied in the run 429027. The left peak corresponds to the C-side and the right one to the A-side. . . . 12
3.4 Raw time distributions in run 429027 after the cut on the time for train 3 for each channel: A (top left), B (top right), C (bottom left) and D (bottom right). 13
3.5 Raw time distributions in run 428770 after the cut on the time for train 3 for each channel: A (top left), B (top right), C (bottom left) and D (bottom right). 13
3.6 Examples of the Δt distributions before the high performance time-to-digital converter (HPTDC) calibration for the run 429027 with a double Gaussian fitted curve overlaid for 4 combinations (0AC - top left, 1BD - top right, 2BC bottom left, 3AB bottom right) of the ToF channels for A-side. 15
3.7 Examples of the Δt distributions before the HPTDC calibration for the run 429027 with a double Gaussian fitted curve overlaid for 4 combinations (0AC - top left, 1BD - top right, 2BC bottom left, 3AB bottom right) of the ToF channels for C-side. 15

3.8 Width of Δt (ps) distributions before the HPTDC calibration for the run 429027 using a double Gaussian fit for all combinations of the ToF channels inside one train. Trains: 0-3, bars: A-D. 16
3.9 Fit of six widths of the Δt distributions for trains 0 (top left), 1 (top right), 2 (bottom left), 3 (bottom right) before the HPTDC calibration for the run 429027, a double Gaussian, for A-side. . . 17
3.10 Fit of six widths of the Δt distributions for trains 0 (top left), 1 (top right), 2 (bottom left), 3 (bottom right) before the HPTDC calibration for the run 429027, a double Gaussian, for C-side. . . 17
3.11 ToF time resolution (ps) before the HPTDC calibration for the run 429027, a double Gaussian fit. Trains: 0-3, bars: A-D. 18
3.12 ToF time resolution (ps) before the HPTDC calibration for the low-μ run 428770, a double Gaussian fit. Trains: 0-3, bars: A-D. 18
3.13 Worst cases of the Δt distributions for the high-μ run 429027 (top) and low-μ run 428770 (bottom) for the C-side on examples of the ToF channels 2BC (left) and 2BD (right). 19
3.14 Track profile in SiT tracker in logarithmic scale on the color Z-axis for the low-μ run 435229 for the A-side (top) and C-side (bottom). 20
3.15 Track profile in SiT tracker in logarithmic scale on the color Z-axis for the high-μ run 429027 for the A-side (top) and C-side (bottom). 21
3.16 Raw time distributions before (blue) and after (red) the calibration in run 429027 (left) and low-μ run 428770 (right) for side A, channel 0B. 22
3.17 Examples of the Δt distributions after the HPTDC calibration for the run 429027 with a multiple-Gaussian fitted curve overlaid for 4 combinations (0AC - top left, 1BD - top right, 2BC bottom left, 3AB bottom right) of the ToF channels for A-side. 23
3.18 Examples of the Δt distributions after the HPTDC calibration for the run 429027 with a multiple-Gaussian fitted curve overlaid for 4 combinations (0AC - top left, 1BD - top right, 2BC bottom left, 3AB bottom right) of the ToF channels for C-side. 24
3.19 Examples of the Δt distributions after the HPTDC calibration for the low-μ run 428770 with a multiple-Gaussian fitted curve overlaid for 4 combinations (0AC - top left, 1BD - top right, 2BC bottom left, 3AB bottom right) of the ToF channels for A-side. 24
3.20 Examples of the Δt distributions after the HPTDC calibration for the low-μ run 428770 with a multiple-Gaussian fitted curve overlaid for 4 combinations (0AC - top left, 1BD - top right, 2BC bottom left, 3AB bottom right) of the ToF channels for C-side. 25

3.21 Examples of the Δt distributions after the likelihood cleanup procedure was applied, for the run 429027 with a Gaussian fitted curve overlaid for 4 combinations (0AC - top left, 1BD - top right, 2BC bottom left, 3AB bottom right) of the ToF channels for A-side. 26
3.22 Examples of the Δt distributions after the likelihood cleanup procedure was applied, for the run 429027 with a Gaussian fitted curve overlaid for 4 combinations (0AC - top left, 1BD - top right, 2BC bottom left, 3AB bottom right) of the ToF channels for C-side. 27
3.23 Examples of the Δt distributions after the likelihood cleanup procedure was applied, for the low-μ run 428770 with a Gaussian fitted curve overlaid for 4 combinations (0AC - top left, 1BD - top right, 2BC bottom left, 3AB bottom right) of the ToF channels for A-side. 27
3.24 Examples of the Δt distributions after the likelihood cleanup procedure was applied, for the low-μ run 428770 with a Gaussian fitted curve overlaid for 4 combinations (0AC - top left, 1BD - top right, 2BC bottom left, 3AB bottom right) of the ToF channels for C-side. 28
3.25 Width of Δt (ps) distributions after the likelihood cleanup procedure was applied for the run 429027 using a Gaussian fit for all combinations of the ToF channels inside one train. Trains: 0-3, bars: A-D. 29
3.26 Width of Δt (ps) distributions after the likelihood cleanup procedure was applied for the low-μ run 428770 using a Gaussian fit for all combinations of the ToF channels inside one train. Trains: 0-3, bars: A-D. 30
3.27 Fit of six widths of the Δt distributions for trains 0 (top left), 1 (top right), 2 (bottom left), 3 (bottom right) after the likelihood cleanup procedure was applied, for the run 429027 for A-side. . 31
3.28 Fit of six widths of the Δt distributions for trains 0 (top left), 1 (top right), 2 (bottom left), 3 (bottom right) after the likelihood cleanup procedure was applied, for the run 429027 for C-side. . . 31
3.29 ToF time resolution (ps) after the likelihood cleanup procedure was applied, for the run 429027. Trains: 0-3, bars: A-D. 32
3.30 Fit of six widths of the Δt distributions for trains 0 (top left), 1 (top right), 2 (bottom left), 3 (bottom right) after the likelihood cleanup procedure was applied, for the low-μ run 428770 for A-side. 33
3.31 Fit of six widths of the Δt distributions for trains 0 (top left), 1 (top right), 2 (bottom left), 3 (bottom right) after the likelihood cleanup procedure was applied, for the low-μ run 428770 for C-side. 33

3.32 ToF time resolution (ps) after the likelihood cleanup procedure was applied, for the low-μ run 428770. Trains: 0-3, bars: A-D. . 34
3.33 Ratios, which define efficiencies for the run 429027, for the case of cuts "one train ON" for A-side for each train and one bar: 0B (top left), 1B (top right), 2B (bottom left) and 3B (bottom right). 36
3.34 Ratios, which defines efficiencies for the run 429027, for the case of cuts "one train OFF" for A-side for each train and one bar: 0B (top left), 1B (top right), 2B (bottom left) and 3B (bottom right). 36
3.35 Efficiencies (%) for the run 429027 for each channel of ToF for A (left) and C (right) sides with the requirement "one train ON", (top) and OFF, (bottom) for the "histogram" method. 37
3.36 Efficiencies (%) for the run 429027 for each channel of ToF for A (left) and C (right) sides with the requirement "one train ON", (top) and OFF, (bottom) for the "direct numbers" method. . . . 38
3.37 Efficiencies (%) for the run 429027 for each channel of ToF for C-side with the requirement "one train OFF" for the "histogram" method: 200 bins (top left), 600 bins (top right), 2000 bins (bottom left); and "direct numbers" method (bottom right). 39
3.38 Efficiencies (%) for the run 428770 for each channel of ToF for A (left) and C (right) sides with the requirement "one train ON", (top) and OFF, (bottom) for the "direct numbers" method. . . . 40
3.39 Efficiencies (%) for the run 429027 for each channel of the ToF with track pointing to train 0 for A (left) and C (right) sides with the requirement "one train ON", (top) and OFF, (bottom) for the "direct numbers" method. 41
3.40 Efficiencies (%) for the run 429027 for each channel of the ToF with track pointing to train 3 for A (left) and C (right) sides with the requirement "one train ON", (top) and OFF, (bottom) for the "direct numbers" method. 42
3.41 Efficiencies (%) for the low-μ run 428770 for each channel of the ToF with track pointing to train 0 for A (left) and C (right) sides with the requirement "one train ON", (top) and OFF, (bottom) for the "direct numbers" method. Empty boxes represents zero response of the corresponding channel. 43
3.42 Efficiencies (%) for the low-μ run 428770 for each channel of the ToF with track pointing to train 3 for A (left) and C (right) sides with the requirement "one train ON", (top) and OFF, (bottom) for the "direct numbers" method. Empty boxes represents zero response of the corresponding channel. 44
3.43 Hit correlation map for the high-μ run 429027 for each channel of the ToF with track pointing to train 0 (top left), train 1 (top right), train 2 (bottom left) and train 3 (bottom right) for the C-side with the requirement "one train OFF". 45

3.44 Hit correlation map for the low-μ run 428770 for each channel of the ToF with track pointing to train 0 (top left), train 1 (top right), train 2 (bottom left) and train 3 (bottom right) for the C-side with the requirement "one train OFF". 46

3.45 Hit correlation map for the longest low-μ run so far in the Run-3, 435229, for each channel of the ToF with track pointing to train 0 (top left), train 1 (top right), train 2 (bottom left) and train 3 (bottom right) for the C-side with the requirement "one train OFF". 47

3.46 Efficiency summary for the 2022 data for the A-side (top) and the C-side (bottom) with the requirement "one train OFF" for the period from 05 July to 27 November 2022. Labels on Y-axis correspond to the beginning of the month. 48

4.1 $z_{\mathrm{ToF}} - z_{\mathrm{BS}}$ distributions for the run 429027 with a Gaussian fitted curve overlaid for 2 combinations of the ToF channels. Left - side A 0A (train 0, bar A) with side C 1B (train 1, bar B). Right - side A 2B (train 2, bar B) with side C 0D (train 0, bar D). 51

4.2 $z_{\mathrm{ToF}} - z_{\mathrm{BS}}$ distributions for the low-μ run 428770 with Gaussian fitted curve overlaid for 2 combinations of the ToF channels. Left - side A 0A (train 0, bar A) with side C 1B (train 1, bar B). Right - side A 2B (train 2, bar B) with side C 0D (train 0, bar D). 51

4.3 All differences between delay correction constants for each of the 256 combinations of the ToF channels for the run 429027 (left) and for the low-μ run 428770 (right). 52

4.4 All differences between delay correction constants for each of the 256 combinations of the ToF channels with fit overlaid for the run 429027 (left) and for the low-μ run 428770 (right). . . . 53

4.5 Delay correction constants for all ToF channels on A-side (top) and C-side (bottom) for the run 429027 (left) and for the low-μ run 428770 (right). 53

4.6 Dependence of the z_{BS} and z_{ToF} per lumiblock (LB) before (top) and after (bottom) the corrections on time delays for the run 429027 (left) and for the low-μ run 428770 (right). 54

4.7 Dependence of the z_{BS} and z_{ToF} per LB after the corrections on time delays for the run 429027 (left) and for the low-μ run 428770 (right), magnified version. 55

4.8 Precision of the fit for the run 429027 (left) and for the low-μ run 428770 (right). Details are given in the text. 55

4.9 The distribution of the $z_{\mathrm{ATLAS}} - z_{\mathrm{ToF}}$ for the low-μ run 428770. 56

4.10 The distribution of $z_{\mathrm{ATLAS}} - z_{\mathrm{ToF}}$ measured in events with ToF signals on both sides of the interaction region in run 341419 in data 2017, where z_{ATLAS} is the primary vertex z-position reconstructed by ATLAS. The z_{ToF} is obtained as $z_{\mathrm{ToF}} = -\frac{c}{2}\Delta t$, where Δt is the time difference of proton arrival times in A and C far stations of the AFP measured by ToF. The distribution correspond to the ATLAS data containing a reconstructed primary vertex together with coincidence of signals in both ToF detectors in scenario with no cut on number of vertices reconstructed by ATLAS. A double Gaussian function representing the signal and background components is fitted to unbinned data samples using the extended likelihood fit as implemented in RooFit. The mean of the signal component as well as the mean and width of the background component are always estimated from a Gaussian fit to the mixed event data, denoted as μ_{sig}^{FIX}, μ_{bgd}^{FIX} and σ_{bgd}^{FIX}. The mixed event data $z_{\mathrm{ATLAS}} - z_{\mathrm{ToF}}$ distributions are obtained by random mixing of times measured by ToF in either station and the z_{ATLAS} values which do not originate in the same collision event. The expected resolution of the ToF detector, quoted as $\sigma_{expected}^{ToF}$ is obtained from the known single-channel resolutions convoluted with the actual channel-hit-patterns observed in the data [18]. 58

5.1 Resolutions for converted (left) and unconverted (right) photons for first Run-3 data from 2022 using the calorimeter pointing method with fitted curve overlaid. The values, z_0 and z_1, correspond to the z-position of the leading and the sub-leading photons, respectively. 60

1 Raw time distributions in run 429027 after the cut on the time for train 0 for each channel: A (top left), B (top right), C (bottom left) and D (bottom right). 70

2 Raw time distributions in run 429027 after the cut on the time for train 1 for each channel: A (top left), B (top right), C (bottom left) and D (bottom right). 71

3 Raw time distributions in run 429027 after the cut on the time for train 2 for each channel: A (top left), B (top right), C (bottom left) and D (bottom right). 71

4 Raw time distributions in run 429027 after the cut on the time for train 3 for each channel: A (top left), B (top right), C (bottom left) and D (bottom right). 72

5 Raw time distributions in low-μ run 428770 after the cut on the time for train 0 for each channel: A (top left), B (top right), C (bottom left) and D (bottom right). 72

6 Raw time distributions in low-μ run 428770 after the cut on the time for train 1 for each channel: A (top left), B (top right), C (bottom left) and D (bottom right). 73
7 Raw time distributions in low-μ run 428770 after the cut on the time for train 2 for each channel: A (top left), B (top right), C (bottom left) and D (bottom right). 73
8 Raw time distributions in low-μ run 428770 after the cut on the time for train 3 for each channel: A (top left), B (top right), C (bottom left) and D (bottom right). 74
9 Δt distributions for the run 429027 with a double Gaussian fitted curve overlaid for all combinations of the ToF channels in train 0 for the A-side. 75
10 Δt distributions for the run 429027 with a double Gaussian fitted curve overlaid for all combinations of the ToF channels in train 1 for the A-side. 76
11 Δt distributions for the run 429027 with a double Gaussian fitted curve overlaid for all combinations of the ToF channels in train 2 for the A-side. 77
12 Δt distributions for the run 429027 with a double Gaussian fitted curve overlaid for all combinations of the ToF channels in train 3 for the A-side. 78
13 Δt distributions for the run 429027 with a double Gaussian fitted curve overlaid for all combinations of the ToF channels in train 0 for the C-side. 79
14 Δt distributions for the run 429027 with a double Gaussian fitted curve overlaid for all combinations of the ToF channels in train 1 for the C-side. 80
15 Δt distributions for the run 429027 with a double Gaussian fitted curve overlaid for all combinations of the ToF channels in train 2 for the C-side. 81
16 Δt distributions for the run 429027 with a double Gaussian fitted curve overlaid for all combinations of the ToF channels in train 3 for the C-side. 82
17 Δt distributions for the low-μ run 428770 with a double Gaussian fitted curve overlaid for all combinations of the ToF channels in train 0 for the A-side. 83
18 Δt distributions for the low-μ run 428770 with a double Gaussian fitted curve overlaid for all combinations of the ToF channels in train 1 for the A-side. 84
19 Δt distributions for the low-μ run 428770 with a double Gaussian fitted curve overlaid for all combinations of the ToF channels in train 2 for the A-side. 85

20 Δt distributions for the low-μ run 428770 with a double Gaussian fitted curve overlaid for all combinations of the ToF channels in train 3 for the A-side. 86
21 Δt distributions for the low-μ run 428770 with a double Gaussian fitted curve overlaid for all combinations of the ToF channels in train 0 for the C-side. 87
22 Δt distributions for the low-μ run 428770 with a double Gaussian fitted curve overlaid for all combinations of the ToF channels in train 1 for the C-side. 88
23 Δt distributions for the low-μ run 428770 with a double Gaussian fitted curve overlaid for all combinations of the ToF channels in train 2 for the C-side. 89
24 Δt distributions for the low-μ run 428770 with a double Gaussian fitted curve overlaid for all combinations of the ToF channels in train 3 for the C-side. 90
25 Raw time distributions before (blue) and after (red) the calibration in high-μ run 429027 for all ToF channels in train 0 for the A-side. 91
26 Raw time distributions before (blue) and after (red) the calibration in high-μ run 429027 for all ToF channels in train 1 for the A-side. 91
27 Raw time distributions before (blue) and after (red) the calibration in high-μ run 429027 for all ToF channels in train 2 for the A-side. 92
28 Raw time distributions before (blue) and after (red) the calibration in high-μ run 429027 for all ToF channels in train 3 for the A-side. 92
29 Raw time distributions before (blue) and after (red) the calibration in high-μ run 429027 for all ToF channels in train 0 for the C-side. 93
30 Raw time distributions before (blue) and after (red) the calibration in high-μ run 429027 for all ToF channels in train 1 for the C-side. 93
31 Raw time distributions before (blue) and after (red) the calibration in high-μ run 429027 for all ToF channels in train 2 for the C-side. 94
32 Raw time distributions before (blue) and after (red) the calibration in high-μ run 429027 for all ToF channels in train 3 for the C-side. 94
33 Raw time distributions before (blue) and after (red) the calibration in low-μ run 428770 for all ToF channels in train 0 for the A-side. 95

34 Raw time distributions before (blue) and after (red) the calibration in low-μ run 428770 for all ToF channels in train 1 for the A-side. 95
35 Raw time distributions before (blue) and after (red) the calibration in low-μ run 428770 for all ToF channels in train 2 for the A-side. 96
36 Raw time distributions before (blue) and after (red) the calibration in low-μ run 428770 for all ToF channels in train 3 for the A-side. 96
37 Raw time distributions before (blue) and after (red) the calibration in low-μ run 428770 for all ToF channels in train 0 for the C-side. 97
38 Raw time distributions before (blue) and after (red) the calibration in low-μ run 428770 for all ToF channels in train 1 for the C-side. 97
39 Raw time distributions before (blue) and after (red) the calibration in low-μ run 428770 for all ToF channels in train 2 for the C-side. 98
40 Raw time distributions before (blue) and after (red) the calibration in low-μ run 428770 for all ToF channels in train 3 for the C-side. 98
41 Δt distributions after the HPTDC calibration for the run 429027 with a double Gaussian fitted curve overlaid for all combinations of the ToF channels in train 0 for the A-side. 99
42 Δt distributions after the HPTDC calibration for the run 429027 with a double Gaussian fitted curve overlaid for all combinations of the ToF channels in train 1 for the A-side. 100
43 Δt distributions after the HPTDC calibration for the run 429027 with a double Gaussian fitted curve overlaid for all combinations of the ToF channels in train 2 for the A-side. 101
44 Δt distributions after the HPTDC calibration for the run 429027 with a double Gaussian fitted curve overlaid for all combinations of the ToF channels in train 3 for the A-side. 102
45 Δt distributions after the HPTDC calibration for the run 429027 with a double Gaussian fitted curve overlaid for all combinations of the ToF channels in train 0 for the C-side. 103
46 Δt distributions after the HPTDC calibration for the run 429027 with a double Gaussian fitted curve overlaid for all combinations of the ToF channels in train 1 for the C-side. 104
47 Δt distributions after the HPTDC calibration for the run 429027 with a double Gaussian fitted curve overlaid for all combinations of the ToF channels in train 2 for the C-side. 105

48 Δt distributions after the HPTDC calibration for the run 429027 with a double Gaussian fitted curve overlaid for all combinations of the ToF channels in train 3 for the C-side. 106
49 Δt distributions after the HPTDC calibration for the low-μ run 428770 with a double Gaussian fitted curve overlaid for all combinations of the ToF channels in train 0 for the A-side. 107
50 Δt distributions after the HPTDC calibration for the low-μ run 428770 with a double Gaussian fitted curve overlaid for all combinations of the ToF channels in train 1 for the A-side. 108
51 Δt distributions after the HPTDC calibration for the low-μ run 428770 with a double Gaussian fitted curve overlaid for all combinations of the ToF channels in train 2 for the A-side. 109
52 Δt distributions after the HPTDC calibration for the low-μ run 428770 with a double Gaussian fitted curve overlaid for all combinations of the ToF channels in train 3 for the A-side. 110
53 Δt distributions after the HPTDC calibration for the low-μ run 428770 with a double Gaussian fitted curve overlaid for all combinations of the ToF channels in train 0 for the C-side. 111
54 Δt distributions after the HPTDC calibration for the low-μ run 428770 with a double Gaussian fitted curve overlaid for all combinations of the ToF channels in train 1 for the C-side. 112
55 Δt distributions after the HPTDC calibration for the low-μ run 428770 with a double Gaussian fitted curve overlaid for all combinations of the ToF channels in train 2 for the C-side. 113
56 Δt distributions after the HPTDC calibration for the low-μ run 428770 with a double Gaussian fitted curve overlaid for all combinations of the ToF channels in train 3 for the C-side. 114
57 Δt distributions after the likelihood cleanup procedure for the run 429027 with a Gaussian fitted curve overlaid for all combinations of the ToF channels in train 0 for the A-side. 115
58 Δt distributions after the likelihood cleanup procedure for the run 429027 with a Gaussian fitted curve overlaid for all combinations of the ToF channels in train 1 for the A-side. 116
59 Δt distributions after the likelihood cleanup procedure for the run 429027 with a Gaussian fitted curve overlaid for all combinations of the ToF channels in train 2 for the A-side. 117
60 Δt distributions after the likelihood cleanup procedure for the run 429027 with a Gaussian fitted curve overlaid for all combinations of the ToF channels in train 3 for the A-side. 118
61 Δt distributions after the likelihood cleanup procedure for the run 429027 with a Gaussian fitted curve overlaid for all combinations of the ToF channels in train 0 for the C-side. 119

62 Δt distributions after the likelihood cleanup procedure for the run 429027 with a Gaussian fitted curve overlaid for all combinations of the ToF channels in train 1 for the C-side. 120
63 Δt distributions after the likelihood cleanup procedure for the run 429027 with a Gaussian fitted curve overlaid for all combinations of the ToF channels in train 2 for the C-side. 121
64 Δt distributions after the likelihood cleanup procedure for the run 429027 with a Gaussian fitted curve overlaid for all combinations of the ToF channels in train 3 for the C-side. 122
65 Δt distributions after the likelihood cleanup procedure for the low-μ run 428770 with a Gaussian fitted curve overlaid for all combinations of the ToF channels in train 0 for the A-side. . . . 123
66 Δt distributions after the likelihood cleanup procedure for the low-μ run 428770 with a Gaussian fitted curve overlaid for all combinations of the ToF channels in train 1 for the A-side. . . . 124
67 Δt distributions after the likelihood cleanup procedure for the low-μ run 428770 with a Gaussian fitted curve overlaid for all combinations of the ToF channels in train 2 for the A-side. . . . 125
68 Δt distributions after the likelihood cleanup procedure for the low-μ run 428770 with a Gaussian fitted curve overlaid for all combinations of the ToF channels in train 3 for the A-side. . . . 126
69 Δt distributions after the likelihood cleanup procedure for the low-μ run 428770 with a Gaussian fitted curve overlaid for all combinations of the ToF channels in train 0 for the C-side. . . . 127
70 Δt distributions after the likelihood cleanup procedure for the low-μ run 428770 with a Gaussian fitted curve overlaid for all combinations of the ToF channels in train 1 for the C-side. . . . 128
71 Δt distributions after the likelihood cleanup procedure for the low-μ run 428770 with a Gaussian fitted curve overlaid for all combinations of the ToF channels in train 2 for the C-side. . . . 129
72 Δt distributions after the likelihood cleanup procedure for the low-μ run 428770 with a Gaussian fitted curve overlaid for all combinations of the ToF channels in train 3 for the C-side. . . . 130
73 Efficiencies (%) for the run 429027 for each channel of the ToF with track pointing to train 0 for A (left) and C (right) sides with the requirement "one train ON", (top) and OFF, (bottom) for the "direct numbers" method. Empty boxes represents zero response of the corresponding channel. 131
74 Efficiencies (%) for the run 429027 for each channel of the ToF with track pointing to train 1 for A (left) and C (right) sides with the requirement "one train ON", (top) and OFF, (bottom) for the "direct numbers" method. 132

75 Efficiencies (%) for the run 429027 for each channel of the ToF with track pointing to train 2 for A (left) and C (right) sides with the requirement "one train ON", (top) and OFF, (bottom) for the "direct numbers" method. 133
76 Efficiencies (%) for the run 429027 for each channel of the ToF with track pointing to train 3 for A (left) and C (right) sides with the requirement "one train ON", (top) and OFF, (bottom) for the "direct numbers" method. 134
77 Efficiencies (%) for the low-μ run 428770 for each channel of the ToF with track pointing to train 0 for A (left) and C (right) sides with the requirement "one train ON", (top) and OFF, (bottom) for the "direct numbers" method. Empty boxes represents zero response of the corresponding channel. 135
78 Efficiencies (%) for the low-μ run 428770 for each channel of the ToF with track pointing to train 1 for A (left) and C (right) sides with the requirement "one train ON", (top) and OFF, (bottom) for "direct numbers" method. Empty boxes represents zero response of the corresponding channel. 136
79 Efficiencies (%) for the low-μ run 428770 for each channel of the ToF with track pointing to train 2 for A (left) and C (right) sides with the requirement "one train ON", (top) and OFF, (bottom) for the "direct numbers" method. Empty boxes represents zero response of the corresponding channel. 137
80 Efficiencies (%) for the low-μ run 428770 for each channel of the ToF with track pointing to train 3 for A (left) and C (right) sides with the requirement "one train ON", (top) and OFF, (bottom) for the "direct numbers" method. Empty boxes represents zero response of the corresponding channel. 138
81 Hit correlation map for the high-μ run 429027 for each channel of the ToF with track pointing to train 0 (top left), train 1 (top right), train 2 (bottom left) and train 3 (bottom right) for the A-side with the requirement "one train OFF". 139
82 Hit correlation map for the high-μ run 429027 for each channel of the ToF with track pointing to train 0 (top left), train 1 (top right), train 2 (bottom left) and train 3 (bottom right) for the C-side with the requirement "one train OFF". 140
83 Hit correlation map for the low-μ run 428770 for each channel of the ToF with track pointing to train 0 (top left), train 1 (top right), train 2 (bottom left) and train 3 (bottom right) for the A-side with the requirement "one train OFF". 141
84 Hit correlation map for the low-μ run 428770 for each channel of the ToF with track pointing to train 0 (top left), train 1 (top right), train 2 (bottom left) and train 3 (bottom right) for the C-side with the requirement "one train OFF". 142

85 Hit correlation map for the longest low-μ run so far in Large Hadron Collider (LHC) Run-3, 435229, for each channel of the ToF with track pointing to train 0 (top left), train 1 (top right), train 2 (bottom left) and train 3 (bottom right) for the A-side with the requirement "one train OFF". 143
86 Hit correlation map for the longest low-μ run so far in LHC Run-3, 435229, for each channel of the ToF with track pointing to train 0 (top left), train 1 (top right), train 2 (bottom left) and train 3 (bottom right) for the C-side with the requirement "one train OFF". 144

List of Tables

3.1 Regions for the X-value of the SiT, corresponding to the ToF trains. 35

Chapter 1

Introduction

Many extensions of the Standard Model (SM) use Axions and Axion-like particles (ALPs), which are considered as candidates for the particles that constitute the missing matter in the universe, the so-called dark matter [1, 2]. The ALPs are hypothetical particles with spin 0, which, according to some predictions, can explain the observed lack of Charge conjugation times Parity (CP) violation in quantum chromodynamics [3]. Usually, ALPs couple to fermions only through dimension-five operators proportional to fermion mass. Moreover, (pseudo) scalars predominantly couple to gauge bosons through dimension-five operators containing derivatives [4]. This means that in energy regimes exceeding the top quark mass, ALPs are only accessible through their coupling to the gauge bosons and the Higgs boson. They can be produced in different processes.

At the LHC [5], the electromagnetic fields between colliding protons are strong enough to create strong fluxes of high-energy virtual photons. These photons can interact, for example, by merging together, after which the product can decay into various final states. Photon fusion is a distinctive way of looking for physics Beyond the Standard Model (BSM), as only electromagnetic coupling needs to be considered. This search is therefore independent of the strong and weak coupling forces on which most other LHC searches are based. High-precision measurements of these types of Quantum Electrodynamics (QED) processes can set limits on various theories, and any non-coincidence with SM can indicate the presence of new physics [6].

Photon fusion is also known as light-by-light scattering. Scattering of light by light mediated by ALPs is prohibited in the classical theory of electrodynamics [7]. In various extensions, additional contributions are possible, which makes light-by-light scattering measurements sensitive to physics BSM, which can be used to search for Axion-like particles [4, 8].

In this study, the main focus is on the process of central exclusive di-photon production $pp \to p(\gamma\gamma)p$, which is shown in Figure 1.1.

These di-photon events can be recorded with the ATLAS central detector. The vertex position of di-photons is used as a criterion to distinguish di-photon

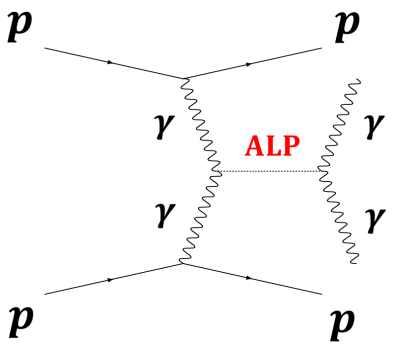

Figure 1.1: Feynman diagram illustrating ALP mediated light-by-light scattering in process of central exclusive di-photons production.

events coming from an ALP signal from di-photon events produced in other background processes. Therefore, an improved di-photon vertex resolution will contribute to better separation of signal and background events.

The ATLAS Forward Proton (AFP) detector [9] is designed to measure trajectories of the leading protons far from the interaction point. After passing through the LHC magnet system, these protons may deviate from the nominal proton beam to such an extent that their deviations can be measured. The two AFP stations are located approximately 210 m on either side of the ATLAS interaction area. The AFP detectors are placed in the so-called Roman Pots (RP). They allow sensitive detectors to be placed close to the beam while maintaining vacuum in the primary beam tube. Position of the deflected protons is measured by the SiT. The forward detector is a useful tool for improvement of the background reduction [10, 11].

The two AFP FAR stations are equipped with the ToF detector. The initial ToF detector performance is determined using July 2022 data. Two data sets were used in this analysis (Section 3.1), which are different from those used in the author's previous study [12].

The resolution of time measurements in individual channels of the ToF detector and the efficiency are evaluated (Chapter 3). In comparison with the author's previous study [12], the efficiency analysis includes an additional comparison of the methods (Section 3.3), a detailed background analysis (Section 3.3.1), and a detailed evaluation of all available 2022 data (Section 3.3.2). The technique for the determination of single-channel resolutions from the author's previous study [12] is improved with an analysis of artefacts of the data (Section 3.2.1). An additional calibration of the data and an extra cleanup requirement are applied for the time resolution analysis (Section 3.2.2).

The capability of the ToF detector to measure the z-coordinate of the primary vertex in interactions of $pp \to pXp$ is investigated (Chapter 4). This analysis follows the author's previous analysis [12] with a different data set. A vertex matching analysis is performed after a necessary time delay calibration.

The ToF detector provides data to improve the vertex reconstruction

(Chapter 5). In particular, for di-photon events, as the photon reconstruction uses data from calorimeters at a large distance from the interaction point.

Chapter 2

Detector design

2.1 ATLAS Central Detector

The ATLAS (A Toroidal LHC ApparatuS) detector [13] is one of the experiments at the LHC at CERN and is a general-purpose detector that covers almost the entire solid angle around the interaction point. It is nominally forward-backward symmetric with respect to the interaction point, having dimensions of 25 m in height, 44 m in length and a weight of approximately 7000 tonnes. The brief scheme of the detector is given in Figure 2.1.

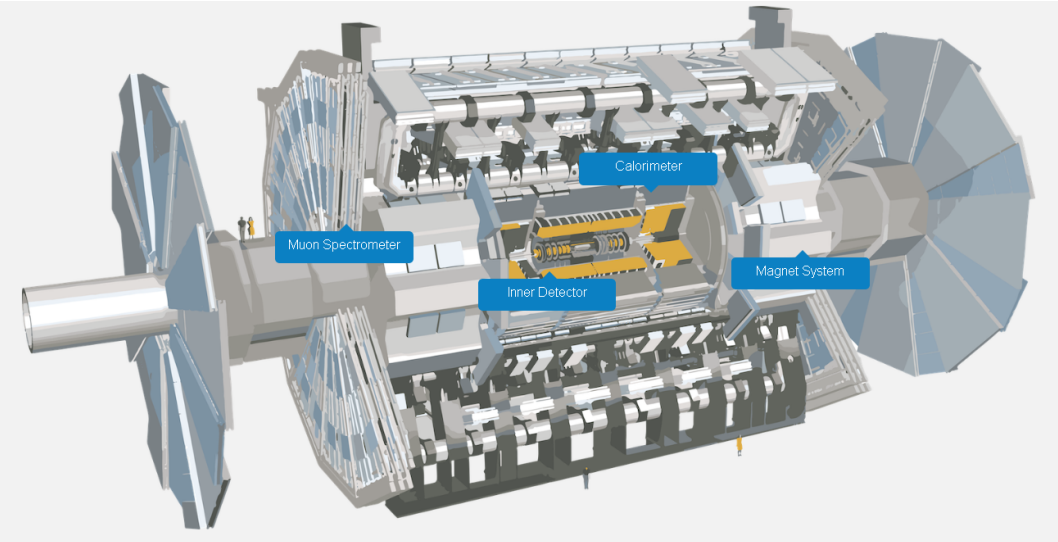

Figure 2.1: Cut-away view of the ATLAS detector.

The central detector consists of 4 layers: the inner detector, the electromagnetic and hadronic calorimeters, and the muon spectrometer.

The inner detector is used to track charged particles in the pseudorapidity region of $|\eta| < 2.5$. It is immersed in a 2 T solenoidal magnetic field. Combination of the inner (discrete high-resolution semiconductor pixel and

strip detectors) and the outer (straw-tube detectors, which can detect transition radiation) parts of the tracking volume are used for momentum and vertex measurements, electron identification, and pattern recognition.

Electromagnetic calorimeter is provided by a high granularity liquid-argon calorimeter and cover the pseudorapidity region of $|\eta| < 3.2$.
The hadronic calorimeter is provided by a scintillator-like calorimeter and cover the range of $|\eta| < 1.7$. Both electromagnetic and hadron energy measurements are taken by the liquid-argon forward calorimeters, they extend pseudorapidity acceptance to the $|\eta| < 4.9$.

The calorimeters are surrounded by the muon spectrometer, which uses high precision tracking chambers and covers regions of $|\eta| < 2.7$. In addition, forward calorimeters cover the region of $3.2 < |\eta| < 4.9$. The ATLAS Forward Proton detectors are described in the next Section 2.2.

2.2 ATLAS Forward Proton Detector

The AFP detector consists of four stations, which are located at approximately 205 m and 217 m - NEAR and FAR stations, on anticlockwise (A) and clockwise (C) sides of the ATLAS interaction region. A plan view of the detector is presented in Figure 2.2.

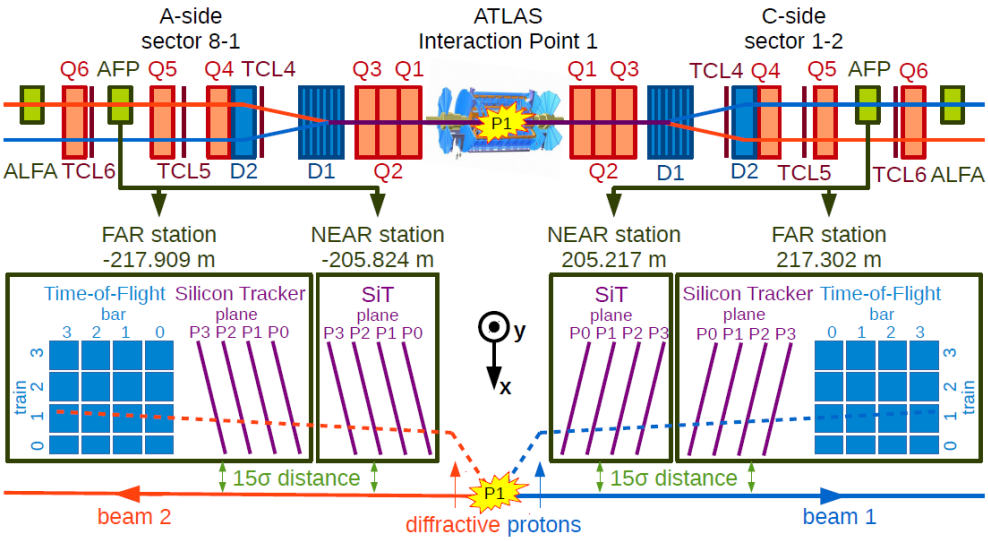

Figure 2.2: AFP design.

The FAR stations are the only ones equipped with the ToF detectors, and therefore only data from them are the subject of this study. In this section only a brief description of the design and function of the AFP and ToF are given, for more detail see [9].

For tracking the SiT is used, which consists of four layers of silicon pixel detectors. The active area of the detector is approximately 20×20 mm^2, the

pixel size is 50×250 μm^2 and they form a pixel grid with a size of 336 by 80 pixels on each SiT plane. The planes of SiT are tilted by 14° providing a spatial resolution of the 10 μm in x and 30 μm in y, as measured in beam tests [14].

2.3 Time-of-Flight Detector

The ToF detectors collect Cherenkov photons created in L-shaped fused silica bars (LQ-bars), which are placed behind the tracker plates. Details of the design are given in [15], only a brief description is provided here. The geometry of the ToF detector was designed to optimize light yield given the space constraints of the Roman Pot stations. The LQ-bar consists of two arms: a radiator arm exposed to beam protons and a light guide arm. The elbow presents an Al-mirror and a taper cut to achieve better focusing of the Cherenkov photons (Figure 2.3).

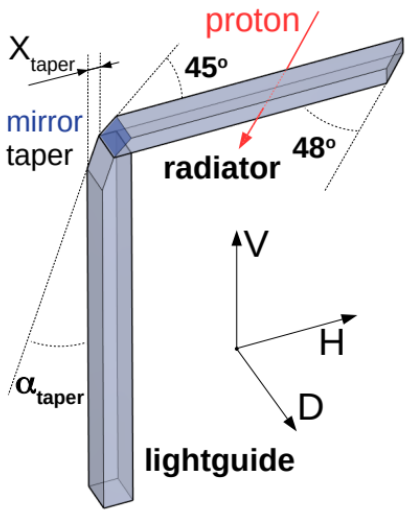

Figure 2.3: ToF LQ-bar design. Vertical × Horizontal × Depth.

Photons emitted along a proton trajectory inside the radiator arm propagate to the light-guide arm and to the end of the bars which is attached to a photo-multiplier. To minimize the number of total reflections, the radiator arms are tilted under the Cherenkov angle of 48° with respect to the beam axis, which leads to the optimization of the time needed for light propagation through the bar. To reflect downward-emitted photons back to the bar, the trailing ends of the radiators are cut parallel to the beam axis. Four bars are placed one after another to form a train. There are four trains on each side. The bars and the corresponding channels are denoted as A, B, C, D (or 0 − 3), bar A being the first one to be crossed by protons. Each ToF detector consists of four trains numbered from 0 to 3, 0 being the closest to the beam.

The geometry of the bars is such that the optical path in all bars is equalized. Figure 2.4 shows the design of the assembled LQ bars and SiT mounted on the Roman Pot flange. The proton beam passes first through the SiT. The direction of the X-axis is up.

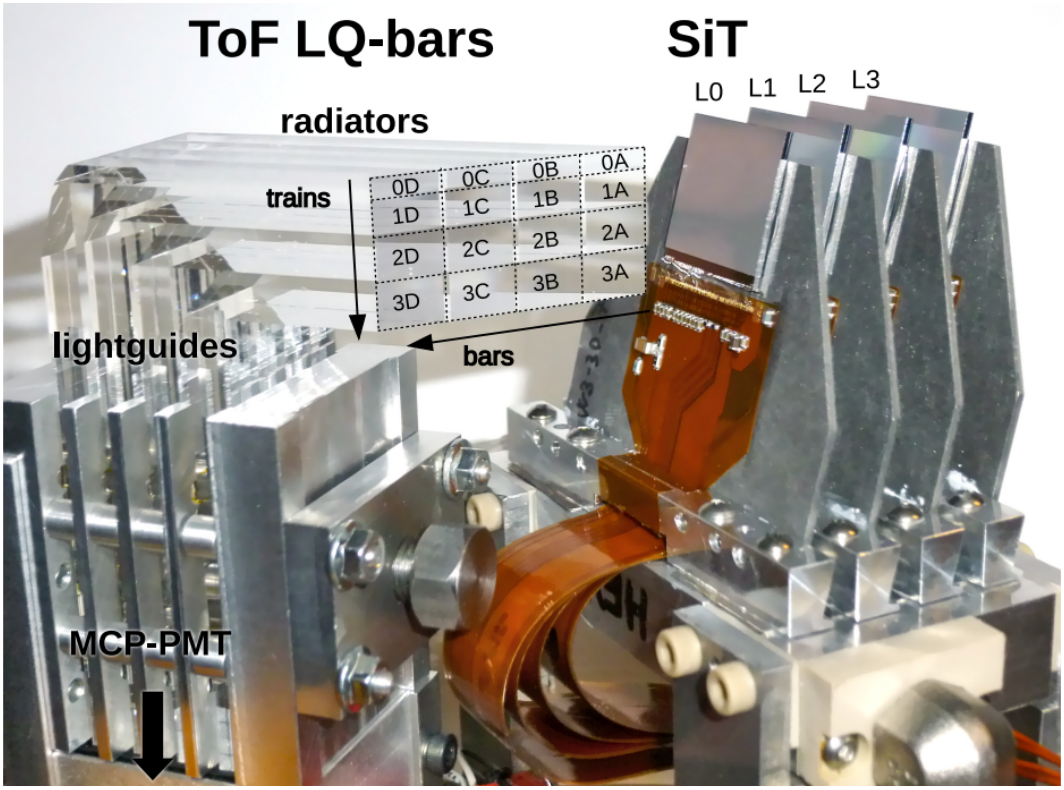

Figure 2.4: AFP SiT and ToF LQ-bars. Proton beam comes from the right side.

The Cherenkov photon statistics translates to the number of photo-electrons via the quantum efficiency of the Photomultiplier Tube (PMT) photo-cathode. The number of photo-electrons is amplified by the high voltage applied to the micro-channel plates of the PMTs. The voltage pulses from the PMT anodes are amplified and processed by a constant fraction discriminator (CFD) [16] providing a square signal for a HPTDC [17]. The signals are sampled in 1024 bins of about 25 ns time window which corresponds to the LHC bunch spacing. The overall time resolution of the detector is therefore affected at several stages during the formation of the signal and its read-out in the front-end electronics [18].

Chapter 3

Analysis of the ToF detector with LHC Run-3 Data

3.1 Data selection

The first analysis of the ToF detector with Run-3 data was performed in the author's previous work [12]. In this analysis I continue ans expand this study.

For the resolution and the efficiency analyses, two runs were chosen, namely 429027 and 428770, different from the author's previous analysis [12]. These runs have a clear step-like structure in the correlation SiT versus ToF data (Figure 3.1), which is required to identify a run that can be used in such a study.

Run 429027 data were collected on July 23, 2022, with CFD [16] thresholds set to 250 mV and corresponds to an ATLAS integrated luminosity of 122.9 pb^{-1}. The average pile-up (number of *pp* collisions in the same beam crossing) for this run was 31.6.

Run 428770 data were collected on July 20, 2022, with CFD [16] thresholds set to 250 mV and corresponds to an ATLAS integrated luminosity of 455.5 nb^{-1}. The average pile-up is 0.05.

The pre-processing of the data included the correction of the channel map and creating n-tuples from Analysis Object Data (AOD) [19] on the grid.

Before obtaining the resolutions and efficiencies, some general requirements on the data sample were applied:

- One track in the SiT per event.
- At most one cluster per plane in the SiT per event.

Additionally two more requirements were used:

- One active train in the ToF per event.
- A cut on measured ToF arriving time period.

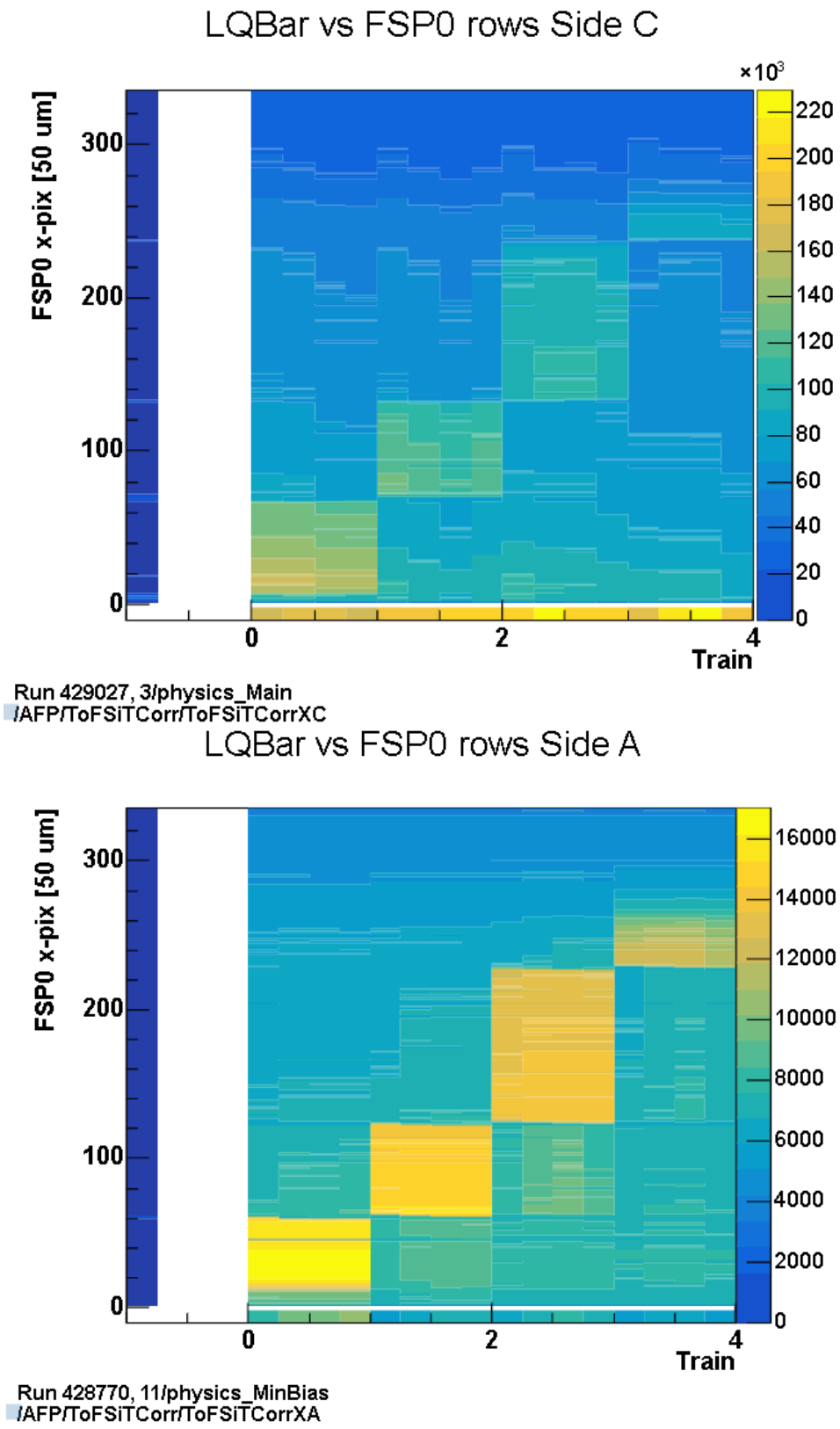

Figure 3.1: Correlation of SiT versus ToF in run 429027 for C-side (top) and run 428770 for the A-side (bottom). The horizontal axis stands for the ToF trains, the vertical axis stands for the X-position in the SiT in mm.

3.2 Time resolution

The HPTDC [17] measures the time in terms of one of the 1024 raw time bin numbers within a 25 ns time window of LHC collisions. In order to estimate the non-linear effects that change the HPTDC raw time bin widths, running the HPTDC in an internal calibration mode can be done. The idea is that irregularities in raw time distributions for uniform input times can be traced back to individual raw time bin widths. The internal HPTDC calibration is not available in data. Therefore, a calibration procedure was developed in previous studies of 2017 data [18]. The circuitry behind the time HPTDC introduces repeating patterns in the raw time distributions. This effect manifests as nearly regular modulation of raw time distributions in the real ToF data (Figure 3.2).

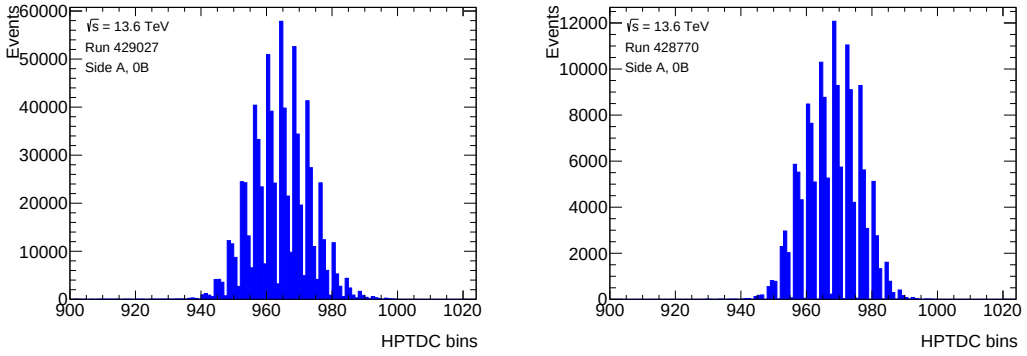

Figure 3.2: Raw time distributions in run 429027 (left) and low-μ run 428770 (right) for side A, channel 0B.

The time stored in the AOD [19] is not in nanoseconds, but in an uncalibrated HPTDC output (raw time). A HPTDC calibration following the 2017 data analysis [18] is performed in Section 3.2.2. The raw time in terms of one of the 1024 HPTDC bin numbers (0 .. 1023) is translated to nanoseconds by

$$\text{time[ns]} = \text{rawbin} \times 25\text{[ns]}/1024.$$

The 25 ns correspond to the 40 MHz LHC frequency.

In the raw time distributions small modulations are seen near the main peaks. This is caused by slower or faster protons spilling into different Radiofrequency (RF) buckets [20] that are associated with the timings of circulating protons in the LHC. One RF bucket is 2.5 ns long. This is the frequency used by the RF cavities to accelerate the beam. The RF buckets are so small in order to make the beam more intense, and only one of ten is used for better bunch separation. These modulations were cleaned to obtain better resolution. This is one of the additional requirements (a cut on measured ToF arriving time period), mentioned before.

Figure 3.3 shows the raw time distribution before and after this additional requirement for only one channel in run 429027 (0A - train 0, bar A), as an

example. Such distributions were created for each ToF channel in both runs and are given in Appendix B.1. The left peak corresponds to the C-side and the right one to the A-side, so they are both plotted on the same histogram.

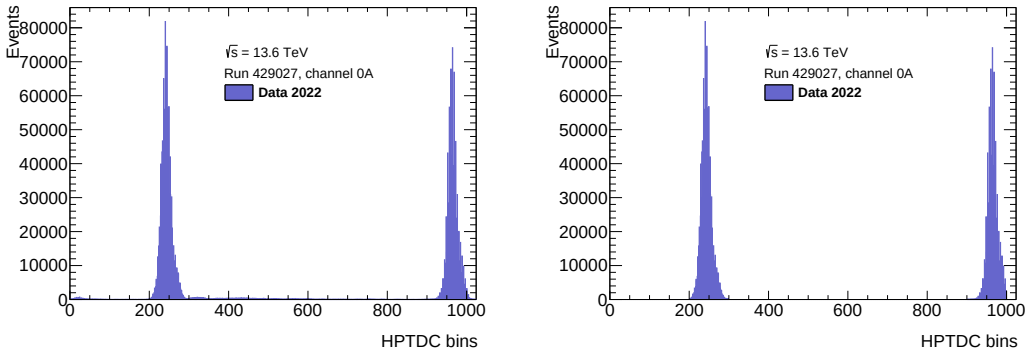

Figure 3.3: Raw time distribution before (left) and after (right) additional cuts on time were applied in the run 429027. The left peak corresponds to the C-side and the right one to the A-side.

Figures 3.4 (run 429027) and 3.5 (run 428770) show the raw time distributions after cleaning the sample, focusing on the main peak. The double-peak structure is observed only in train 3 in both runs. This could be a feature of the ToF construction. It is also possible that the readout is confused between bunch crossings[1].

[1] as discussed at an ATLAS Combined Performance meeting

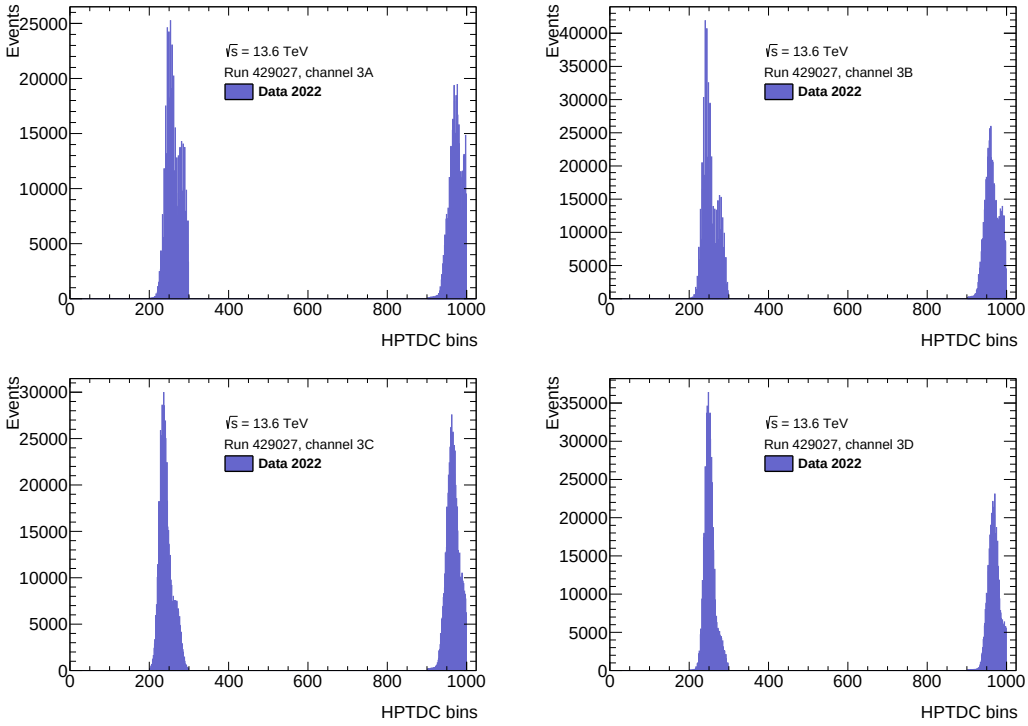

Figure 3.4: Raw time distributions in run 429027 after the cut on the time for train 3 for each channel: A (top left), B (top right), C (bottom left) and D (bottom right).

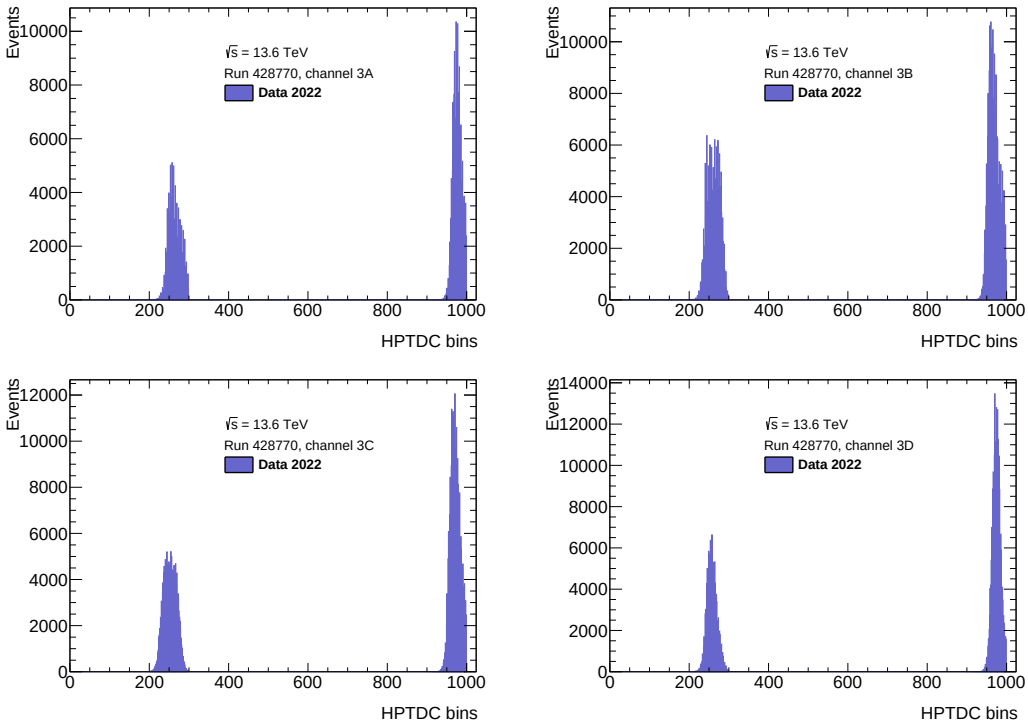

Figure 3.5: Raw time distributions in run 428770 after the cut on the time for train 3 for each channel: A (top left), B (top right), C (bottom left) and D (bottom right).

The previous analysis with 2017 data [18] showed that the HPTDC calibration does not affect much the time resolution. Thus, in the author's previous analysis [12], the calibration was not applied to obtain time resolutions. However, in 2017 data some artefacts of the data were not present due to the different detector configurations. Consequently, as continuation of the author's previous work, the HPTDC calibration was done, as described in Section 3.2.2. First, the procedure of obtaining the single-channel time resolutions is described before the HPTDC calibration for comparison.

The resolutions were obtained as single-channel resolutions for each channel of the ToF. The following requirements were imposed on the data:

- One track in the SiT per event.
- At most one cluster per plane in the SiT per event.
- Cut on measured ToF arriving time period.
- One active train in the ToF per event.

The widths of the Δt distributions will serve for the determination of the single-channel time resolutions. The Δt here stands for the difference of arrival times in two ToF channels, i and j. There are six Δt values, however, there are only four channels, thus the single-channel resolutions will be obtained using chi-squared minimization [18]. We assume no correlations, which requires a separate study, and set $\rho_{ij} = 0$.

$$\chi^2 = \Sigma_{ij} \frac{(\sigma_{ij} - \sqrt{\sigma_i^2 + \sigma_j^2 - 2\rho_{ij}\sigma_i\sigma_j})^2}{(\delta_{\text{fit}}(\sigma_{ij}))^2}, \tag{3.1}$$

The shapes of the distributions are not fully Gaussian, therefore these results assume a Gaussian approximation. In the author's previous analysis [12] single-Gaussian fit and hypothesis of a double-Gaussian shape were tested. Based on this analysis, where double-Gaussian approach was proved to be more precise, in this work sum of two Gaussians is applied to both runs.

Few examples of the Δt distributions before the HPTDC calibration for the run 429027 with a fitted curve overlaid to obtain the widths of the distributions are shown in Figure 3.6 for side A and in Figure 3.7 for side C. All widths are listed in Figure 3.8. All Δt distributions before the HPTDC calibration are given in Appendix B.1.

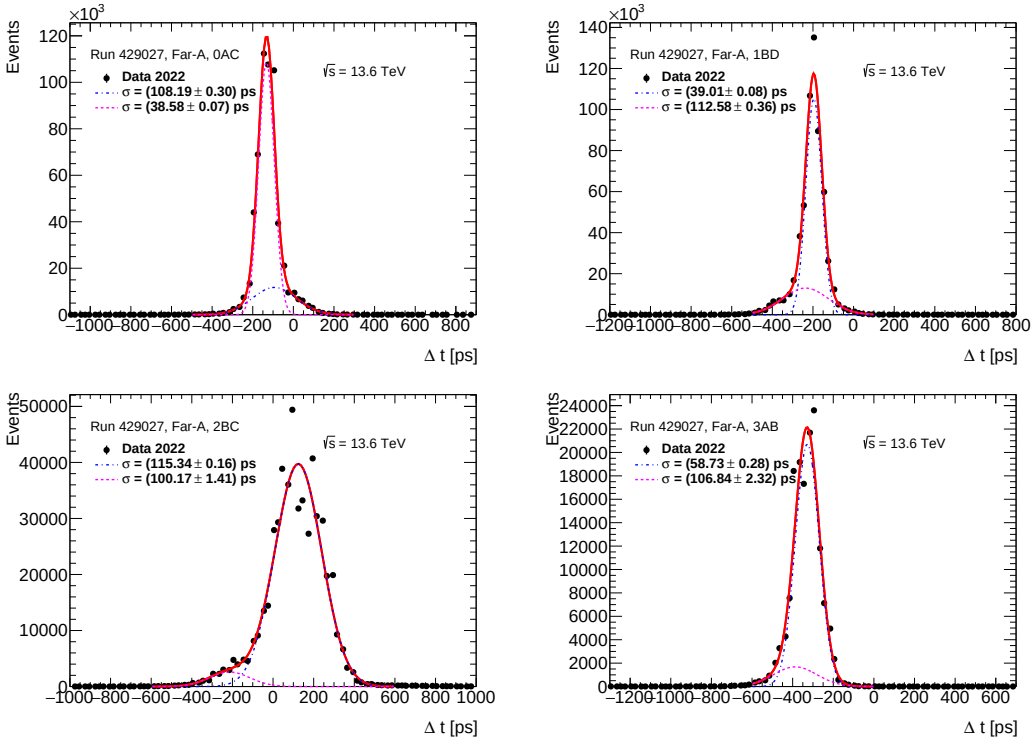

Figure 3.6: Examples of the Δt distributions before the HPTDC calibration for the run 429027 with a double Gaussian fitted curve overlaid for 4 combinations (0AC - top left, 1BD - top right, 2BC bottom left, 3AB bottom right) of the ToF channels for A-side.

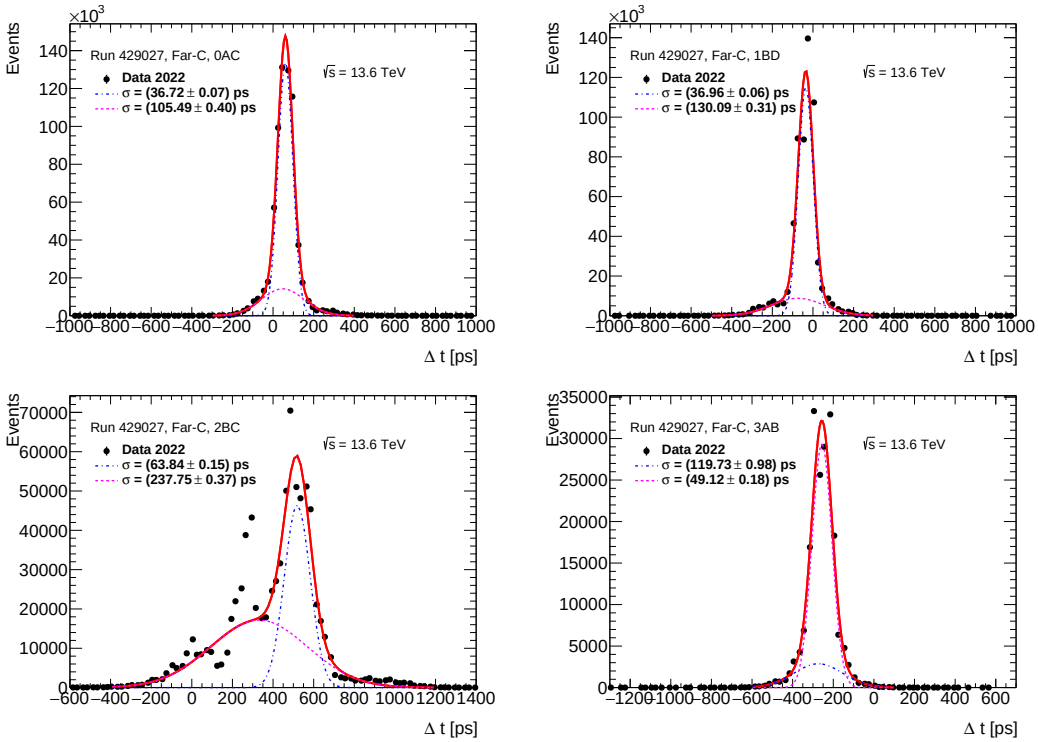

Figure 3.7: Examples of the Δt distributions before the HPTDC calibration for the run 429027 with a double Gaussian fitted curve overlaid for 4 combinations (0AC - top left, 1BD - top right, 2BC bottom left, 3AB bottom right) of the ToF channels for C-side.

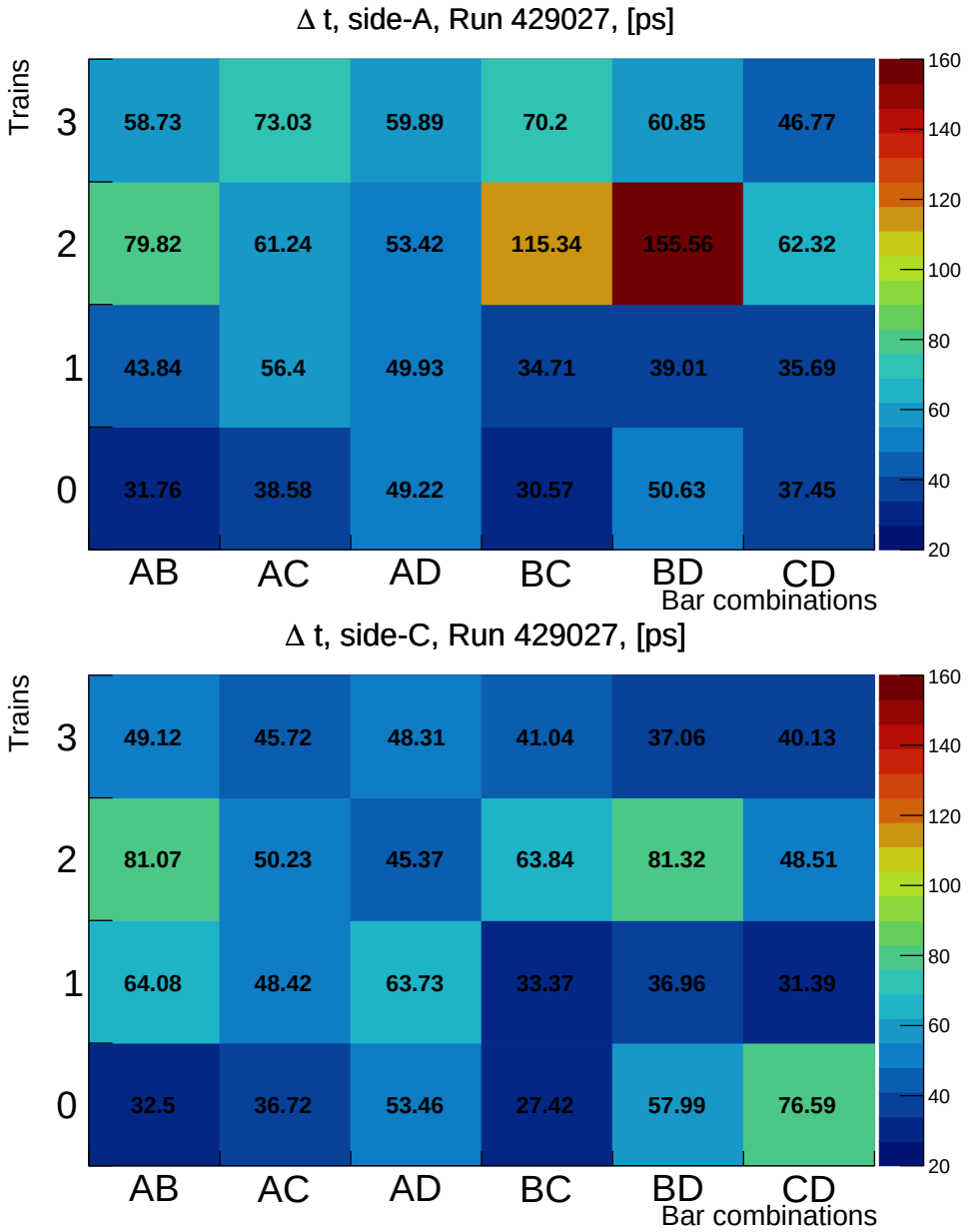

Figure 3.8: Width of Δt (ps) distributions before the HPTDC calibration for the run 429027 using a double Gaussian fit for all combinations of the ToF channels inside one train. Trains: 0-3, bars: A-D.

The resulting time resolutions before the HPTDC calibration for the run 429027 are given in Figure 3.11, as determined from a fit of the six time differences for the four bars as previously proposed [18]. The χ^2 is defined in Equation 3.1 for $\rho_{ij} = 0$. Figures 3.9 and 3.10 show this fit for A and C sides, respectively, with channels combinations on X-axis in the same order as in Figure 3.8 and widths of the Δt distributions on the Y-axis.

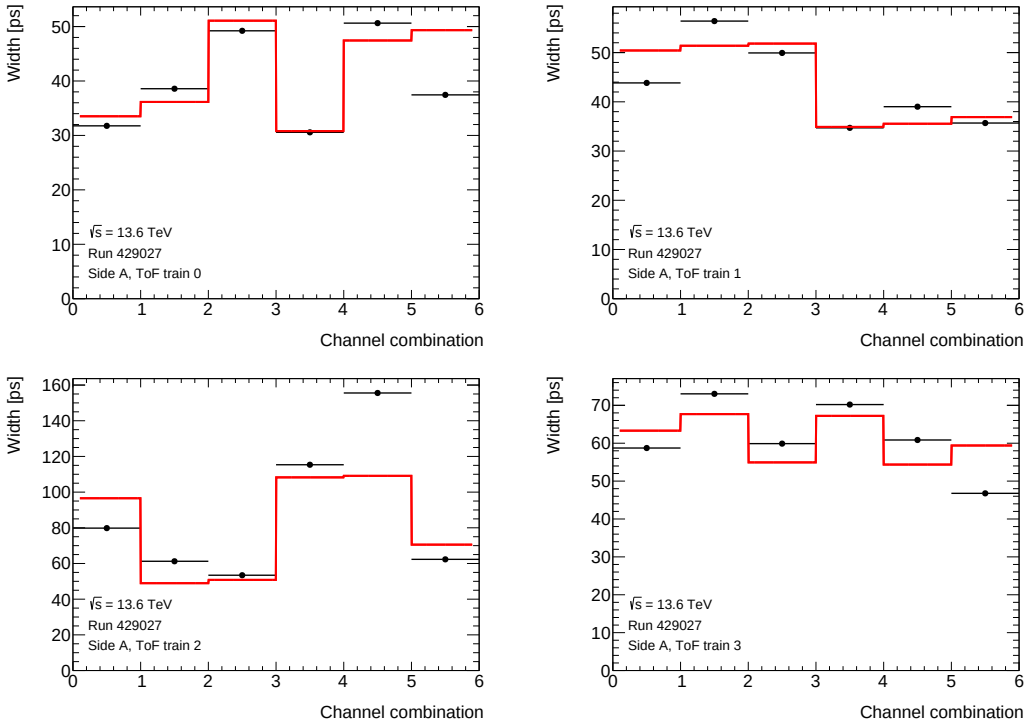

Figure 3.9: Fit of six widths of the Δt distributions for trains 0 (top left), 1 (top right), 2 (bottom left), 3 (bottom right) before the HPTDC calibration for the run 429027, a double Gaussian, for A-side.

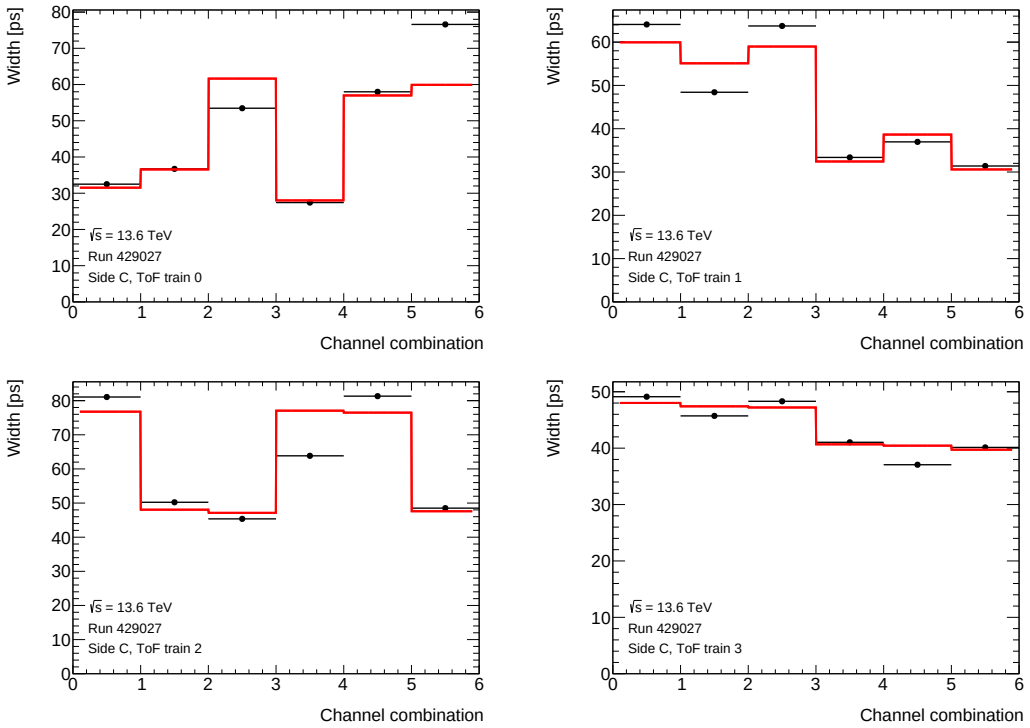

Figure 3.10: Fit of six widths of the Δt distributions for trains 0 (top left), 1 (top right), 2 (bottom left), 3 (bottom right) before the HPTDC calibration for the run 429027, a double Gaussian, for C-side.

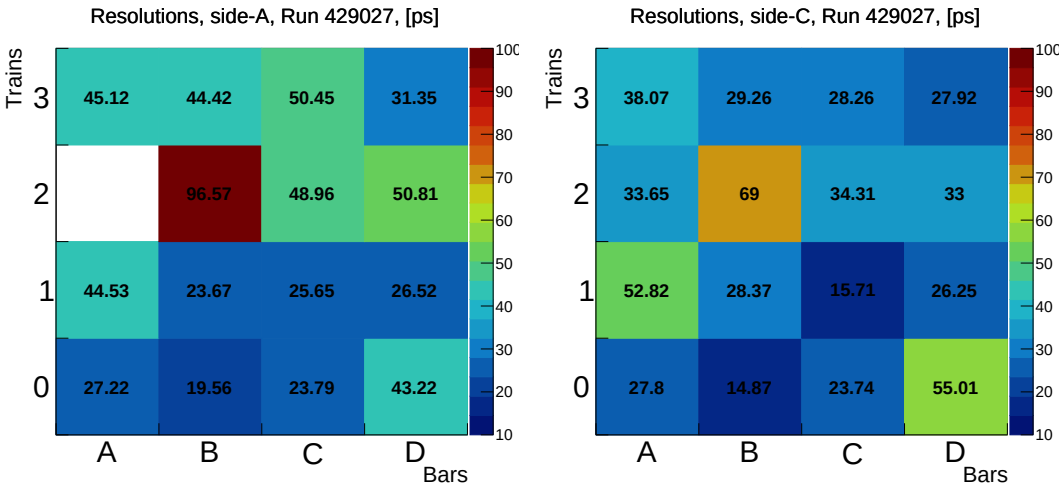

Figure 3.11: ToF time resolution (ps) before the HPTDC calibration for the run 429027, a double Gaussian fit. Trains: 0-3, bars: A-D.

Main purpose of such a fit is to obtain single-channel resolutions (4 channels) from 6 combinations of the ToF channels in one train. Fit is minimizing chi-square, as shown in Equation 3.1. The resulting resolutions for the run 429027 shows that C-side gives better performance than A-side.

The same procedure was also applied to the and low-μ run 428770, only resulting time resolutions before the HPTDC calibration are shown in Figure 3.12.

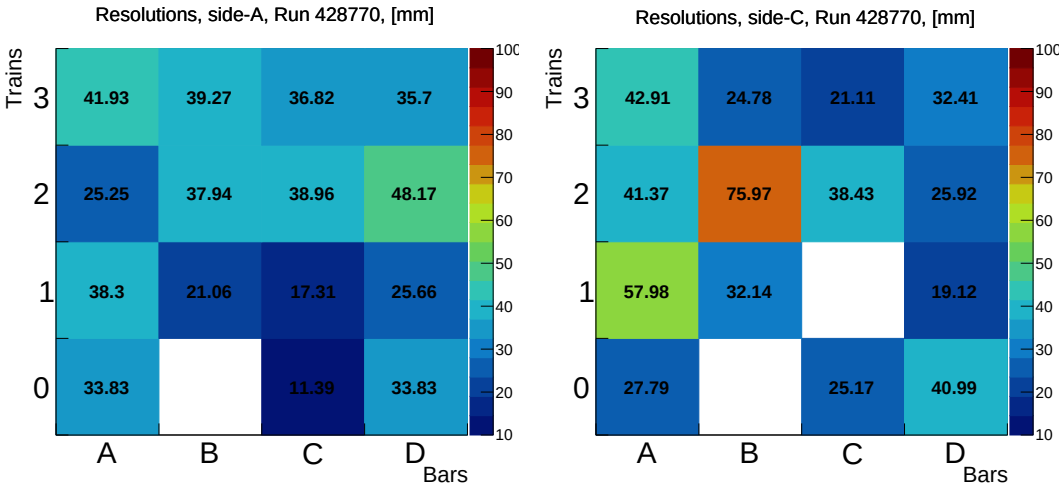

Figure 3.12: ToF time resolution (ps) before the HPTDC calibration for the low-μ run 428770, a double Gaussian fit. Trains: 0-3, bars: A-D.

3.2.1 Multi-peak structure analysis

The Δt distributions (Figures 3.6 and 3.7) are not fully Gaussian and, moreover, sometimes a multi-peak structure was observed. Mainly such structures appear in the train 2 of the ToF detector. Detailed examples of the worst cases are shown in Figure 3.13 for the low-μ run 428770 and the high-μ run 429027. All Δt distributions before the HPTDC calibration are given in Appendix B.1.

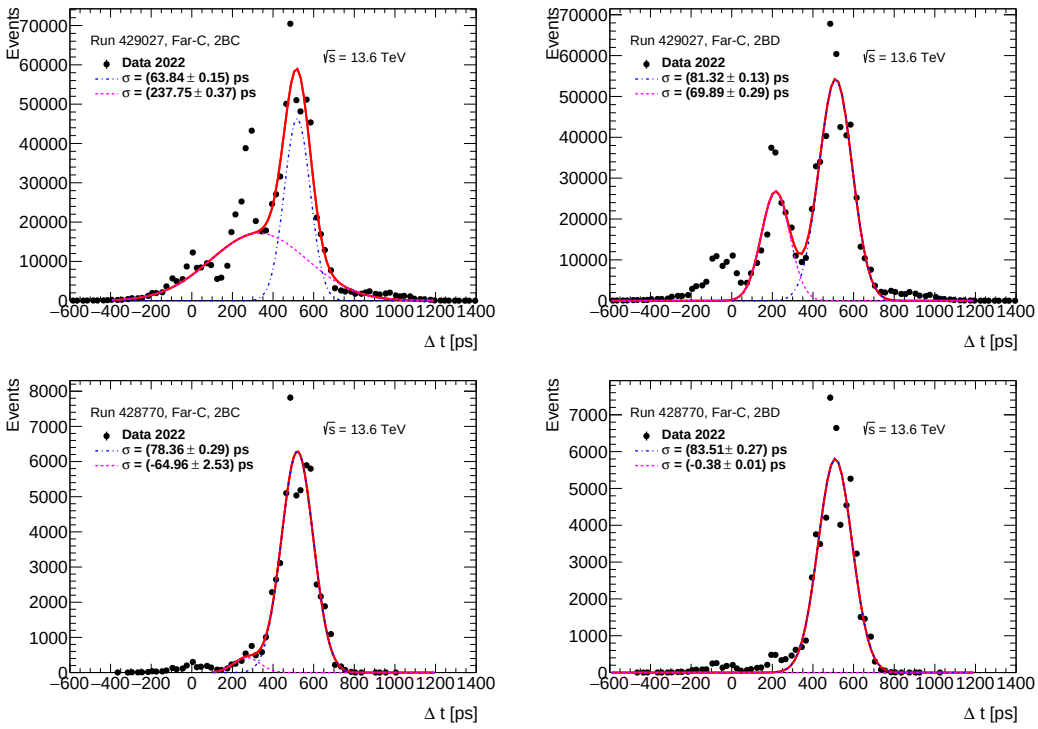

Figure 3.13: Worst cases of the Δt distributions for the high-μ run 429027 (top) and low-μ run 428770 (bottom) for the C-side on examples of the ToF channels 2BC (left) and 2BD (right).

This anomaly of the data significantly worsens single-channel time resolutions, which can be seen most clearly by the worse resolution of the channel 2B on both sides, especially on side-C (Figures 3.11). Side-C has higher efficiency and better performance in general, compared to the side-A. Therefore, side-C is also more sensitive to artifacts in the distributions.

In order to investigate the multi-peak structure, the track profile in the SiT tracker was studied. For this analysis the low-μ run 435229 was taken, the same as was used for efficiency studies in the author's previous work [12]. The reason is to use the longest low-μ run, taken in Run-3 so far, having the highest statistics. The track profile in X and Y axes is shown in Figure 3.14 for the low-μ run 435229 in logarithmic scale on the Z-axis, which is shown in color.

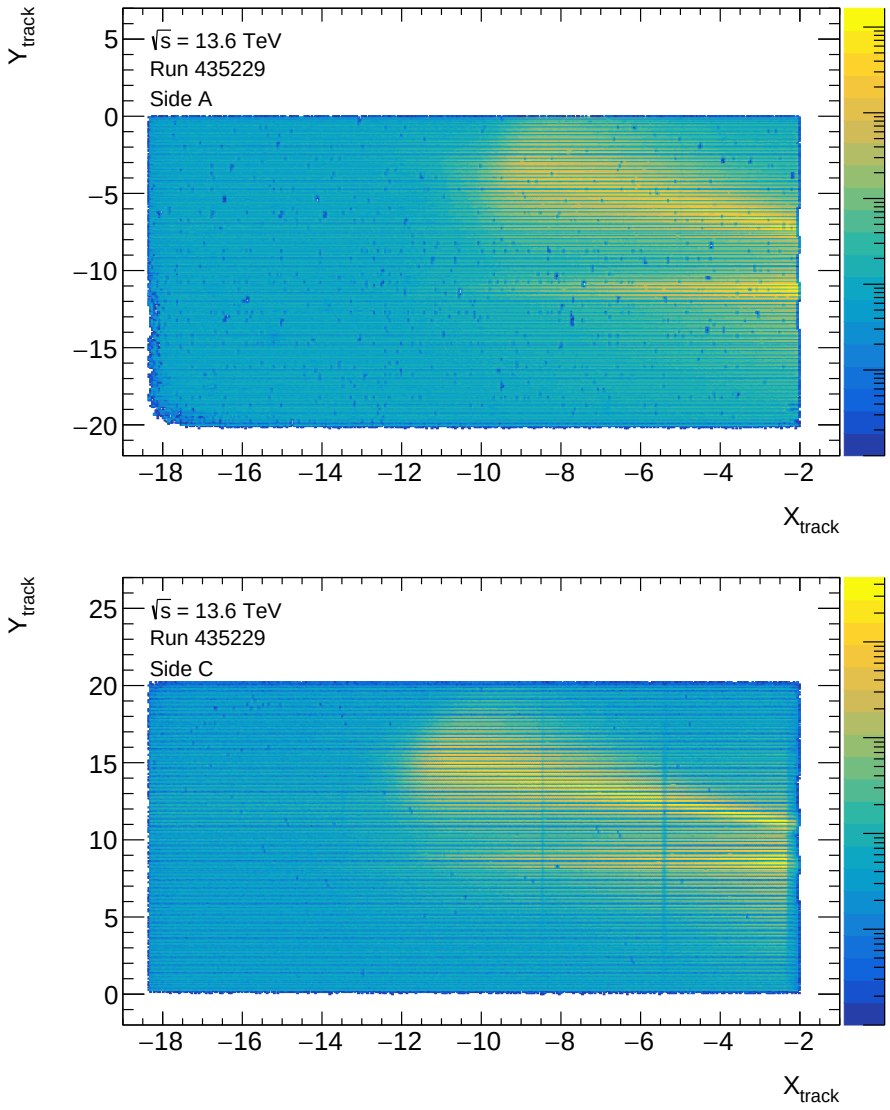

Figure 3.14: Track profile in SiT tracker in logarithmic scale on the color Z-axis for the low-μ run 435229 for the A-side (top) and C-side (bottom).

Clear indications of tracks in the X-Y plane can be seen, main one and additional one, which goes horizontally. This trace was considered as possible candidate for the reason for the multi-peak structures in Δt distributions. In order to check this hypothesis, the track profile was checked on a few high-μ runs. As example, run 429027 is shown in Figure 3.15. This run has a clear trace of the main track, however, no additional trace was observed. Nevertheless, the multi-peak structure in the high-μ runs is even more visible than in the low-μ runs. Based on this study, it was preliminary concluded[2] that the additional trace is not the main reason for the multi-peak structure.

[2]as discussed at an ATLAS Combined Performance meeting

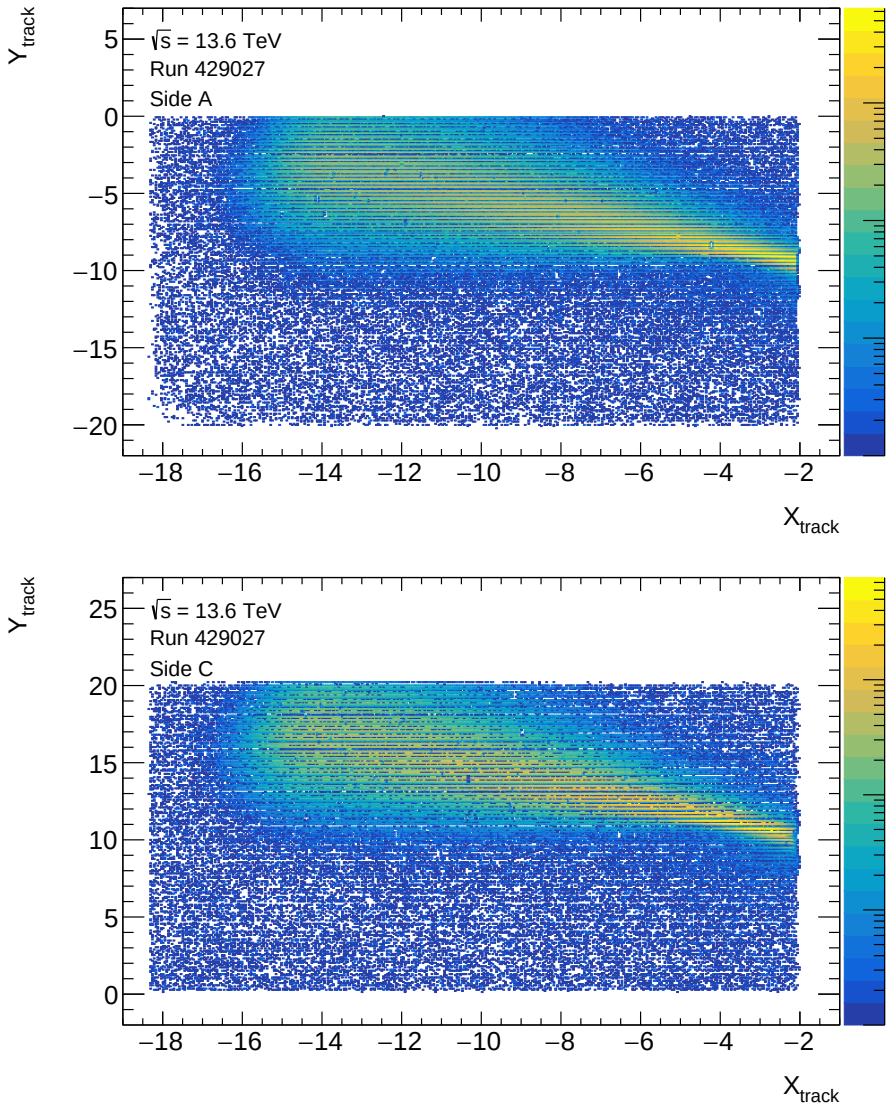

Figure 3.15: Track profile in SiT tracker in logarithmic scale on the color Z-axis for the high-μ run 429027 for the A-side (top) and C-side (bottom).

Nevertheless, the hypothesis for the appearance of the additional trace was put forward. The low-μ run 435229 was the longest Run-3 run so far with a duration of 2 days and 20 hours. Therefore, there is a non-zero possibility of optics settings changes during this long run. In this case the first trace corresponds to one set of settings, and another one to second set. To check this hypothesis the track profile was checked regardless on the different time ranges in the run. If in each time range of the run only one trace is observed, it could explain the double peak.

It turned out that was not the case, and both main and additional traces were observed in each time range of the run. Consequently, the reason for appearance of the additional trace remains to be determined.

3.2.2 HPTDC calibration

The reason for the appearance of the multi-peak structures is not yet determined, nonetheless, the single-channel time resolutions can be calculated more precisely than it was done in the beginning of the Section 3.2. Parasitic multi-peak structures can be cleaned using a likelihood cleanup approach to the data with a principal Gaussian from a multiple-Gaussian fit of the Δt distributions. To perform this procedure, data should be smooth, free of the HPTDC binning artefacts.

The modulations in the uncalibrated ToF data, introduced by the circuitry behind the time HPTDC, can be suppressed in the space of discrete Fourier transform of the raw time distributions. The time distributions can be reconstructed by inverse transform represent the reference for the calculation of the underlying HPTDC bin widths. The method was developed in previous studies of 2017 data [18].

The inverse Fast Fourier Transform (FFT) with magnitudes of the FFT coefficients corresponding to the oscillations suppressed was performed. Such a uniform raw time distribution was considered as a reference. From this reference, the raw distributions can fluctuate upwards or downwards in cases where the physical bin width of the HPTDC is wider or narrower than the nominal one, which is assumed to be 25/1024 ns. After the new bin widths are known, the positions of the bins were shifted. These shifts arise because the widths are no longer trivial, and each bin exerts an influence on the position of all subsequent bins. In addition, the uniform randomization of the raw times across the actual bin widths were done in order to get smooth distributions, especially the Δt ones.

The differences observed in the low statistics tails cause shifts of the bin position corrections, unique for each run. Such artificial shifts can be ignored, since they are absorbed into the constant time delay of each channel in every run.

Figure 3.16 shows examples of the raw time distributions before and after the HPTDC calibration for the side A, channel 0B for both high-μ and low-μ runs. All raw time distributions before and after the HPTDC calibration are given in Appendix B.2.

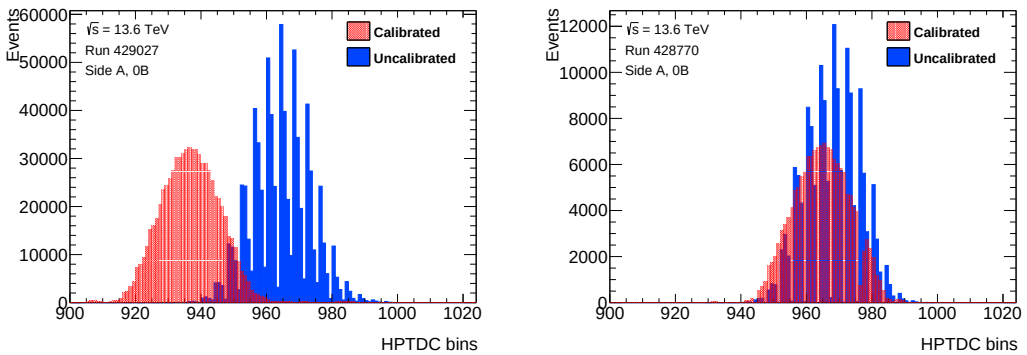

Figure 3.16: Raw time distributions before (blue) and after (red) the calibration in run 429027 (left) and low-μ run 428770 (right) for side A, channel 0B.

A few examples of the Δt distributions after the HPTDC calibration for the run 429027 with a fitted curve overlaid to obtain the widths of the distributions are shown in Figure 3.17 for side A and in Figure 3.18 for side C. The same examples for the low-μ run 428770 are shown in Figure 3.19 for side A and in Figure 3.20 for side C. All Δt distributions after the HPTDC calibration are given in Appendix B.2. Fits for the worst distributions (train 2) were improved with a third Gaussian.

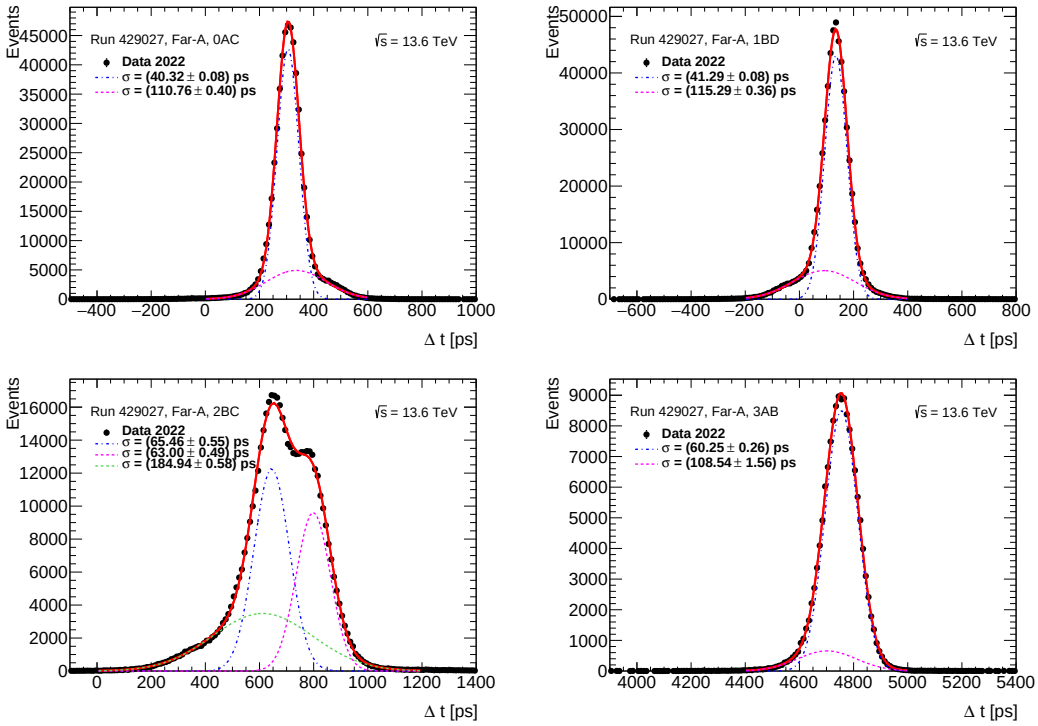

Figure 3.17: Examples of the Δt distributions after the HPTDC calibration for the run 429027 with a multiple-Gaussian fitted curve overlaid for 4 combinations (0AC - top left, 1BD - top right, 2BC bottom left, 3AB bottom right) of the ToF channels for A-side.

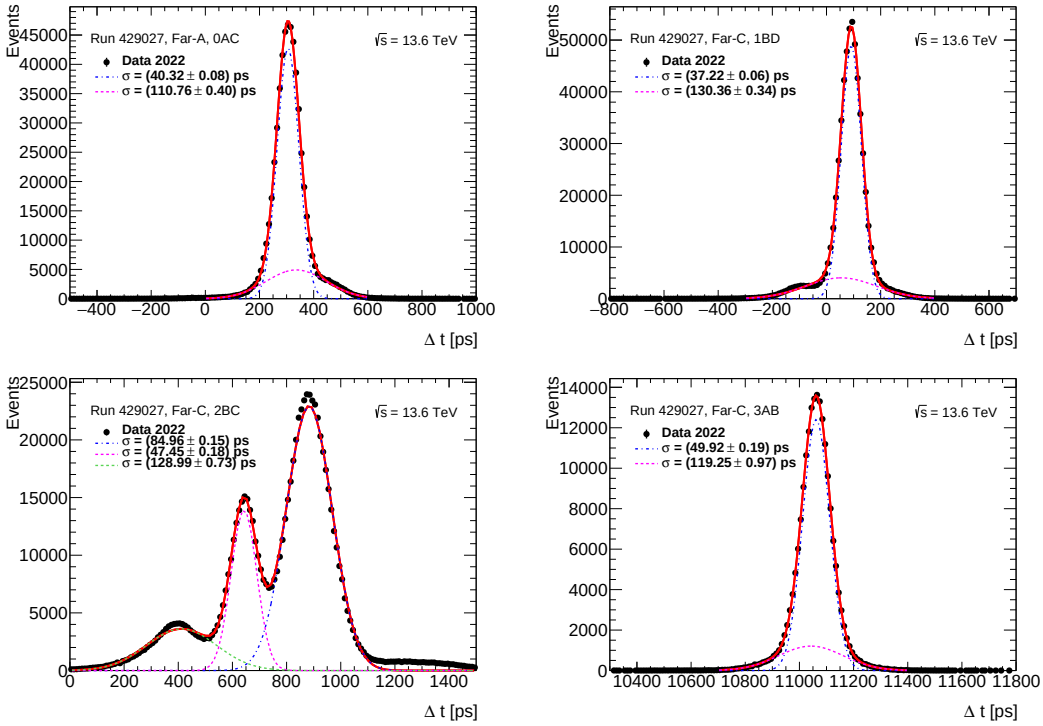

Figure 3.18: Examples of the Δt distributions after the HPTDC calibration for the run 429027 with a multiple-Gaussian fitted curve overlaid for 4 combinations (0AC - top left, 1BD - top right, 2BC bottom left, 3AB bottom right) of the ToF channels for C-side.

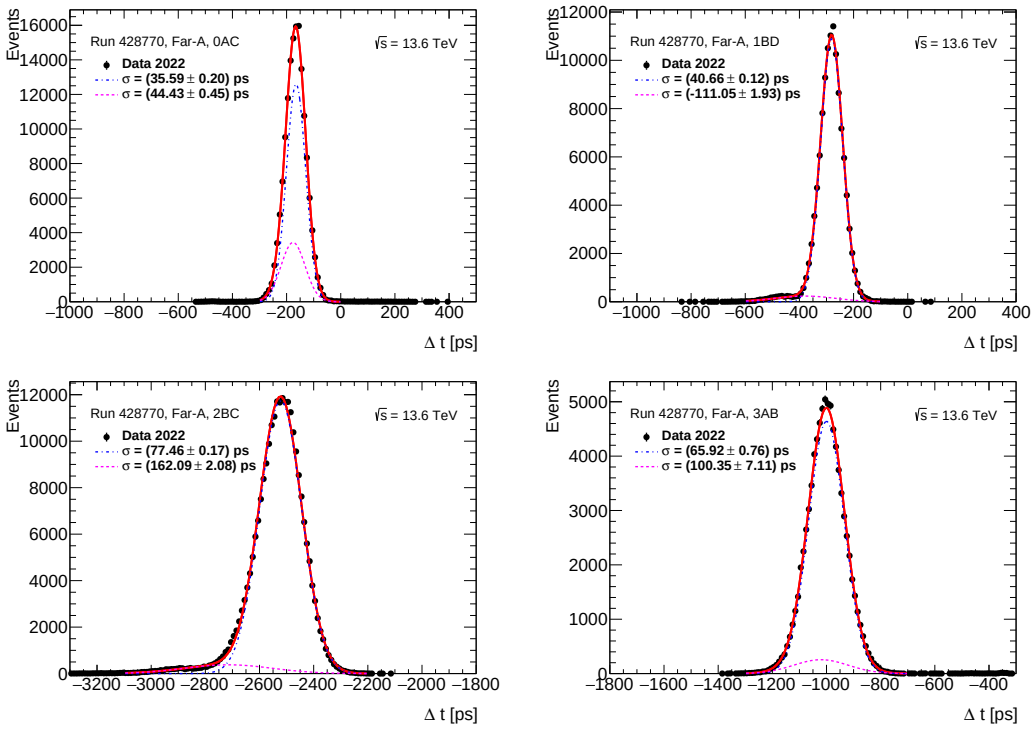

Figure 3.19: Examples of the Δt distributions after the HPTDC calibration for the low-μ run 428770 with a multiple-Gaussian fitted curve overlaid for 4 combinations (0AC - top left, 1BD - top right, 2BC bottom left, 3AB bottom right) of the ToF channels for A-side.

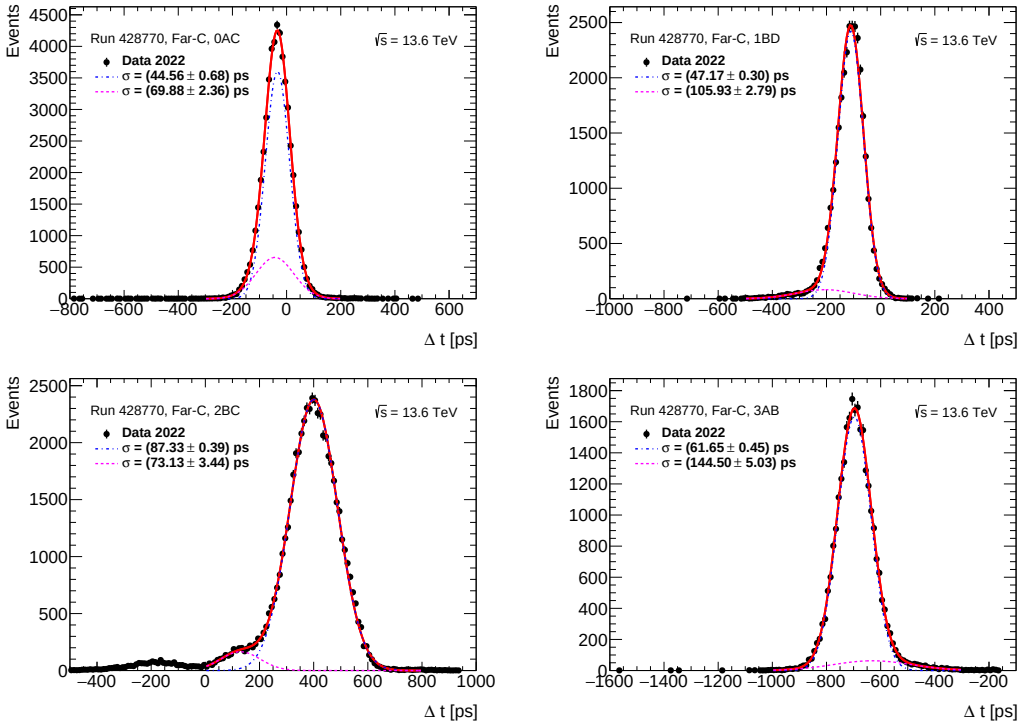

Figure 3.20: Examples of the Δt distributions after the HPTDC calibration for the low-μ run 428770 with a multiple-Gaussian fitted curve overlaid for 4 combinations (0AC - top left, 1BD - top right, 2BC bottom left, 3AB bottom right) of the ToF channels for C-side.

In comparison with the same Δt distributions before the HPTDC calibration, shown in Figures 3.6 and 3.7), the calibrated data is more smooth and better suitable for the fitting and further analysis.

After the calibration was done, a multiple-Gaussian fit was performed and the Gaussian with the highest normalisation (here - blue one) was determined as a principal Gaussian for the Likelihood cleaning procedure. For this approach, the principal Gaussian is chosen from all Gaussians, used for fitting, assuming that one of them contains most of the signal (leading component) and others represent mostly background or problems in the detector readout (sub-leading components). Afterwards, the principal Gaussian (denoted as $f(x)$ below, with its mean value μ) was used as a guide function for the data.

Equation 3.2 represents a general approach of the cleanup cut. Each Δt value in the data is used as variable X for usage in the principal Gaussian function. If a fraction of the mean of the function in this X-point and the mean of the function in Gaussian mean value is less then some random value between 0 and 1, this data point is being cut.

$$\frac{f(x)}{f(\mu)} < R, \tag{3.2}$$

where R is a random number between 0 and 1.

The same examples of the Δt distributions after the likelihood cleanup procedure are shown in Figure 3.21 for side A and in Figure 3.22 for side C for the run 429027 with a fitted curve overlaid to obtain the widths of the distributions. For the low-μ run 428770 results shown in Figure 3.23 for side A and in Figure 3.24 for side C. All these Δt distributions after the likelihood cleanup procedure was applied, are given in Appendix B.3.

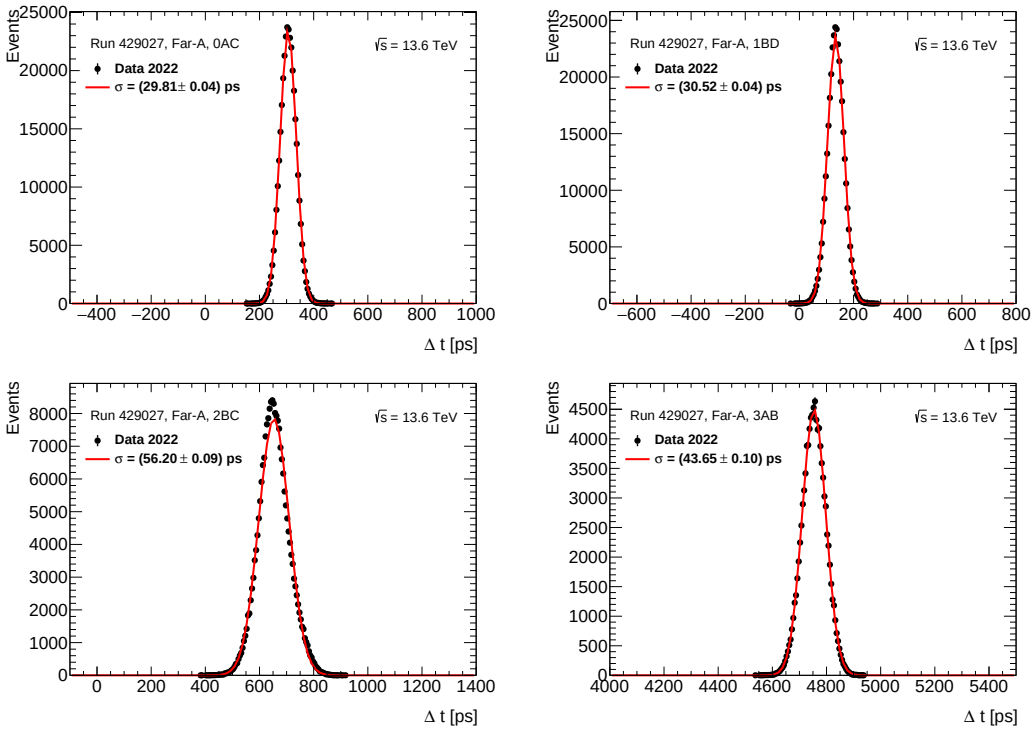

Figure 3.21: Examples of the Δt distributions after the likelihood cleanup procedure was applied, for the run 429027 with a Gaussian fitted curve overlaid for 4 combinations (0AC - top left, 1BD - top right, 2BC bottom left, 3AB bottom right) of the ToF channels for A-side.

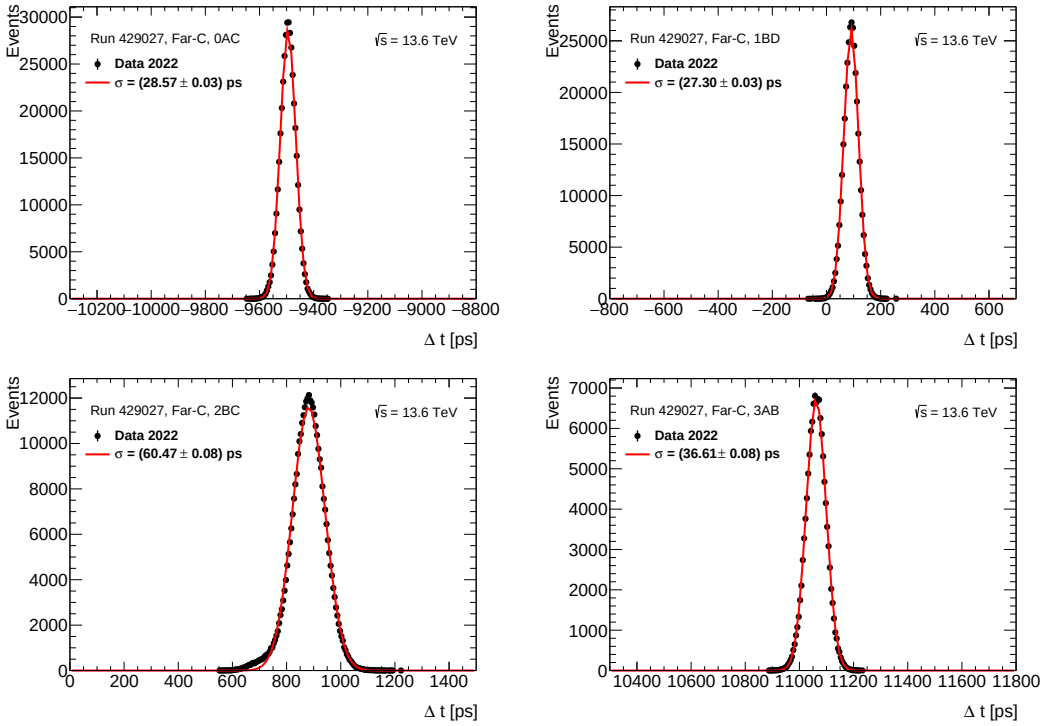

Figure 3.22: Examples of the Δt distributions after the likelihood cleanup procedure was applied, for the run 429027 with a Gaussian fitted curve overlaid for 4 combinations (0AC - top left, 1BD - top right, 2BC bottom left, 3AB bottom right) of the ToF channels for C-side.

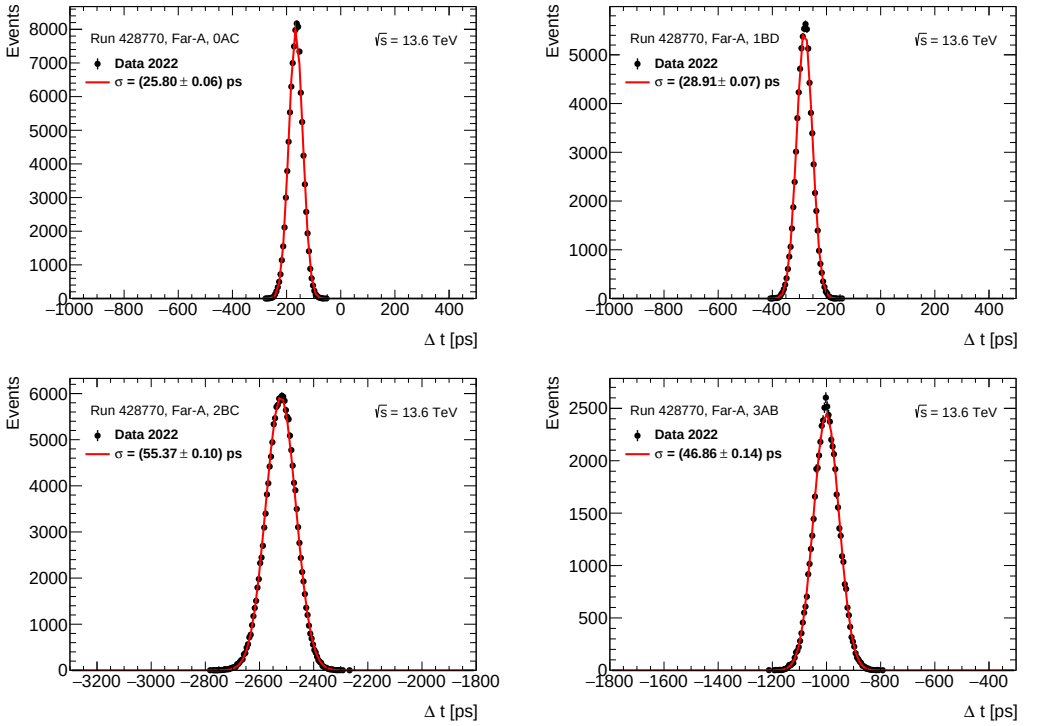

Figure 3.23: Examples of the Δt distributions after the likelihood cleanup procedure was applied, for the low-μ run 428770 with a Gaussian fitted curve overlaid for 4 combinations (0AC - top left, 1BD - top right, 2BC bottom left, 3AB bottom right) of the ToF channels for A-side.

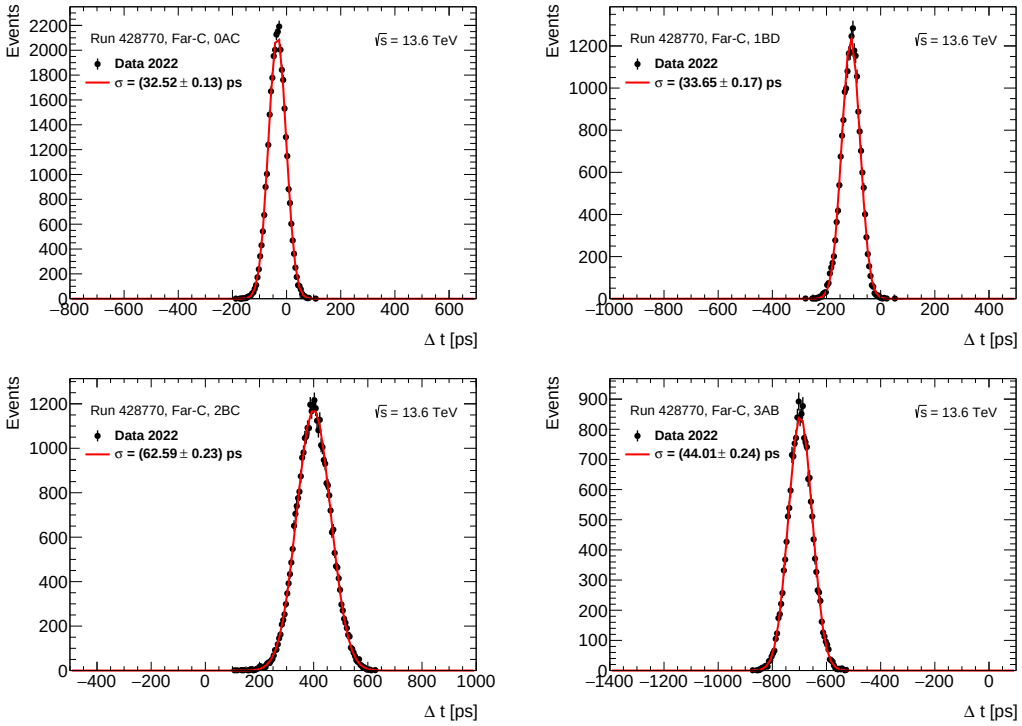

Figure 3.24: Examples of the Δt distributions after the likelihood cleanup procedure was applied, for the low-μ run 428770 with a Gaussian fitted curve overlaid for 4 combinations (0AC - top left, 1BD - top right, 2BC bottom left, 3AB bottom right) of the ToF channels for C-side.

All widths are listed in Figure 3.25 for the high-μ run 429027 and in Figure 3.26 for the low-μ run 428770.

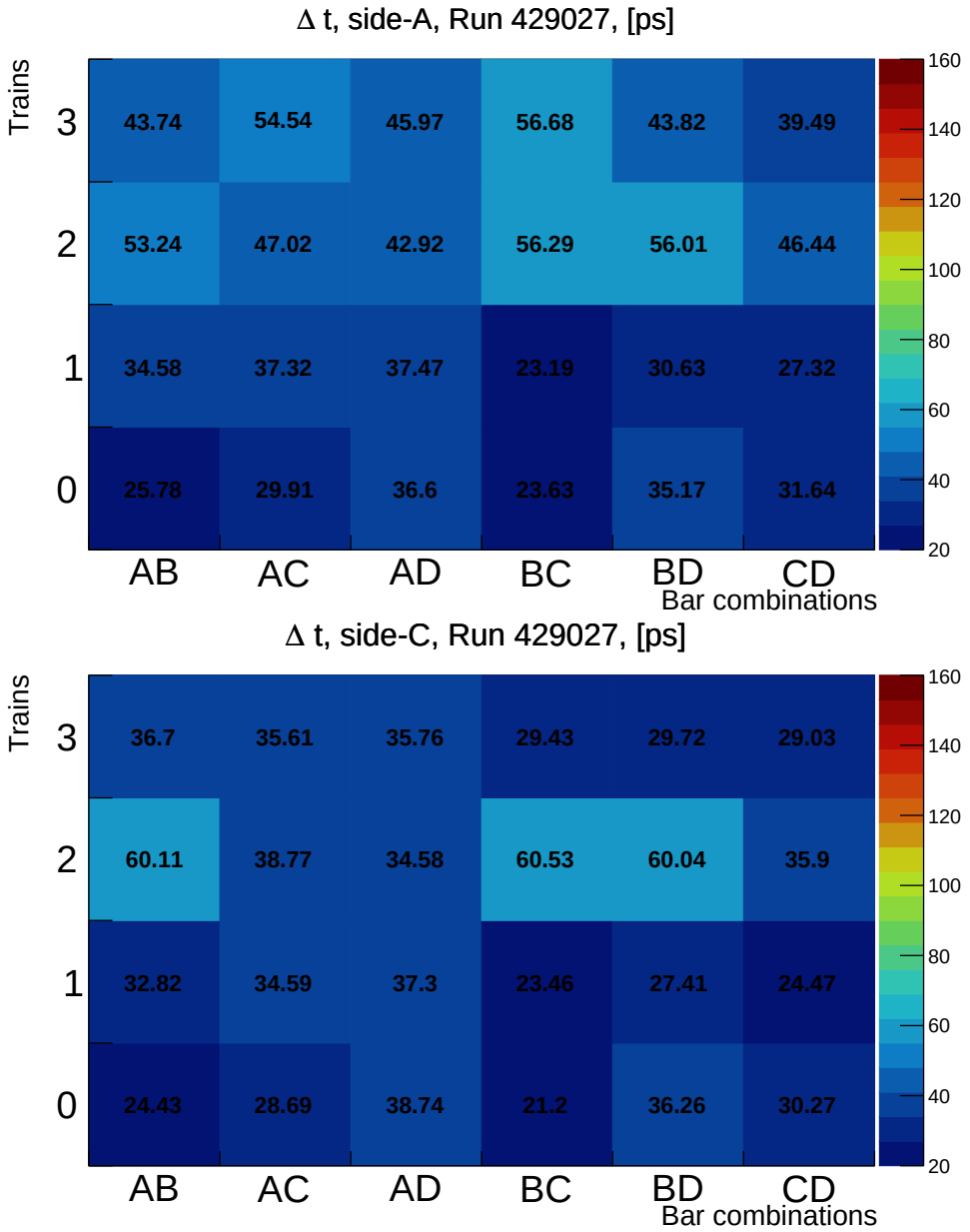

Figure 3.25: Width of Δt (ps) distributions after the likelihood cleanup procedure was applied for the run 429027 using a Gaussian fit for all combinations of the ToF channels inside one train. Trains: 0-3, bars: A-D.

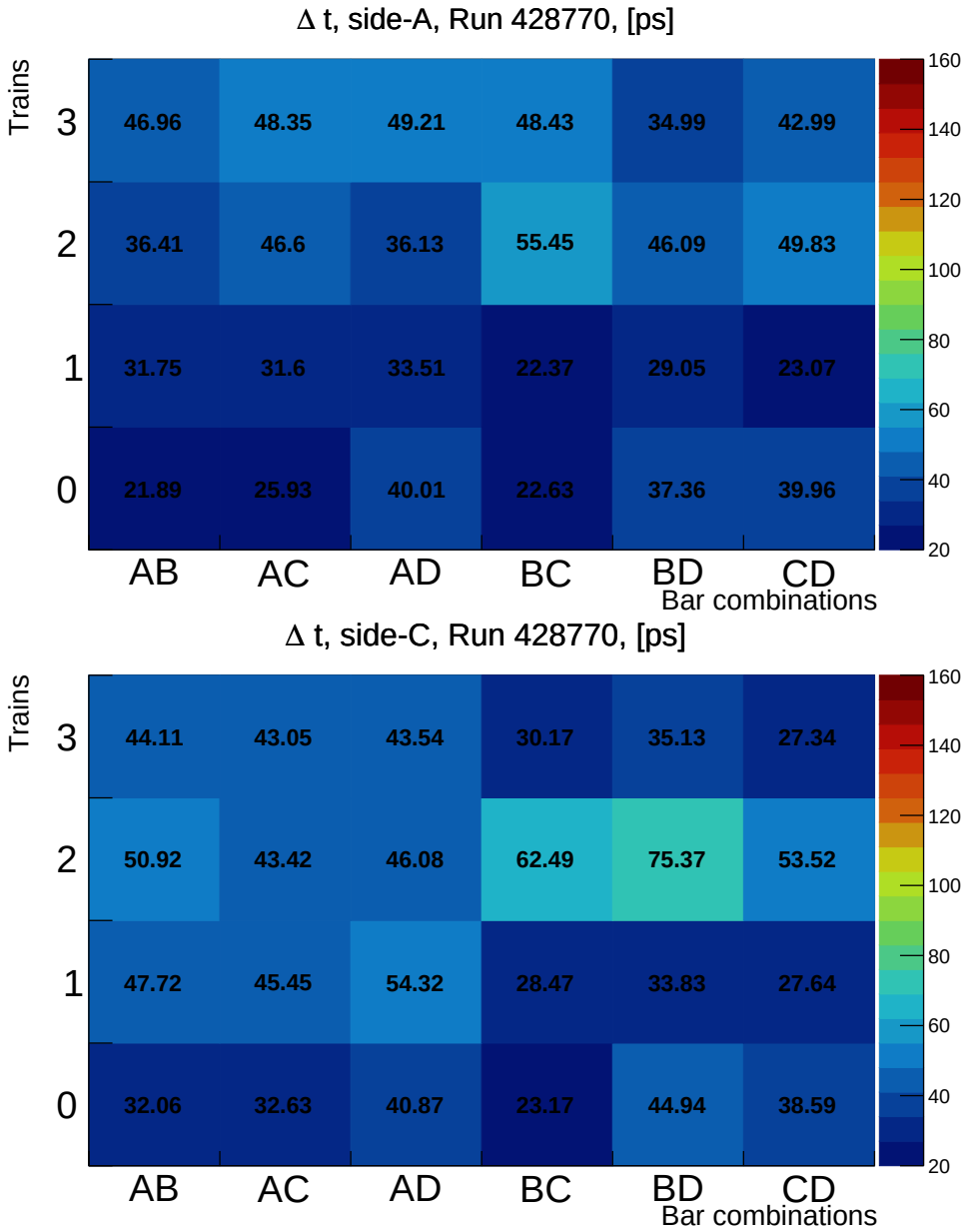

Figure 3.26: Width of Δt (ps) distributions after the likelihood cleanup procedure was applied for the low-μ run 428770 using a Gaussian fit for all combinations of the ToF channels inside one train. Trains: 0-3, bars: A-D.

The resulting time resolutions after the likelihood cleanup procedure was applied for the run 429027 are given in Figure 3.29, as determined from a fit of the six time differences for the four bars as previously proposed [18]. The χ^2 is defined in Equation 3.1 for $\rho_{ij} = 0$. Figures 3.27 and 3.28 show this fit for A and C sides, respectively, with channels combinations on X-axis in the same order as in Figure 3.25 and widths of the Δt distributions on the Y-axis.

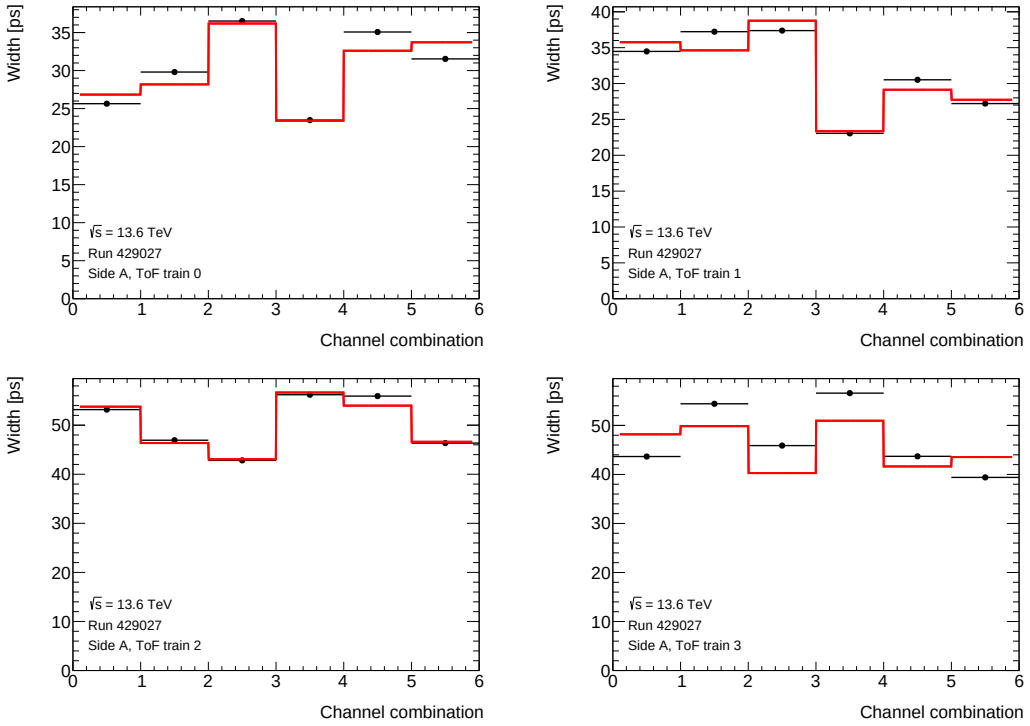

Figure 3.27: Fit of six widths of the Δt distributions for trains 0 (top left), 1 (top right), 2 (bottom left), 3 (bottom right) after the likelihood cleanup procedure was applied, for the run 429027 for A-side.

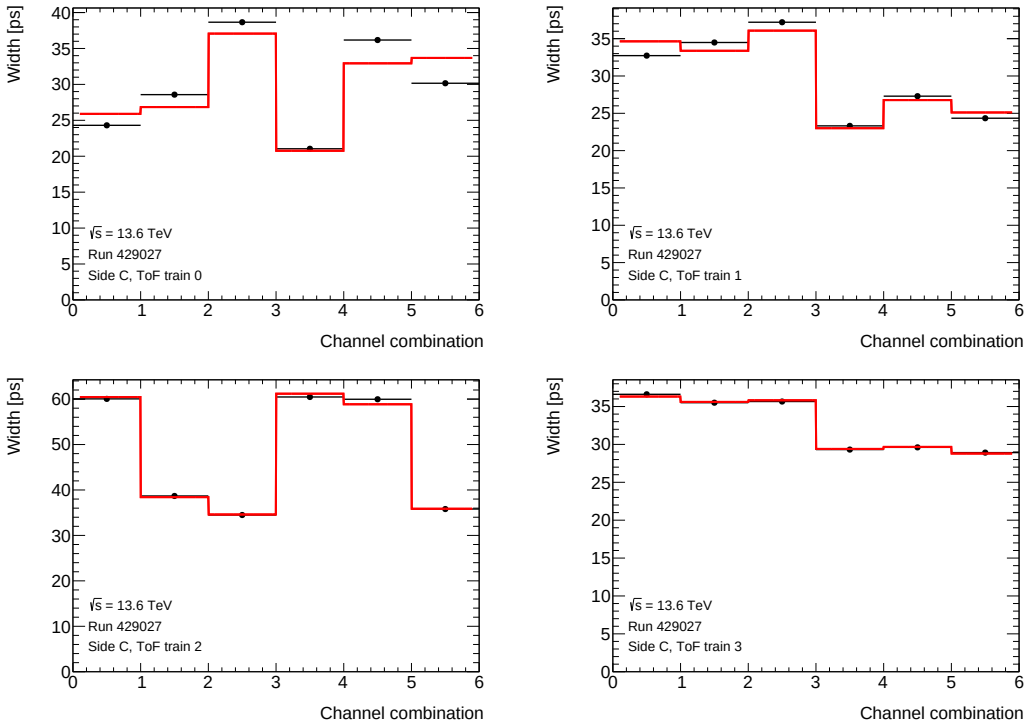

Figure 3.28: Fit of six widths of the Δt distributions for trains 0 (top left), 1 (top right), 2 (bottom left), 3 (bottom right) after the likelihood cleanup procedure was applied, for the run 429027 for C-side.

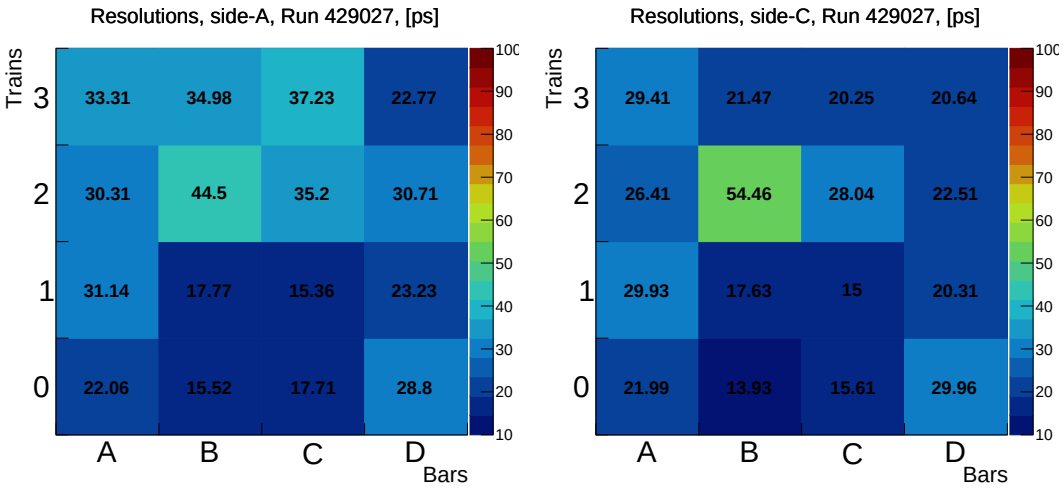

Figure 3.29: ToF time resolution (ps) after the likelihood cleanup procedure was applied, for the run 429027. Trains: 0-3, bars: A-D.

The resulting resolutions after the HPTDC calibration for the run 429027 show that the C-side gives better performance than the A-side.

The same procedure was used on low-μ (low pile-up) run 428770. The resulting time resolutions for the run 428770 are given in Figure 3.32. Figures 3.30 and 3.31 show this fit for A and C sides, respectively, with channels combinations on X-axis in the same order as in Figure 3.26 and widths of the Δt distributions on the Y-axis. The resulting resolutions for the low-μ run 428770 shows that the C-side gives better performance than the A-side, same as it was for the run 429027.

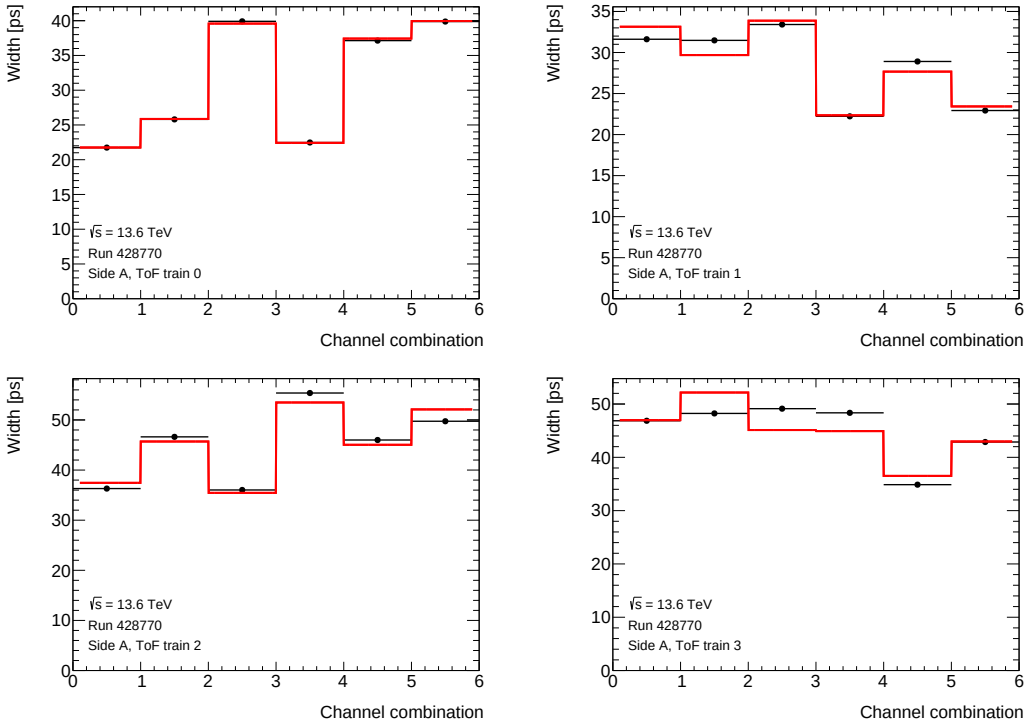

Figure 3.30: Fit of six widths of the Δt distributions for trains 0 (top left), 1 (top right), 2 (bottom left), 3 (bottom right) after the likelihood cleanup procedure was

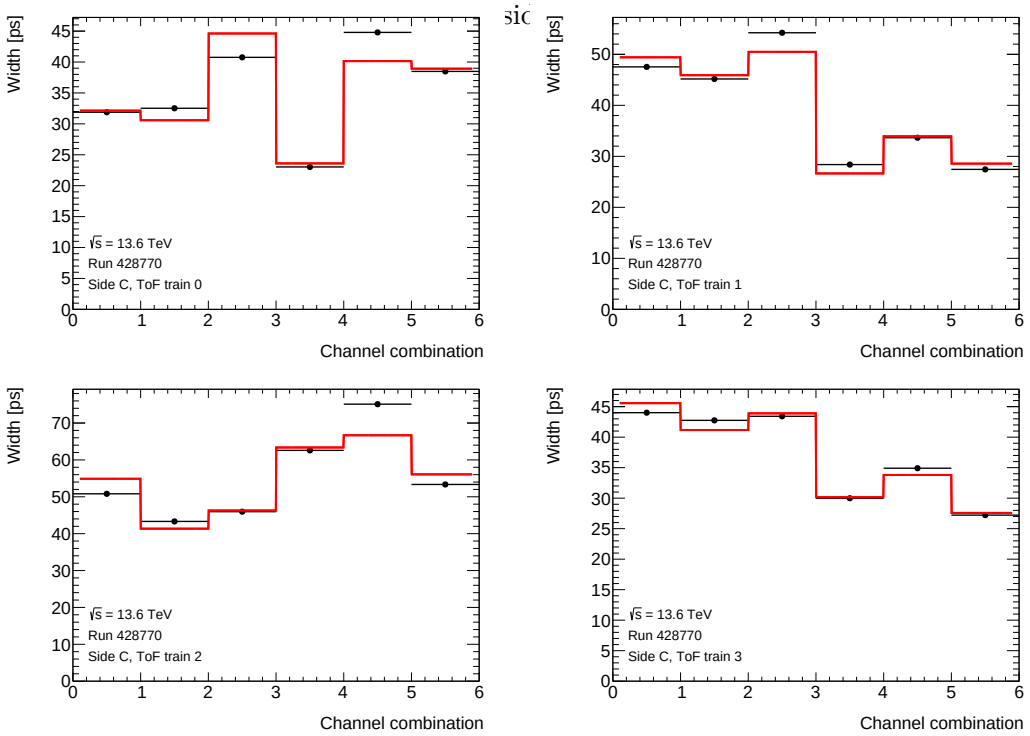

Figure 3.31: Fit of six widths of the Δt distributions for trains 0 (top left), 1 (top right), 2 (bottom left), 3 (bottom right) after the likelihood cleanup procedure was applied, for the low-μ run 428770 for C-side.

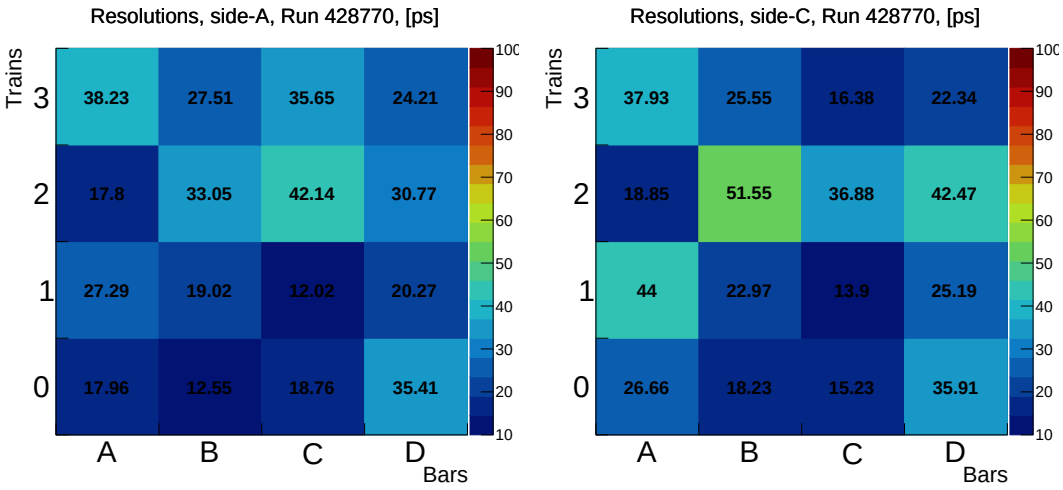

Figure 3.32: ToF time resolution (ps) after the likelihood cleanup procedure was applied, for the low-μ run 428770. Trains: 0-3, bars: A-D.

Comparing the resolutions before the HPTDC calibration and the likelihood cleanup procedure was done, shows an improvement in the final results. They became more uniform and closer to the designed values. The reason for the multiple-peak structures is not determined and fixed yet. Therefore, the presented analysis is most suitable to obtain single-channel resolutions of the ToF detector. Overall, these resolutions are preliminary.

3.3 Efficiency

Information about the reconstructed SiT tracks is stored in the AFPTrackContainer [21]. This container was used as a basis for the measurement of the ToF response. The efficiency in each channel is defined as a fraction based on two samples, first where the given ToF channel provided time information, and second a reference sample of events with reconstructed SiT tracks. Based on the author's previous analysis [12], two methods were used for comparison: dividing histograms and calculating the ratio of sums of events. The reason for the differences in them was studied.

For both methods the following requirements were imposed on the data:

- One track in the SiT per event.
- At most one cluster per plane in the SiT per event.
- One active train in the ToF per event (ON/OFF)

The last requirement was imposed a as cleanup cut to remove unwanted events. However, this requirement decreases the statistics as not all tracks are in one train only. Thus, both cases (ON/OFF) were investigated. For both methods the whole procedure was performed separately for side A and side C.

The regions for the X-value of the SiT, corresponding to the ToF train, were defined for each side (A and C). These regions are shown in Table 3.1.

Train	A-side (mm)	C-side (mm)
0	−4.9 to −2.0	−5.3 to −2.0
1	−8.0 to −5.0	−8.4 to −5.4
2	−13.0 to −8.1	−13.4 to −8.5
3	−15.0 to −13.1	−15.0 to −13.5

Table 3.1: Regions for the X-value of the SiT, corresponding to the ToF trains.

For the first method, dividing histograms, the reference histogram was defined for events passing the selection criteria without the optional requirement (OFF), only for events with reconstructed SiT tracks. The other 16 histograms include (or not, depending on the case under investigation) the additional requirement (ON) for each of the 16 ToF channels.

The next step was dividing each of 16 channel histograms by the reference histogram bin by bin. So, the number of events in each individual bin of one of the 16 histograms of the ToF is divided by the number of events in the corresponding bin of the reference histogram. This ratio defines the efficiency in each bin which is shown in Figure 3.33. The case with the requirement (ON) is shown for the 4 trains, side-A, bar B. In order to define efficiency in each channel the mean value of the bins in the region, corresponding to the exact train, was calculated. For the last train (3) the active region was cut in order to avoid noise, possibly originating from the collimator shadow[3].

The procedure described above is for the case with the requirement (ON). Next, the procedure was repeated without the requirement (OFF) and results are given in Figure 3.34 for the ToF trains of side-A and bar B. Some background is visible for the case without the requirement (OFF), and the reason needs to be further studied.

[3]as discussed at an ATLAS Combined Performance meeting

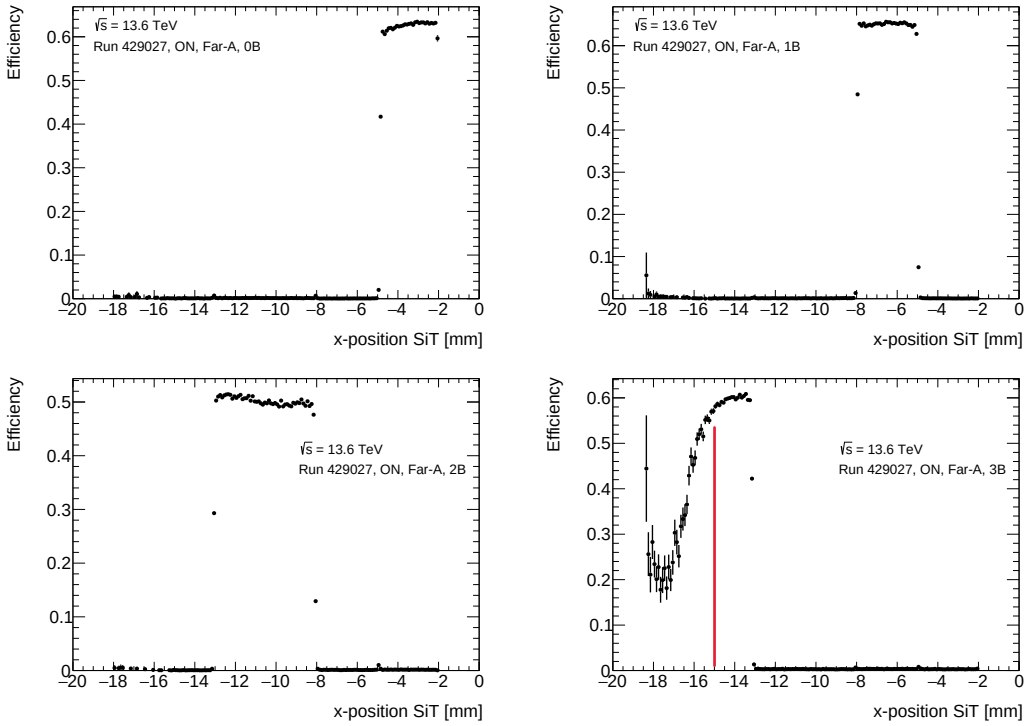

Figure 3.33: Ratios, which define efficiencies for the run 429027, for the case of cuts "one train ON" for A-side for each train and one bar: 0B (top left), 1B (top right), 2B (bottom left) and 3B (bottom right).

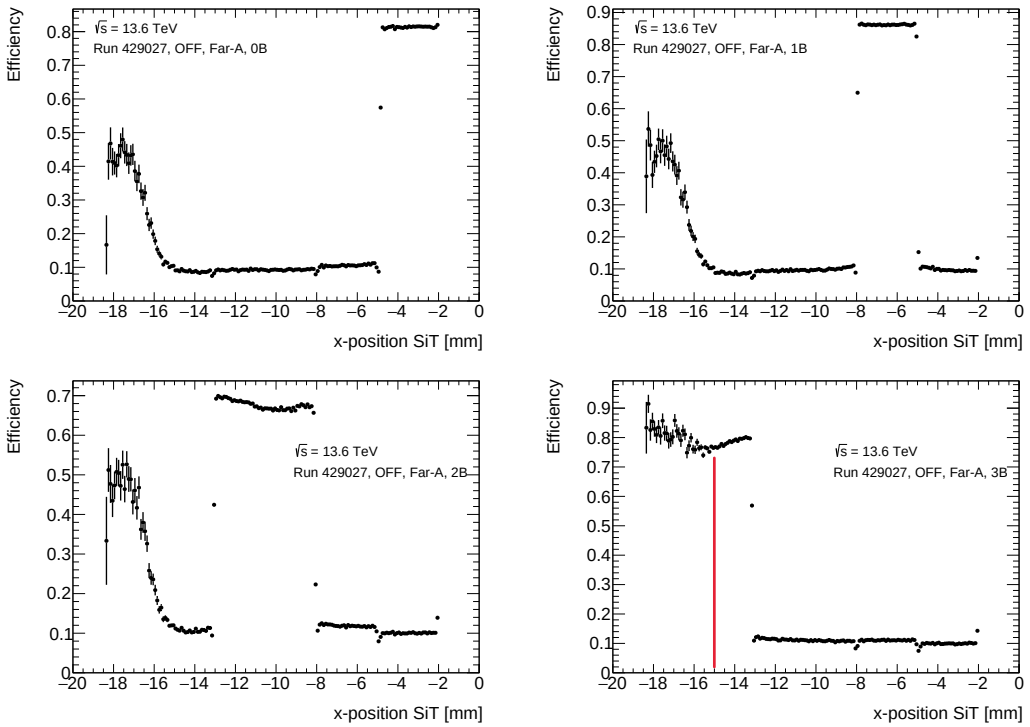

Figure 3.34: Ratios, which defines efficiencies for the run 429027, for the case of cuts "one train OFF" for A-side for each train and one bar: 0B (top left), 1B (top right), 2B (bottom left) and 3B (bottom right).

The resulting efficiencies for both cases (ON/OFF) for the histogram ratio method are shown in Figure 3.35, top: ON, bottom: OFF. Each cell on that plot corresponds to the efficiency in this channel assuming that SiT track points on respective ToF train.

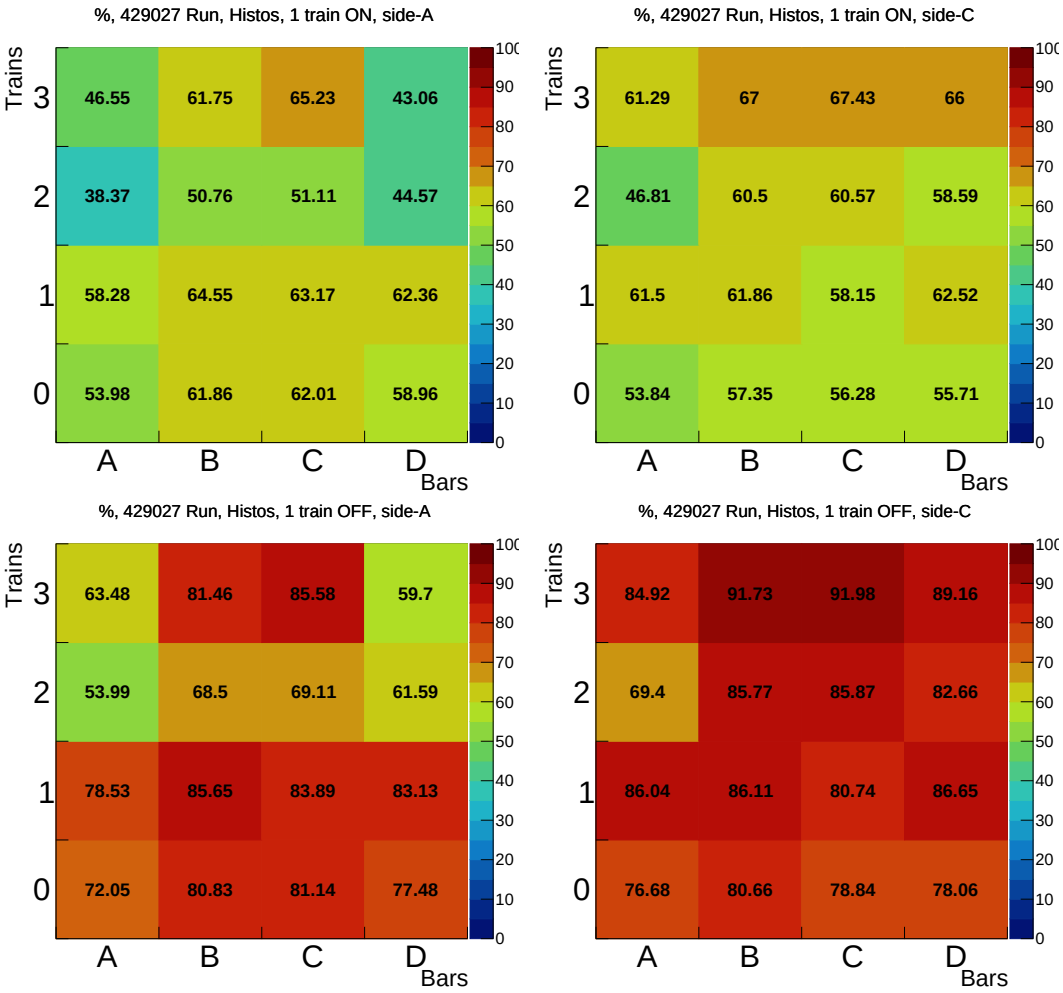

Figure 3.35: Efficiencies (%) for the run 429027 for each channel of ToF for A (left) and C (right) sides with the requirement "one train ON", (top) and OFF, (bottom) for the "histogram" method.

For the second method, direct numbers, i.e. the number of events in the two samples were counted. For the first sample an event has to pass the main requirements (OFF) and in addition the track has to be inside a given region in X, as measured by the silicon detector (Table 3.1). For the second sample, the event has to pass the requirement ON (or not, depending on the case under investigation) and there must be a hit in a corresponding channel of the ToF. There are 16 values for the second sample (for each channel), and 4 numbers for the first sample (for each train). The efficiency is defined as the ratio of the number of events in the second sample divided by the number of events

in the first sample. The resulting efficiencies for both cases (ON/OFF) for this method are shown in Figure 3.36, top: ON, bottom: OFF. Each cell on that plot corresponds to the efficiency in this channel assuming that SiT track points on respective ToF train.

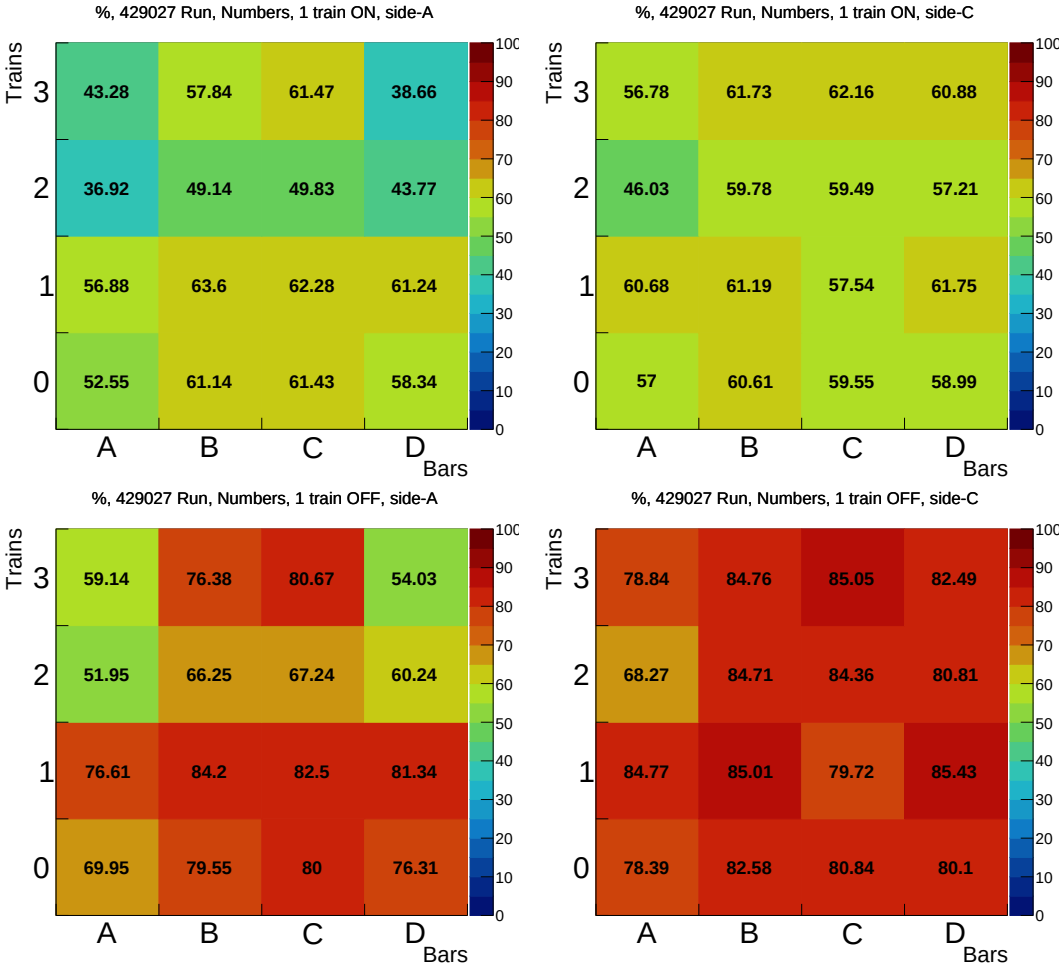

Figure 3.36: Efficiencies (%) for the run 429027 for each channel of ToF for A (left) and C (right) sides with the requirement "one train ON", (top) and OFF, (bottom) for the "direct numbers" method.

The efficiencies for both methods are very similar with minor differences. The reason for such differences is the binning of the histogram in the histogram method. Since the values are grouped into bins before calculating the average, the final result will be more precise with increasing number of histogram bins. This effect is shown in Figure 3.37 on example of one train OFF case, side C, where values from algorithm with original binning (200 bins) are compared with values from the algorithms with increasing number of bins (600 and 2000) and with results from the "direct numbers" method. With increasing number of bins, the results from the "histogram" method are getting closer to the results from the "direct numbers" method.

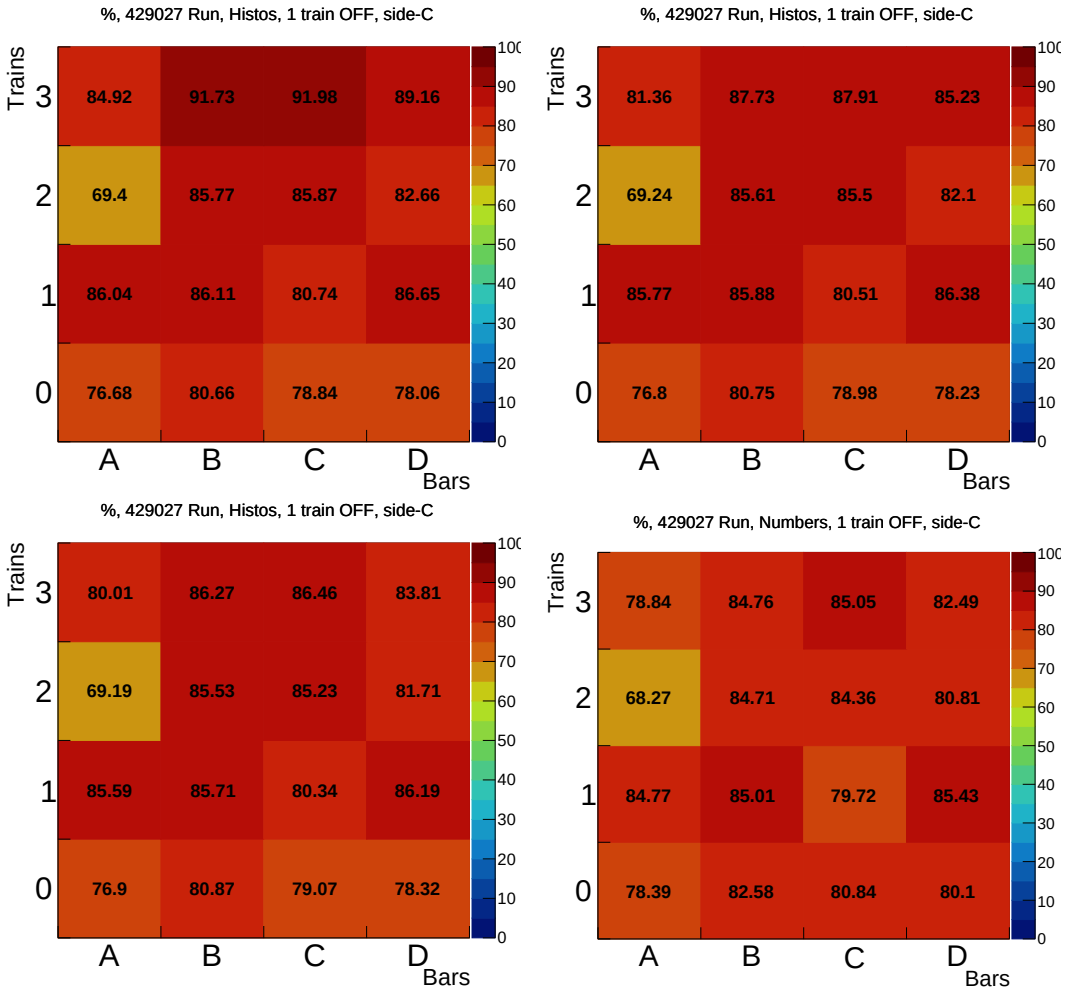

Figure 3.37: Efficiencies (%) for the run 429027 for each channel of ToF for C-side with the requirement "one train OFF" for the "histogram" method: 200 bins (top left), 600 bins (top right), 2000 bins (bottom left); and "direct numbers" method (bottom right).

The efficiencies for case OFF is higher than for case ON, as far as it includes non ideal events and some background. For the further studies only "direct numbers" method will be used, as this algorithm gives the most precise result.

The same procedure for the "direct numbers" method was applied to the low-μ run 428770. The resulting efficiencies for both cases (ON/OFF) for the method of "direct numbers" are shown in Figure 3.38, top: ON, bottom: OFF. Each cell on that plot corresponds to the efficiency in this channel assuming that SiT track points to the respective ToF train.

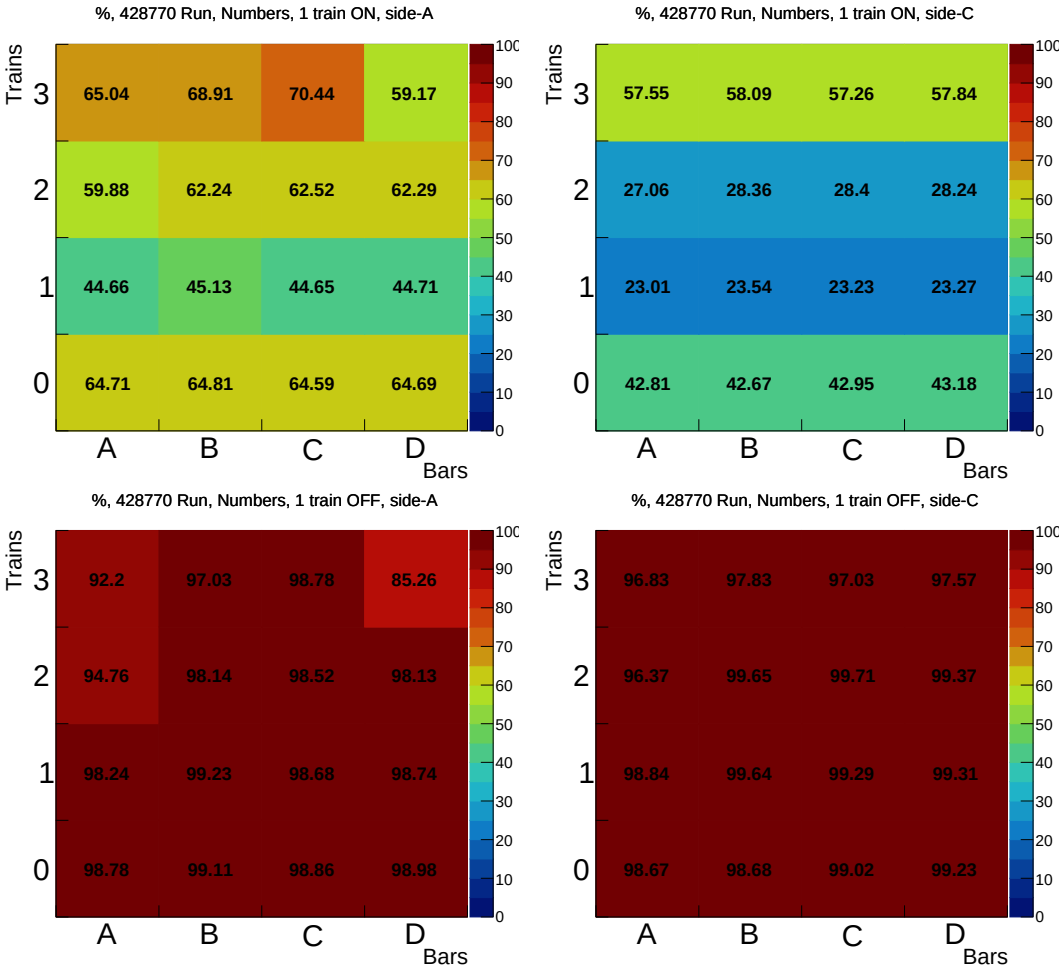

Figure 3.38: Efficiencies (%) for the run 428770 for each channel of ToF for A (left) and C (right) sides with the requirement "one train ON", (top) and OFF, (bottom) for the "direct numbers" method.

The low-μ run 428770 case ON shows structure close to the step-like with higher efficiencies in train 0 and lower in train 3. The possible reason for such a structure is proximity to the beam. Since this run has very low pile-up, the beam is more focused than for a usual high-μ run[4].

[4]as discussed at an ATLAS Combined Performance meeting

3.3.1 Background analysis

Another useful method of representing efficiencies is calculate efficiency in all channels assuming that SiT track points to one of the ToF trains. With such a representation a full map of ToF activity can be seen. Both for the train to which the track points, and for other trains. Therefore, more information about possible systematic background can be obtained.

Efficiencies calculated in such a way for the run 429027 for both cases (ON/OFF) using the method "direct numbers" are shown in Figure 3.39 for train 0 and in Figure 3.40 for train 3. Empty boxes represents zero response of the corresponding channel. Edge trains are chosen as examples, full set of efficiencies calculated by "track pointing" technique are given in Appendix C.

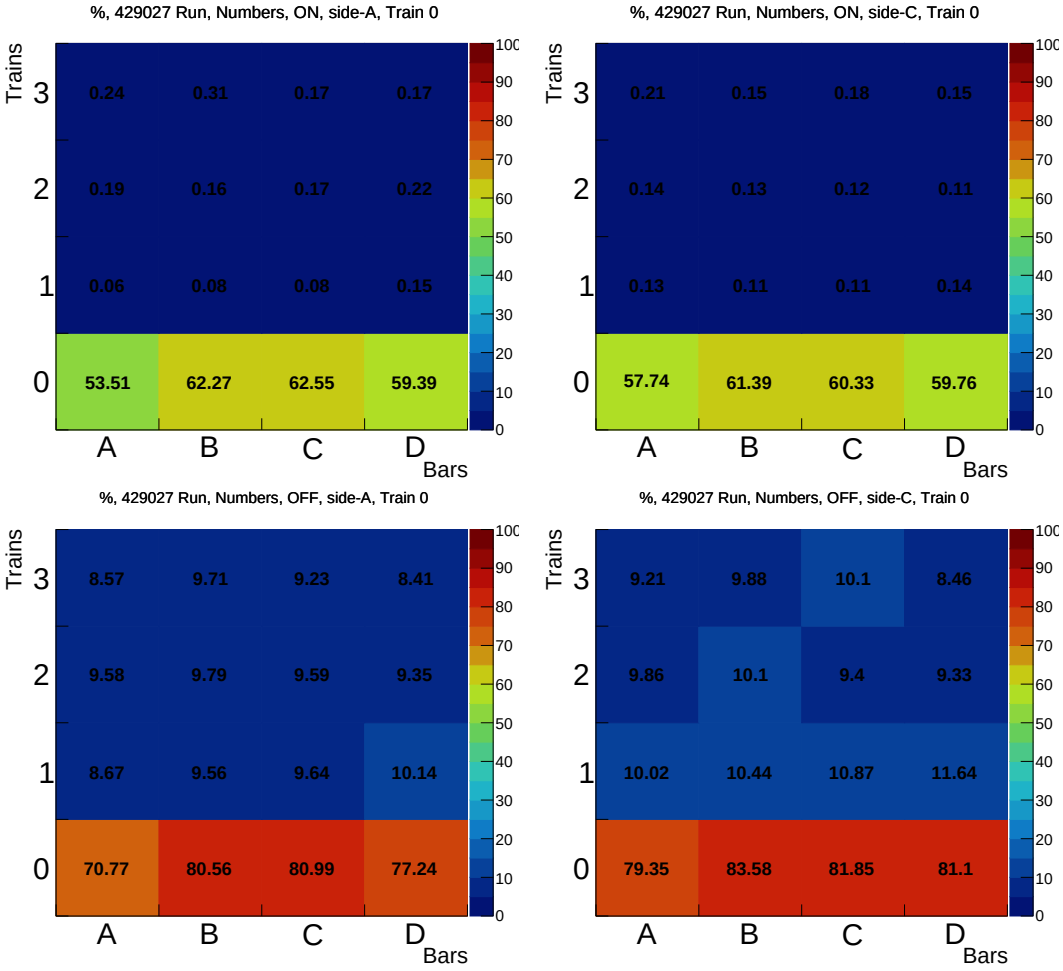

Figure 3.39: Efficiencies (%) for the run 429027 for each channel of the ToF with track pointing to train 0 for A (left) and C (right) sides with the requirement "one train ON", (top) and OFF, (bottom) for the "direct numbers" method.

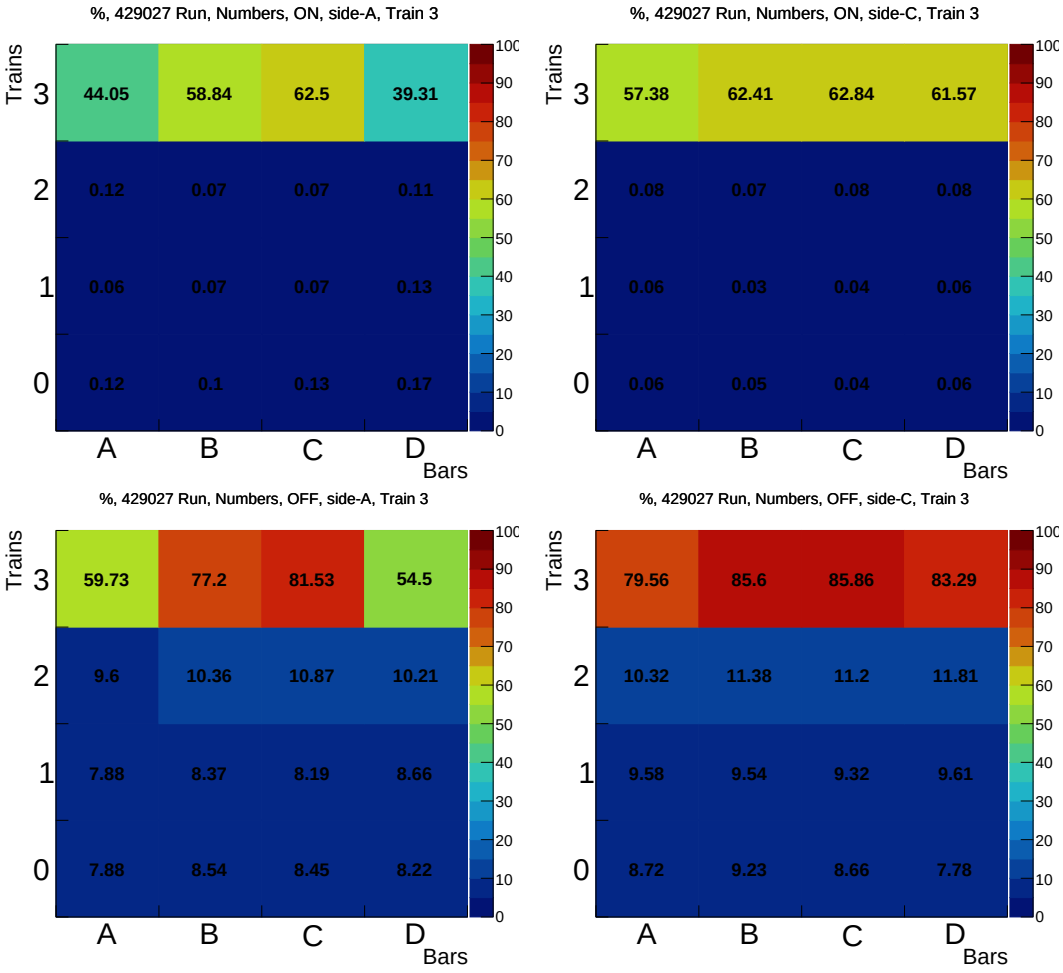

Figure 3.40: Efficiencies (%) for the run 429027 for each channel of the ToF with track pointing to train 3 for A (left) and C (right) sides with the requirement "one train ON", (top) and OFF, (bottom) for the "direct numbers" method.

Efficiencies calculated in such a way for the low-μ run 428770 for both cases (ON/OFF) using the method "direct numbers" are shown in Figure 3.41 for the train 0 and in Figure 3.42 for train 3. Empty boxes represents zero response of the corresponding channel. Edge trains are chosen as examples, full set of efficiencies calculated by "track pointing" technique are given in Appendix C.

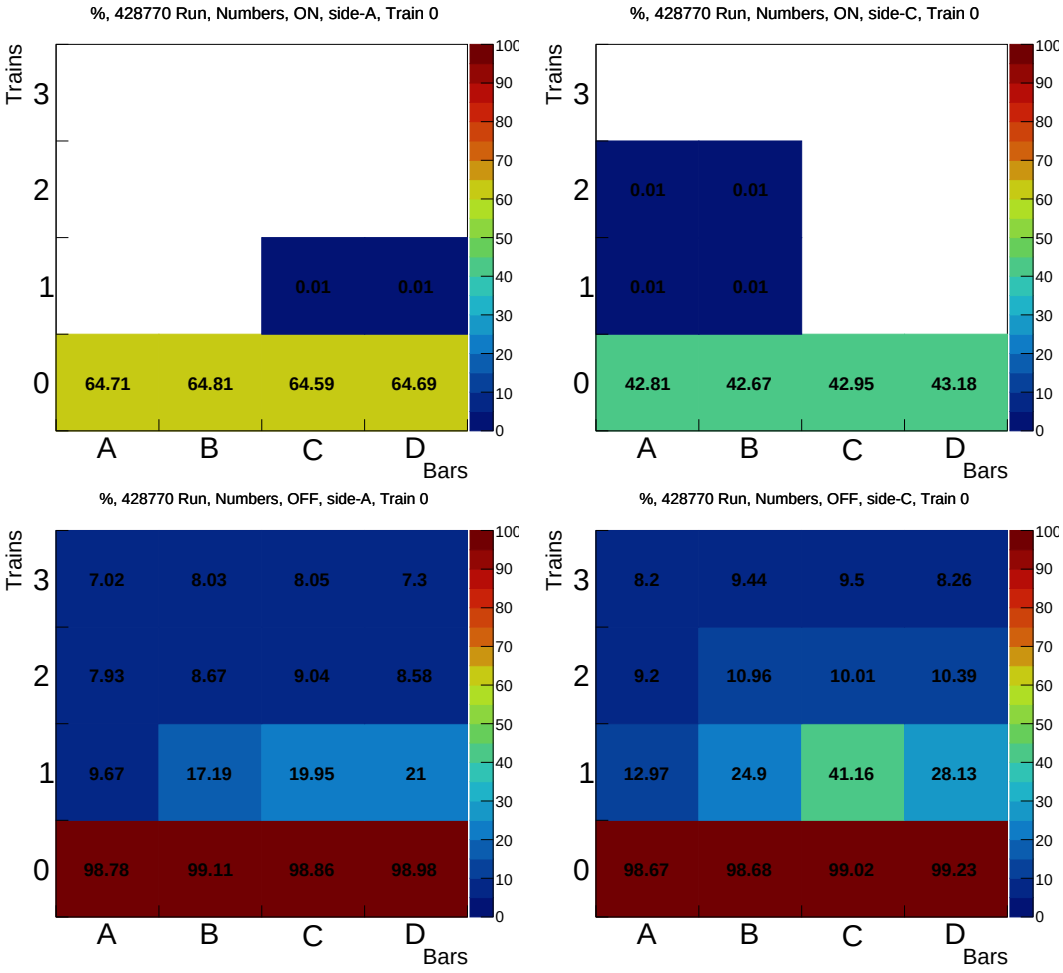

Figure 3.41: Efficiencies (%) for the low-μ run 428770 for each channel of the ToF with track pointing to train 0 for A (left) and C (right) sides with the requirement "one train ON", (top) and OFF, (bottom) for the "direct numbers" method. Empty boxes represents zero response of the corresponding channel.

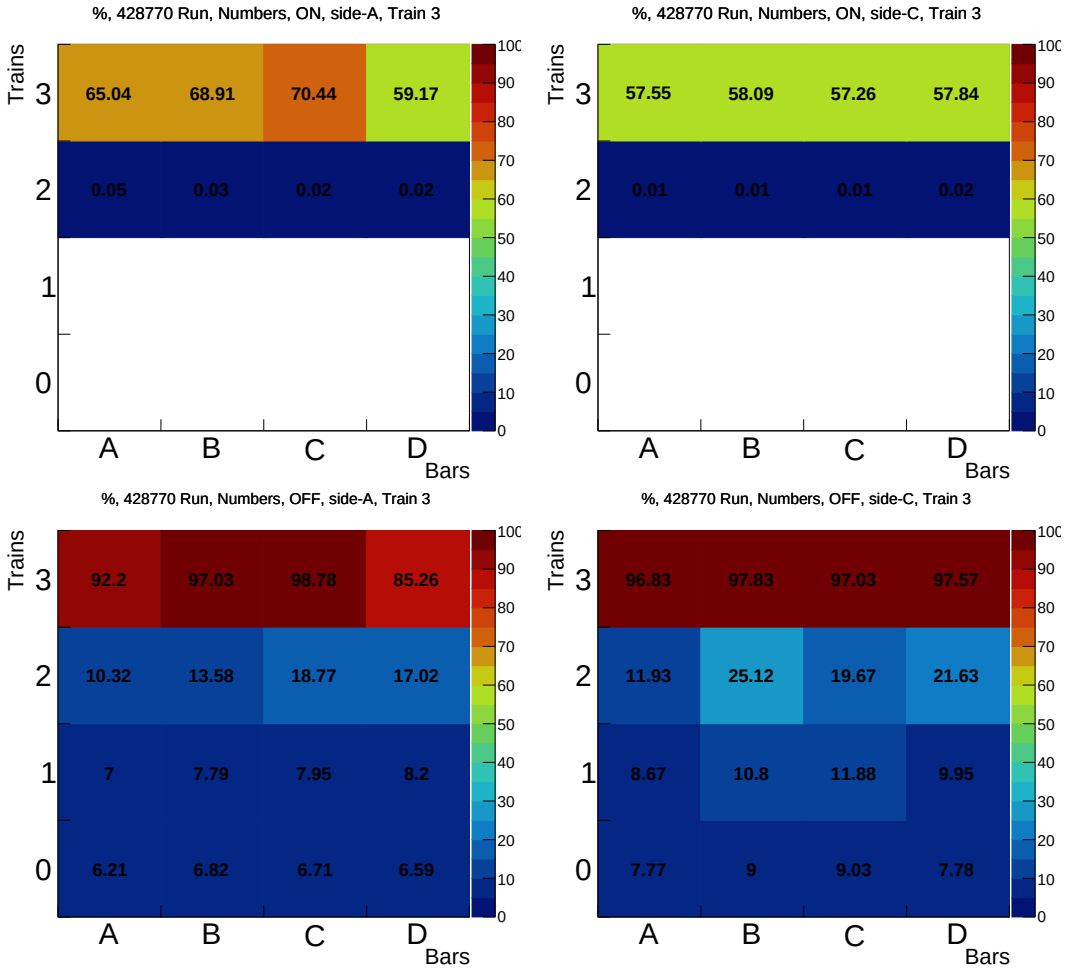

Figure 3.42: Efficiencies (%) for the low-μ run 428770 for each channel of the ToF with track pointing to train 3 for A (left) and C (right) sides with the requirement "one train ON", (top) and OFF, (bottom) for the "direct numbers" method. Empty boxes represents zero response of the corresponding channel.

Typically the efficiency is maximized in the ToF train to which SiT track is pointing. For the case one train ON a clear structure can be seen. Only the pointed train is active, all other trains do not contribute in both runs. For the case one active train OFF efficiencies in pointed train are maximized, however other trains are still active, usually neighboring. This effect is magnified in the low-μ run 428770, therefore it was investigated more detailed.

Data from the ToF detector is stored as hits in the chosen channels, when a particle goes through the detector in the AFPToFHitContainer [22]. This basic information was processed to obtain the efficiencies. However, this basic information can also be used in a raw way. As a new detailed analysis, the hit correlation map in all channels was studied. This assumes that the SiT track points to one of the ToF trains.

Such a correlation represents the response of the ToF channels as a function of other channels. Therefore, the detailed activity of the detector can be studied. For this analysis the requirement "one train OFF" was used. This means that all trains can be active in the event. Figures 3.43 and 3.44 show hit correlation maps for the high-μ run 429027 and the low-μ run 428770 for the C-side, as an example. All hit correlation maps are given in Appendix C.

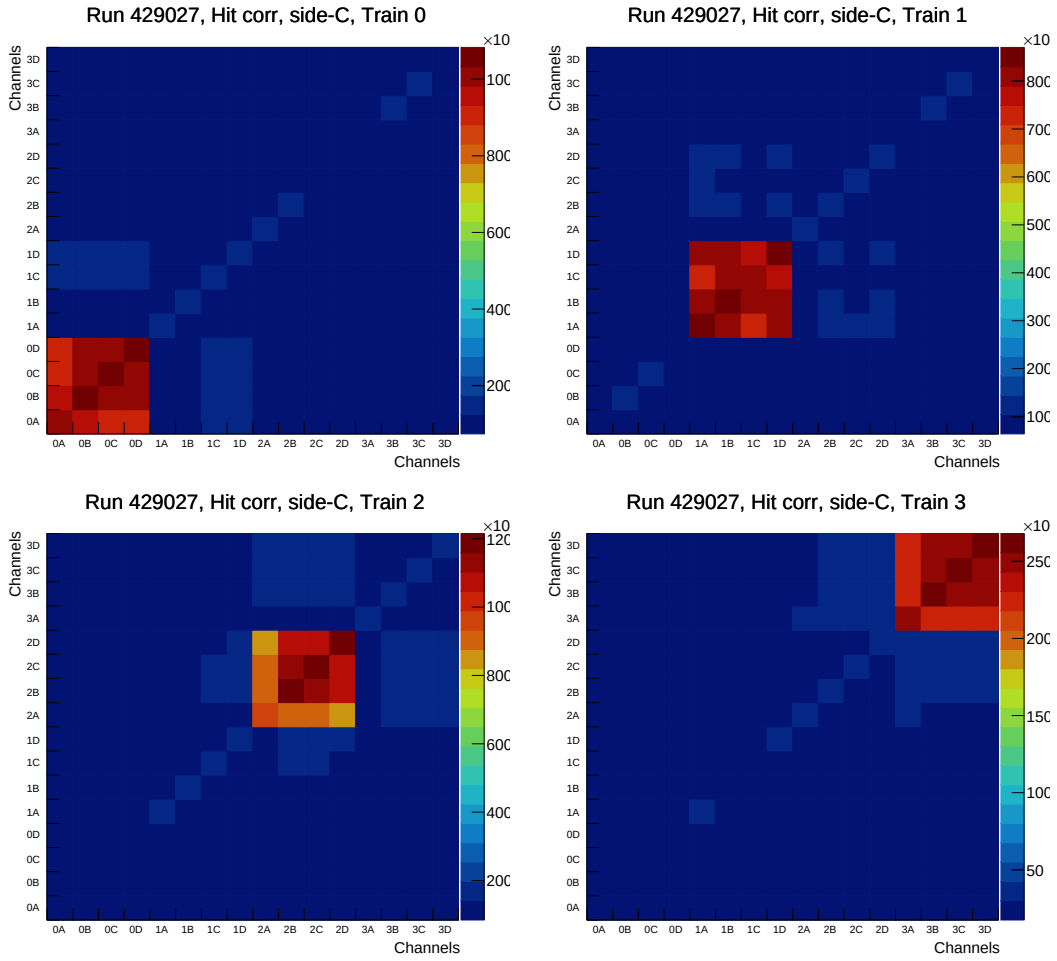

Figure 3.43: Hit correlation map for the high-μ run 429027 for each channel of the ToF with track pointing to train 0 (top left), train 1 (top right), train 2 (bottom left) and train 3 (bottom right) for the C-side with the requirement "one train OFF".

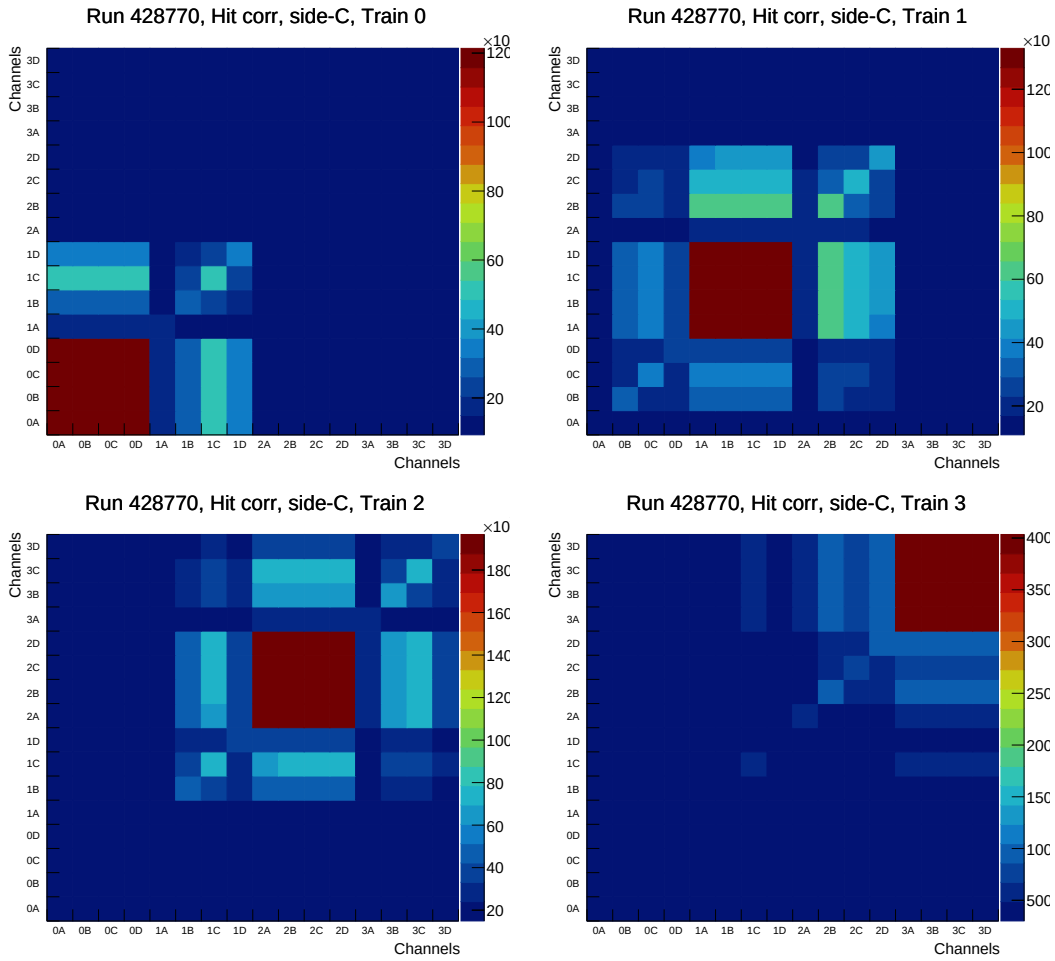

Figure 3.44: Hit correlation map for the low-μ run 428770 for each channel of the ToF with track pointing to train 0 (top left), train 1 (top right), train 2 (bottom left) and train 3 (bottom right) for the C-side with the requirement "one train OFF".

The hit correlation map shows the effect of activity in trains neighboring the one train to which the track points. In the low-μ run this effect is magnified in comparison with the high-μ one. Therefore, it would be interesting to check this with another low-μ run. The longest low-μ run in Run-3 so far has the number 435229. It was used in the author's previous analysis [12]. Figure 3.45 shows the hit correlation maps for this low-μ run, for the side-C, as an example. All hit correlation maps are given in Appendix C.

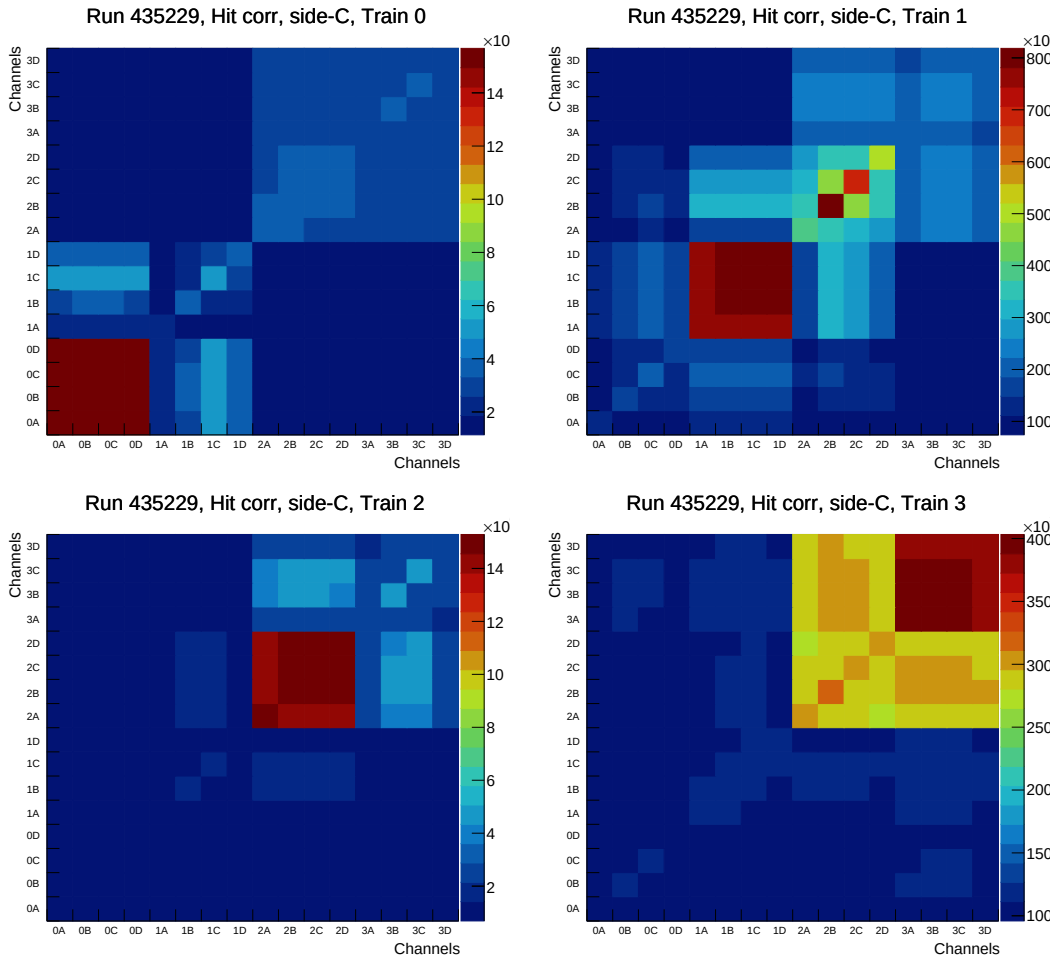

Figure 3.45: Hit correlation map for the longest low-μ run so far in the Run-3, 435229, for each channel of the ToF with track pointing to train 0 (top left), train 1 (top right), train 2 (bottom left) and train 3 (bottom right) for the C-side with the requirement "one train OFF".

The effect of neighboring activity became stronger in larger low-μ run. The train 3 has the biggest "shadow effect" on neighboring trains. The reason for such a behavior could be the presence of general secondary particles, or collimator shadow, which covers part of the train 3 and it could give secondary particles[5].

[5]as discussed at an ATLAS Combined Performance meeting

3.3.2 2022 efficiency summary

The efficiencies were calculated for all available data from 2022 using the "direct numbers" method with the requirement "one train OFF", as described in Section 3.3 for each train. The summary plots are given in Figure 3.46 for the 2022 data for both sides.

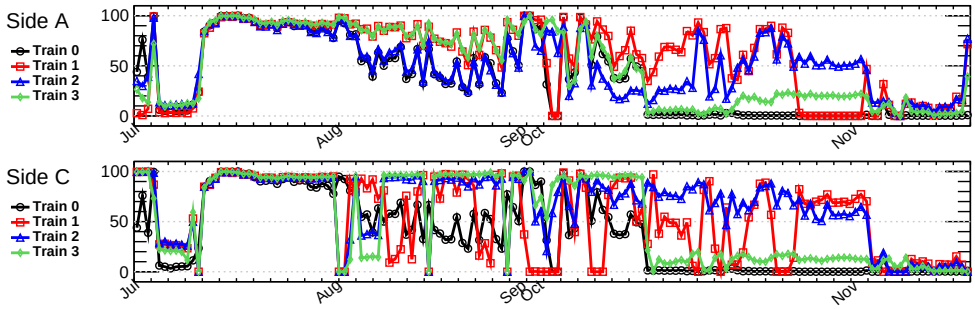

Figure 3.46: Efficiency summary for the 2022 data for the A-side (top) and the C-side (bottom) with the requirement "one train OFF" for the period from 05 July to 27 November 2022. Labels on Y-axis correspond to the beginning of the month.

Summary efficiency plots show downward trend in time. This points on the degradation of the detector elements, which can be caused by the radiation in the collider tunnel[6]. The best detector efficiency was in July 2022, at the start of the Run-3. All analyses described in this work, were performed with data taken at that time.

[6]as discussed at an ATLAS Combined Performance meeting

Chapter 4

ToF vertex reconstruction

The capability of the ToF detector to measure the z-coordinate of the primary vertex in interactions of kind $pp \to pXp$ is investigated in this chapter. Vertex reconstruction using the ToF is based on the proton arrival times on the A and C sides of the AFP system. The z-coordinate of the primary vertex (z_{ToF}) was basically calculated as follows:

$$z_{\mathrm{ToF}} = \frac{c}{2}(t_C - t_A). \tag{4.1}$$

This formula represents a general approach, but cannot be used directly on the data; firstly arrival times should be corrected for possible time offsets, which is shown in first section of this chapter (4.1).

The final corrected z_{ToF} was then used for the distribution $z_{\mathrm{ATLAS}} - z_{\mathrm{ToF}}$, whose width represents the combined resolution of the z_{ToF} and z_{ATLAS} measurement. z_{ATLAS} here is the z-coordinate of the reconstructed primary vertex, provided by the central ATLAS detector with resolution at the level of $\approx 30\,\mu$m. The distribution of $z_{\mathrm{ATLAS}} - z_{\mathrm{ToF}}$ contains a background from the random coincidences of protons measured in the ToF, but not originating from $pp \to pXp$ processes and whose arrival time spreads are mainly driven by the beamspot size.

Following the author's previous work [12], for this analysis some general requirements on the data samples were applied:

- One track in the SiT per event.
- At most one cluster per plane in the SiT per event.
- One active train in the ToF per event.
- Cut on measured ToF arriving time period.

Data from the low-μ run 428770 and the high-μ run 429027 were used and compared in this study. In the author's previous study [12] different runs were used.

4.1 Time delays correction

The time measured in one ToF channel i (for example, channel 0A is train 0, bar A) is made up from several components as follows:

$$t_i = t_{\text{proton}} + t_{i,\text{delay}} + t_{i,\text{smear}} - t_{\text{clock}} \tag{4.2}$$

Here the t_{proton} is the proton arrival time, the $t_{i,\text{delay}}$ is a constant time offset in exact ToF channel, appeared because of the signal delay (for example, it can be caused by signal cable lengths). Therefore, this time delay is constant for the given ToF channel, if there was no intervention into the system (e.g. during data taking of the one run for sure). The $t_{i,\text{smear}}$ represents all random effects of the signal processing, for example variation in Cherenkov photon statistics or effects of electronics. The t_{clock} is a reference clock that opens a 25 ns window within which the leading protons from a single bunch-crossing arrive to the ToF.

The t_{proton} and t_{clock} can be abolished by measuring time differences on the event by event basis within one ToF train. This approach also allows to deal with the $t_{i,\text{delay}}$, which is required for this study.

The main goal of this part was to determine $t_{i,\text{delay}}$, which was done using Δt_{ij} distributions which were defined as follows:

$$\begin{aligned} < \Delta t_{ij} > =< t_i - t_j > =< t_{i,\text{smear}} + t_{i,\text{delay}} - t_{j,\text{smear}} - t_{j,\text{delay}} > \\ =< t_{i,\text{delay}} - t_{j,\text{delay}} >, \end{aligned} \tag{4.3}$$

where $< t_{i,\text{smear}} >$ cancels for all channels.

For determination of the delay correction constants an approach [18] was used with the z-position of the luminous ATLAS beamspot, which is measured by the central ATLAS detector. The z_{ToF} value, determined using Equation 4.1, in its mean value copy the z-position of the luminous ATLAS beamspot, therefore the following relation was used:

$$< z_{\text{ToF}}^{(ij)} >= z_{\text{BS}} - (D_A^i - D_C^j) \tag{4.4}$$

where D_A^i and D_C^j are mentioned above delay correction constants for the given ToF channels i and j in A and C sides, respectively, which were used for determination of the z_{ToF}. The mean value was obtained over the time period of one LHC LB [23] (~ 1 min of data taking). These delay correction constants are unique for the each pair of the ToF channels and basically only their difference matters to correct positions of the z_{ToF} in given ToF channels. The following equation was used for the determination of this difference, assuming that the mean value was obtained over the one lumiblock and the fact that z_{BS} does not change within one LB (showed as sum over LBs, $\sum_{LB}$)

$$< \sum_{LB} z_{\text{ToF}}^{(ij)} - z_{\text{BS}} >= D_C^j - D_A^i \tag{4.5}$$

With the event-by-event approach only double-tag events were used, which means that signal is required in both sides of the AFP system (A and C) simultaneously. However, this significantly reduces the data statistics. Therefore, another approach was used to create pseudo-double-tag events from single-tag events. This approach is called event mixing. For this analysis the time buffers were filled with time values measured during one LB and then pseudo-double-tag events can be produced.

The ToF has 16 channels on each side, therefore there exist $16 \times 16 = 256$ combinations of channels. For each of them the distribution corresponding to Equation 4.5 was created and a Gaussian fit was applied to determine the mean value. A few examples of such distributions with fitted curve overlaid are given in Figure 4.1 for run 429027 and in Figure 4.2 for low-μ run 428770.

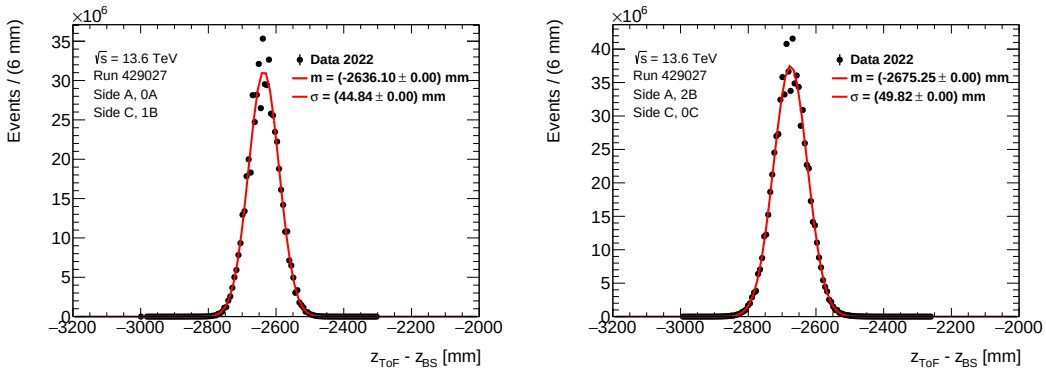

Figure 4.1: $z_{\mathrm{ToF}} - z_{\mathrm{BS}}$ distributions for the run 429027 with a Gaussian fitted curve overlaid for 2 combinations of the ToF channels. Left - side A 0A (train 0, bar A) with side C 1B (train 1, bar B). Right - side A 2B (train 2, bar B) with side C 0D (train 0, bar D).

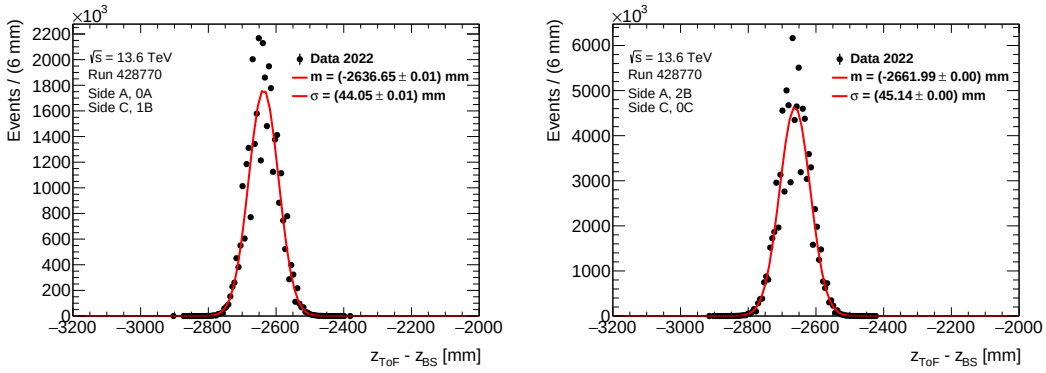

Figure 4.2: $z_{\mathrm{ToF}} - z_{\mathrm{BS}}$ distributions for the low-μ run 428770 with Gaussian fitted curve overlaid for 2 combinations of the ToF channels. Left - side A 0A (train 0, bar A) with side C 1B (train 1, bar B). Right - side A 2B (train 2, bar B) with side C 0D (train 0, bar D).

The mean values of these fits define the differences between the delay correction constants for each of the 256 combinations of the ToF channels, according to Equation 4.5. All combinations are shown in Figure 4.3 for both runs. The mapping of the indices is performed by means of the logic:

$$
\begin{aligned}
&for(i = \text{Index}_{[\text{SideA}]}) \\
&\{ \\
&\quad for(j = \text{Index}_{[\text{SideC}]}) \\
&\quad \{ \\
&\qquad D_C^j - D_A^i \\
&\quad \} \\
&\},
\end{aligned}
\tag{4.6}
$$

which means that in each iteration a channel on the A-side is chosen and channels on the C-side were taken one by one to form combinations, then the procedure is repeated for each channel on the A-side. Some structure in the differences depending on the channel combination can be seen.

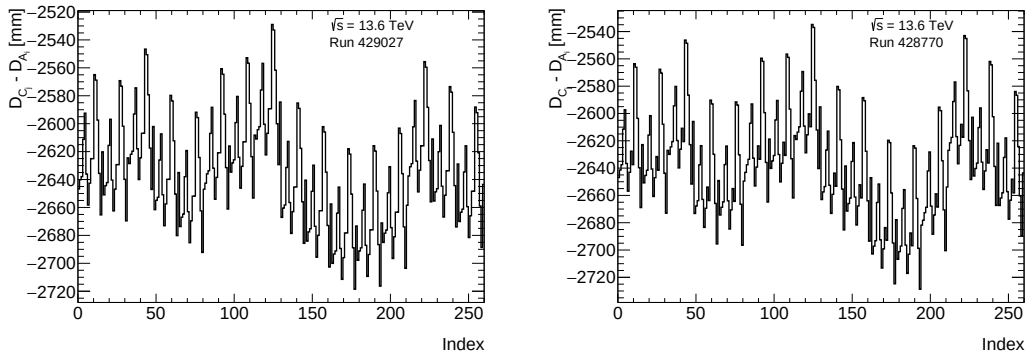

Figure 4.3: All differences between delay correction constants for each of the 256 combinations of the ToF channels for the run 429027 (left) and for the low-μ run 428770 (right).

These 256 differences between delay correction constants can be parameterized in terms of the D_A^i and D_C^j to find 32 correction factors (D_A^i, D_C^j). This was done using a fit as shown in Figure 4.4 for both runs. Finally, all delay correction constants were determined for each channel on both sides for both runs. Figure 4.5 shows them in mm.

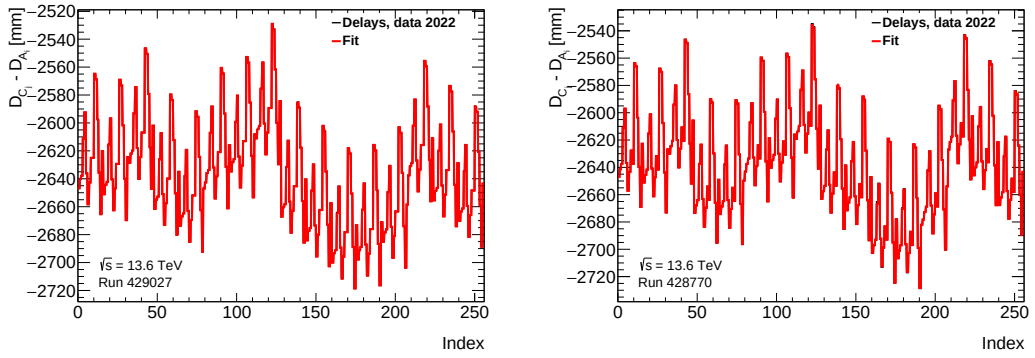

Figure 4.4: All differences between delay correction constants for each of the 256 combinations of the ToF channels with fit overlaid for the run 429027 (left) and for the low-μ run 428770 (right).

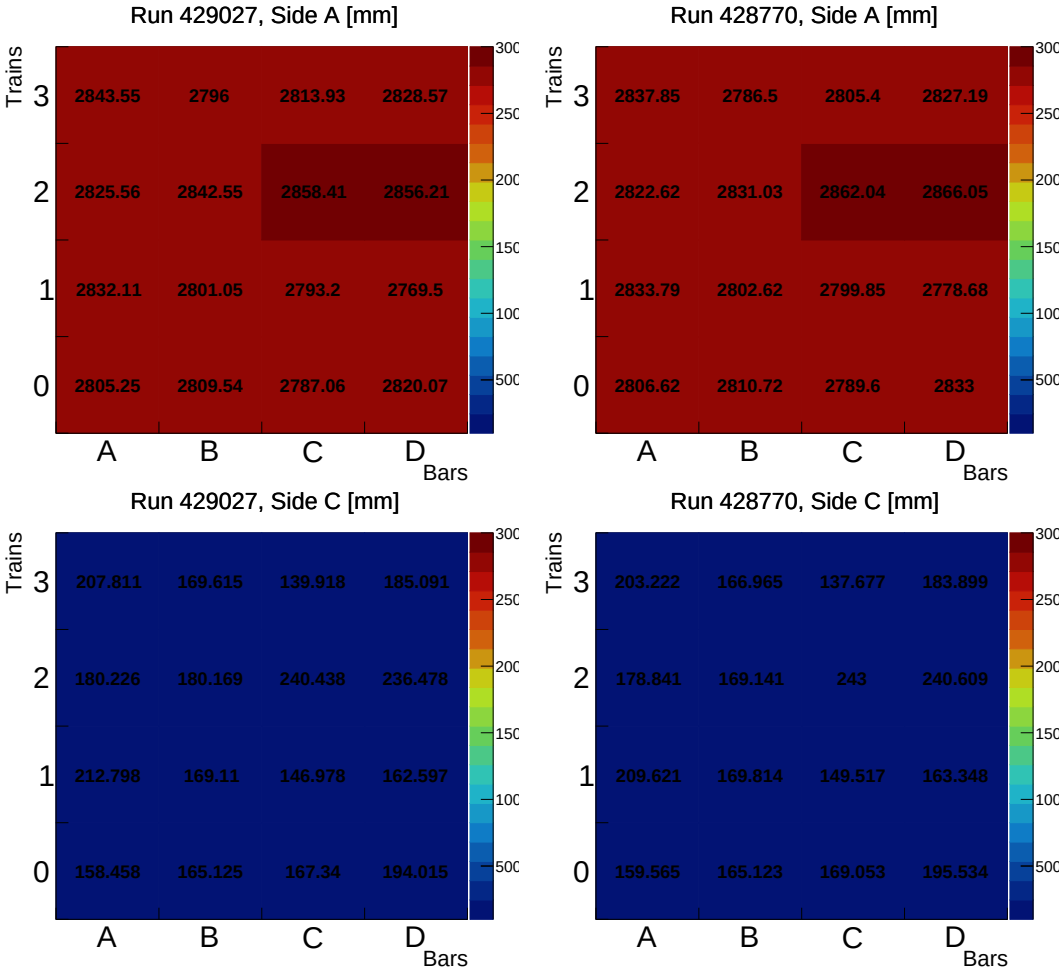

Figure 4.5: Delay correction constants for all ToF channels on A-side (top) and C-side (bottom) for the run 429027 (left) and for the low-μ run 428770 (right).

After all the corrections were determined it is possible to correct the z_{ToF}

position and compare it with the z_{BS} position. The dependence of the z_{BS} on lumiblock (basically - on time) is not uniform and differs in each particular run. As the z_{ToF} copying the z_{BS}, procedure of time delay corrections was checked by comparing the dependence of the z_{BS} and z_{ToF} per LB. The raw positions of z_{ToF} are distributed around the z_{BS} in a Gaussian-like manner. Therefore, Gaussian fit was applied.

Figure 4.6 shows the dependence of the z_{BS} and z_{ToF} per LB before and after the corrections on time delays for both runs. Figure 4.7 shows the dependence of the z_{BS} and z_{ToF} per LB after the corrections on time delays for both runs in a magnified way, which allows it to be seen clearly that the z_{ToF} repeats the form of the z_{BS}. In addition, the precision of the fit was defined by

$$< \sum_{LB} z_{\mathrm{ToF}}^{(ij)} - z_{\mathrm{BS}} > -(D_C^j - D_A^i). \tag{4.7}$$

The graphical representation is shown in Figure 4.8 for both runs. The high-μ run shows better precision of the fit than the low-μ run due to the much higher statistics.

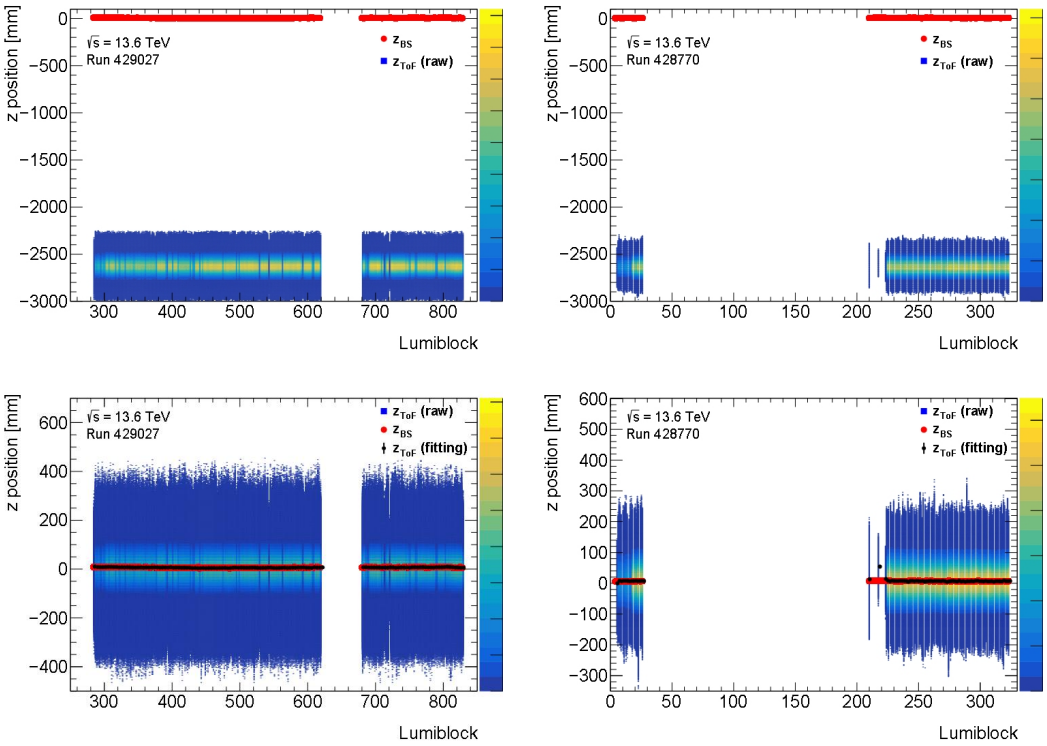

Figure 4.6: Dependence of the z_{BS} and z_{ToF} per LB before (top) and after (bottom) the corrections on time delays for the run 429027 (left) and for the low-μ run 428770 (right).

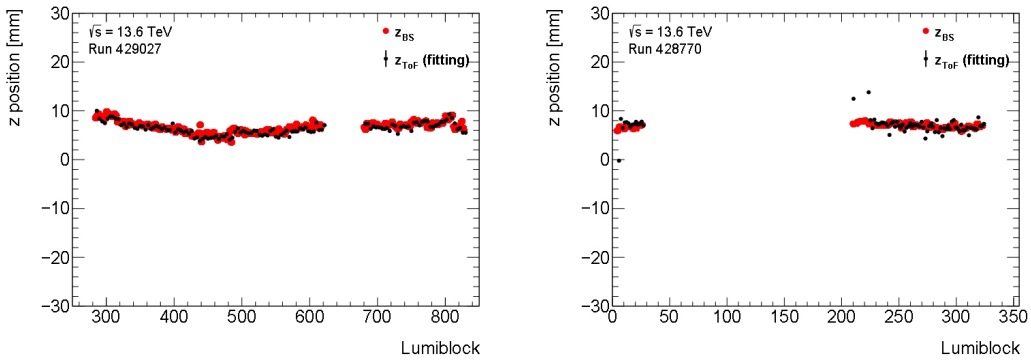

Figure 4.7: Dependence of the z_{BS} and z_{ToF} per LB after the corrections on time delays for the run 429027 (left) and for the low-μ run 428770 (right), magnified version.

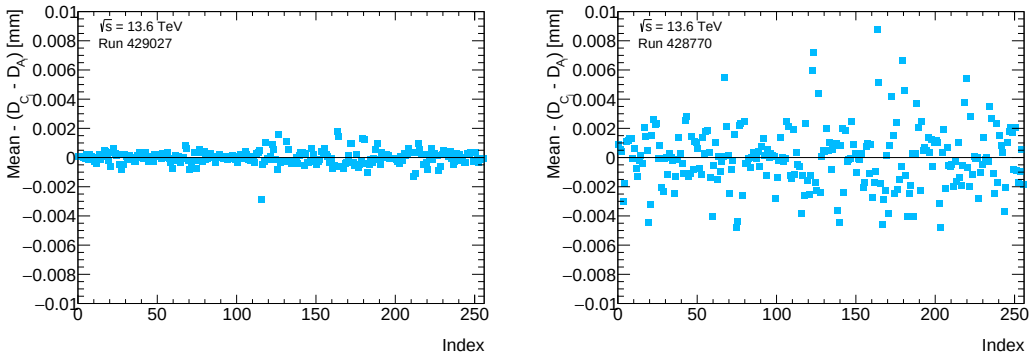

Figure 4.8: Precision of the fit for the run 429027 (left) and for the low-μ run 428770 (right). Details are given in the text.

4.2 Vertex matching

The ToF detector reconstructs the primary vertex in the case of finding two leading protons under the proper conditions. However, it can reconstruct fake vertices caused by a fake double-tag of two leading protons from two unrelated events.

It is possible to measure the production vertex of a $pp \to pXp$ process from the time information of the two leading protons on each side. If z_{ToF} happens to be measured from protons that truly are coming from the primary ATLAS vertex, a narrow enhancement is observed in the otherwise wide $z_{\mathrm{ATLAS}} - z_{\mathrm{ToF}}$ distribution. In other words, the primary vertex position in ATLAS (z_{ATLAS}) and z position from ToF (z_{ToF}) are correlated for the signal processes; the projection to the $z_{\mathrm{ATLAS}} - z_{\mathrm{ToF}}$ is a convenient way for searching for such correspondence.

Then, in a given data sample if a cut is applied on such $z_{\text{ATLAS}} - z_{\text{ToF}}$ observable (e.g. a window around the signal peak, whose width is driven by the resolution) some statistics will be lost (the events in the wide tails are cut away, but these are mostly background) and the signal is enriched, because the sub-selected sample contains larger fraction of genuine signal events than the whole sample.

For this analysis only the low-μ run 428770 was used, since high-mu runs include too much combinatorics. The variable z_{ToF} was corrected on time delays, discussed in Section 4.1. Figure 4.9 shows $z_{\text{ATLAS}} - z_{\text{ToF}}$; the wide distribution indicates background and narrow one is the signal.

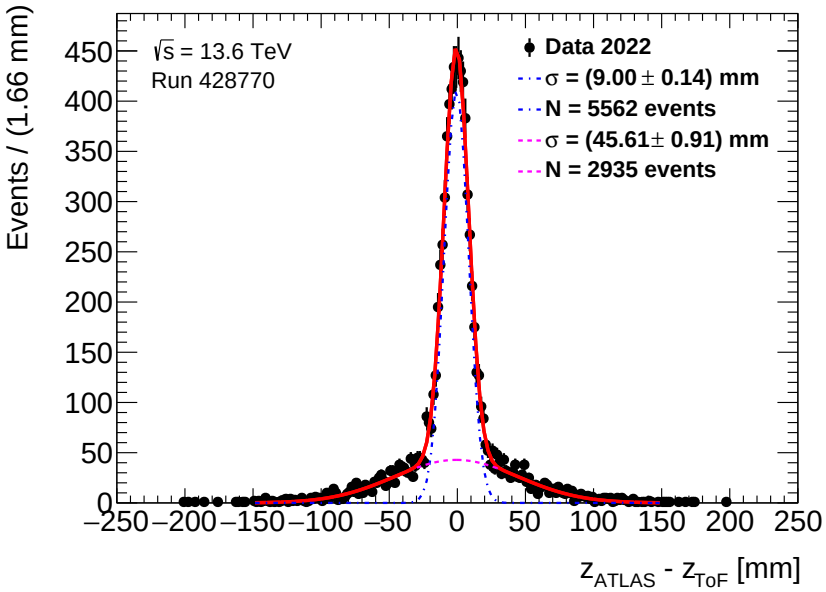

Figure 4.9: The distribution of the $z_{\text{ATLAS}} - z_{\text{ToF}}$ for the low-μ run 428770.

The sensitivity of the approach to the signal can be checked using Equation 4.8:

$$\text{sensitivity} = \text{signal}/\sqrt{\text{background}}, \tag{4.8}$$

according to which sensitivity for the full data is about 102.66.

The width of the signal distribution is $\sigma = 9.00\,\text{mm}$. To convert it to the single-side resolution, Equation 4.1 was used for the determination of z_{ToF}, including a factor 1/2. Thus, the resolution in length units was calculated as follows, assuming that both sides are the same:

$$\sigma_{\text{length}} = \frac{c}{2}\sqrt{\sigma^2_{\text{time,A}} + \sigma^2_{\text{time,C}}} = \frac{c}{2}\sigma_{\text{time}}\sqrt{2}. \tag{4.9}$$

According to Equation 4.9, the single side resolution in ps was calculated:

$$\sigma_{\text{ps}} = \frac{\sqrt{2}}{c}\sigma_{\text{mm}} \times 10^9 \approx 42.45\,\text{ps}, \tag{4.10}$$

where the speed of light is in m/s.

This indicates that the ToF works well and definitely can reconstruct signal events; however, the resolutions are still not fully established, which was also shown in Section 3.2. The HPTDC calibration, done in Section 3.2.2, introduces additional uncertainty. Correction on them is a separate unique task and requires separate analysis. Therefore, in this chapter HPTDC uncalibrated ToF data was used. Nevertheless, vertex matching analysis gives applicable results even without HPTDC calibration, which is most important for the single-channel resolutions in the high-μ data.

Figure 4.10 (from [18]) shows the $z_{\mathrm{ATLAS}} - z_{\mathrm{ToF}}$ distribution for the data from 2017. In the data from 2022 the signal is much better visible, which is the result of a better efficiency of the ToF detector in Run-3 in comparison with Run-2. The resolution in data 2017 was better (5.2 ± 0.9 mm), due to better single-channel resolutions which had less artefacts. Therefore, it must be stressed that results obtained in data from 2022 are very preliminary and cannot be compared with results from 2017 directly.

Applying the ToF data to the di-photon vertex reconstruction is not feasible at the moment because currently the di-photon analysis is possible with high-μ runs and the ToF vertex reconstruction analysis with low-μ runs.

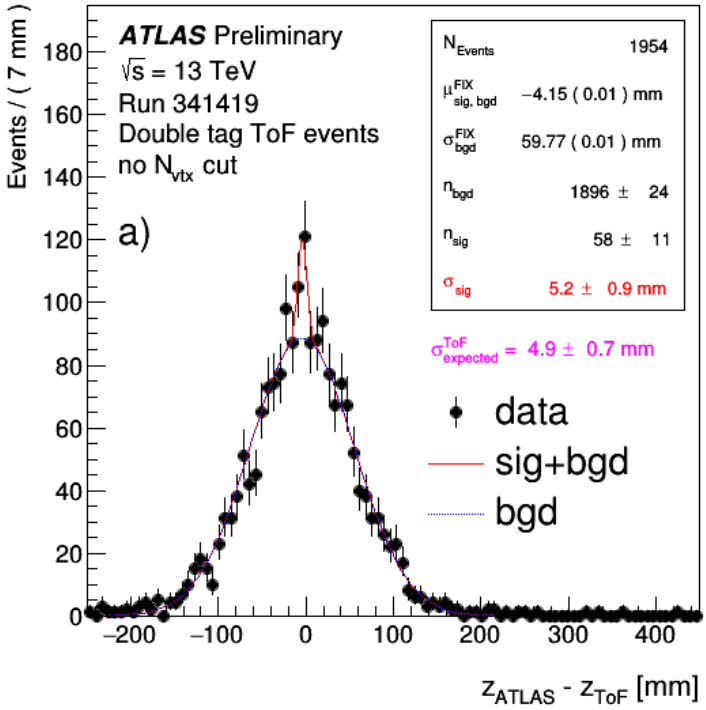

Figure 4.10: The distribution of $z_{\mathrm{ATLAS}} - z_{\mathrm{ToF}}$ measured in events with ToF signals on both sides of the interaction region in run 341419 in data 2017, where z_{ATLAS} is the primary vertex z-position reconstructed by ATLAS. The z_{ToF} is obtained as $z_{\mathrm{ToF}} = -\frac{c}{2}\Delta t$, where Δt is the time difference of proton arrival times in A and C far stations of the AFP measured by ToF. The distribution correspond to the ATLAS data containing a reconstructed primary vertex together with coincidence of signals in both ToF detectors in scenario with no cut on number of vertices reconstructed by ATLAS. A double Gaussian function representing the signal and background components is fitted to unbinned data samples using the extended likelihood fit as implemented in RooFit. The mean of the signal component as well as the mean and width of the background component are always estimated from a Gaussian fit to the mixed event data, denoted as μ_{sig}^{FIX}, μ_{bgd}^{FIX} and σ_{bgd}^{FIX}. The mixed event data $z_{\mathrm{ATLAS}} - z_{\mathrm{ToF}}$ distributions are obtained by random mixing of times measured by ToF in either station and the z_{ATLAS} values which do not originate in the same collision event. The expected resolution of the ToF detector, quoted as $\sigma_{expected}^{ToF}$ is obtained from the known single-channel resolutions convoluted with the actual channel-hit-patterns observed in the data [18].

Chapter 5

Di-photon vertex reconstruction

In the author's previous analysis [12] two approaches were used for determining the vertex of interaction, i.e. photon pointing and calorimeter pointing methods. For the photon pointing method, the position of the event in ATLAS is selected from Primary Vertex (PV) candidates reconstructed using tracks. This method has a good resolution, but for the vertices of photons it can give misleading information (as photons do not leave tracks). The second method uses the calorimeter pointing tool to obtain the vertex of the two photons.

A comparison of the two techniques shows better resolution for the photon pointing method. Nevertheless, this method has limited opportunities in the case of photons, as they do not leave tracks in trackers. Therefore, for the analysis of the Run-3 data the calorimeter pointing method was applied.

For this analysis data from run 429027, taken on July 23, 2022, was used. "Calo Pointing Tool" [1] from the source in ATLAS ATHENA [24] was used directly on the DAOD_HIGG1D1 and n-tuple for analysis was created. Events with two photons only were used for this analysis.

Figure 5.1 shows the distributions for the resolutions in data for converted and unconverted photons with fitted curve overlaid. Resolutions were obtained as a difference between vertices of two photons in the data 2022. These distributions do not have a fully Gaussian shape, therefore a double-Gaussian fit was applied to the data.

[1] Calo Pointing Tool from ATLAS ATHENA, link available at A

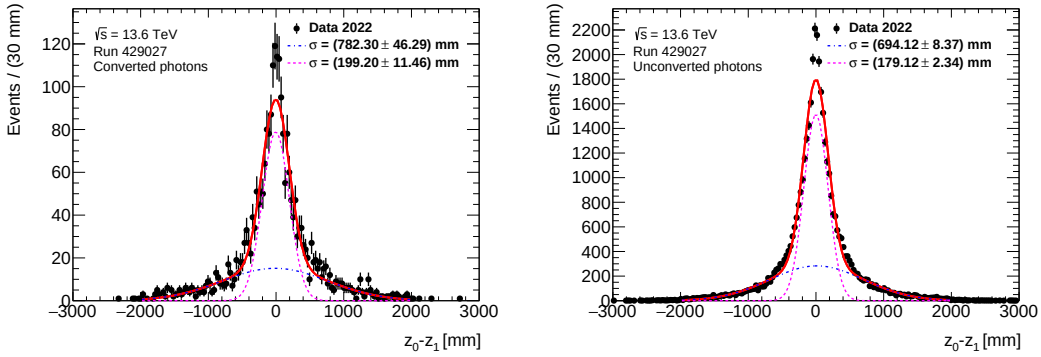

Figure 5.1: Resolutions for converted (left) and unconverted (right) photons for first Run-3 data from 2022 using the calorimeter pointing method with fitted curve overlaid. The values, z_0 and z_1, correspond to the z-position of the leading and the sub-leading photons, respectively.

The distributions for the resolutions of di-photon vertices for the first Run-3 data taken in 2022 are wider than for the data taken in 2017, as was studied in the author's previous analysis [12]. The reason for such a difference is likely to be the newness of the data, for which some di-photon calibrations are not done yet.

In comparison with the author's previous analysis [12], this 2022 data set has better statistics and allows to determine width for the converted protons better. Nevertheless, statistics for them is still poor.

Chapter 6

Future applications on an ALP search

Searches for the hypothetical Axion-like particles are a hot topic in a modern science. Many extensions of the Standard Model use them as possible candidates for particles that make up dark matter.

At the Large Hadron Collider the electromagnetic fields between protons are strong enough to create powerful fluxes of high-energy virtual photons. These photons can interact, for example, by merging together and then decaying into various final states. Photon fusion is a separate way of looking for physics BSM. Scattering of light by light mediated by ALPs is prohibited in the classical theory of electrodynamics. In various extensions, additional contributions are possible, which makes light-by-light scattering measurements sensitive to physics BSM, which can be used to search for an Axion-like particle.

A search for a forward proton scattering in association with light-by-light scattering mediated by an Axion-like particle was performed using central ATLAS detector and Silicon Tracker from the AFP system [25], however without any ToF data.

In processes such as central exclusive di-photon production $pp \to p(\gamma\gamma)p$, photons are recorded with the ATLAS central detector and the vertex position of the di-photons is used as a criterion to separate di-photon events coming from the expected ALP signal, from di-photon events produced in other background processes. Therefore, an improved di-photon vertex resolution will contribute to better separate signal and background events.

The ToF detector can provide data to improve the vertex reconstruction, in particular for di-photon events. This additional data improves largely the di-photon vertex reconstruction as currently the di-photon vertex reconstruction uses calorimeter data which was taken at a large distance from the interaction point in the central detector. The extrapolation from the calorimeters to the interaction point has therefore inherently a large uncertainty.

In this analysis performance of the ToF detector on first Run-3 data was

studied. In future searches data provided by the ToF can be used for improvement of the vertex reconstruction, and therefore will help to reduce background in ALP searches.

The 2017 AFP data have been used in a recent ATLAS publication on an Axion-like particle (ALP) search [25]. It is planned that the ALP analysis will be extended using the LHC Run-3 data. The sensitivity for an ALP will be greatly increased by the larger integrated luminosity and an enhanced background reduction using the ToF detector.

Chapter 7

Conclusions

A performance study of the ToF detector was conducted using first LHC Run-3 data. This analysis extends a previous analysis by the present author with different data sets, and adds new techniques. It provides preliminary efficiencies and time resolutions of the ToF detector for 2022 data. Different approaches for obtaining efficiencies were compared with each other and some reasons of the differences were determined. A complete efficiency summary is presented and the results show a downward trend in time for the performance of the detector.

The preliminary time resolutions were obtained after applying a HPTDC calibration and likelihood selection requirements. In addition, the performance study includes a time delay calibration of the ToF detector. A primary proton-proton vertex reconstruction using the ToF detector and a vertex matching analyses with the central ATLAS detector was performed. The resulting resolution of the ToF vertex reconstruction is less than 10 mm, which is consistent with the expectations. These studies were performed mainly on two data sets, with high $\mu = 31.6$ and one with low $\mu = 0.8$.

In addition, the vertex reconstruction of di-photon events is part of a larger effort to use the AFP information together with central ATLAS detector information to search for an Axion-Like-Particle with a di-photon resonance signature, produced in ultraperipheral pp interactions. This is also known as Light-by-Light (LbyL) scattering. A determination of the di-photon vertex reconstruction was performed using a 2022 central ATLAS detector data set. This resolution was found to be much larger than the one determined from the ToF detector.

Bibliography

1. N. Du, et al. Search for Invisible Axion Dark Matter with the Axion Dark Matter Experiment. *Phys. Rev. Lett.* **120,** 151301. https://link.aps.org/doi/10.1103/PhysRevLett.120.151301 (2018).
2. G. Bertone, et al. Particle dark matter: evidence, candidates and constraints. *Physics Reports* **405,** 279–390. ISSN: 0370-1573. https://www.sciencedirect.com/science/article/pii/S0370157304003515 (2005).
3. R.D. Peccei, H.R. Quinn. CP Conservation in the Presence of Pseudoparticles. *Phys. Rev. Lett.* **38,** 1440–1443. https://link.aps.org/doi/10.1103/PhysRevLett.38.1440 (1977).
4. C. Baldenegro, et al. Searching for axion-like particles with proton tagging at the LHC. *Journal of High Energy Physics* **131.** https://doi.org/10.1007/JHEP06(2018)131 (2018).
5. L. Evans. The Large Hadron Collider. *New Journal of Physics* **9,** 335. https://dx.doi.org/10.1088/1367-2630/9/9/335 (2007).
6. J.M. Butterworth, et al. Constraining new physics with collider measurements of Standard Model signatures. *Journal of High Energy Physics* **78.** https://doi.org/10.1007/JHEP03(2017)078 (2017).
7. H. Euler. Über die Streuung von Licht an Licht nach der Diracschen Theorie. *Annalen der Physik* **418,** 398–448. https://doi.org/10.1002/andp.19364180503 (1936).
8. ATLAS Collaboration. Observation of Light-by-Light Scattering in Ultraperipheral Pb + Pb Collisions with the ATLAS Detector. *Phys. Rev. Lett.* **123,** 052001. https://link.aps.org/doi/10.1103/PhysRevLett.123.052001 (2019).
9. L. Adamczyk, et al. *AFP: A Proposal to Install Proton Detectors at 220 m around ATLAS to Complement the ATLAS High Luminosity Physics Program.* ATL-COM-LUM-2011-006. Geneva, 2011. http://cds.cern.ch/record/1017689.
10. ATLAS Collaboration. Observation and Measurement of Forward Proton Scattering in Association with Lepton Pairs Produced via the Photon Fusion Mechanism at ATLAS. *Phys. Rev. Lett.* **125,** 261801. https://link.aps.org/doi/10.1103/PhysRevLett.125.261801 (2020).

11. CMS Collaboration, TOTEM Collaboration. Observation of proton-tagged, central (semi)exclusive production of high-mass lepton pairs in pp collisions at 13 TeV with the CMS-TOTEM precision proton spectrometer. *Journal of High Energy Physics* **153.** https://doi.org/10.1007/JHEP07(2018)153 (2018).

12. Viktoriia Lysenko. *Search for an axion-like particle in data from LHC Run-3 in the ATLAS experiment. (English title)* Presented 24 May 2023 (Diploma Thesis, Taras Shevchenko National University of Kyiv, 2023).

13. ATLAS Collaboration. The ATLAS Experiment at the CERN Large Hadron Collider. *Journal of Instrumentation* **3,** S08003. https://cds.cern.ch/record/1129811 (2008).

14. J. Lange, et al. Beam tests of an integrated prototype of the ATLAS Forward Proton detector. *Journal of Instrumentation* **11,** P09005. https://dx.doi.org/10.1088/1748-0221/11/09/P09005 (2016).

15. L. Nozka, et al. Design of Cherenkov bars for the optical part of the time-of-flight detector in Geant4. *Opt. Express* **22,** 28984–28996. https://opg.optica.org/oe/abstract.cfm?URI=oe-22-23-28984 (2014).

16. M. Rijssenbeek. ATLAS Forward Proton Detectors: Time-of-Flight Electronics. *Acta Physica Polonica B, Proceedings Supplement* **7.** DOI: 10.5506/APhysPolBSupp.7.751, 751–758. https://api.semanticscholar.org/CorpusID:113123705 (2014).

17. M. Mota, et al. *A flexible multi-channel high-resolution time-to-digital converter ASIC* in *2000. IEEE Nuclear Science Symposium. Conference Record (Cat. No.00CH37149)* **2.** DOI: 10.1109/NSSMIC.2000.949889 (2000), 9/155–9/159 vol.2. https://ieeexplore.ieee.org/document/949889.

18. ATLAS Collaboration. *Performance of the ATLAS Forward Proton Time-of-Flight Detector in 2017* ATL-FWD-PUB-2021-002. 2021. https://cds.cern.ch/record/2749821.

19. J. Catmore, et al. A new petabyte-scale data derivation framework for ATLAS. *Journal of Physics: Conference Series* **664,** 072007. https://dx.doi.org/10.1088/1742-6596/664/7/072007 (2015).

20. S. Baird. *Accelerators for pedestrians.* CERN-AB-Note-2007-014, CERN-PS-OP-Note-95-17-Rev-2. Geneva, 2007. http://cds.cern.ch/record/1017689.

21. *AFPTrackContainer* https://atlas-sw-doxygen.web.cern.ch/atlas-sw-doxygen/atlas_22.0.X-DOX/docs/html/d0/d58/classxAOD_1_1AFPTrack___v1.html.

22. *AFPToFHitContainer* https://atlas-sw-doxygen.web.cern.ch/atlas-sw-doxygen/atlas_22.0.X-DOX/docs/html/dd/d70/classxAOD_1_1AFPToFHit___v1.html.

23. ATLAS Collaboration. Luminosity determination in pp collisions at $\sqrt{s}$ = 8 TeV using the ATLAS detector at the LHC. *The European Physical Journal C* **76,** 653. https://doi.org/10.1140/epjc/s10052-016-4466-1 (2016).

24. *ATLAS ATHENA framework* https://atlassoftwaredocs.web.cern.ch/athena/.

25. ATLAS Collaboration. Search for an axion-like particle with forward proton scattering in association with photon pairs at ATLAS. *Journal of High Energy Physics* **234.** https://doi.org/10.1007/JHEP07(2023)234 (2023).

Appendix

A Codes

In Chapter 5 Calo Pointing Tool from ATLAS ATHENA was used for processing files. Source file to this tool is available at Calo Pointing Tool.
Or see the next url: https://acode-browser2.usatlas.bnl.gov/lxr/source/r22/athena/PhysicsAnalysis/ElectronPhotonID/PhotonVertexSelection/Root/PhotonPointingTool.cxx

All the analysis codes, used for this work are available at GitLab.
Or see the next url: https://gitlab.cern.ch/vlysenko/tof_ctu_masters_2023

B ToF time resolution

B.1 Before the HPTDC calibration

In Section 3.2 a few examples of raw time distributions (for train 3) are given.

In this appendix all raw time distributions for the high-μ run 429027 are shown in Figures 1-4. Each figure corresponds to one ToF train. The left peak corresponds to the C-side and the right one to the A-side.

All raw time distributions for the low-μ run 428770 are shown in Figures 5-8. Each Figure corresponds to the ToF train.

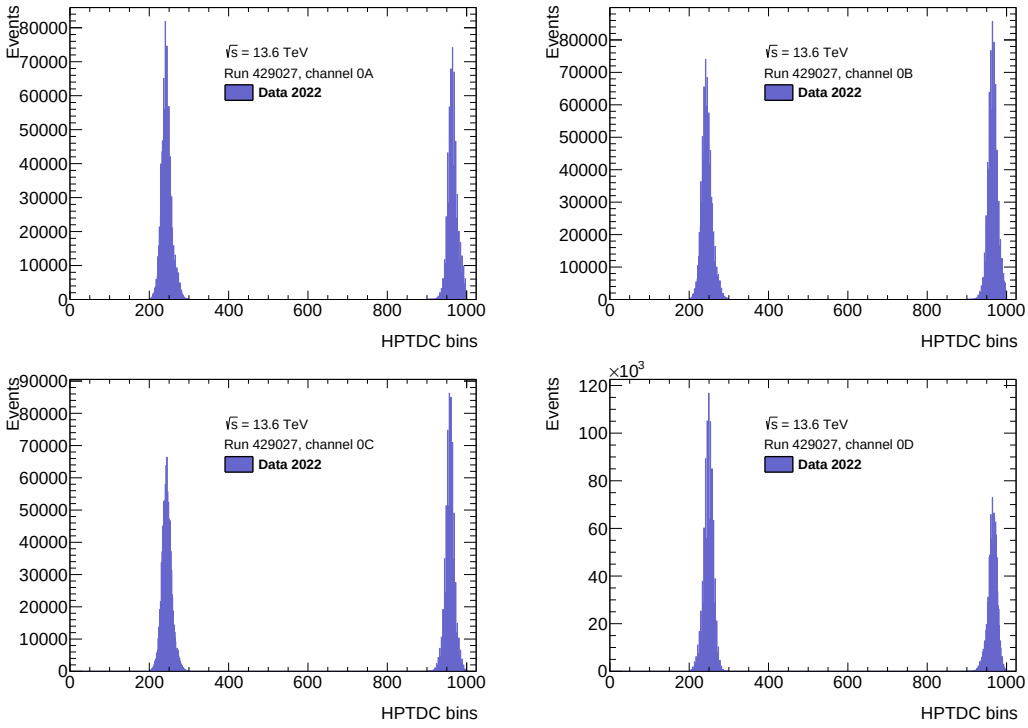

Figure 1: Raw time distributions in run 429027 after the cut on the time for train 0 for each channel: A (top left), B (top right), C (bottom left) and D (bottom right).

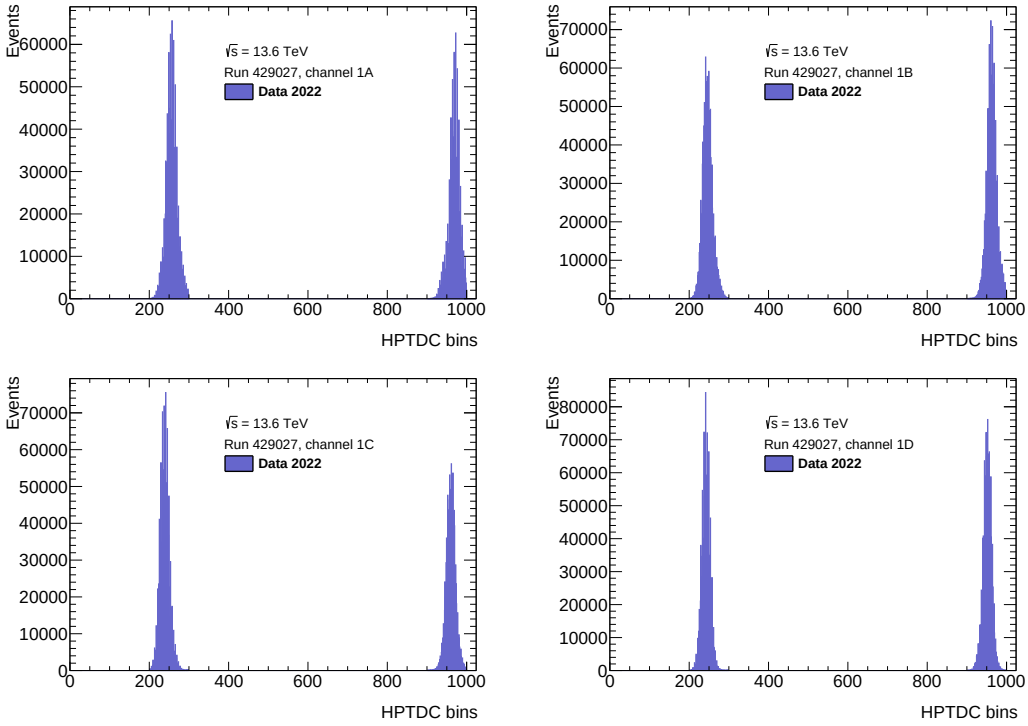

Figure 2: Raw time distributions in run 429027 after the cut on the time for train 1 for each channel: A (top left), B (top right), C (bottom left) and D (bottom right).

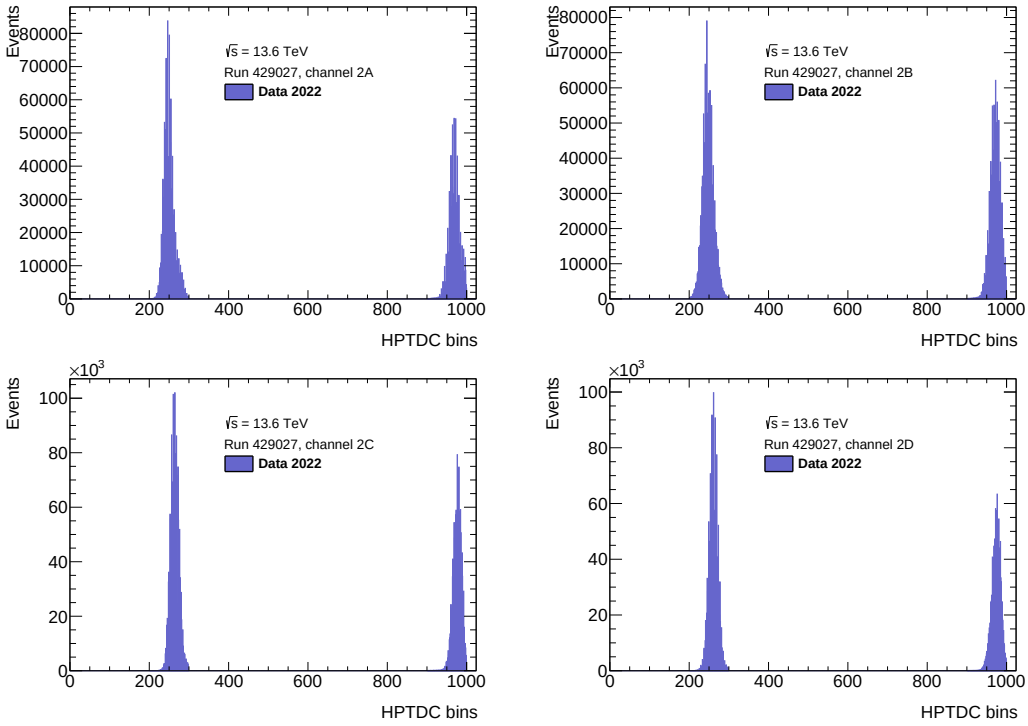

Figure 3: Raw time distributions in run 429027 after the cut on the time for train 2 for each channel: A (top left), B (top right), C (bottom left) and D (bottom right).

,

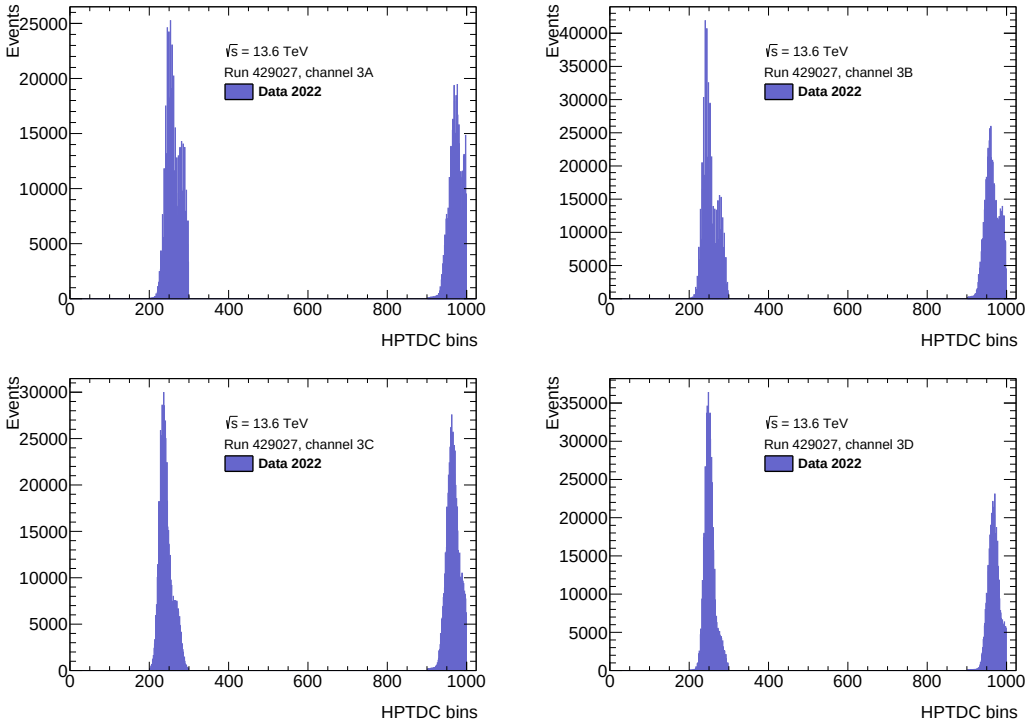

Figure 4: Raw time distributions in run 429027 after the cut on the time for train 3 for each channel: A (top left), B (top right), C (bottom left) and D (bottom right).

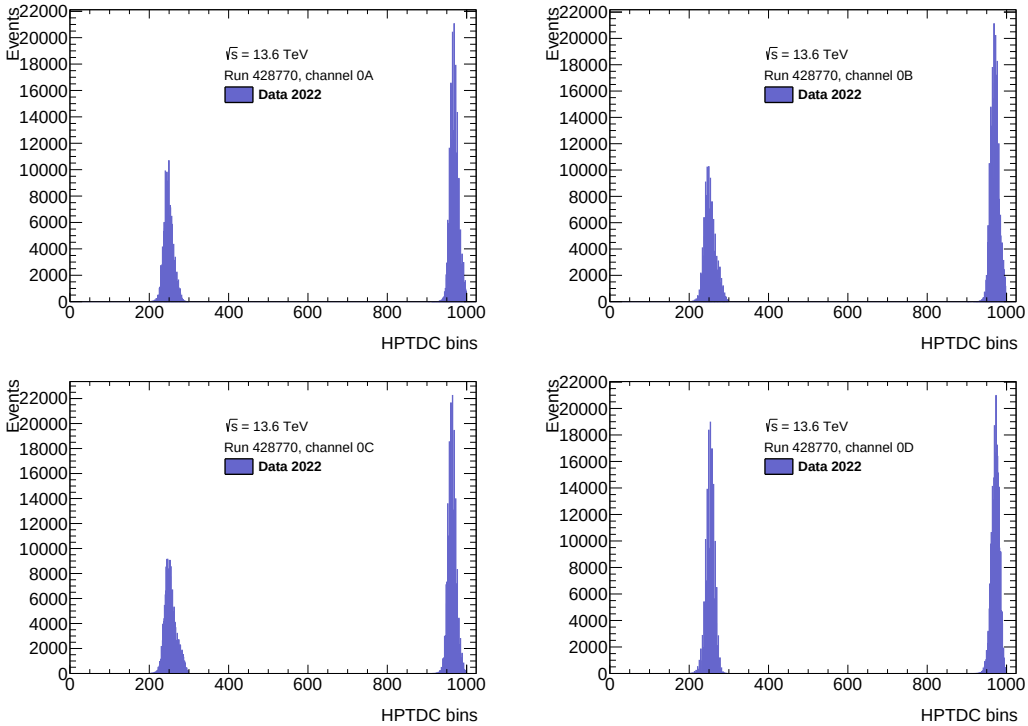

Figure 5: Raw time distributions in low-μ run 428770 after the cut on the time for train 0 for each channel: A (top left), B (top right), C (bottom left) and D (bottom right).

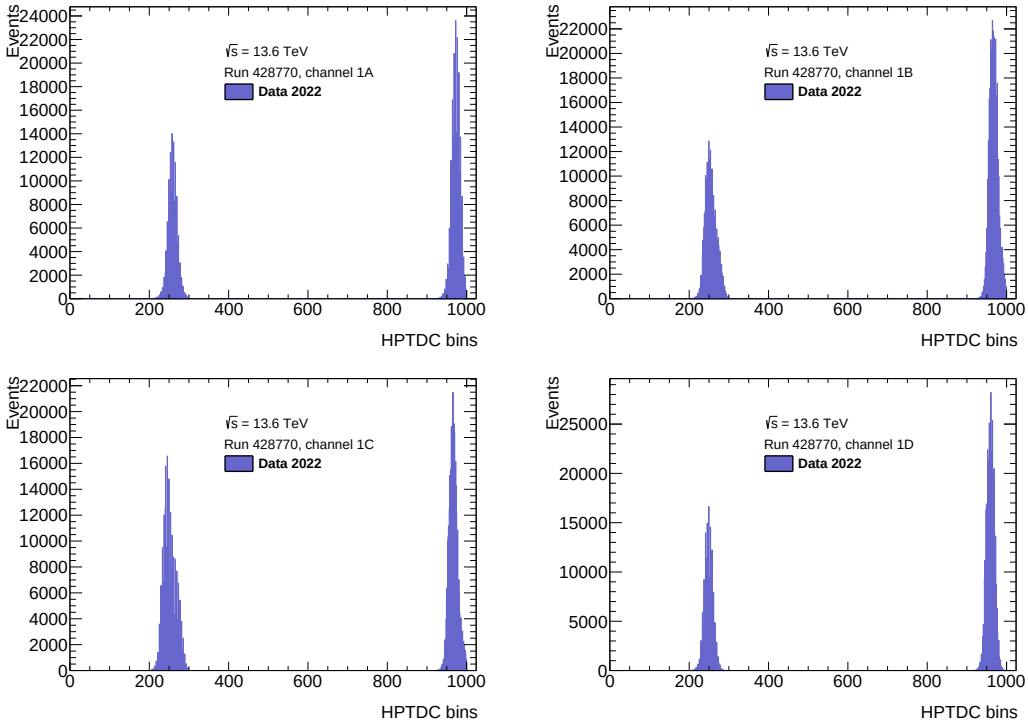

Figure 6: Raw time distributions in low-μ run 428770 after the cut on the time for train 1 for each channel: A (top left), B (top right), C (bottom left) and D (bottom right).

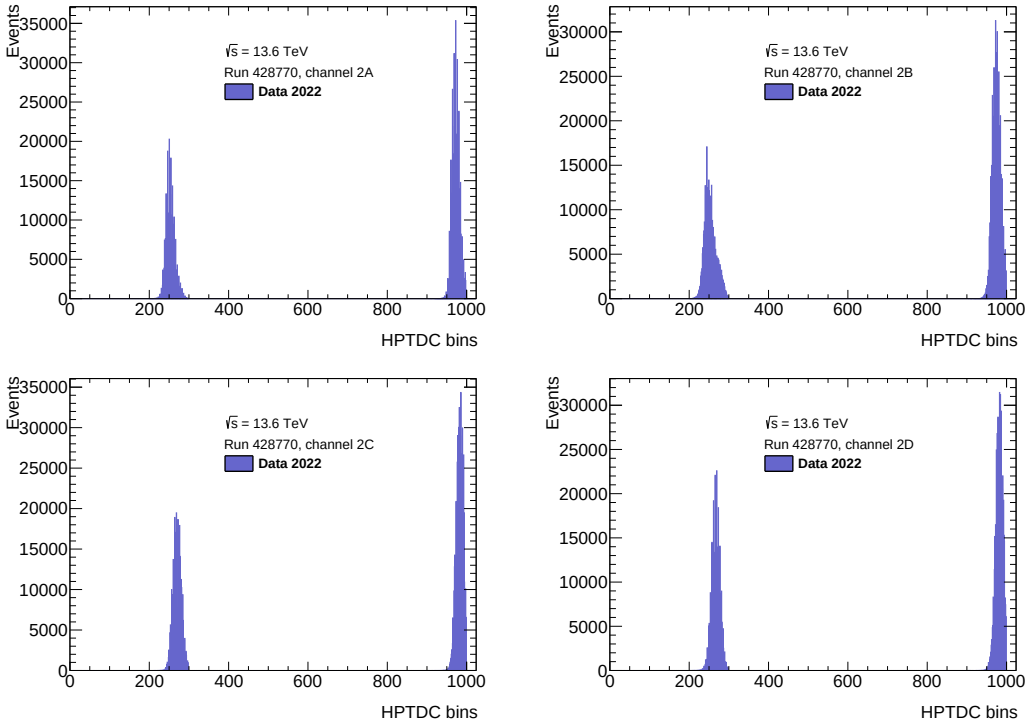

Figure 7: Raw time distributions in low-μ run 428770 after the cut on the time for train 2 for each channel: A (top left), B (top right), C (bottom left) and D (bottom right).

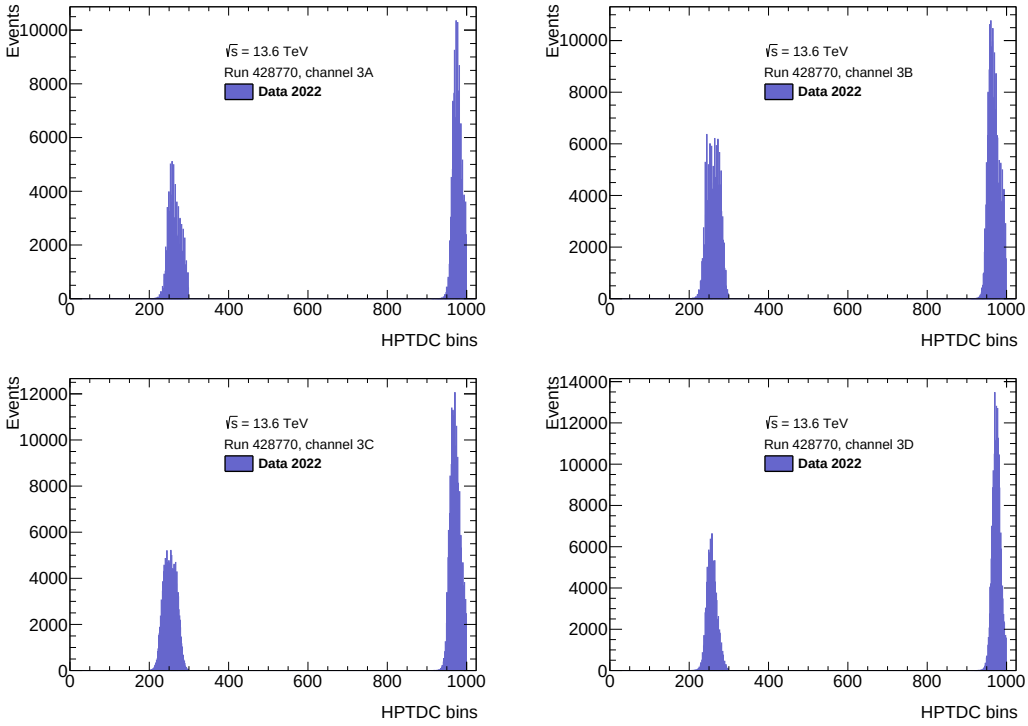

Figure 8: Raw time distributions in low-μ run 428770 after the cut on the time for train 3 for each channel: A (top left), B (top right), C (bottom left) and D (bottom right).

In Section 3.2 the Δt distributions were studied to obtain single-channel time resolution of the ToF detector.

All Δt distributions before the HPTDC calibration for the high-μ run 429027 with a double-Gaussian fitted curve overlaid are shown in Figures 9-12 for the side A and in Figures 13-16 for the side C, each Figure corresponds to the ToF train.

All Δt distributions before the HPTDC calibration for the low-μ run 428770 with a double-Gaussian fitted curve overlaid are shown in Figures 17-20 for the side A and in Figures 21-24 for the side C, each Figure corresponds to the single ToF train.

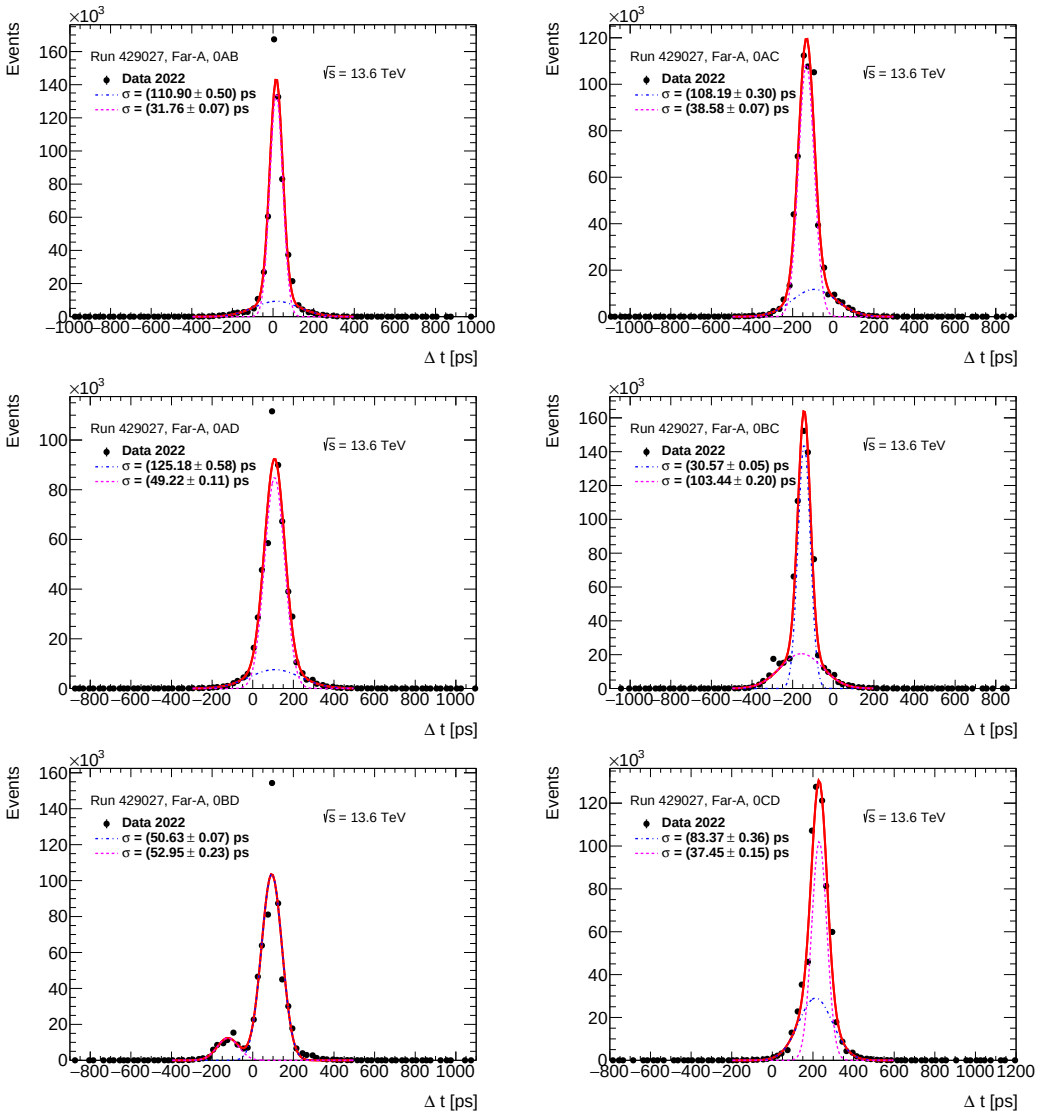

Figure 9: Δt distributions for the run 429027 with a double Gaussian fitted curve overlaid for all combinations of the ToF channels in train 0 for the A-side.

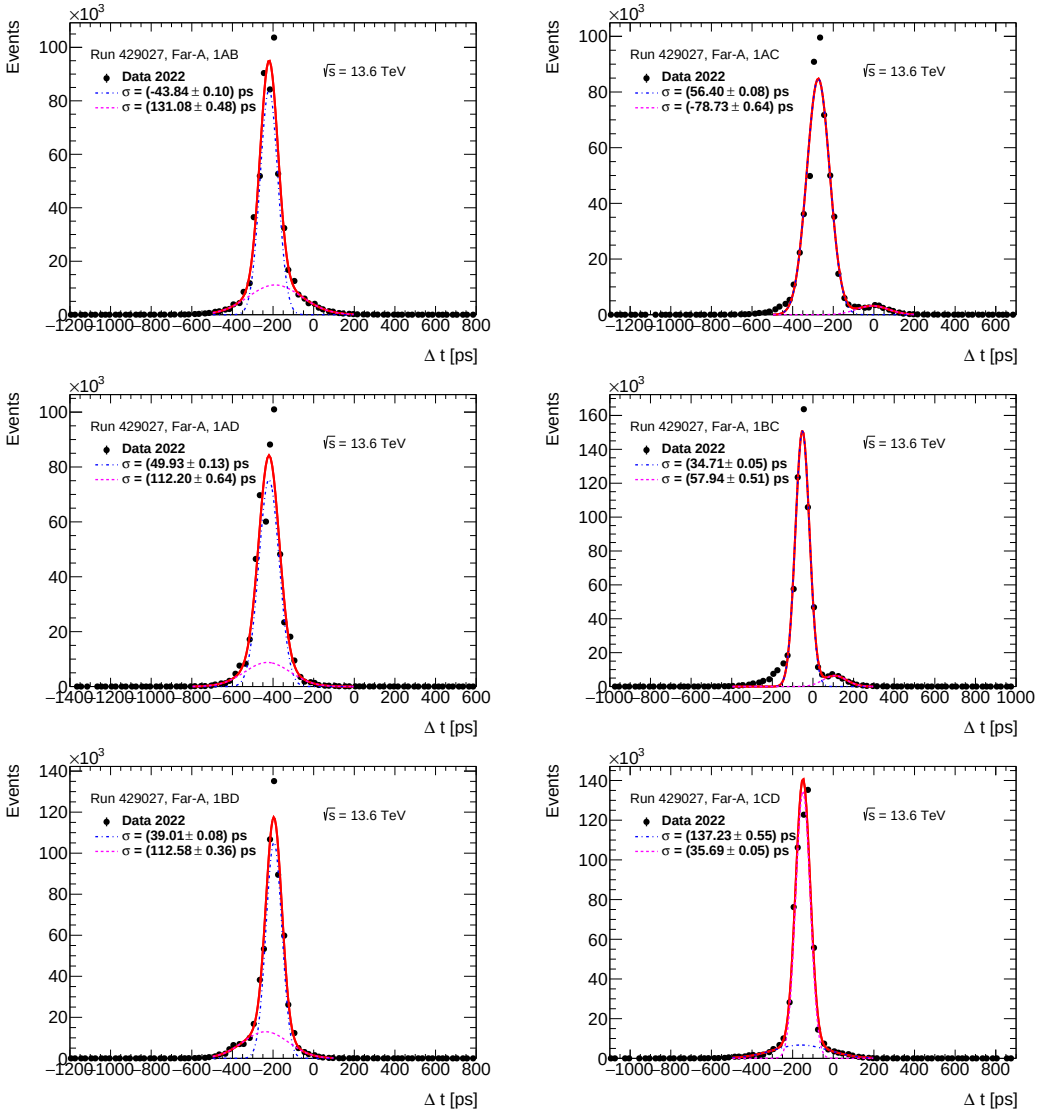

Figure 10: Δt distributions for the run 429027 with a double Gaussian fitted curve overlaid for all combinations of the ToF channels in train 1 for the A-side.

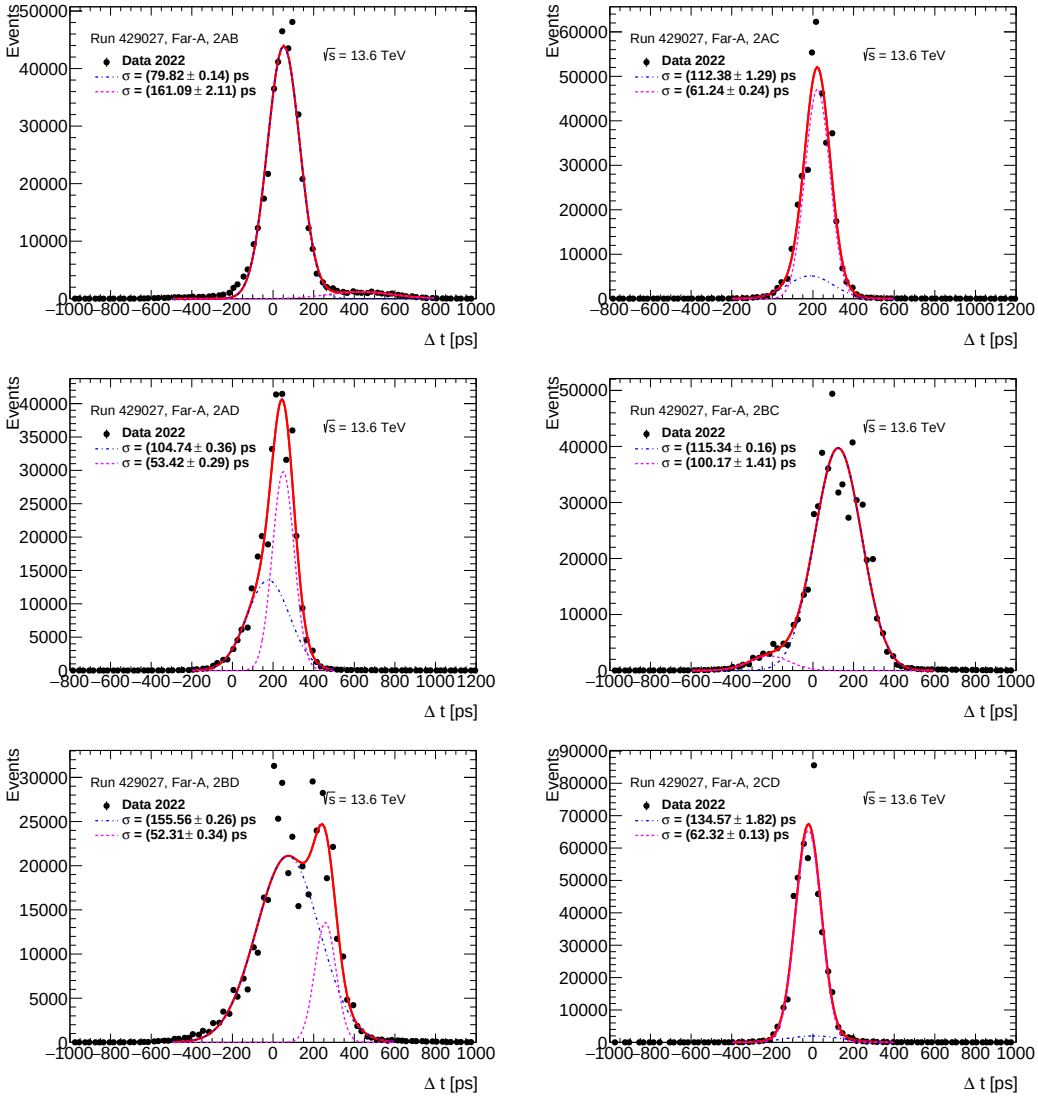

Figure 11: Δt distributions for the run 429027 with a double Gaussian fitted curve overlaid for all combinations of the ToF channels in train 2 for the A-side.

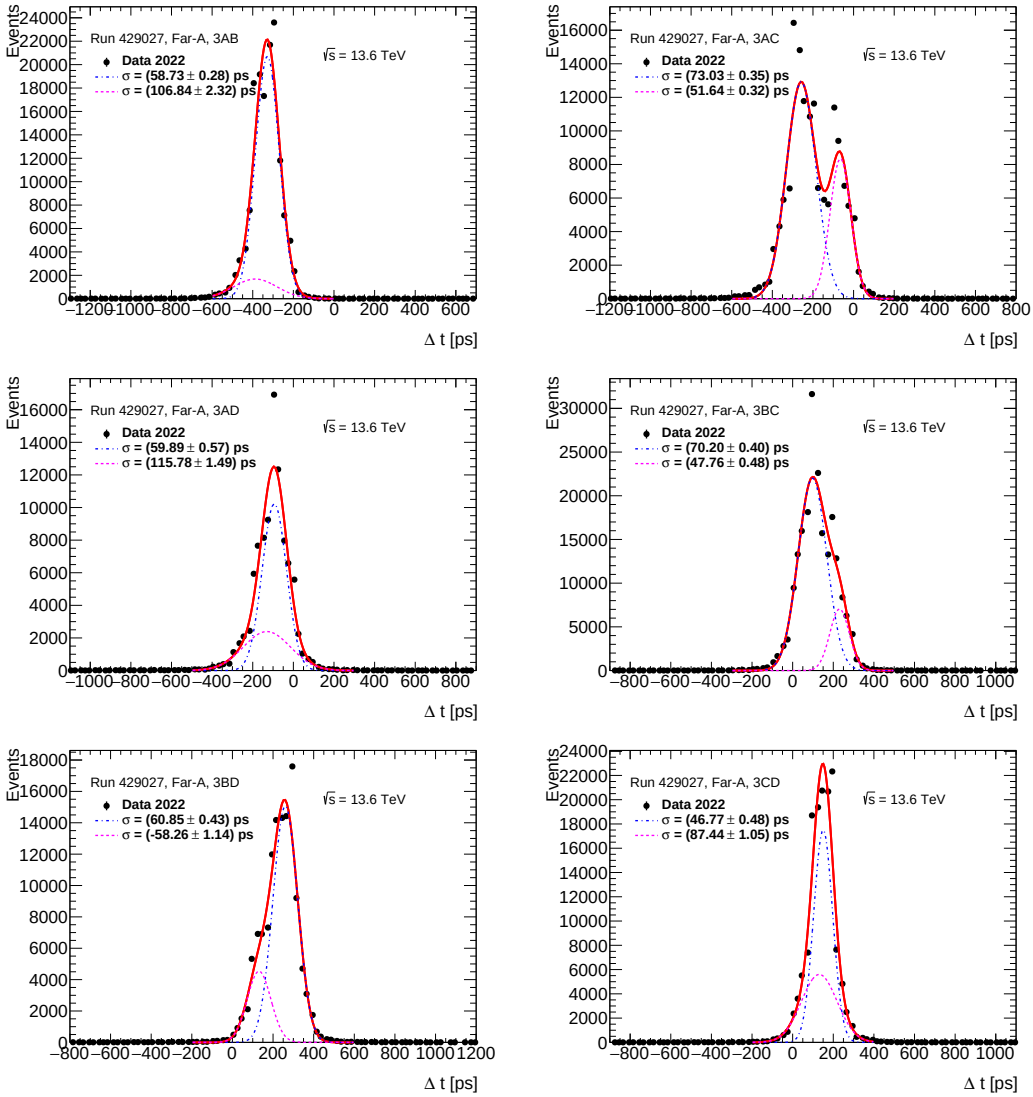

Figure 12: Δt distributions for the run 429027 with a double Gaussian fitted curve overlaid for all combinations of the ToF channels in train 3 for the A-side.

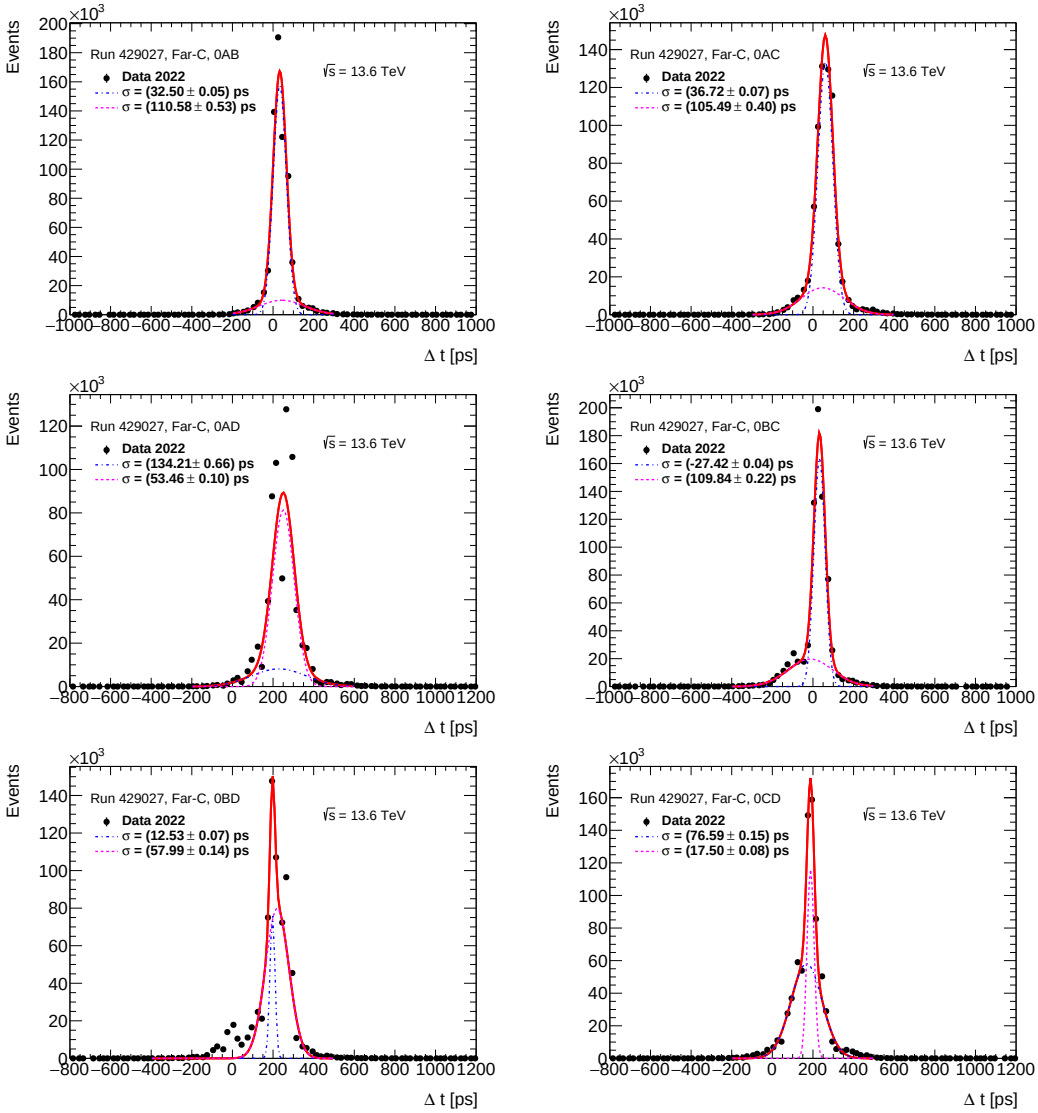

Figure 13: Δt distributions for the run 429027 with a double Gaussian fitted curve overlaid for all combinations of the ToF channels in train 0 for the C-side.

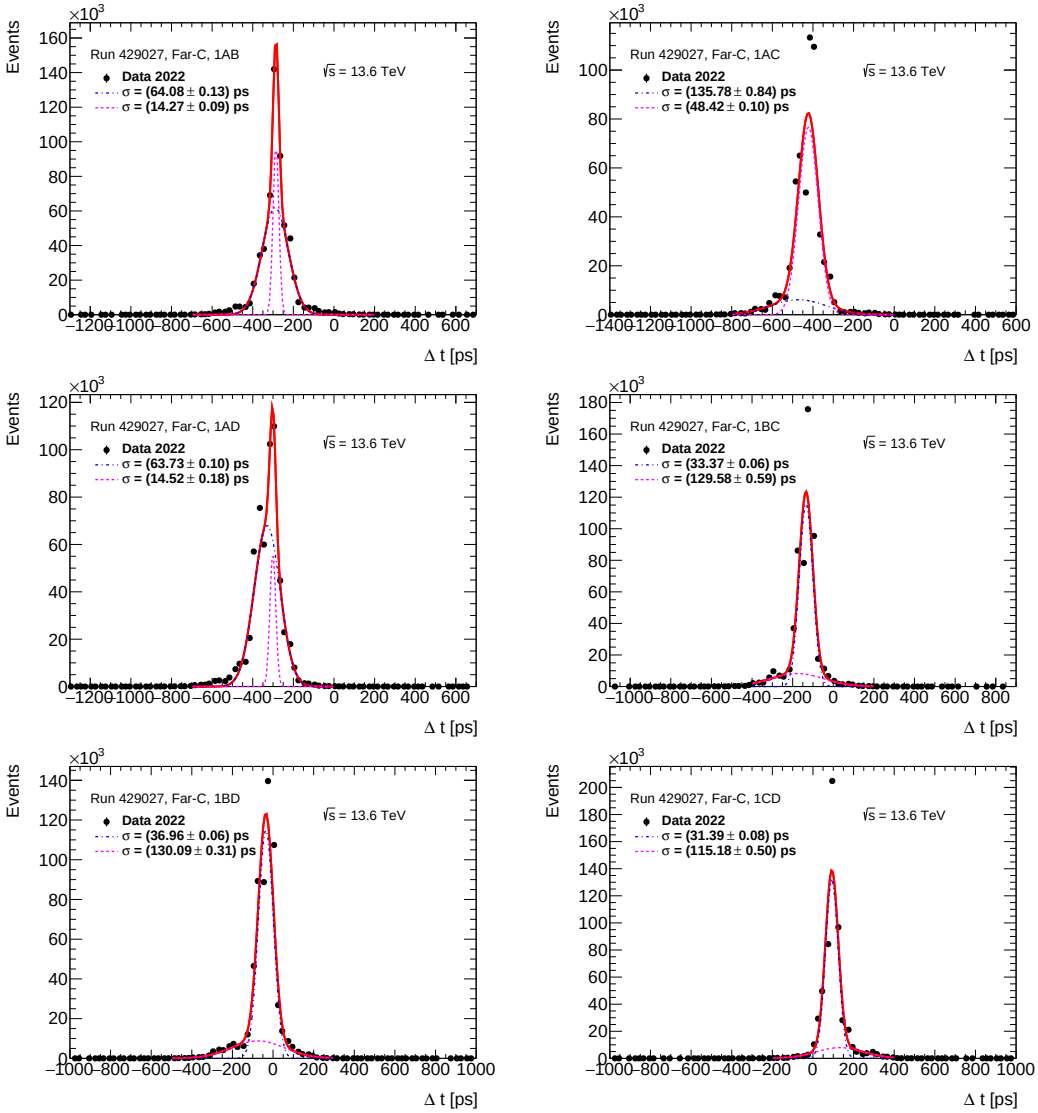

Figure 14: Δt distributions for the run 429027 with a double Gaussian fitted curve overlaid for all combinations of the ToF channels in train 1 for the C-side.

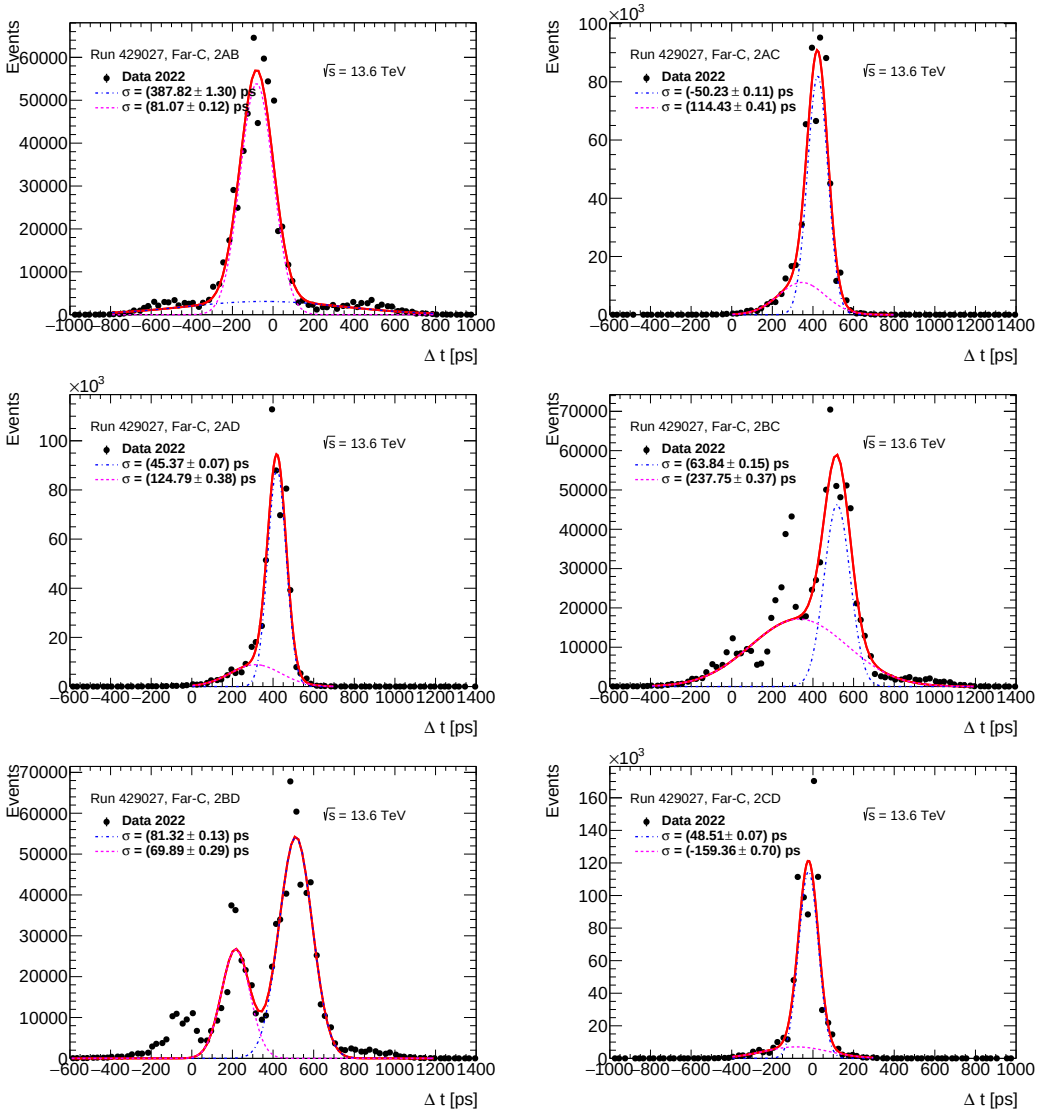

Figure 15: Δt distributions for the run 429027 with a double Gaussian fitted curve overlaid for all combinations of the ToF channels in train 2 for the C-side.

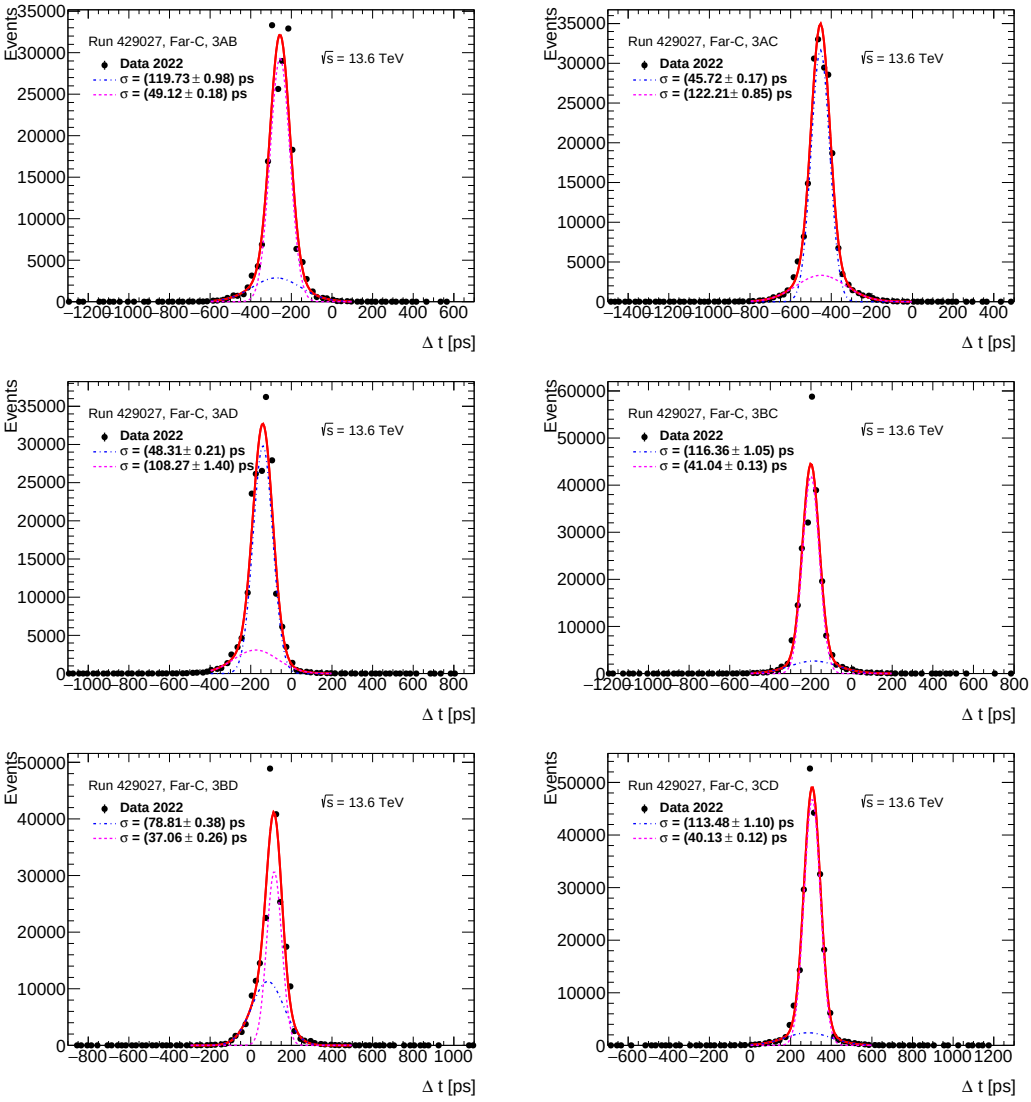

Figure 16: Δt distributions for the run 429027 with a double Gaussian fitted curve overlaid for all combinations of the ToF channels in train 3 for the C-side.

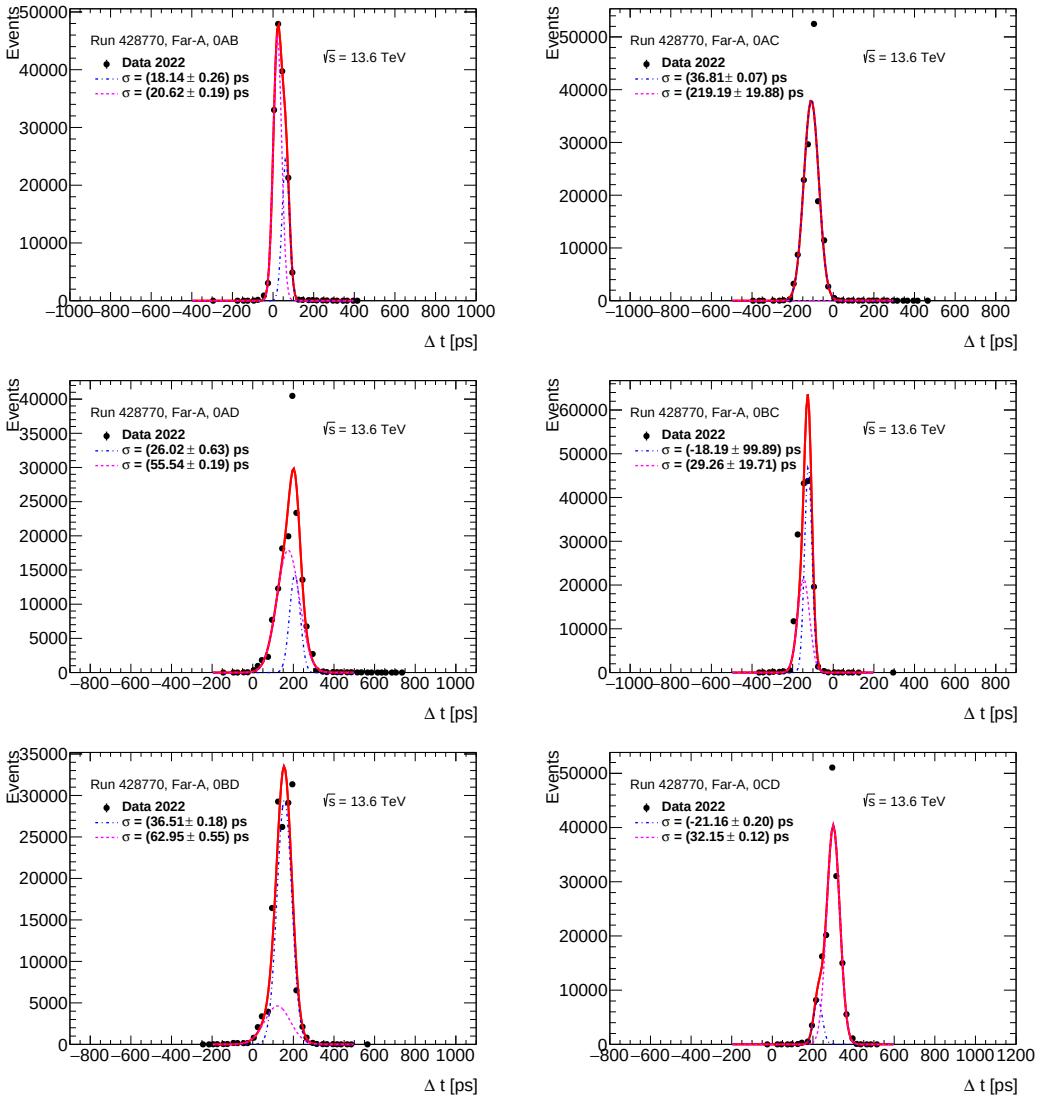

Figure 17: Δt distributions for the low-μ run 428770 with a double Gaussian fitted curve overlaid for all combinations of the ToF channels in train 0 for the A-side.

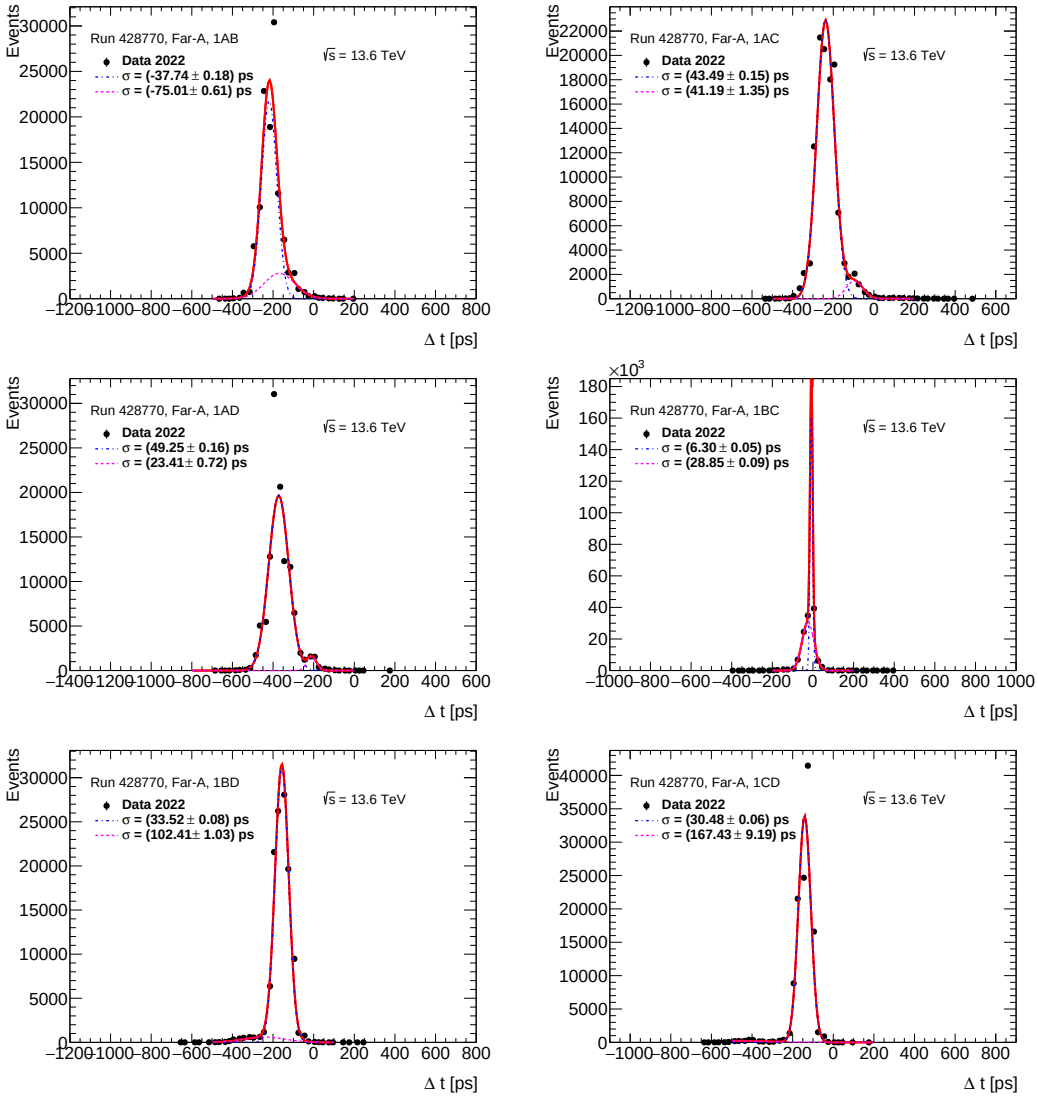

Figure 18: Δt distributions for the low-μ run 428770 with a double Gaussian fitted curve overlaid for all combinations of the ToF channels in train 1 for the A-side.

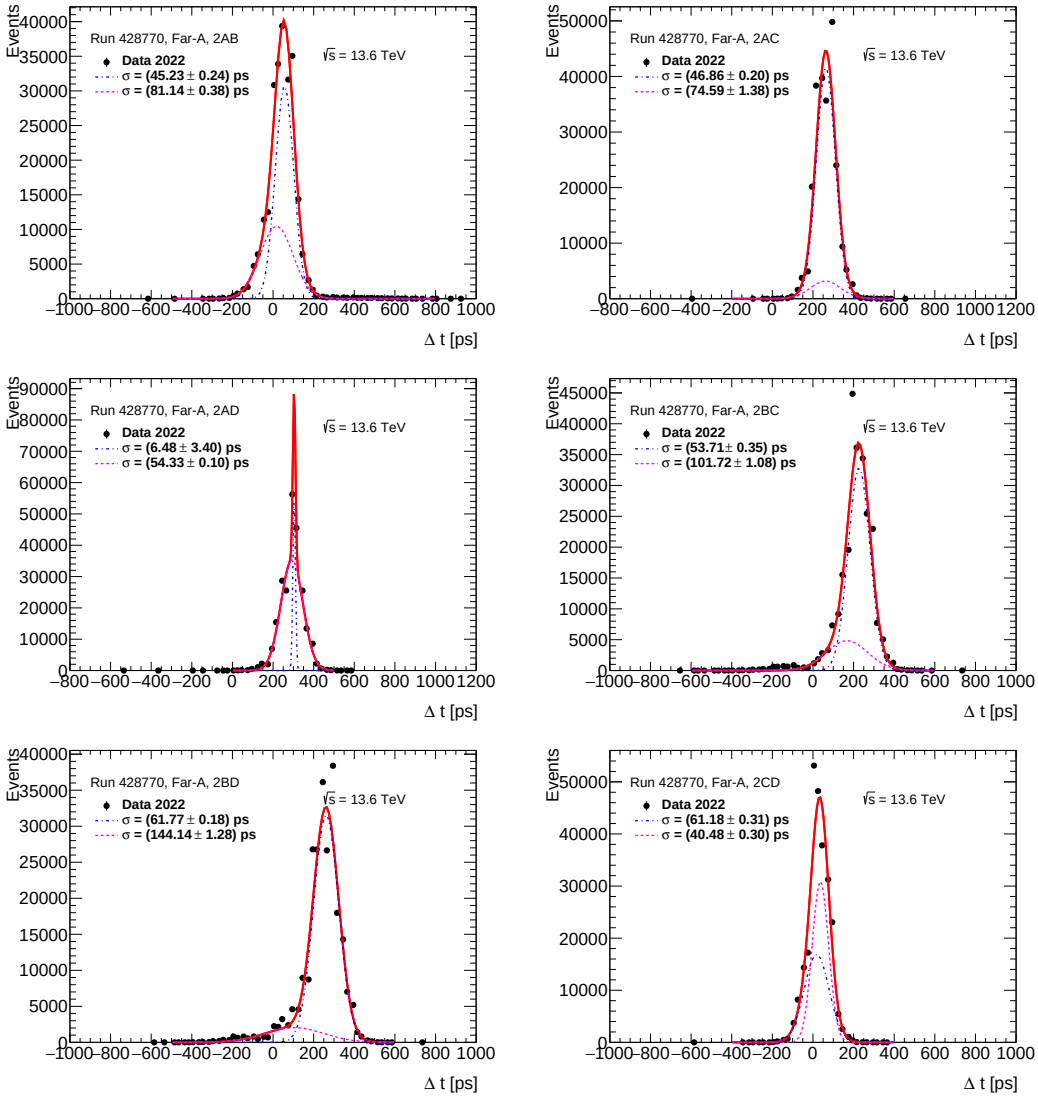

Figure 19: Δt distributions for the low-μ run 428770 with a double Gaussian fitted curve overlaid for all combinations of the ToF channels in train 2 for the A-side.

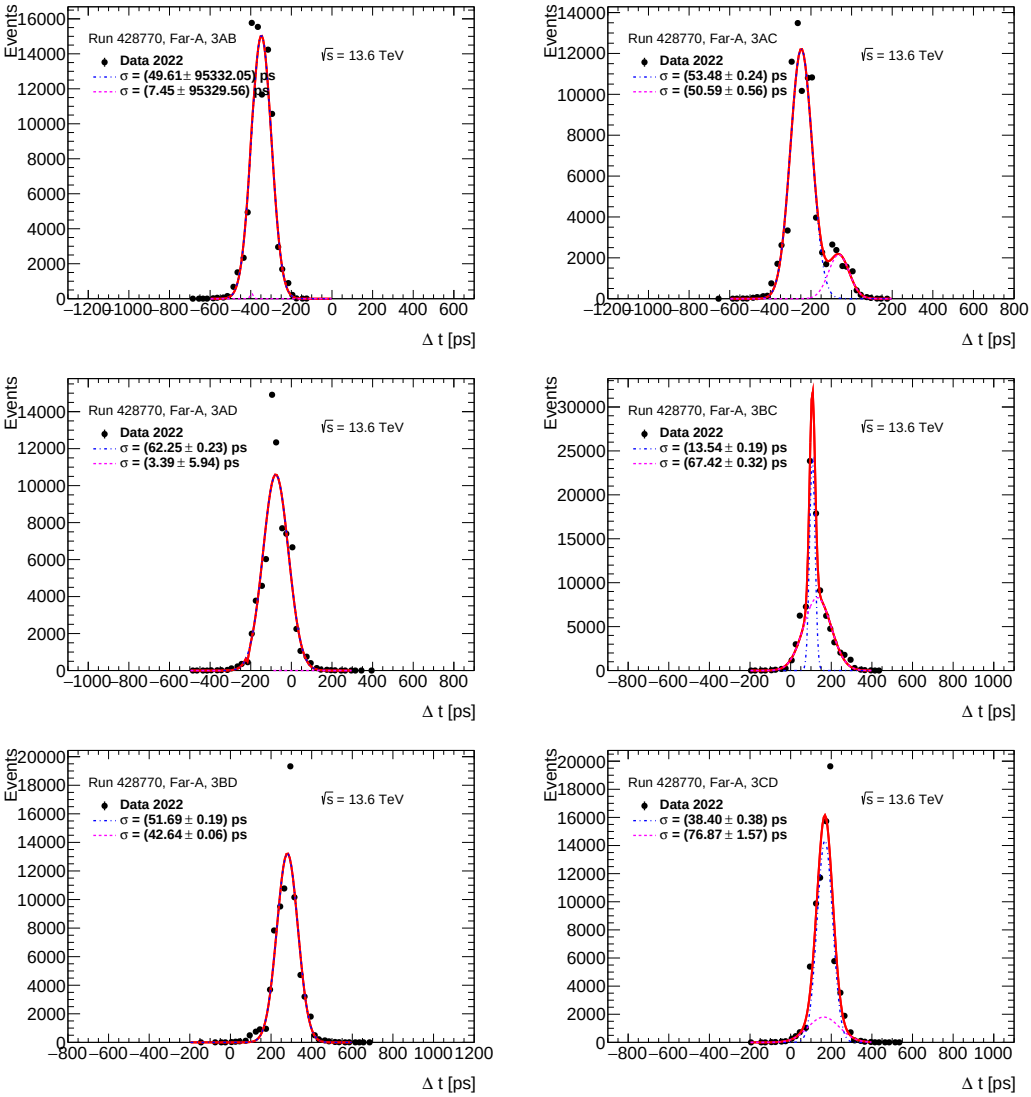

Figure 20: Δt distributions for the low-μ run 428770 with a double Gaussian fitted curve overlaid for all combinations of the ToF channels in train 3 for the A-side.

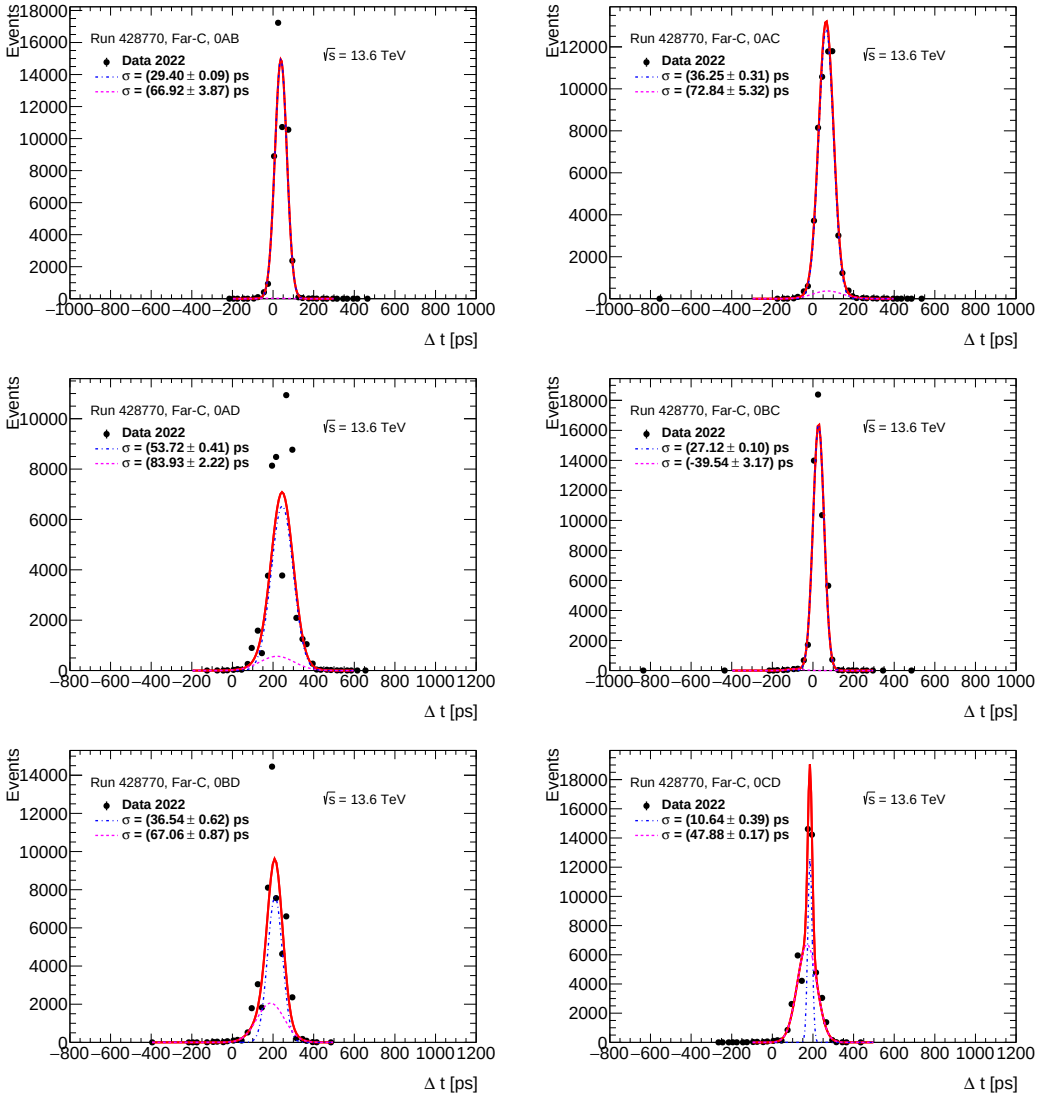

Figure 21: Δt distributions for the low-μ run 428770 with a double Gaussian fitted curve overlaid for all combinations of the ToF channels in train 0 for the C-side.

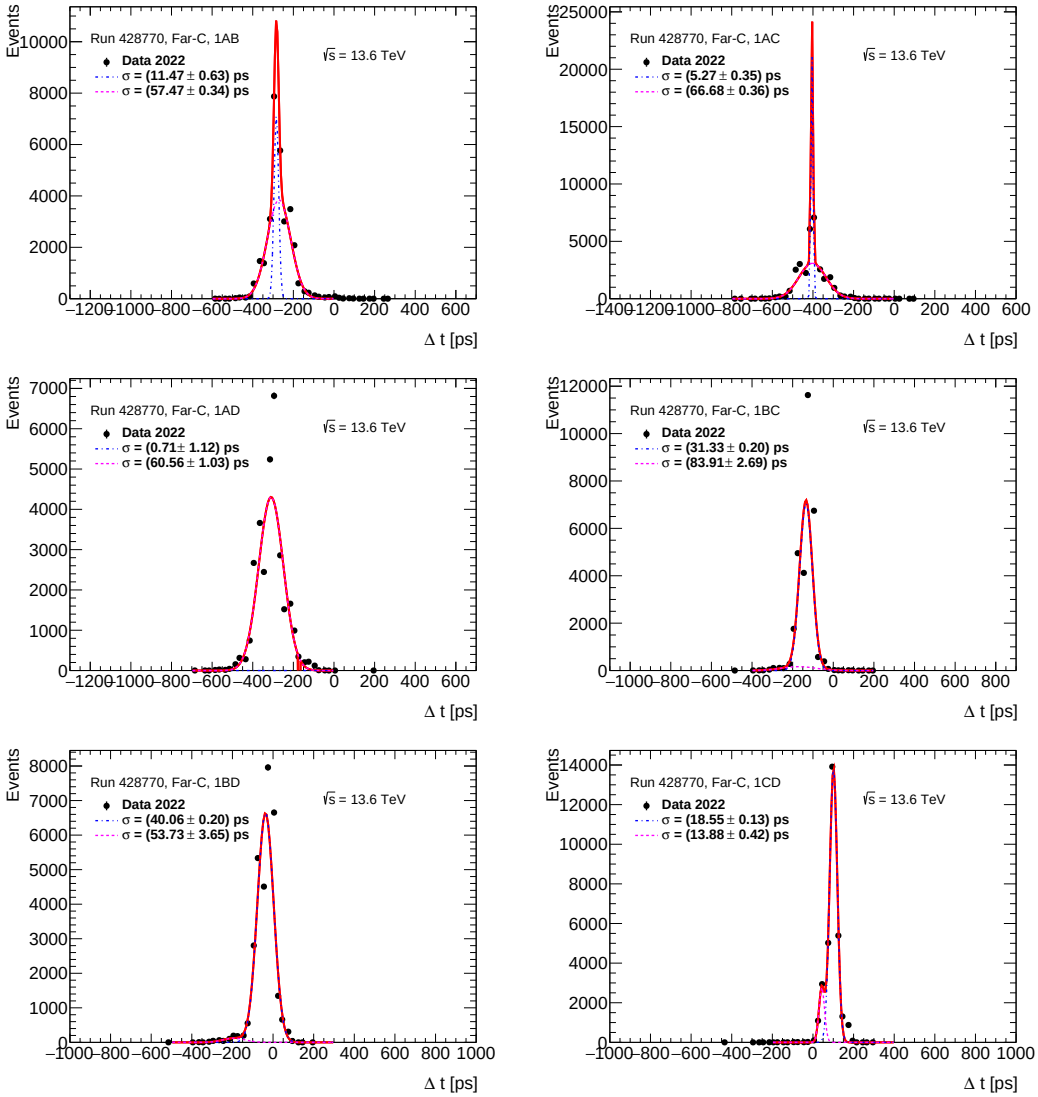

Figure 22: Δt distributions for the low-μ run 428770 with a double Gaussian fitted curve overlaid for all combinations of the ToF channels in train 1 for the C-side.

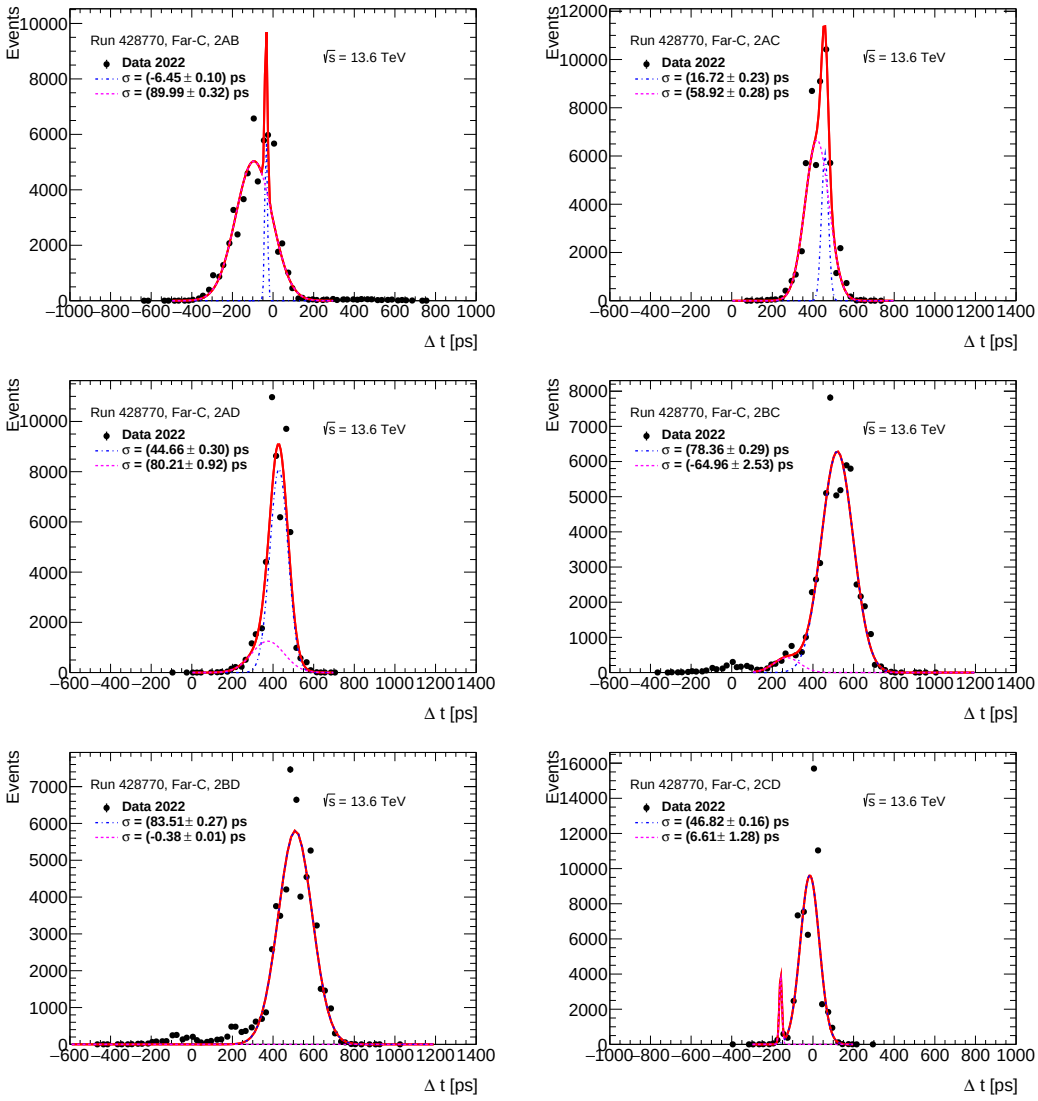

Figure 23: Δt distributions for the low-μ run 428770 with a double Gaussian fitted curve overlaid for all combinations of the ToF channels in train 2 for the C-side.

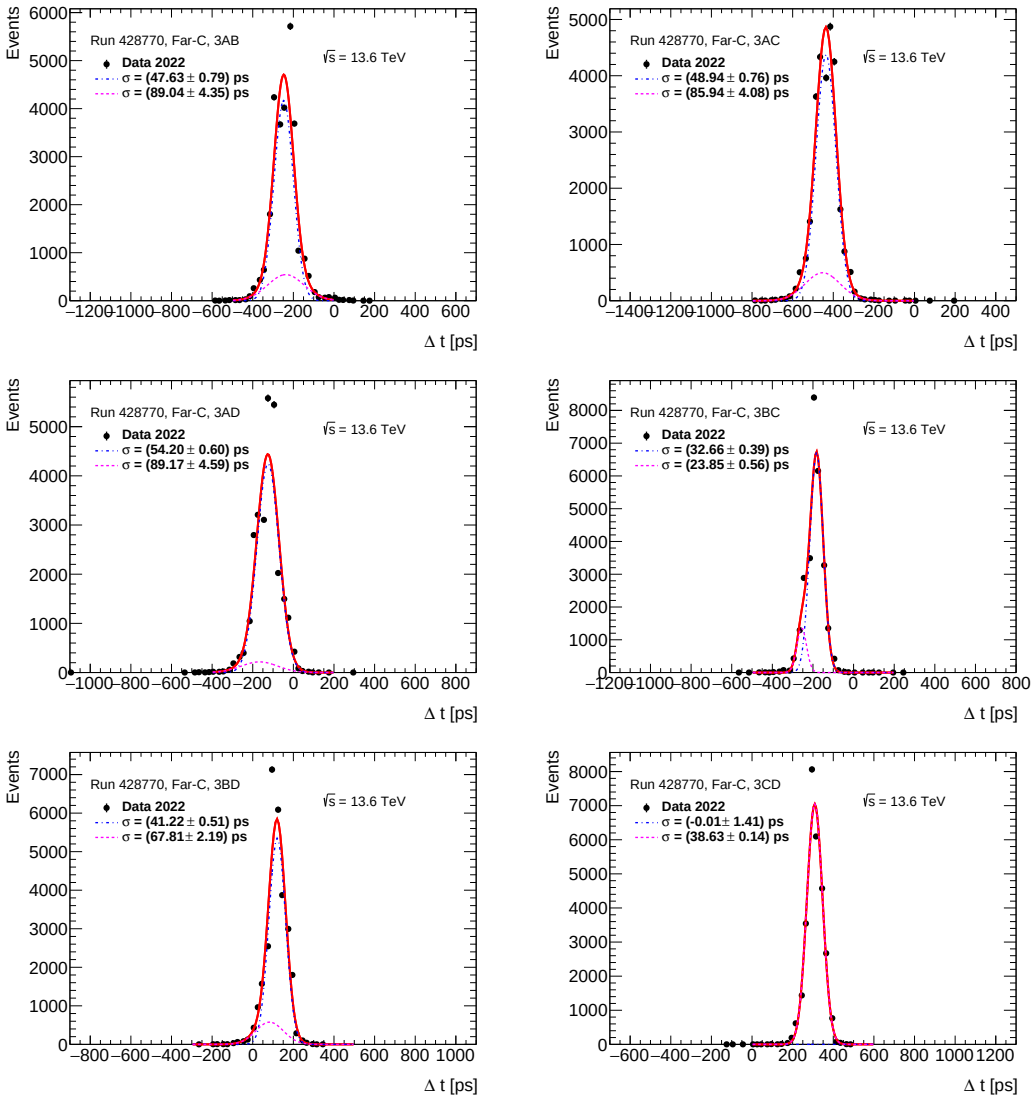

Figure 24: Δt distributions for the low-μ run 428770 with a double Gaussian fitted curve overlaid for all combinations of the ToF channels in train 3 for the C-side.

B.2 After the HPTDC calibration

In Section 3.2.2 the HPTDC calibration was performed.

All raw time distributions before and after the HPTDC calibration for the high-μ run 429027 are shown in Figures 25-28 for the side A and in Figures 29-32 for the side C, each Figure corresponds to one ToF train.

All raw time distributions before and after the HPTDC calibration for the low-μ run 428770 are shown in Figures 33-36 for the side A and in Figures 37-40 for the side C, each Figure corresponds to one ToF train.

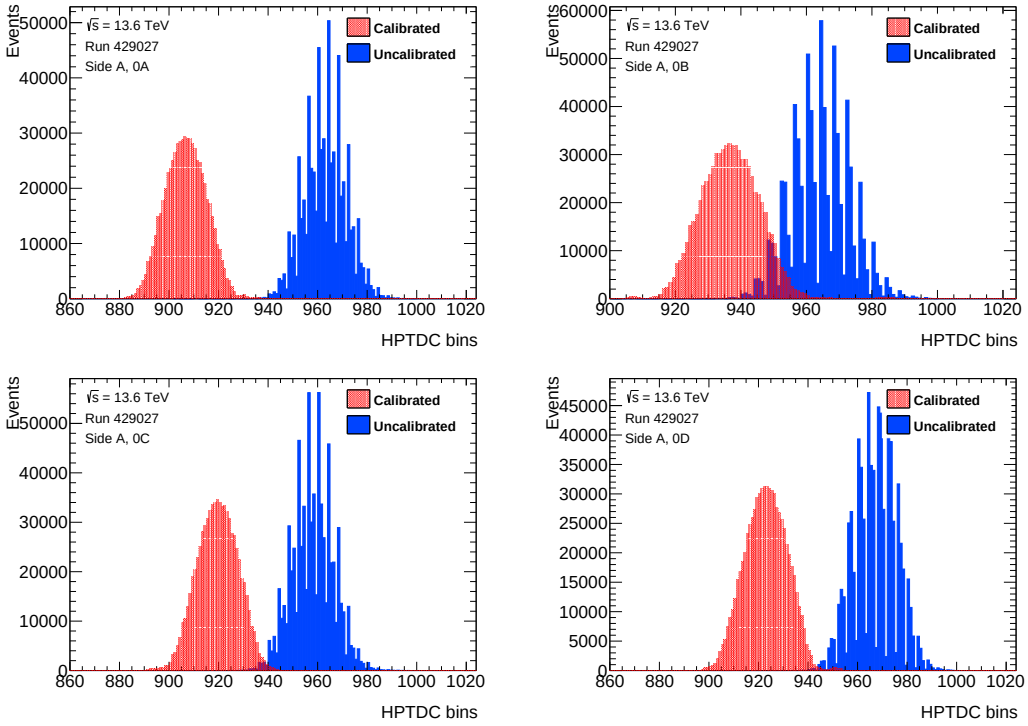

Figure 25: Raw time distributions before (blue) and after (red) the calibration in high-μ run 429027 for all ToF channels in train 0 for the A-side.

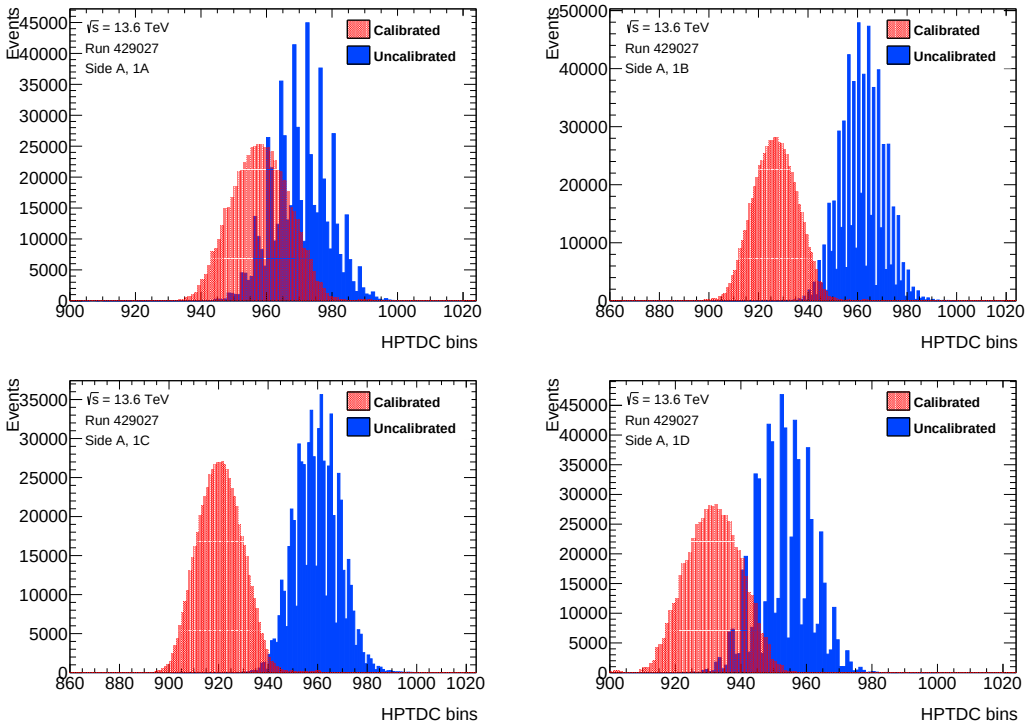

Figure 26: Raw time distributions before (blue) and after (red) the calibration in high-μ run 429027 for all ToF channels in train 1 for the A-side.

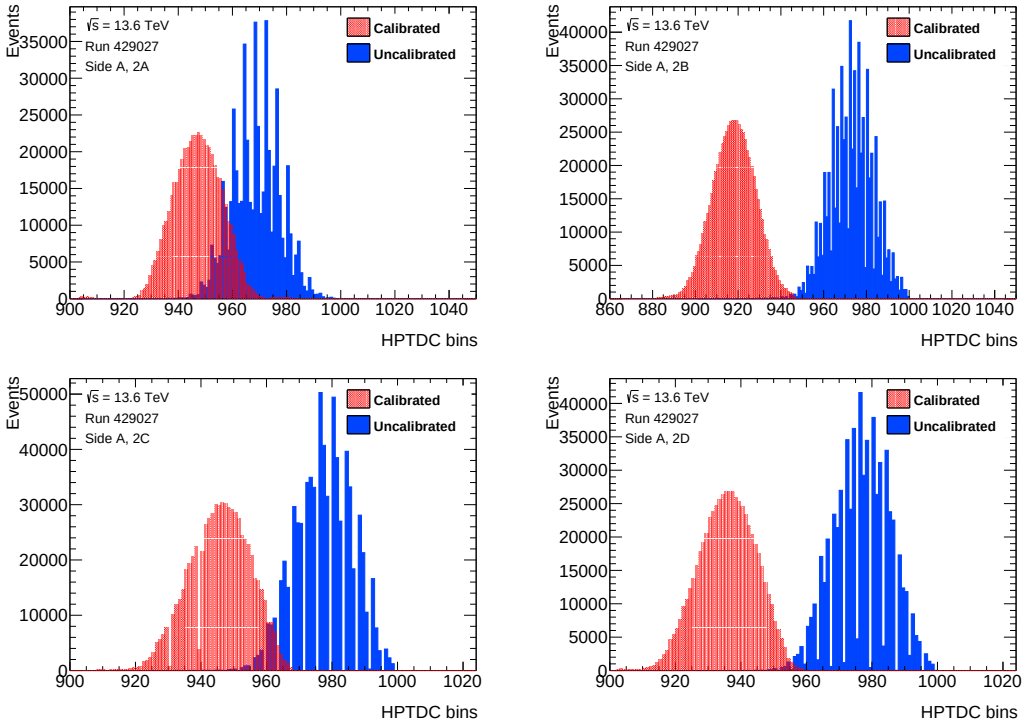

Figure 27: Raw time distributions before (blue) and after (red) the calibration in high-μ run 429027 for all ToF channels in train 2 for the A-side.

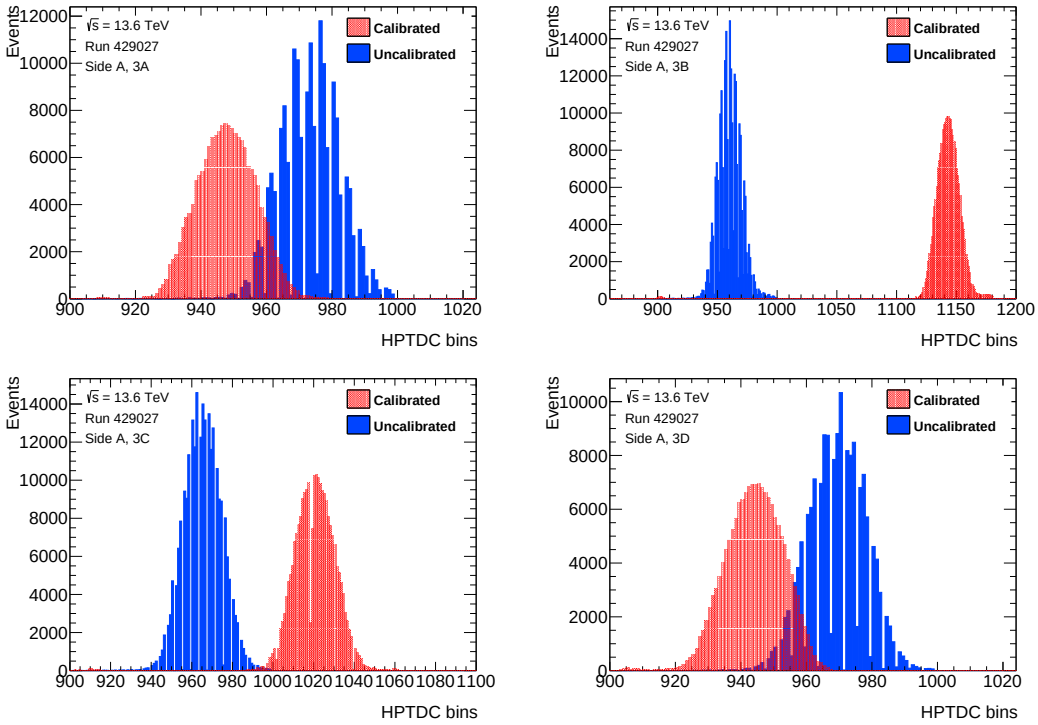

Figure 28: Raw time distributions before (blue) and after (red) the calibration in high-μ run 429027 for all ToF channels in train 3 for the A-side.

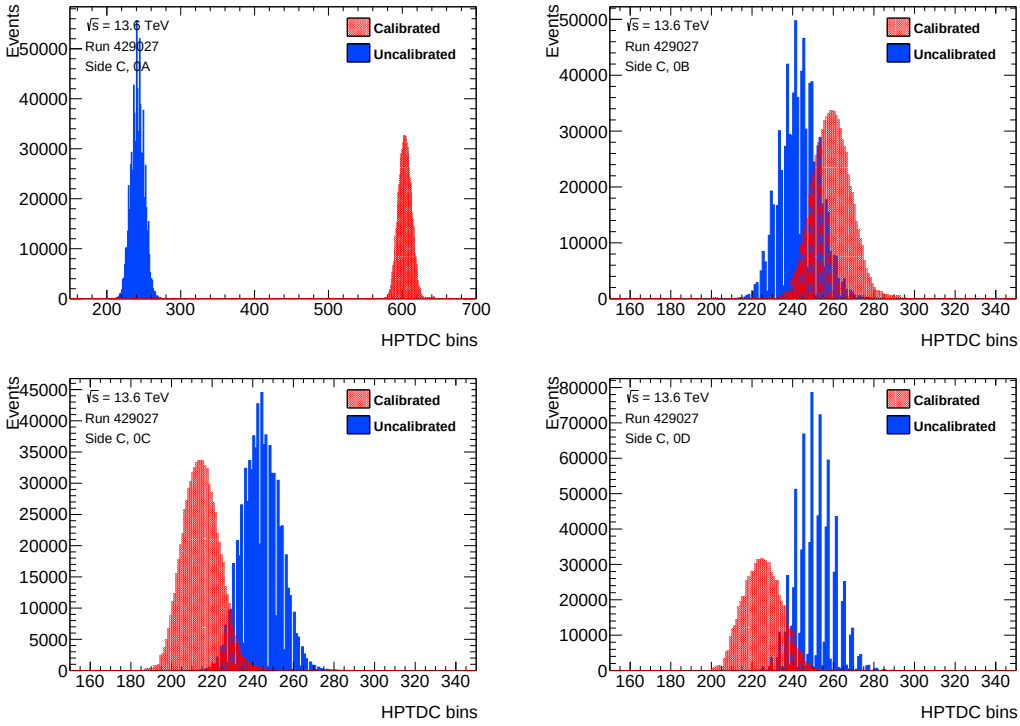

Figure 29: Raw time distributions before (blue) and after (red) the calibration in high-μ run 429027 for all ToF channels in train 0 for the C-side.

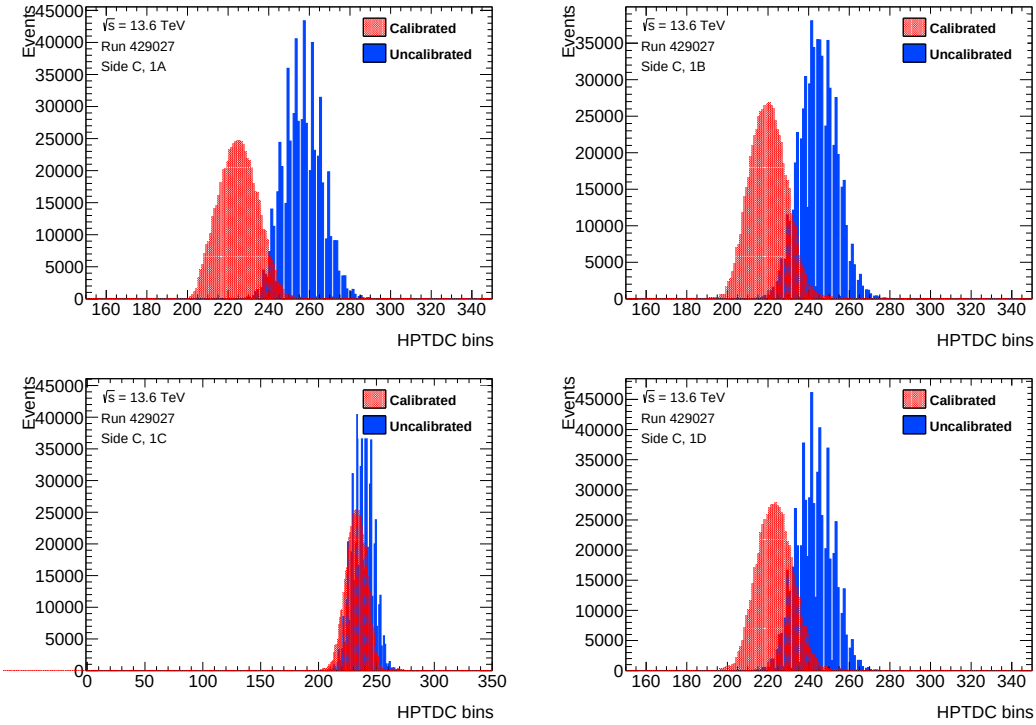

Figure 30: Raw time distributions before (blue) and after (red) the calibration in high-μ run 429027 for all ToF channels in train 1 for the C-side.

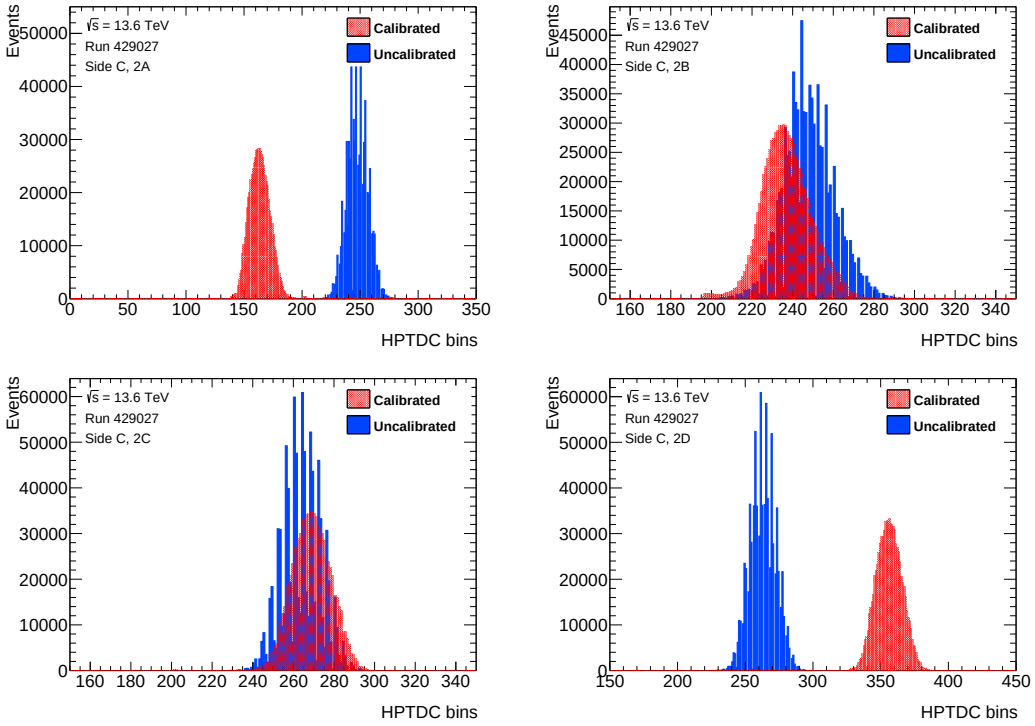

Figure 31: Raw time distributions before (blue) and after (red) the calibration in high-μ run 429027 for all ToF channels in train 2 for the C-side.

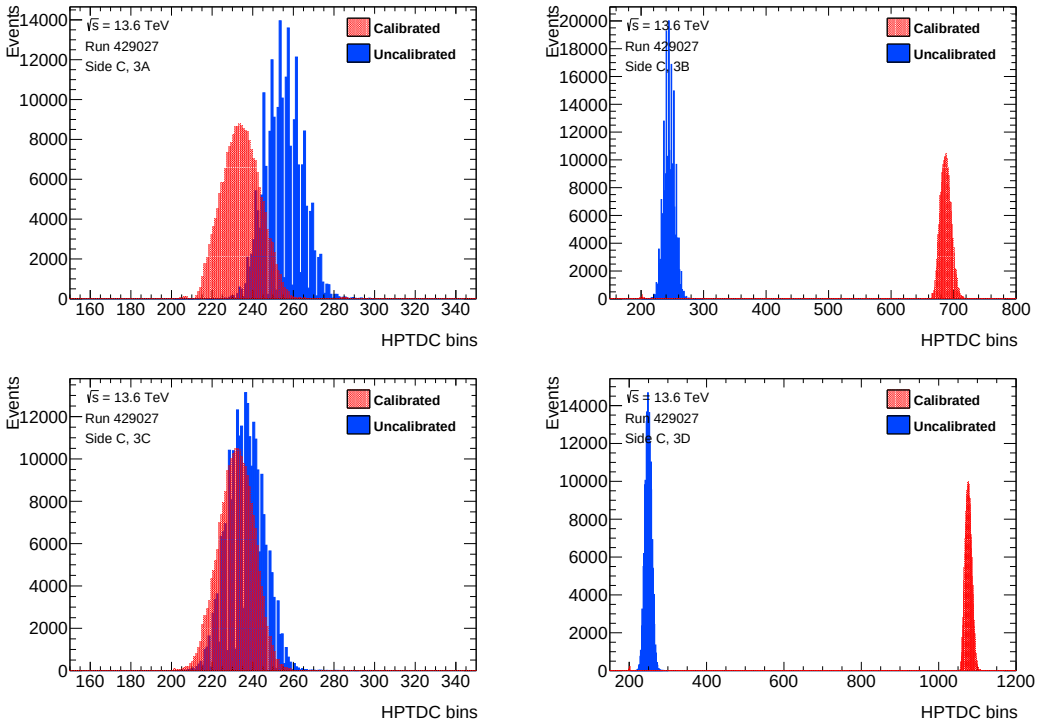

Figure 32: Raw time distributions before (blue) and after (red) the calibration in high-μ run 429027 for all ToF channels in train 3 for the C-side.

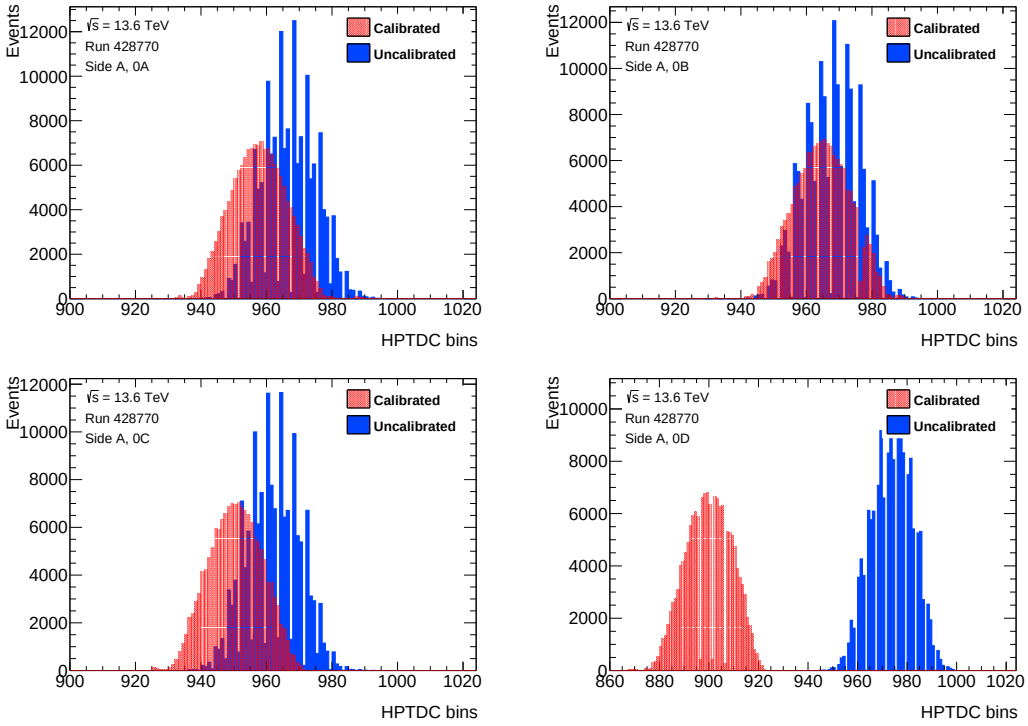

Figure 33: Raw time distributions before (blue) and after (red) the calibration in low-μ run 428770 for all ToF channels in train 0 for the A-side.

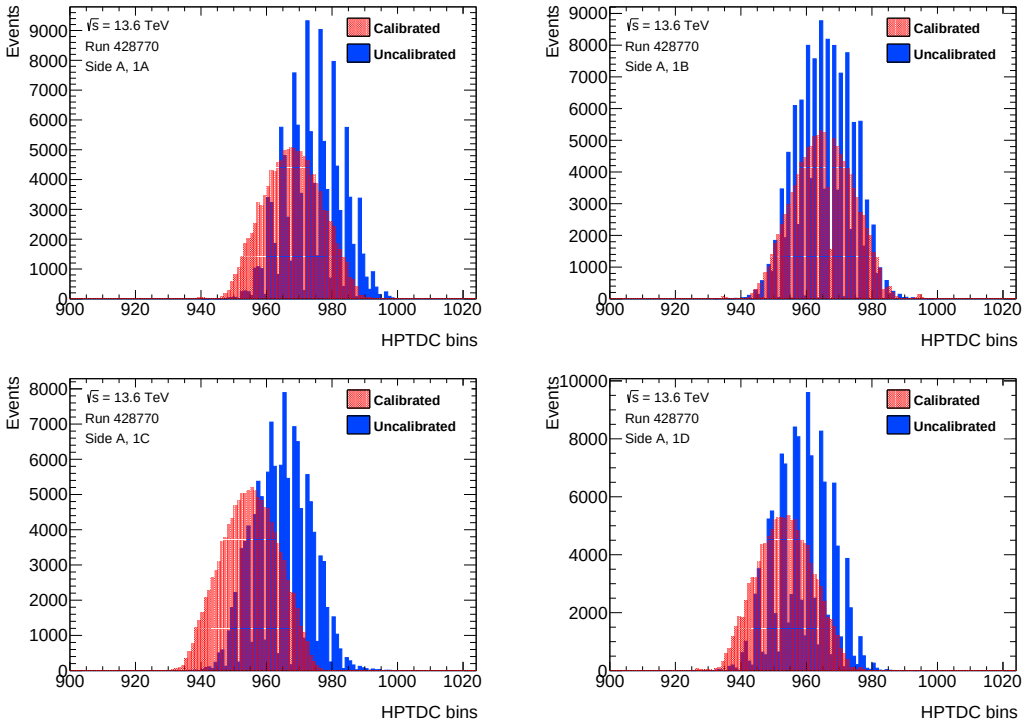

Figure 34: Raw time distributions before (blue) and after (red) the calibration in low-μ run 428770 for all ToF channels in train 1 for the A-side.

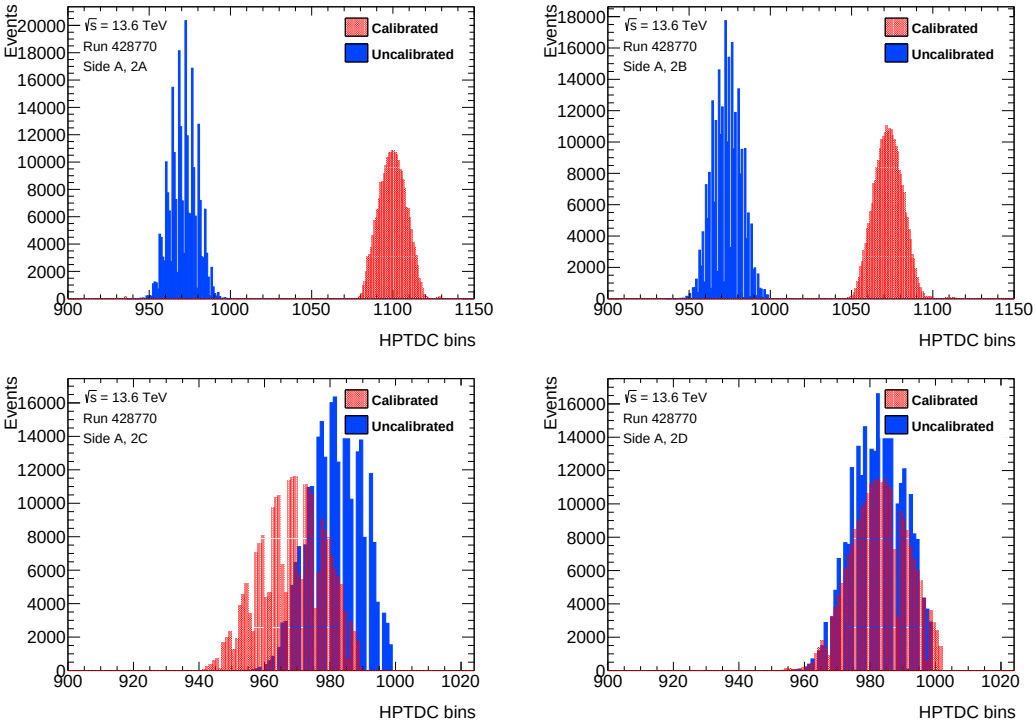

Figure 35: Raw time distributions before (blue) and after (red) the calibration in low-μ run 428770 for all ToF channels in train 2 for the A-side.

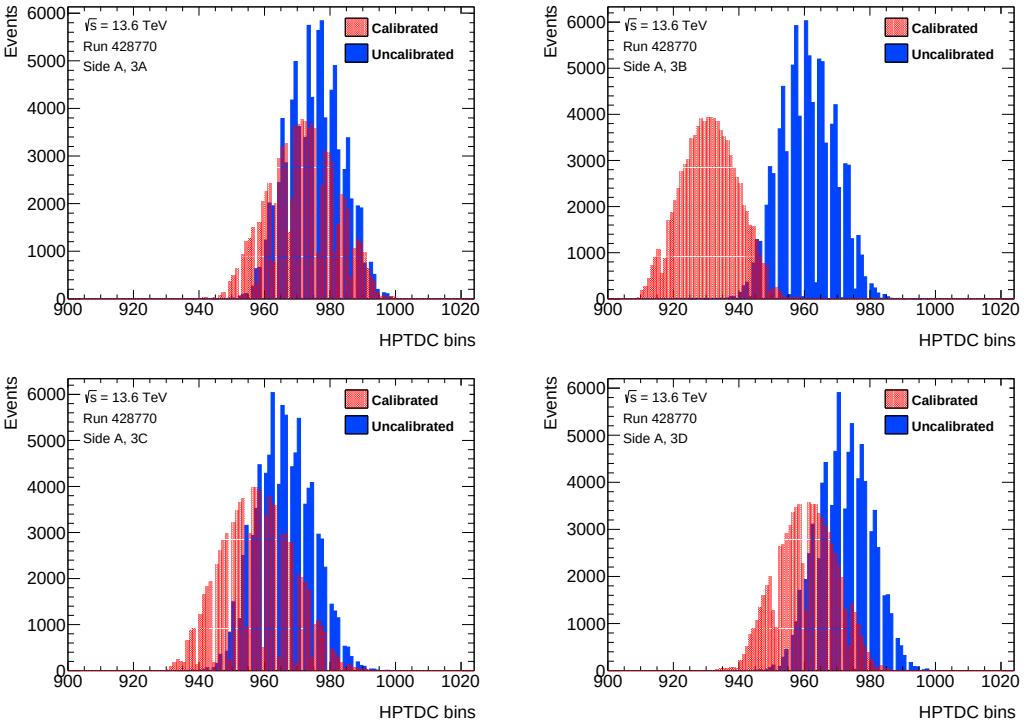

Figure 36: Raw time distributions before (blue) and after (red) the calibration in low-μ run 428770 for all ToF channels in train 3 for the A-side.

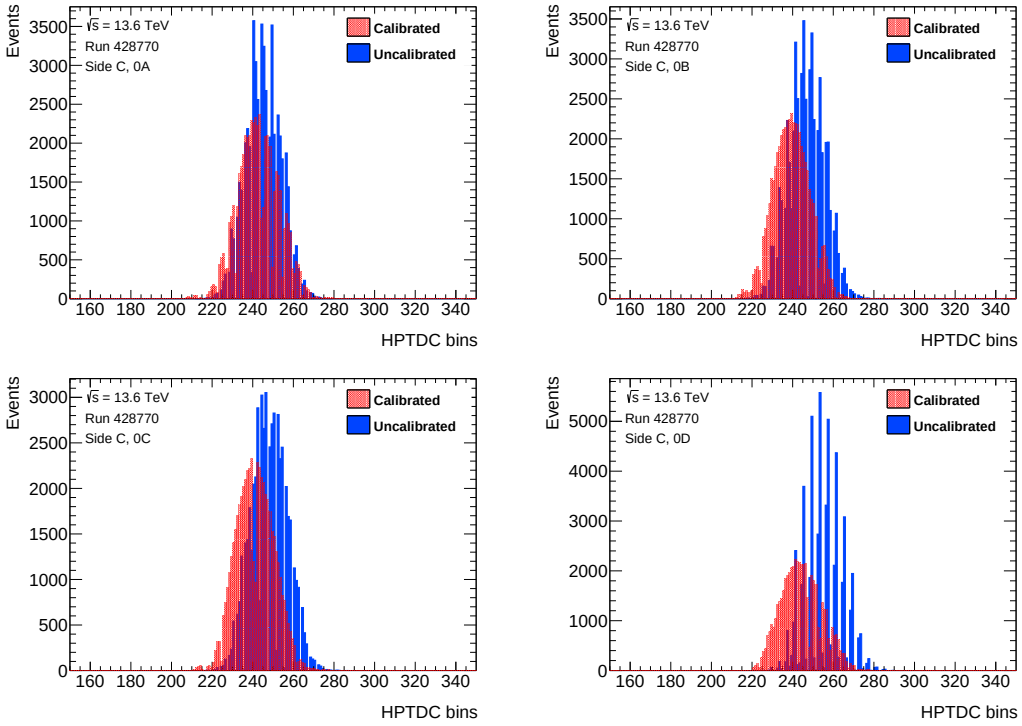

Figure 37: Raw time distributions before (blue) and after (red) the calibration in low-μ run 428770 for all ToF channels in train 0 for the C-side.

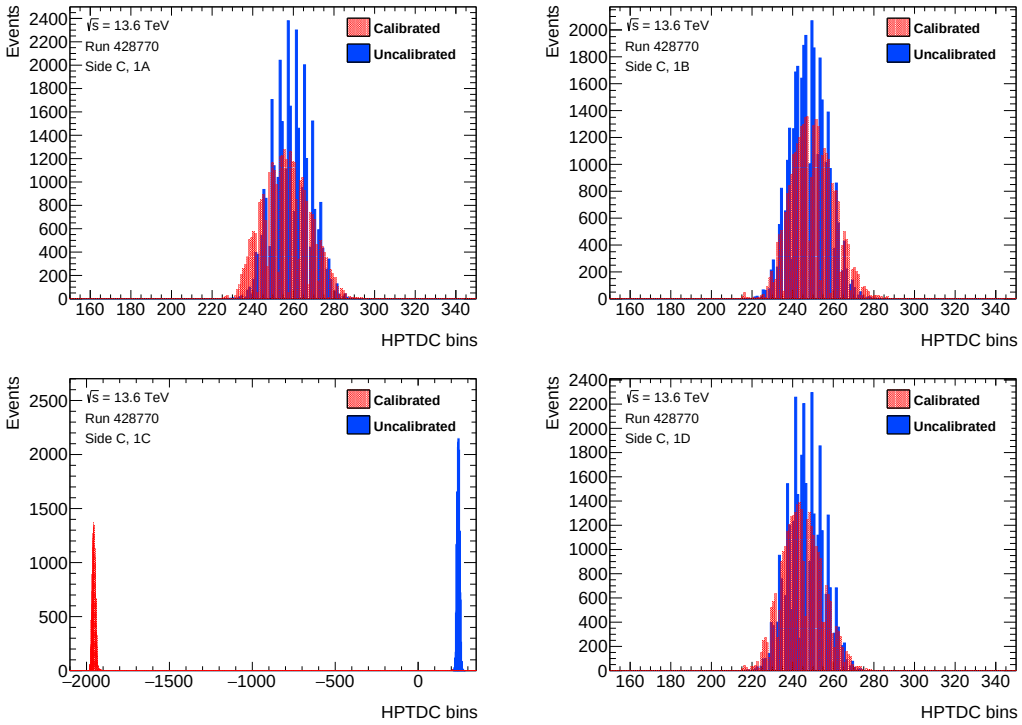

Figure 38: Raw time distributions before (blue) and after (red) the calibration in low-μ run 428770 for all ToF channels in train 1 for the C-side.

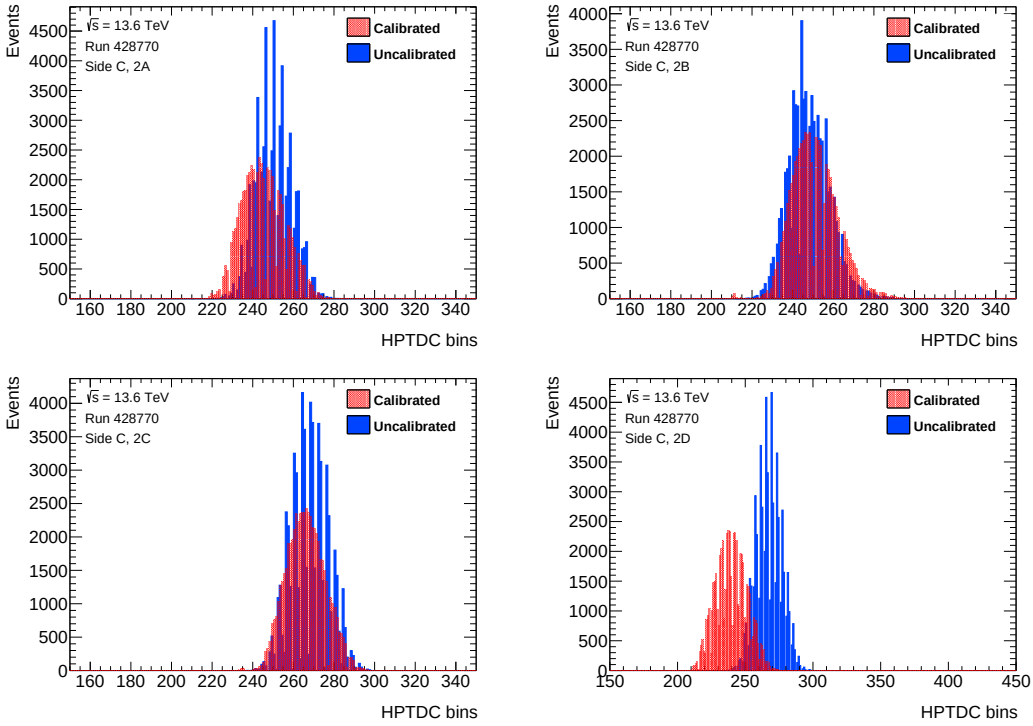

Figure 39: Raw time distributions before (blue) and after (red) the calibration in low-μ run 428770 for all ToF channels in train 2 for the C-side.

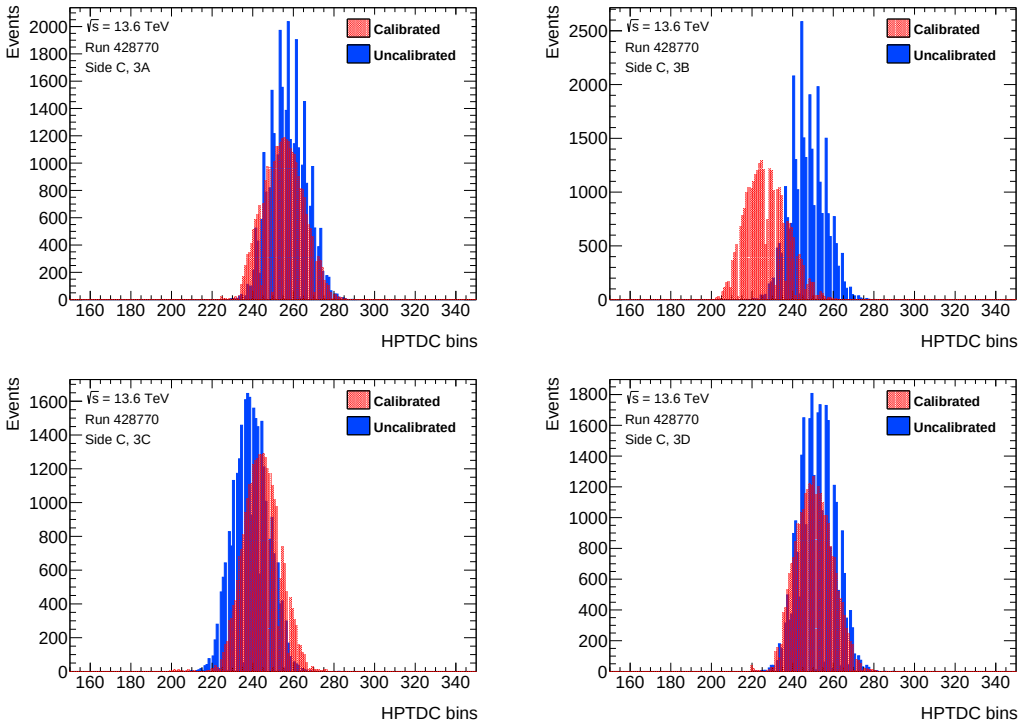

Figure 40: Raw time distributions before (blue) and after (red) the calibration in low-μ run 428770 for all ToF channels in train 3 for the C-side.

All Δt distributions after the HPTDC calibration for the high-μ run 429027 with a double-Gaussian fitted curve overlaid are shown in Figures 41-44 for the side A and in Figures 45-48 for the side C, each Figure corresponds to one ToF train.

All Δt distributions after the HPTDC calibration for the low-μ run 428770 with a double-Gaussian fitted curve overlaid are shown in Figures 49-52 for the side A and in Figures 53-56 for the side C, each Figure corresponds to one ToF train.

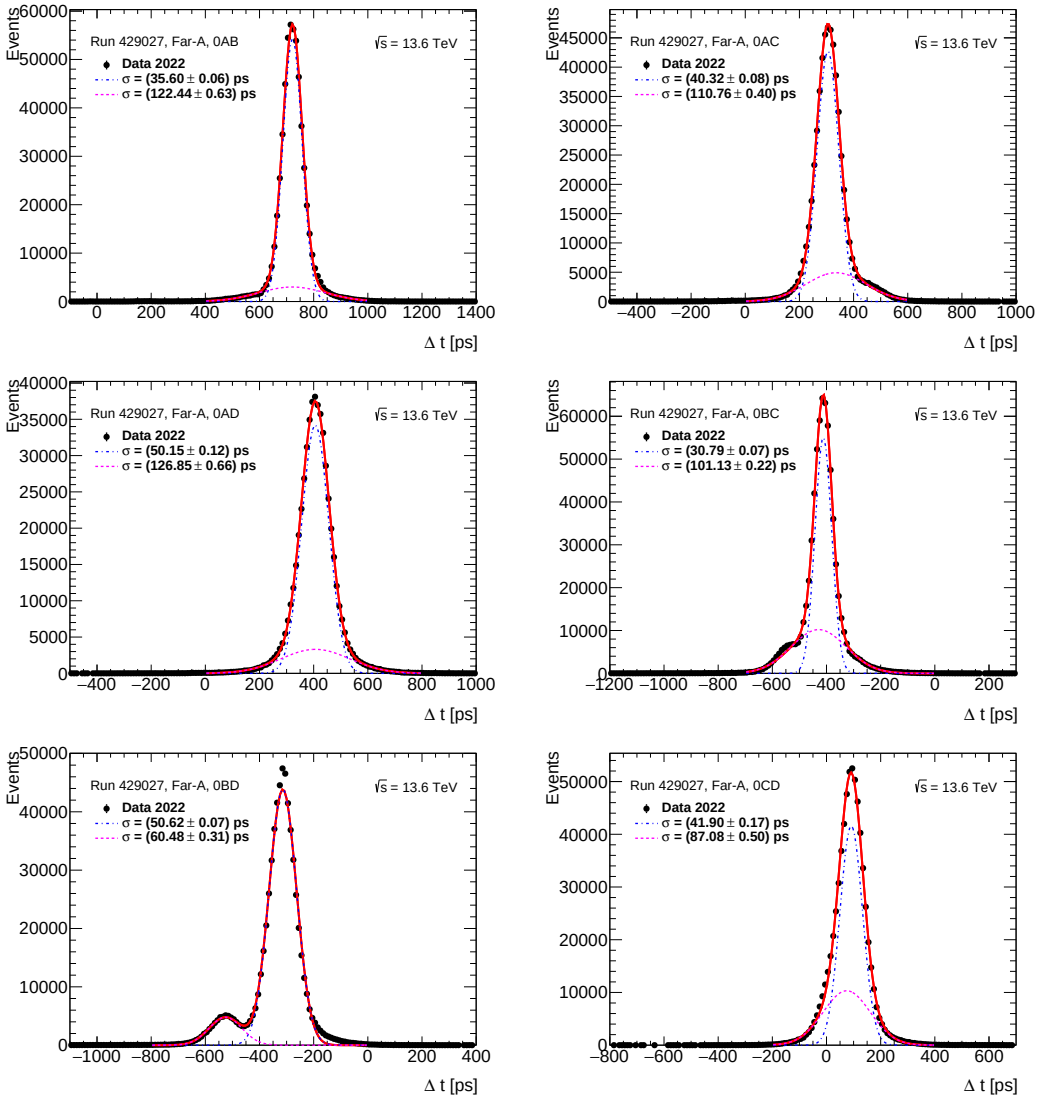

Figure 41: Δt distributions after the HPTDC calibration for the run 429027 with a double Gaussian fitted curve overlaid for all combinations of the ToF channels in train 0 for the A-side.

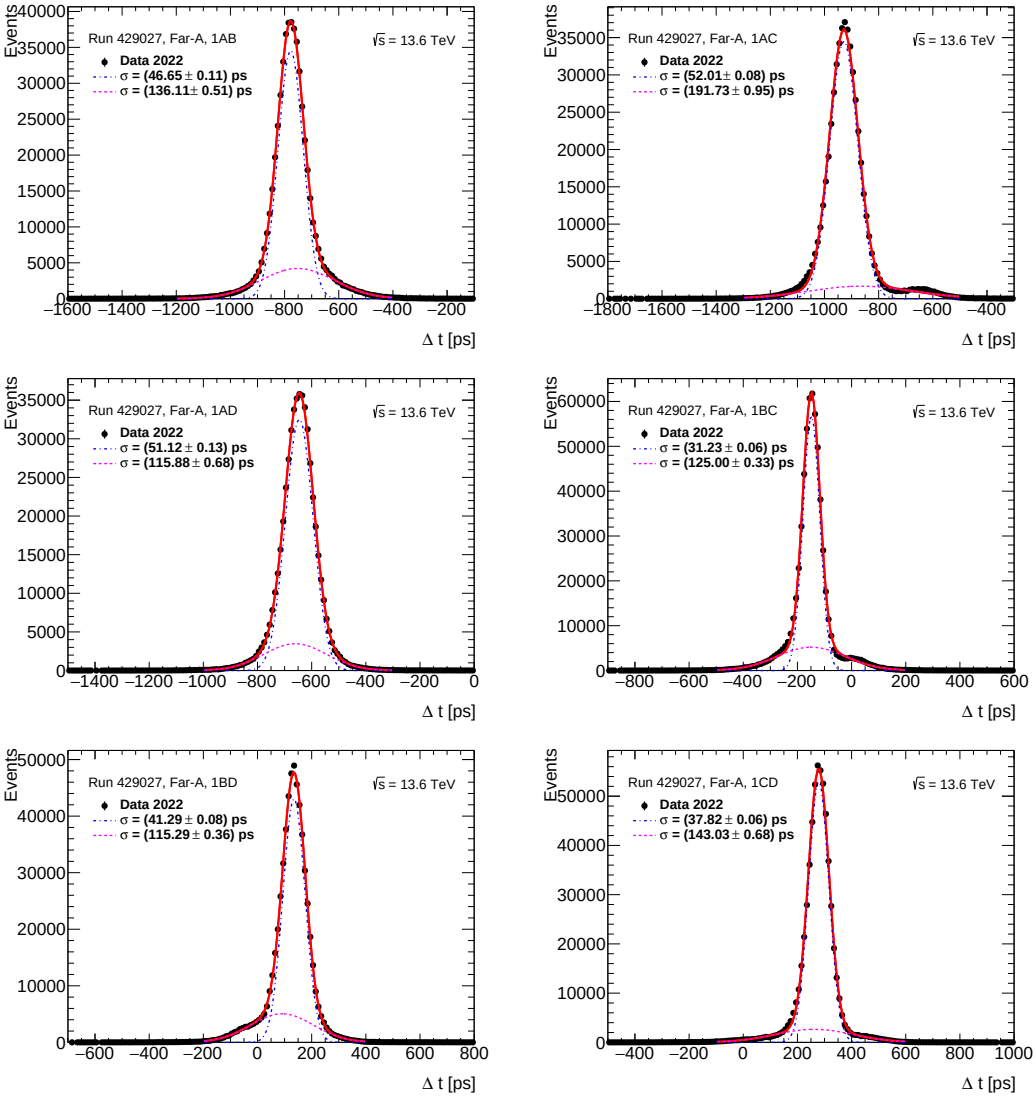

Figure 42: Δt distributions after the HPTDC calibration for the run 429027 with a double Gaussian fitted curve overlaid for all combinations of the ToF channels in train 1 for the A-side.

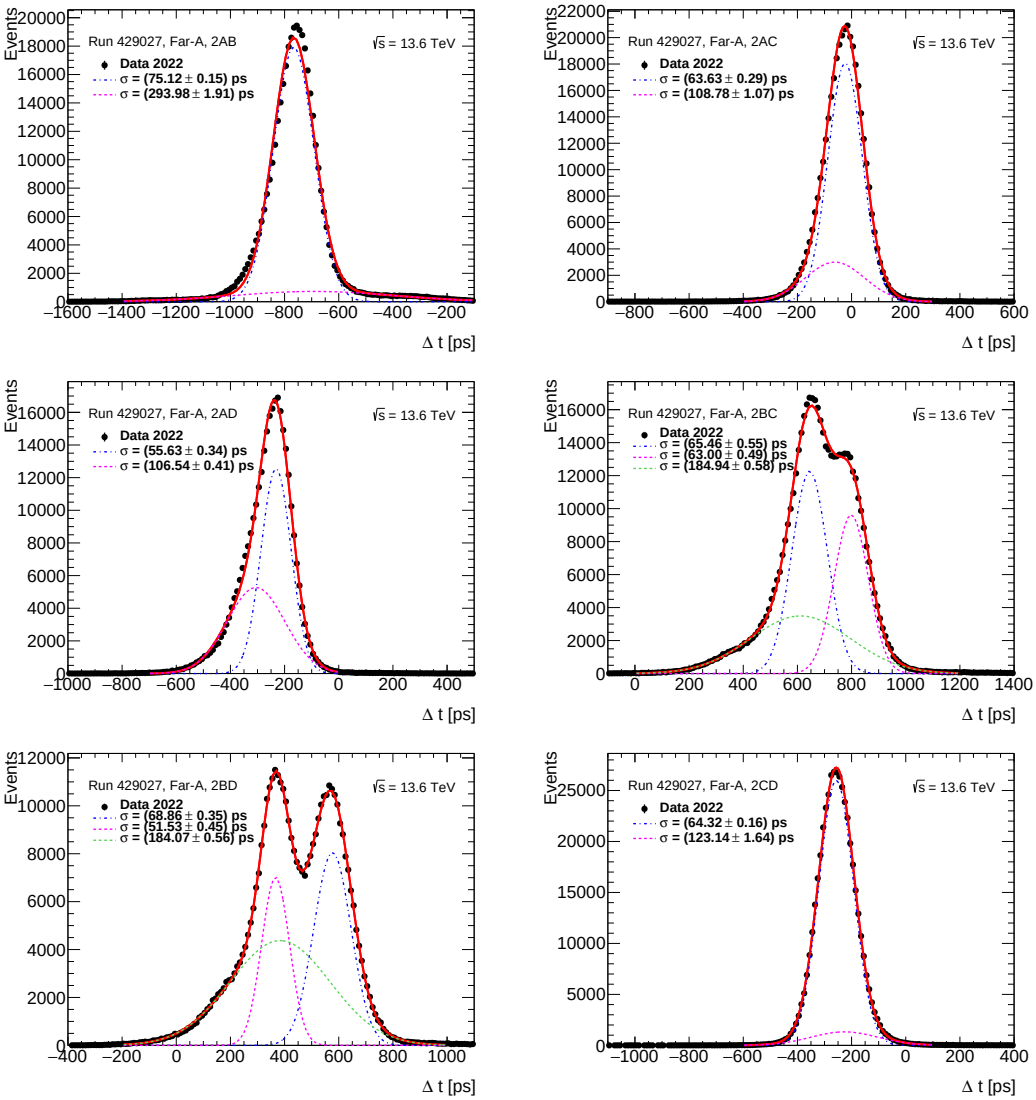

Figure 43: Δt distributions after the HPTDC calibration for the run 429027 with a double Gaussian fitted curve overlaid for all combinations of the ToF channels in train 2 for the A-side.

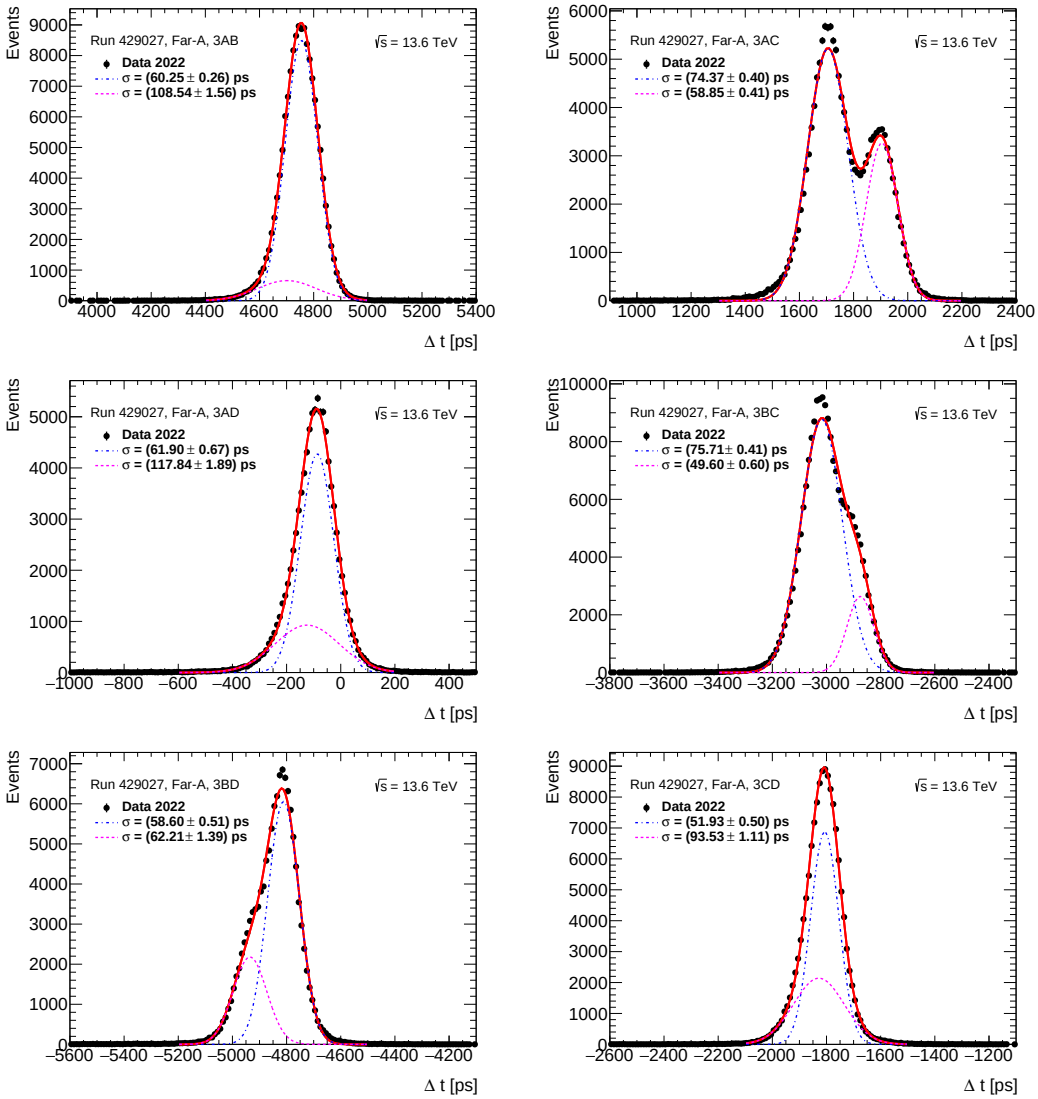

Figure 44: Δt distributions after the HPTDC calibration for the run 429027 with a double Gaussian fitted curve overlaid for all combinations of the ToF channels in train 3 for the A-side.

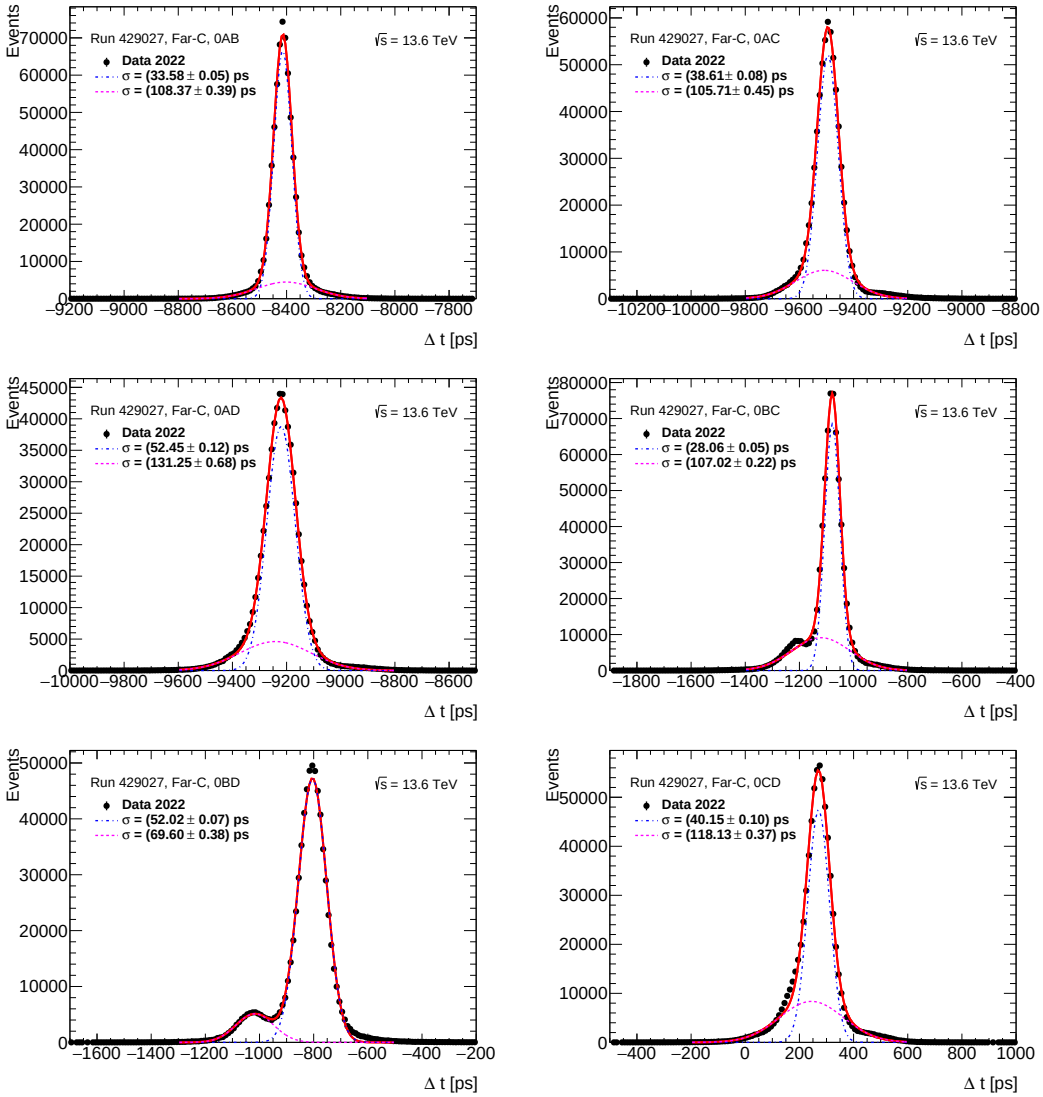

Figure 45: Δt distributions after the HPTDC calibration for the run 429027 with a double Gaussian fitted curve overlaid for all combinations of the ToF channels in train 0 for the C-side.

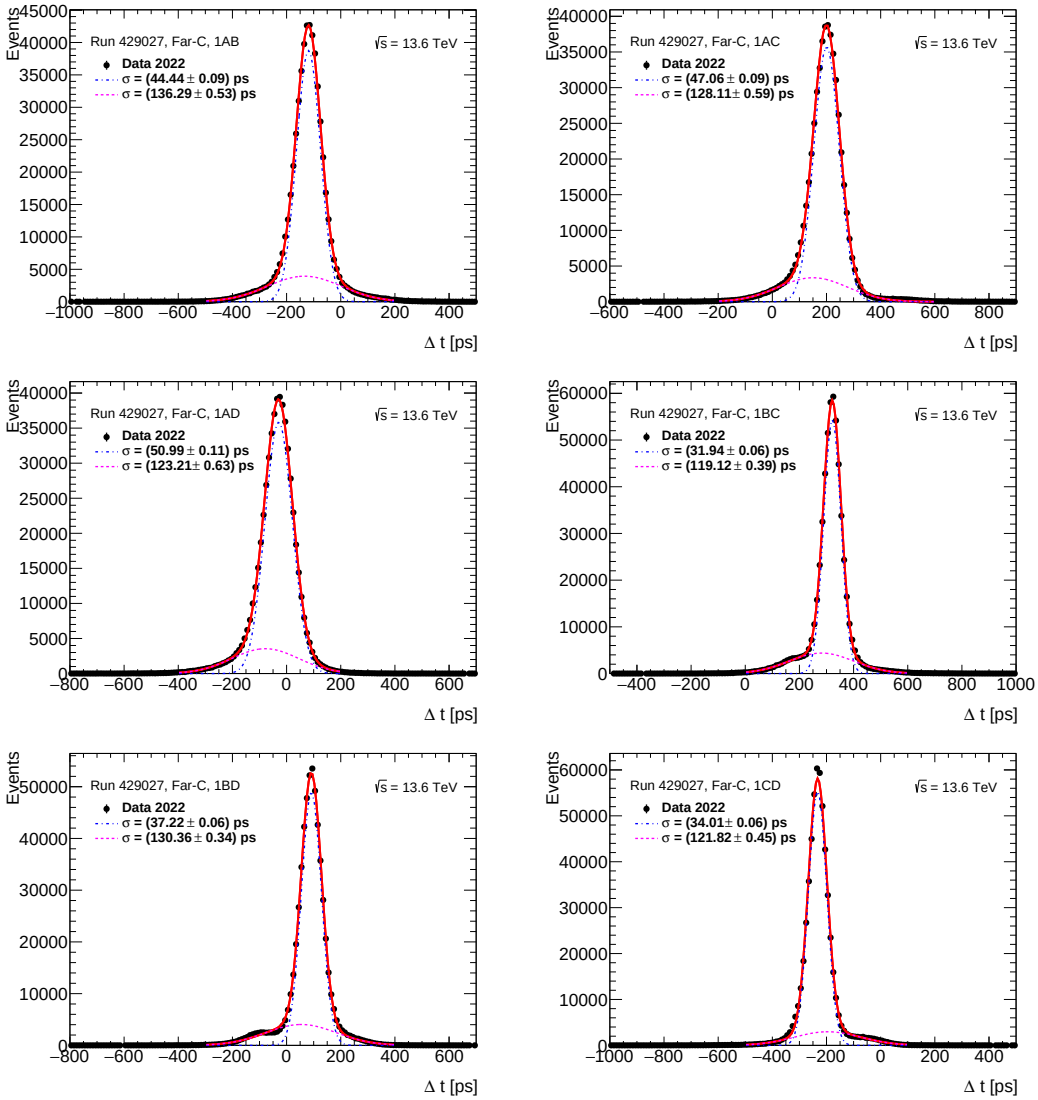

Figure 46: Δt distributions after the HPTDC calibration for the run 429027 with a double Gaussian fitted curve overlaid for all combinations of the ToF channels in train 1 for the C-side.

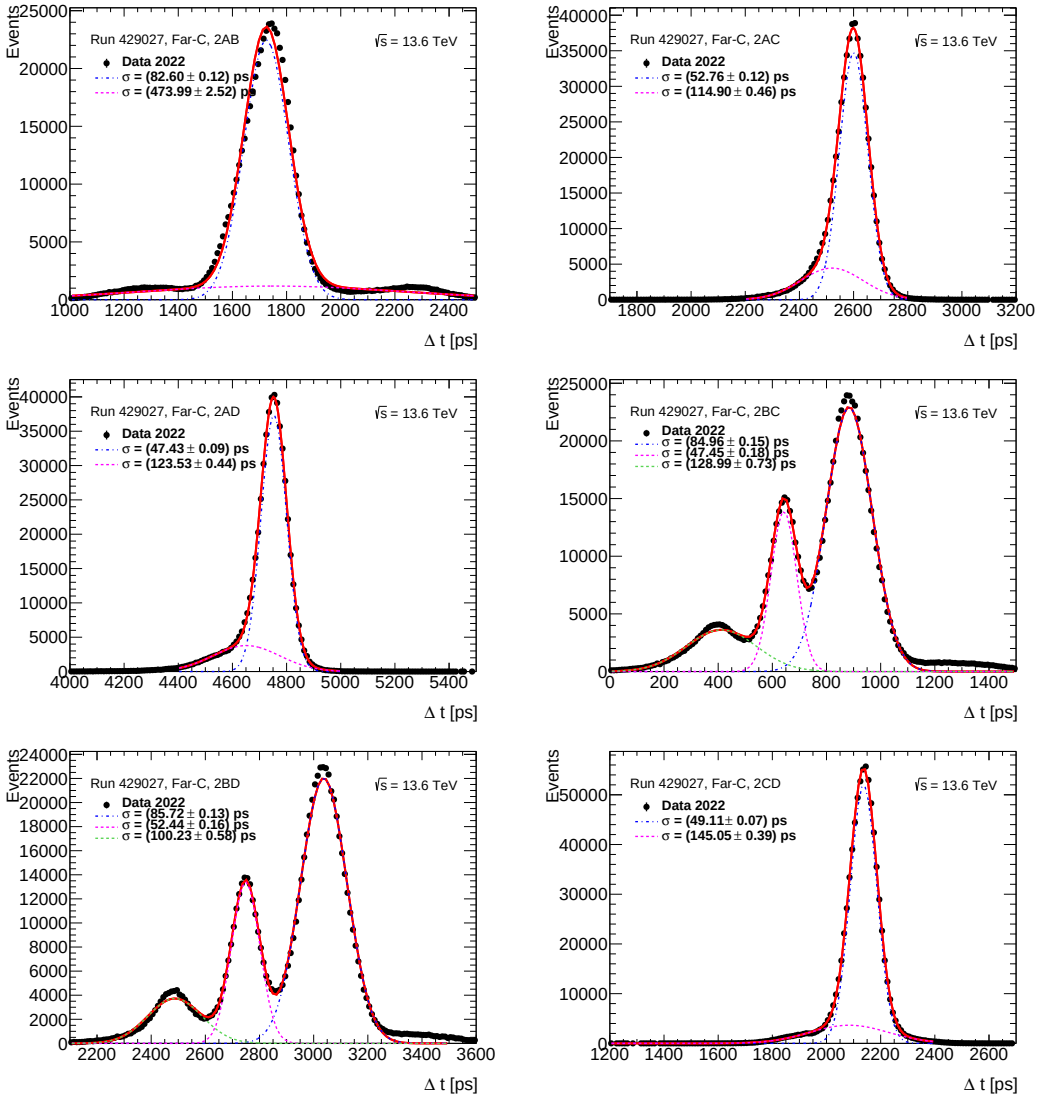

Figure 47: Δt distributions after the HPTDC calibration for the run 429027 with a double Gaussian fitted curve overlaid for all combinations of the ToF channels in train 2 for the C-side.

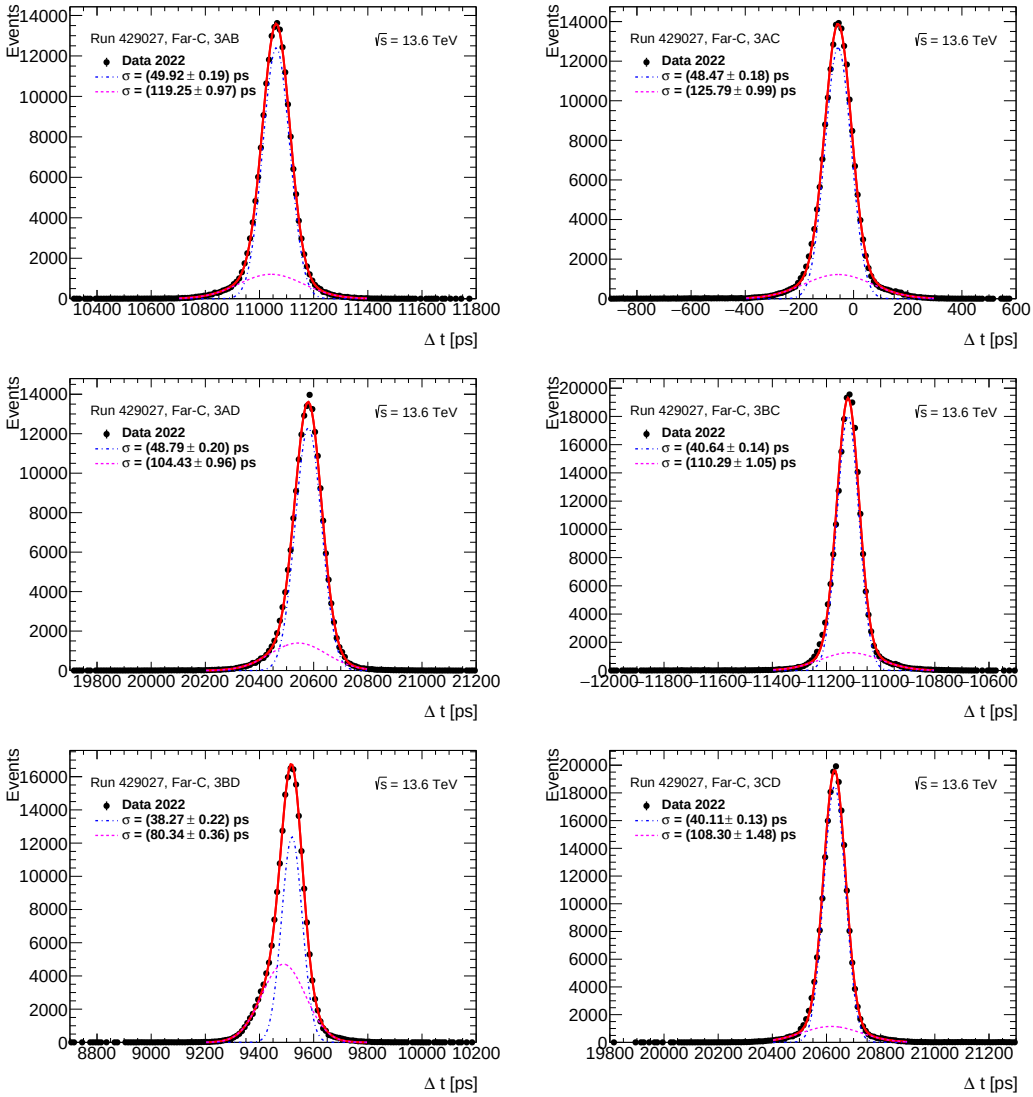

Figure 48: Δt distributions after the HPTDC calibration for the run 429027 with a double Gaussian fitted curve overlaid for all combinations of the ToF channels in train 3 for the C-side.

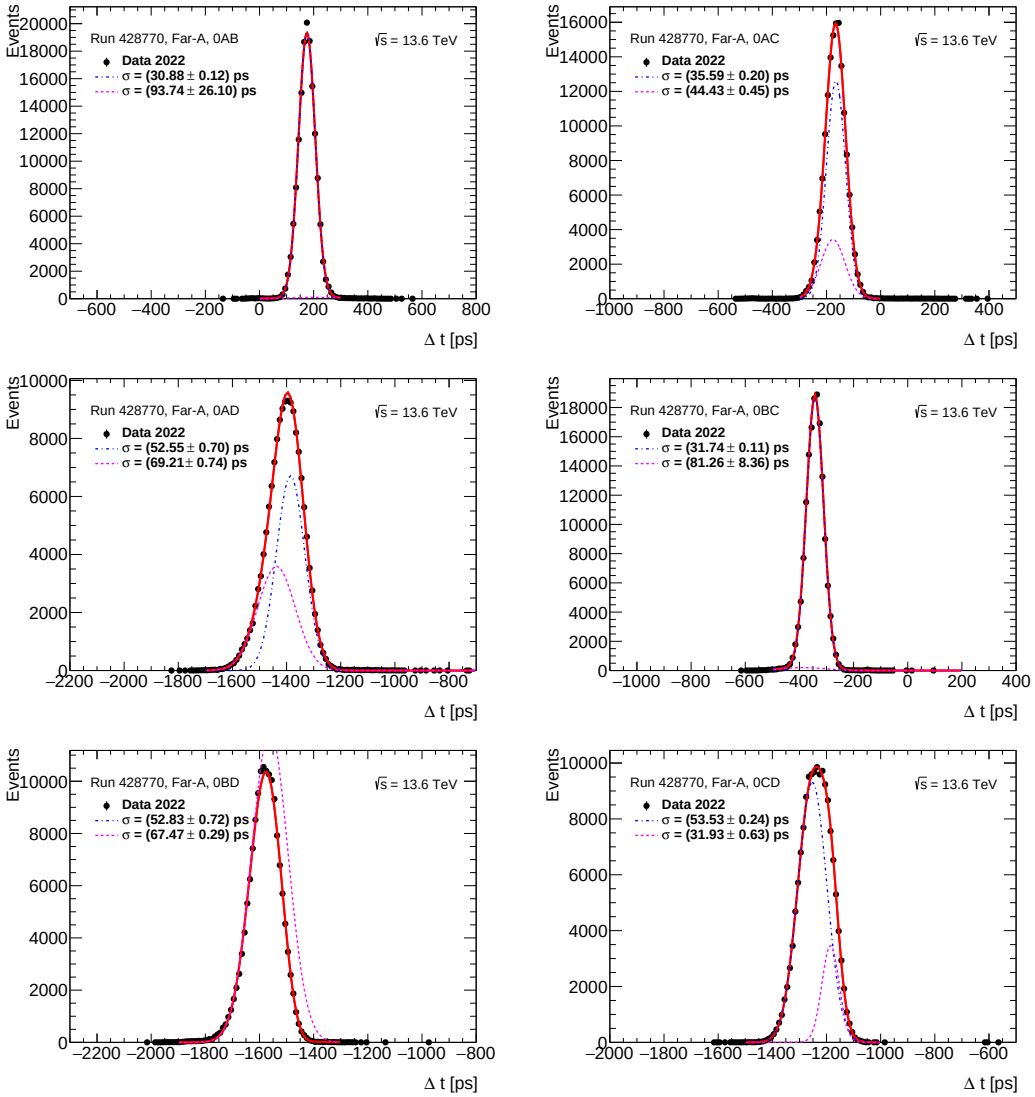

Figure 49: Δt distributions after the HPTDC calibration for the low-μ run 428770 with a double Gaussian fitted curve overlaid for all combinations of the ToF channels in train 0 for the A-side.

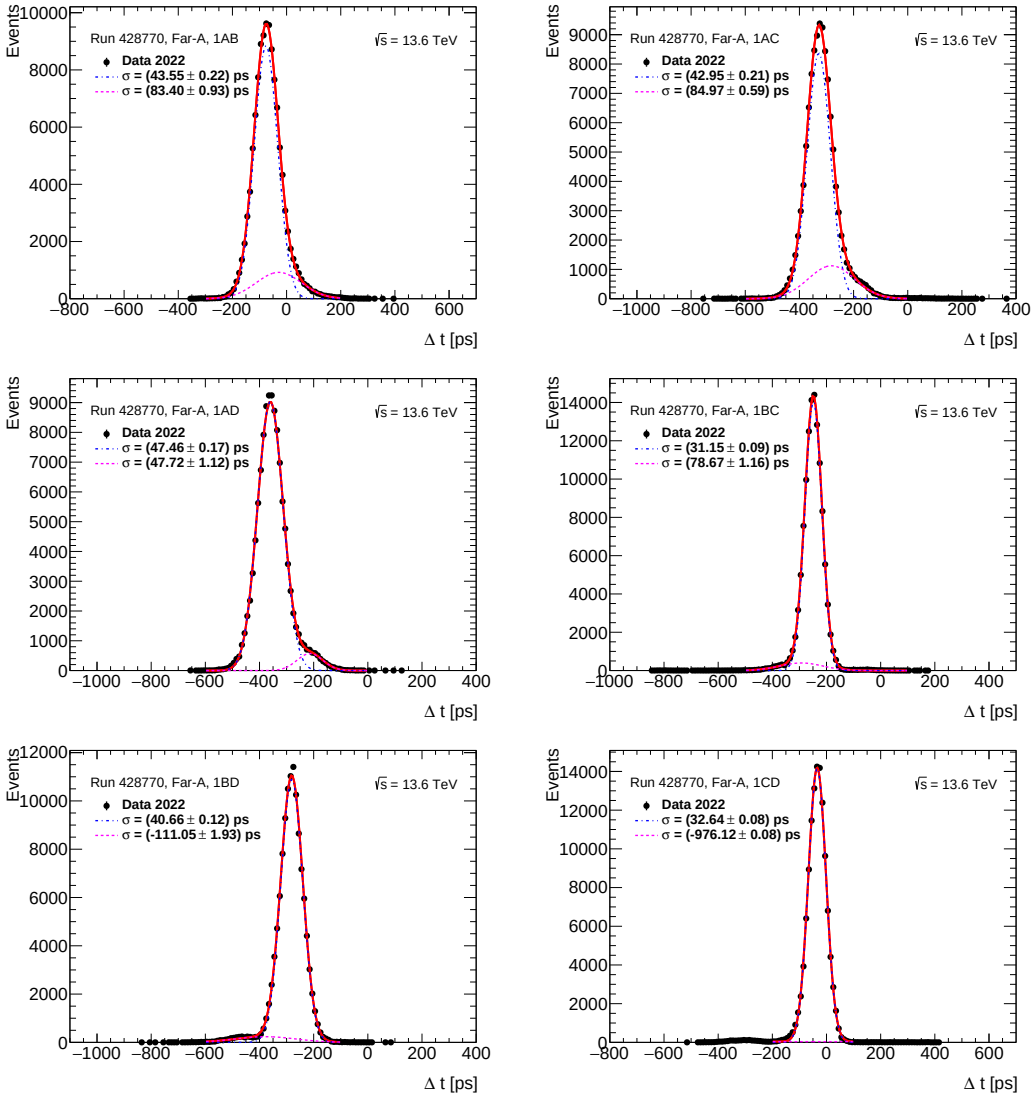

Figure 50: Δt distributions after the HPTDC calibration for the low-μ run 428770 with a double Gaussian fitted curve overlaid for all combinations of the ToF channels in train 1 for the A-side.

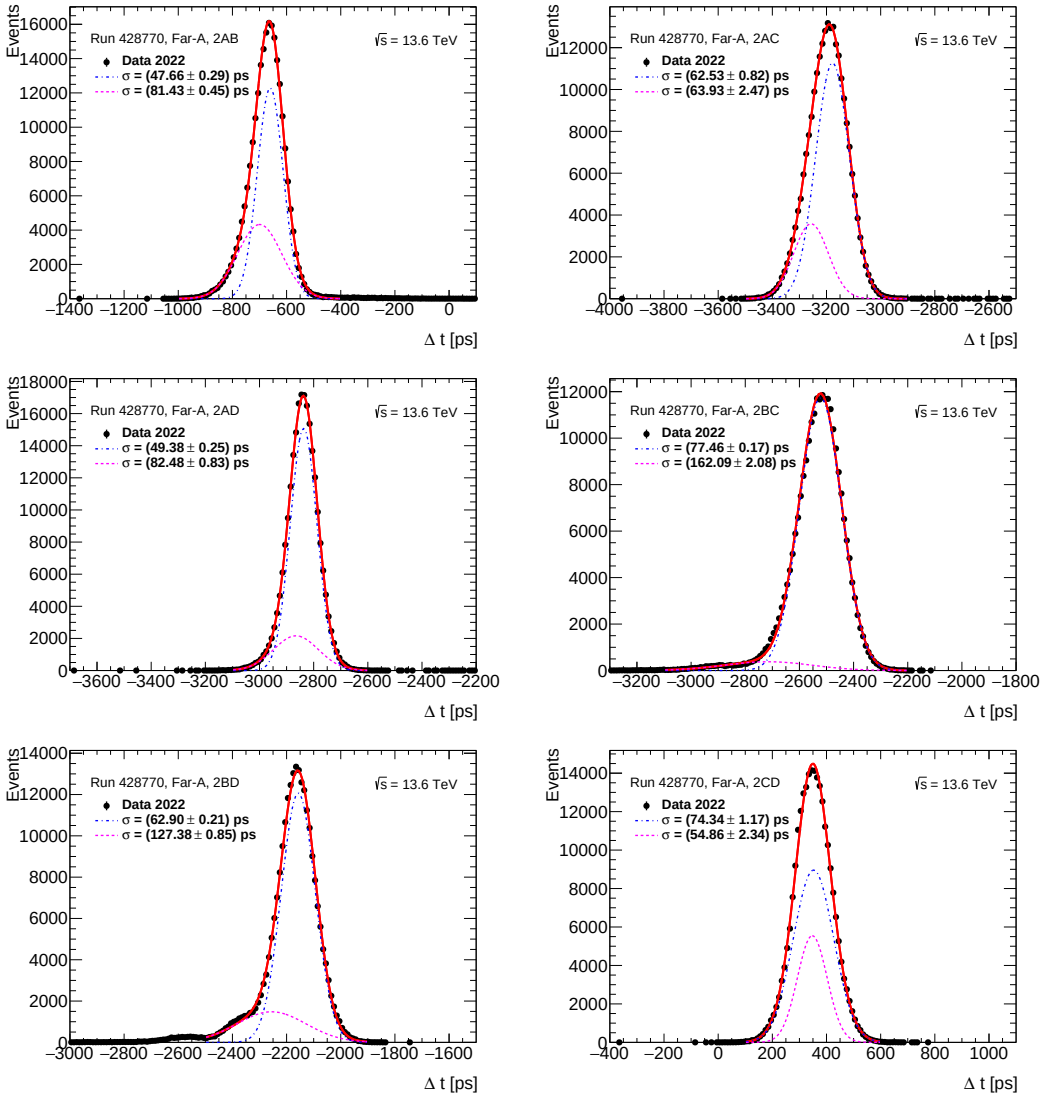

Figure 51: Δt distributions after the HPTDC calibration for the low-μ run 428770 with a double Gaussian fitted curve overlaid for all combinations of the ToF channels in train 2 for the A-side.

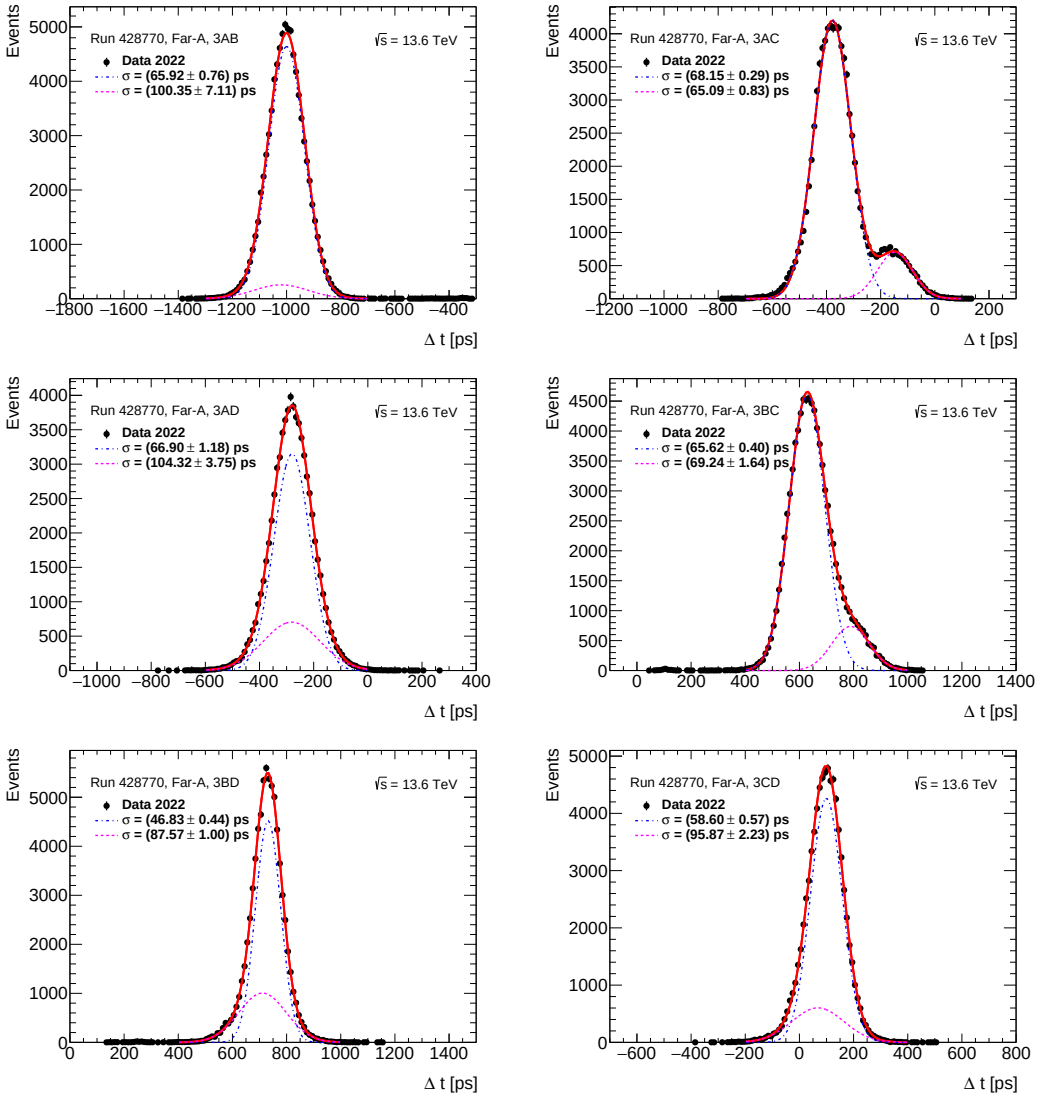

Figure 52: Δt distributions after the HPTDC calibration for the low-μ run 428770 with a double Gaussian fitted curve overlaid for all combinations of the ToF channels in train 3 for the A-side.

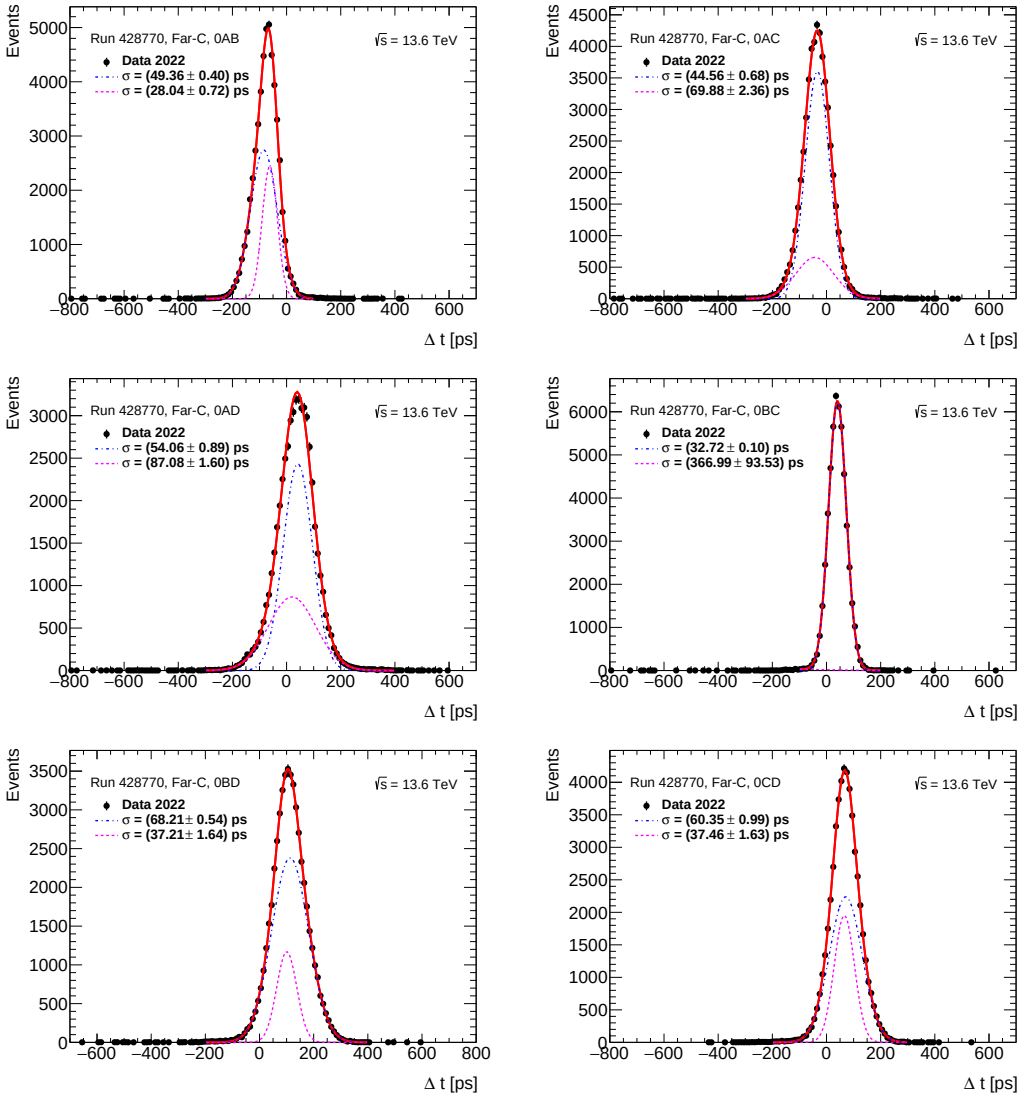

Figure 53: Δt distributions after the HPTDC calibration for the low-μ run 428770 with a double Gaussian fitted curve overlaid for all combinations of the ToF channels in train 0 for the C-side.

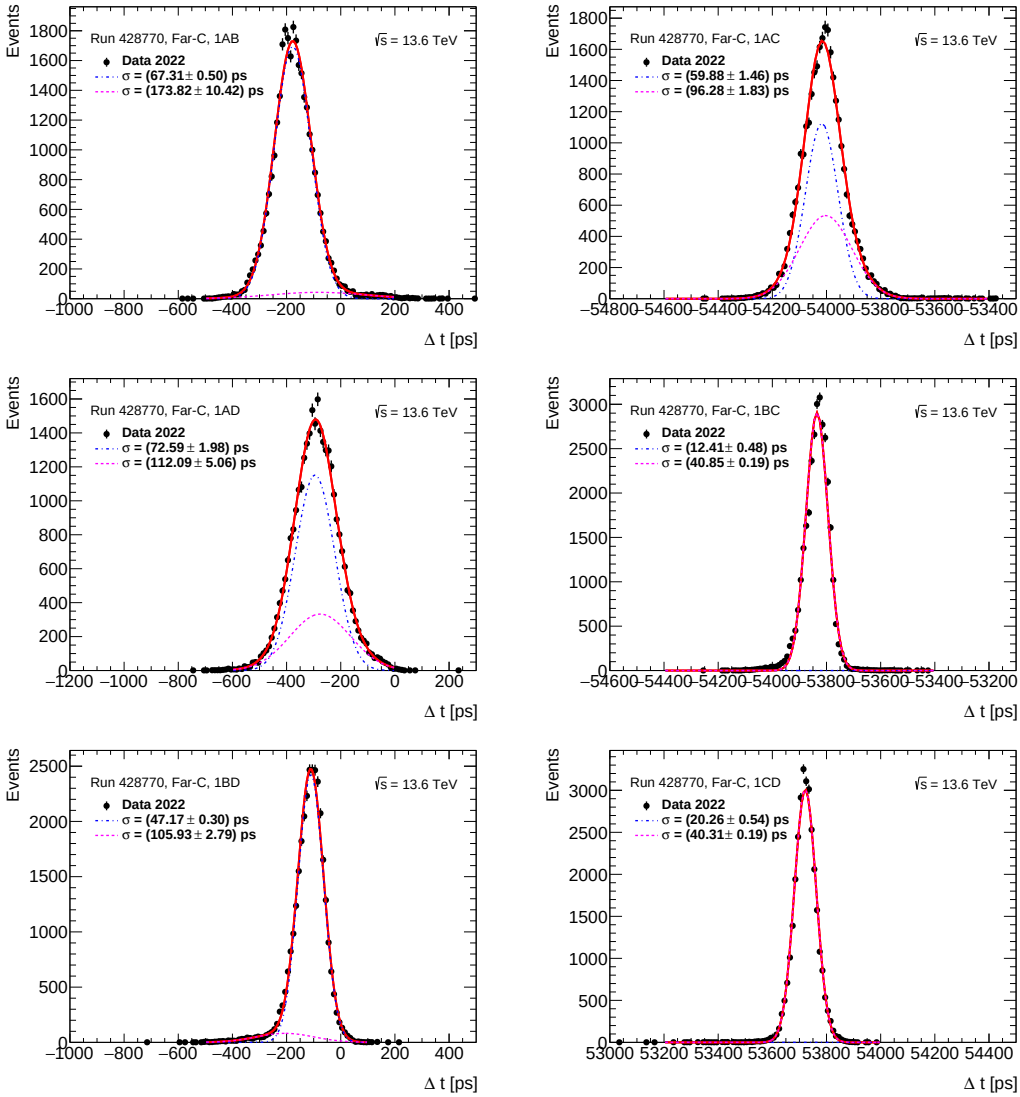

Figure 54: Δt distributions after the HPTDC calibration for the low-μ run 428770 with a double Gaussian fitted curve overlaid for all combinations of the ToF channels in train 1 for the C-side.

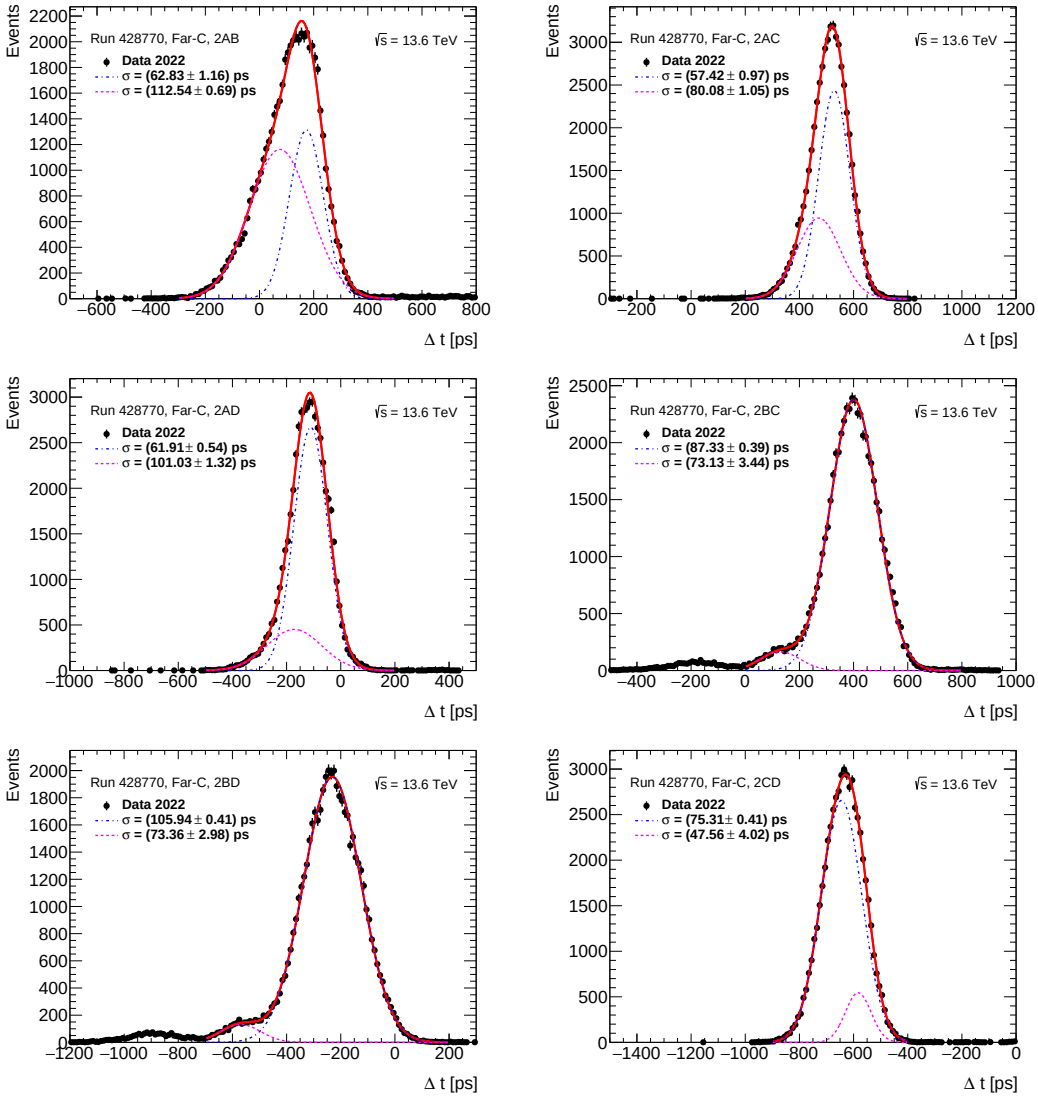

Figure 55: Δt distributions after the HPTDC calibration for the low-μ run 428770 with a double Gaussian fitted curve overlaid for all combinations of the ToF channels in train 2 for the C-side.

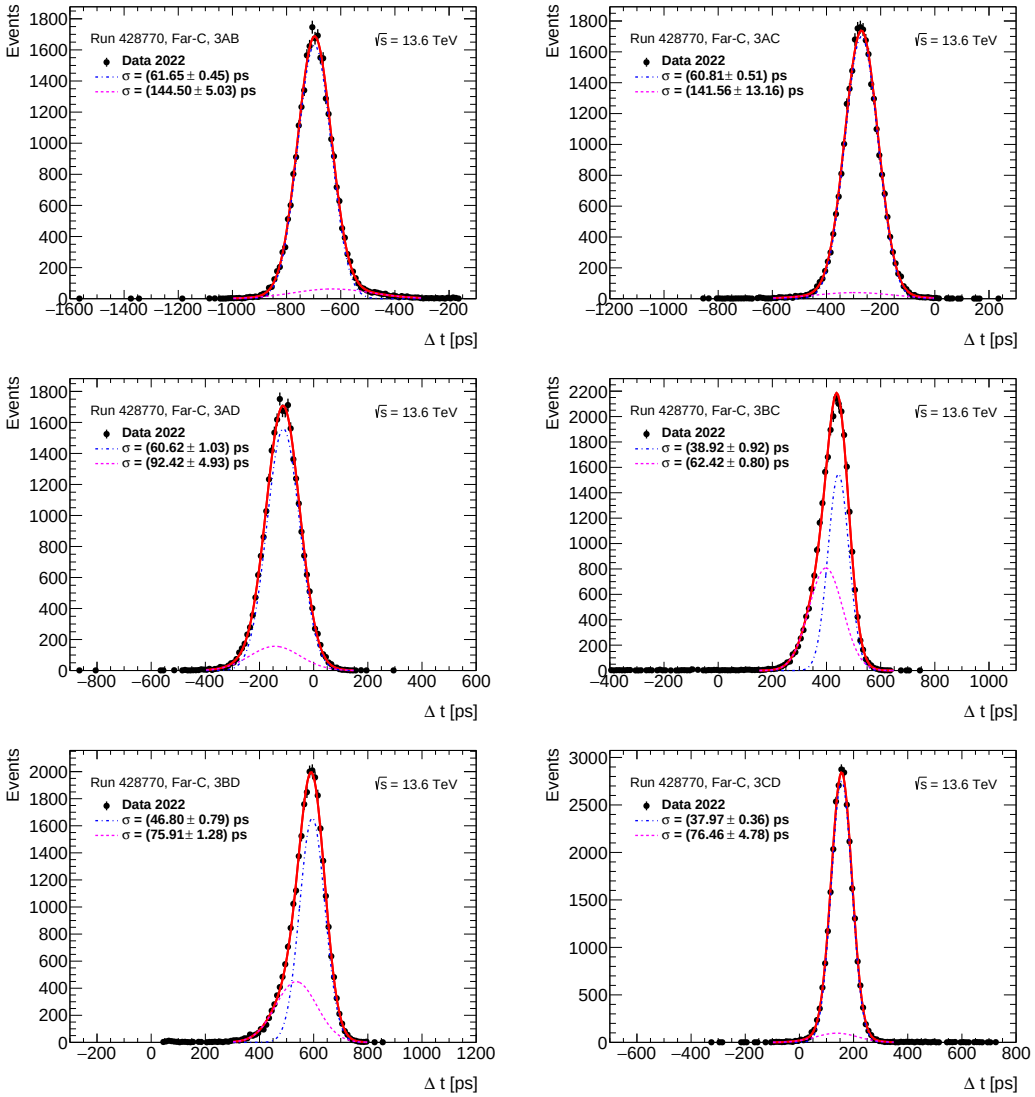

Figure 56: Δt distributions after the HPTDC calibration for the low-μ run 428770 with a double Gaussian fitted curve overlaid for all combinations of the ToF channels in train 3 for the C-side.

B.3 After the likelihood cleanup procedure

In Section 3.2.2 after the HPTDC calibration, the likelihood cleanup procedure was performed.

All Δt distributions after the likelihood cleanup procedure for the high-μ run 429027 with a Gaussian fitted curve overlaid are shown in Figures 57-60 for the side A and in Figures 61-64 for the side C, each Figure corresponds to one ToF train.

All Δt distributions after the likelihood cleanup procedure for the low-μ run 428770 with a Gaussian fitted curve overlaid are shown in Figures 65-68 for the side A and in Figures 69-72 for the side C, each Figure corresponds to one ToF train.

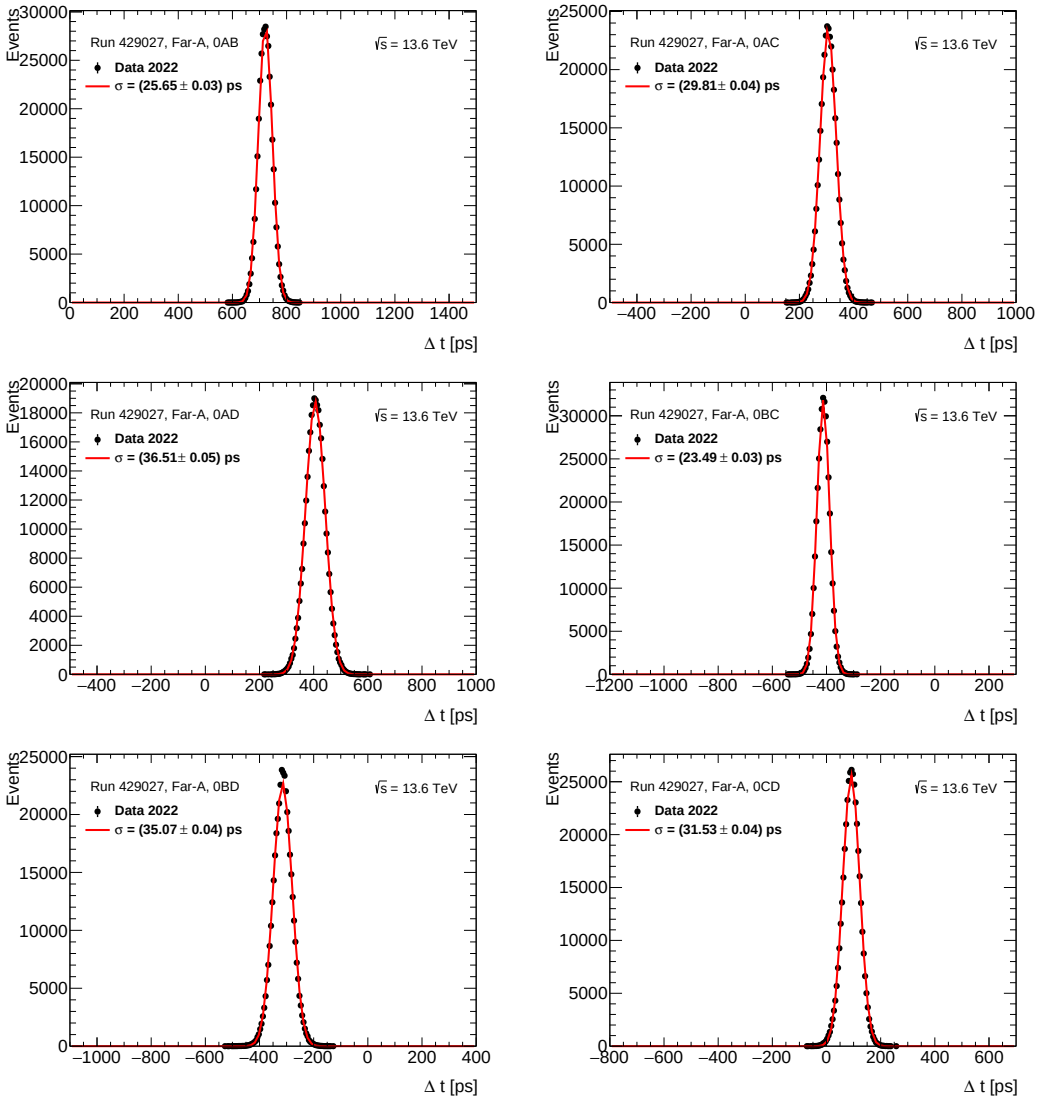

Figure 57: Δt distributions after the likelihood cleanup procedure for the run 429027 with a Gaussian fitted curve overlaid for all combinations of the ToF channels in train 0 for the A-side.

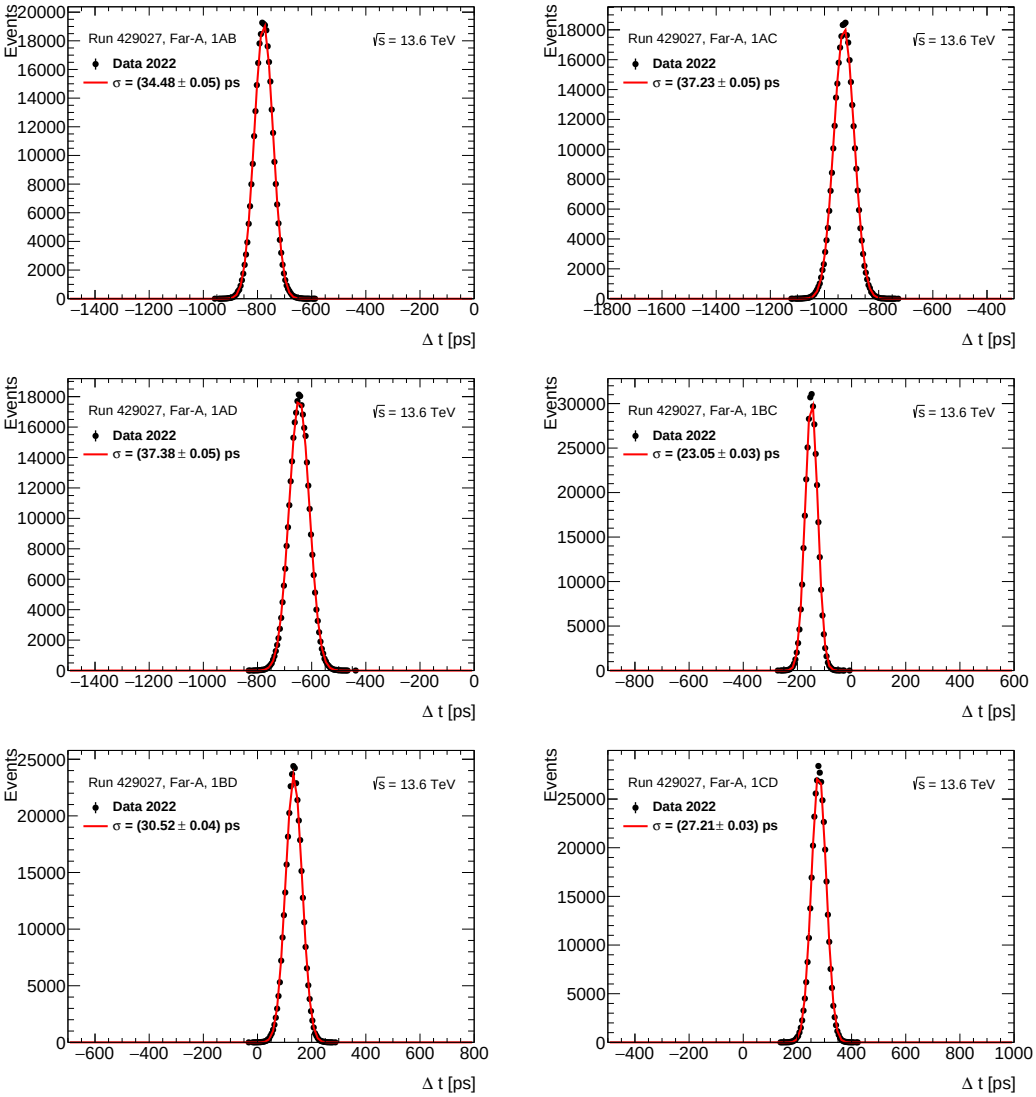

Figure 58: Δt distributions after the likelihood cleanup procedure for the run 429027 with a Gaussian fitted curve overlaid for all combinations of the ToF channels in train 1 for the A-side.

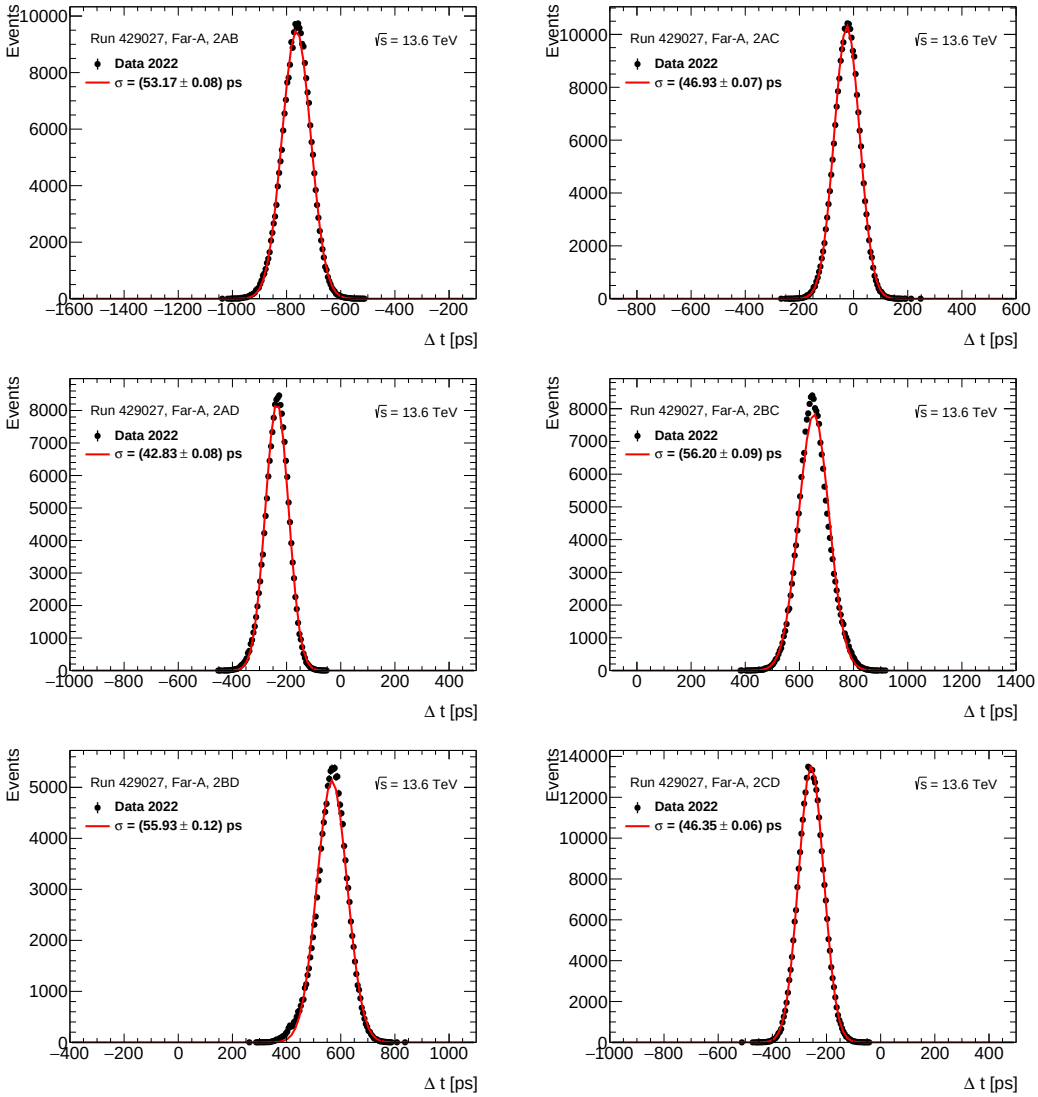

Figure 59: Δt distributions after the likelihood cleanup procedure for the run 429027 with a Gaussian fitted curve overlaid for all combinations of the ToF channels in train 2 for the A-side.

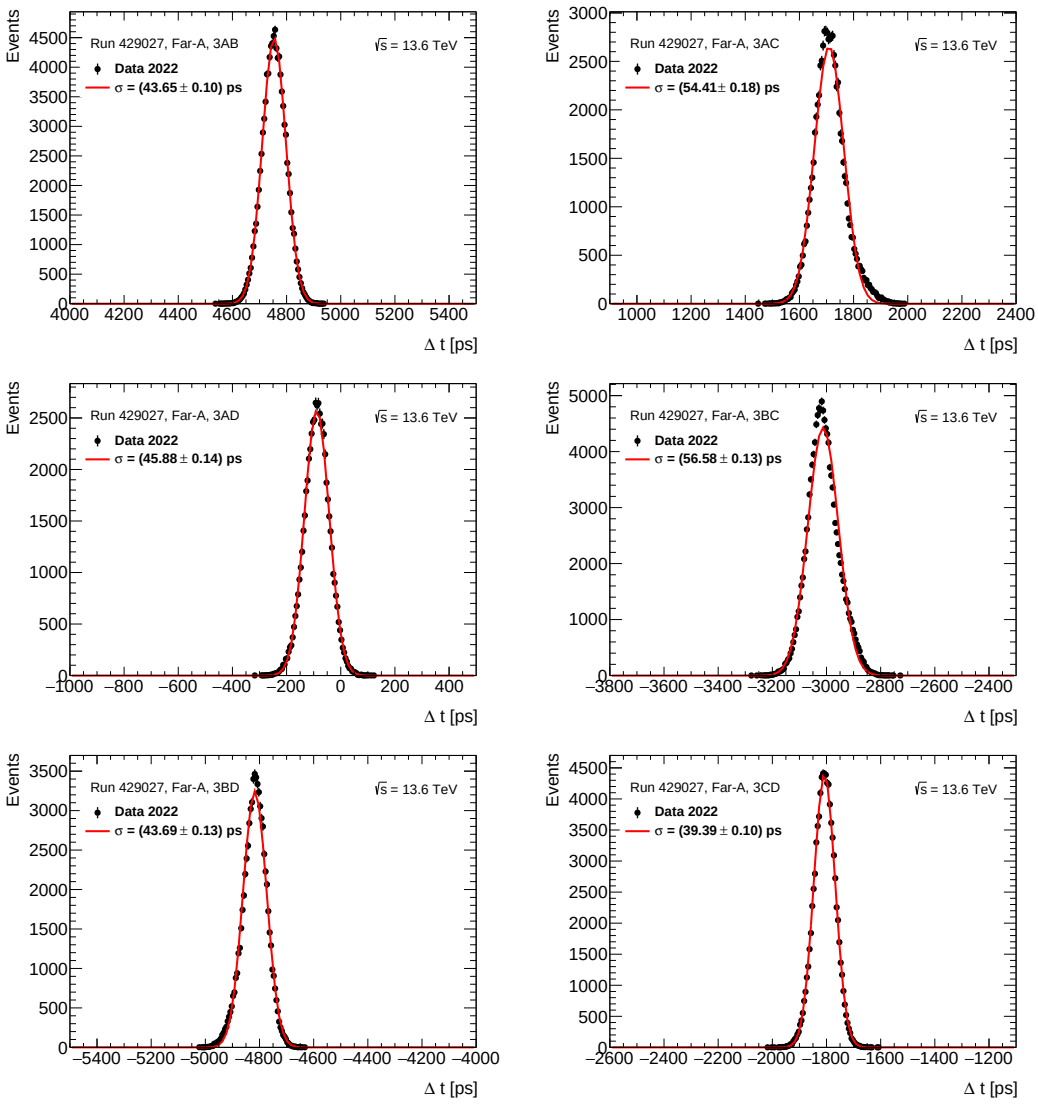

Figure 60: Δt distributions after the likelihood cleanup procedure for the run 429027 with a Gaussian fitted curve overlaid for all combinations of the ToF channels in train 3 for the A-side.

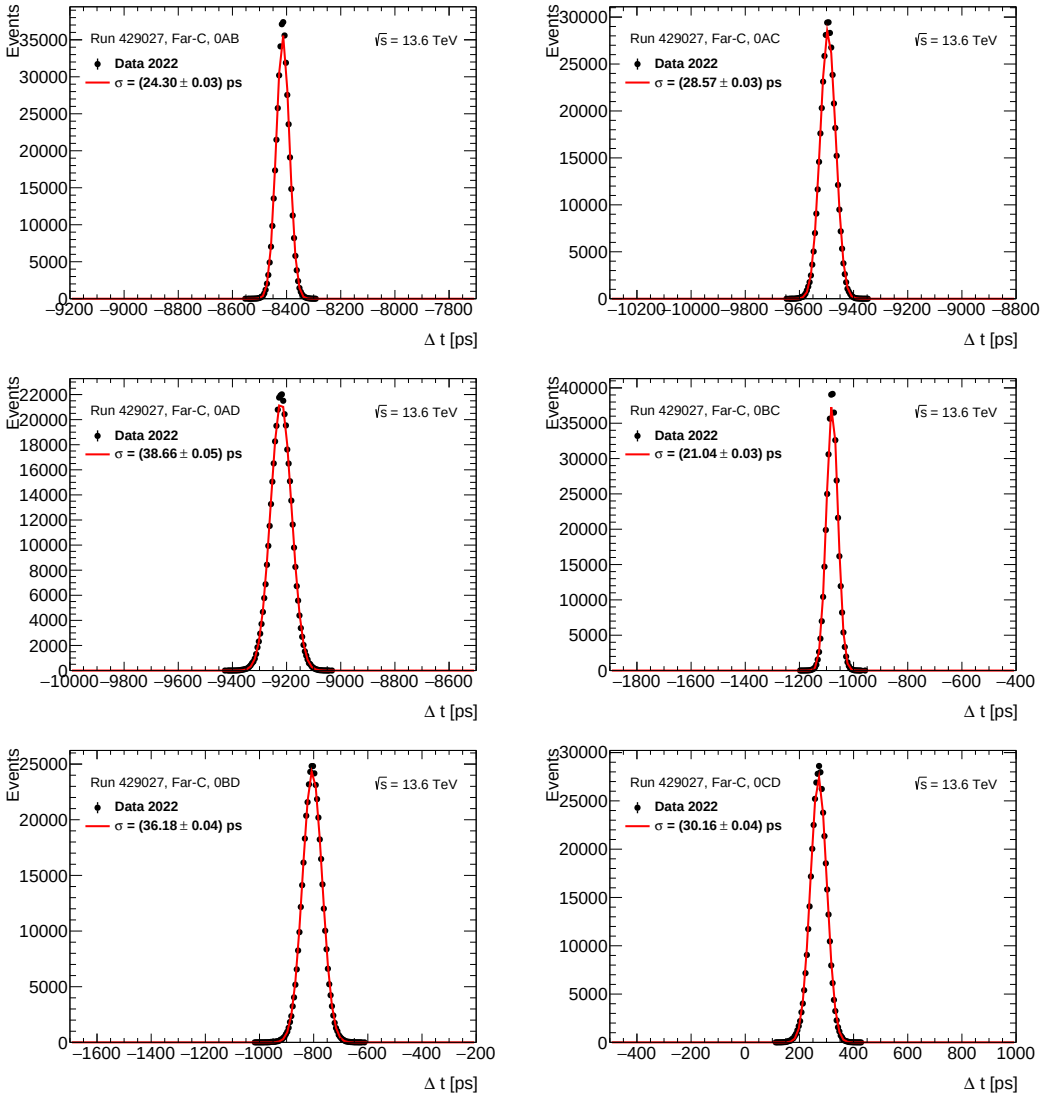

Figure 61: Δt distributions after the likelihood cleanup procedure for the run 429027 with a Gaussian fitted curve overlaid for all combinations of the ToF channels in train 0 for the C-side.

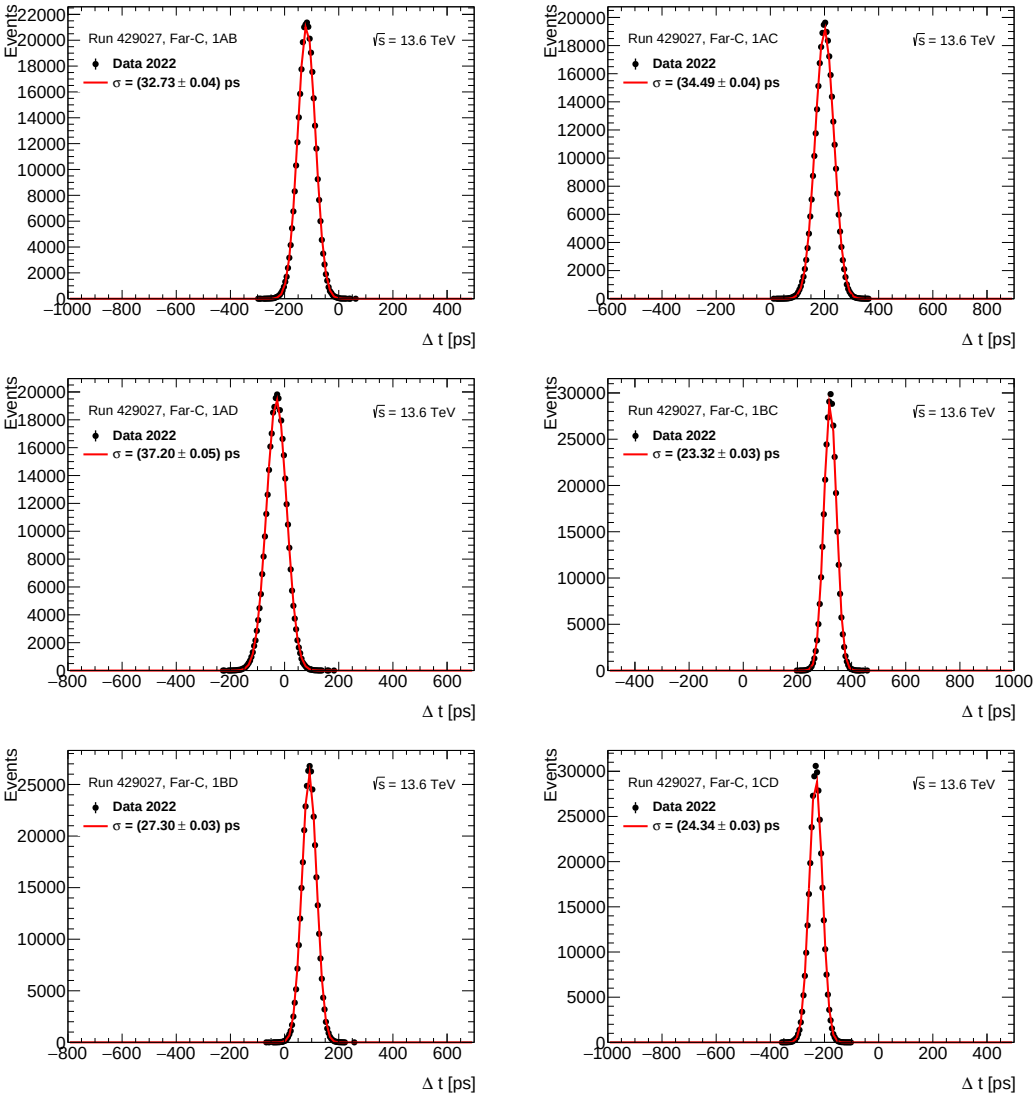

Figure 62: Δt distributions after the likelihood cleanup procedure for the run 429027 with a Gaussian fitted curve overlaid for all combinations of the ToF channels in train 1 for the C-side.

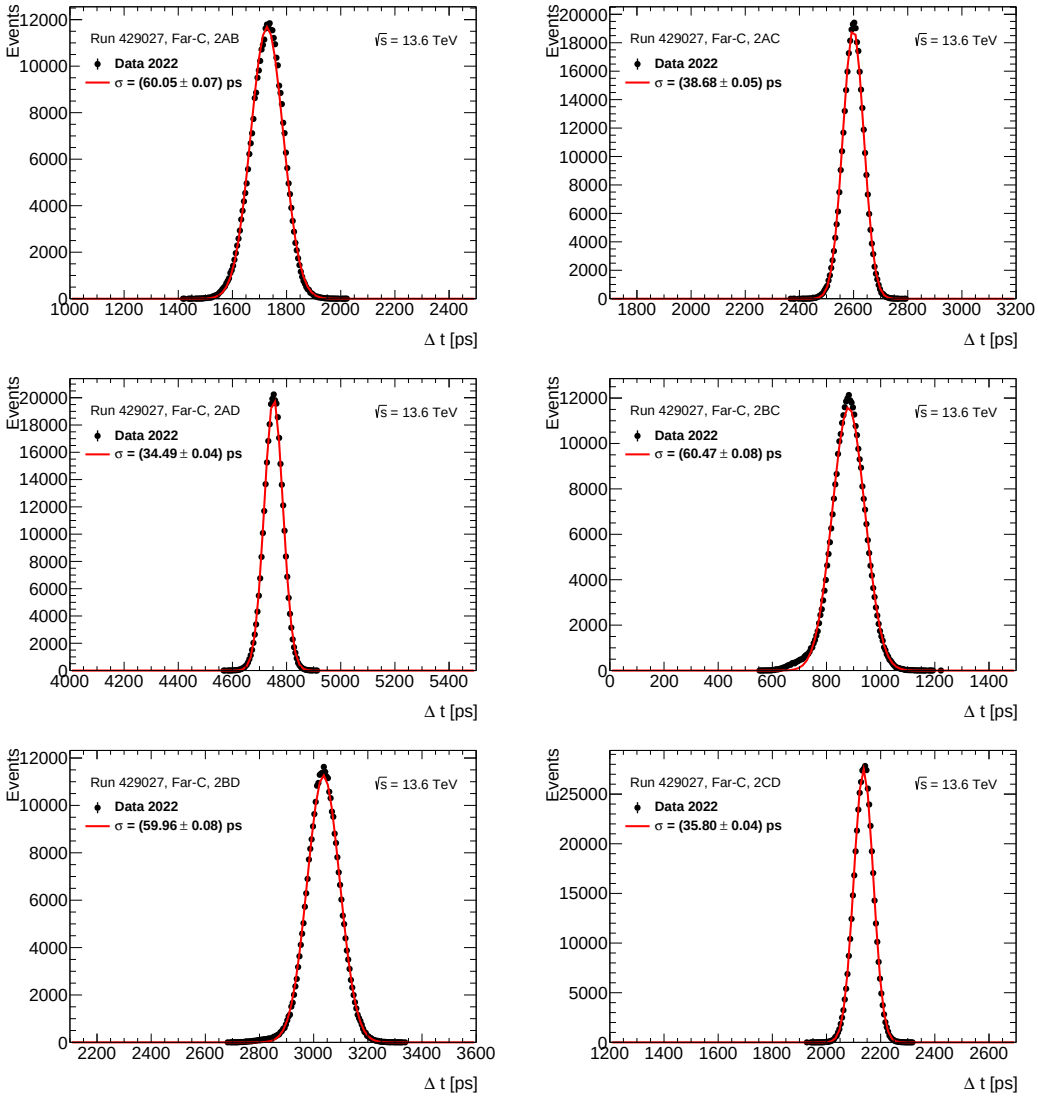

Figure 63: Δt distributions after the likelihood cleanup procedure for the run 429027 with a Gaussian fitted curve overlaid for all combinations of the ToF channels in train 2 for the C-side.

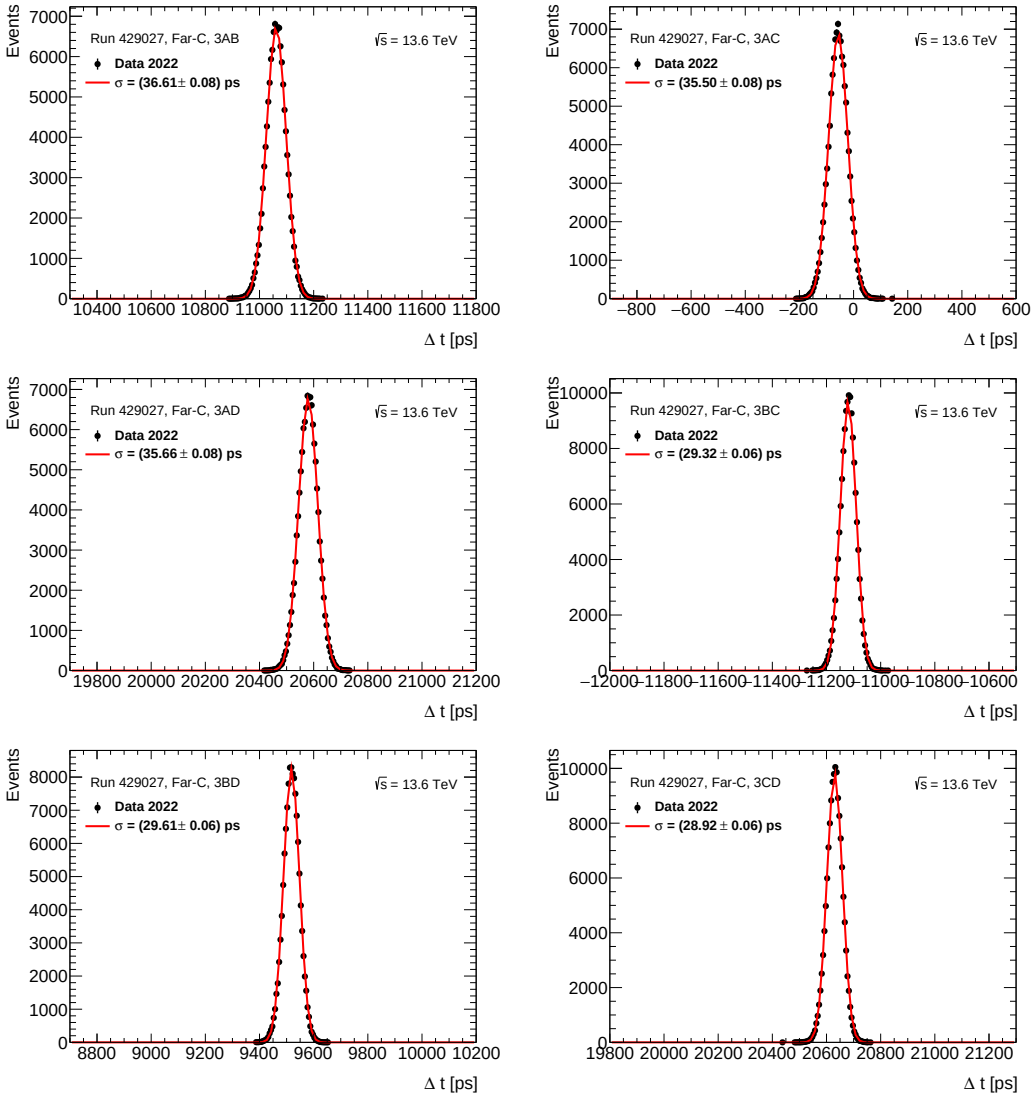

Figure 64: Δt distributions after the likelihood cleanup procedure for the run 429027 with a Gaussian fitted curve overlaid for all combinations of the ToF channels in train 3 for the C-side.

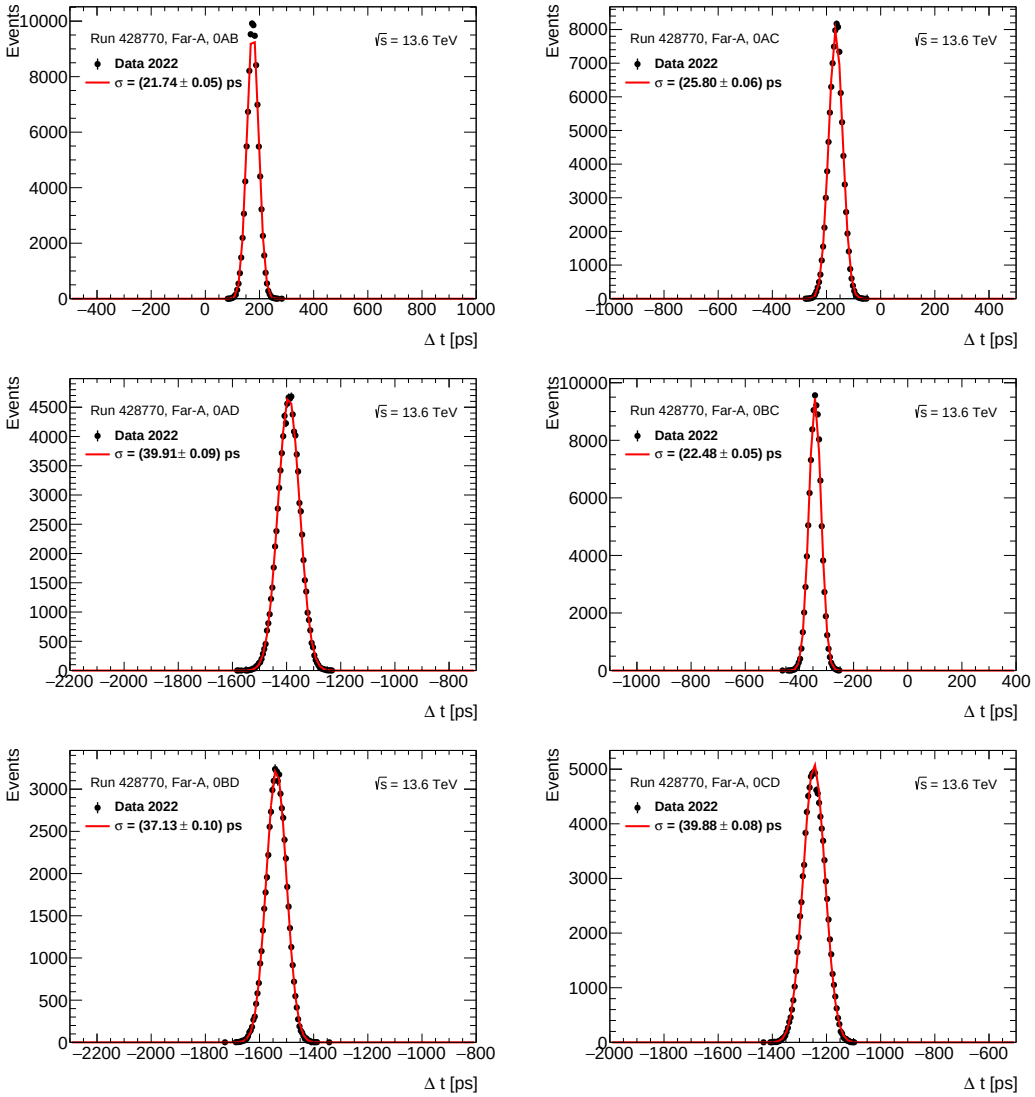

Figure 65: Δt distributions after the likelihood cleanup procedure for the low-μ run 428770 with a Gaussian fitted curve overlaid for all combinations of the ToF channels in train 0 for the A-side.

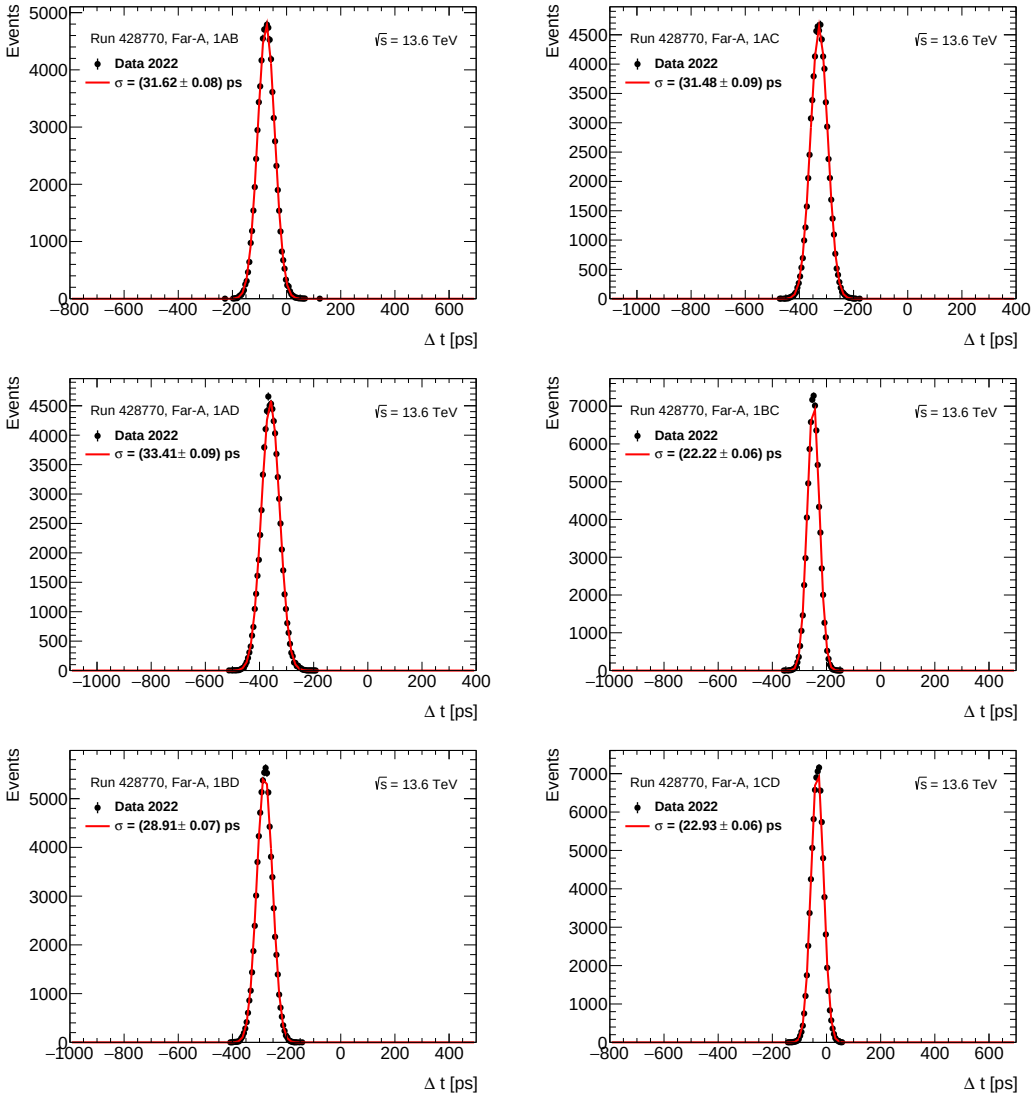

Figure 66: Δt distributions after the likelihood cleanup procedure for the low-μ run 428770 with a Gaussian fitted curve overlaid for all combinations of the ToF channels in train 1 for the A-side.

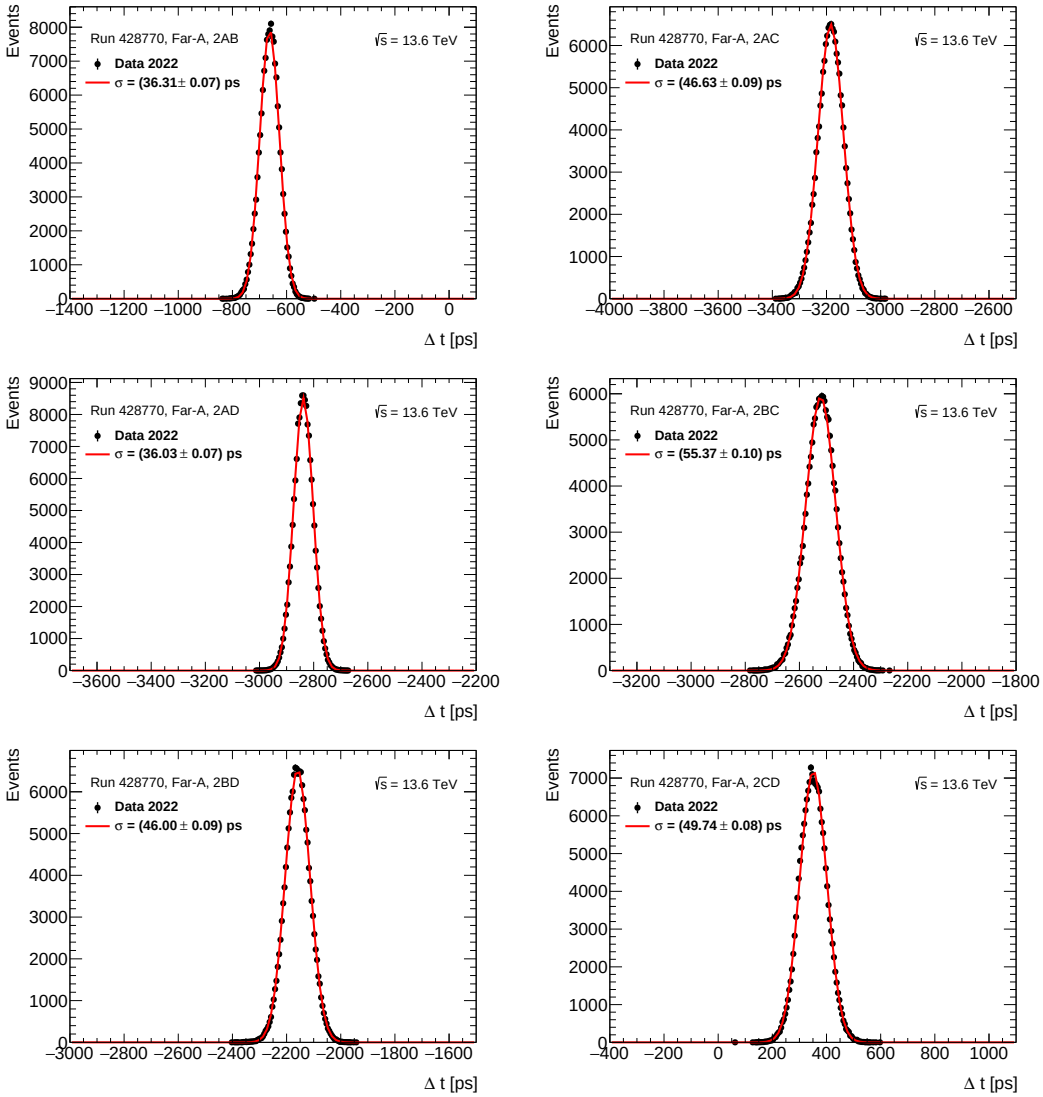

Figure 67: Δt distributions after the likelihood cleanup procedure for the low-μ run 428770 with a Gaussian fitted curve overlaid for all combinations of the ToF channels in train 2 for the A-side.

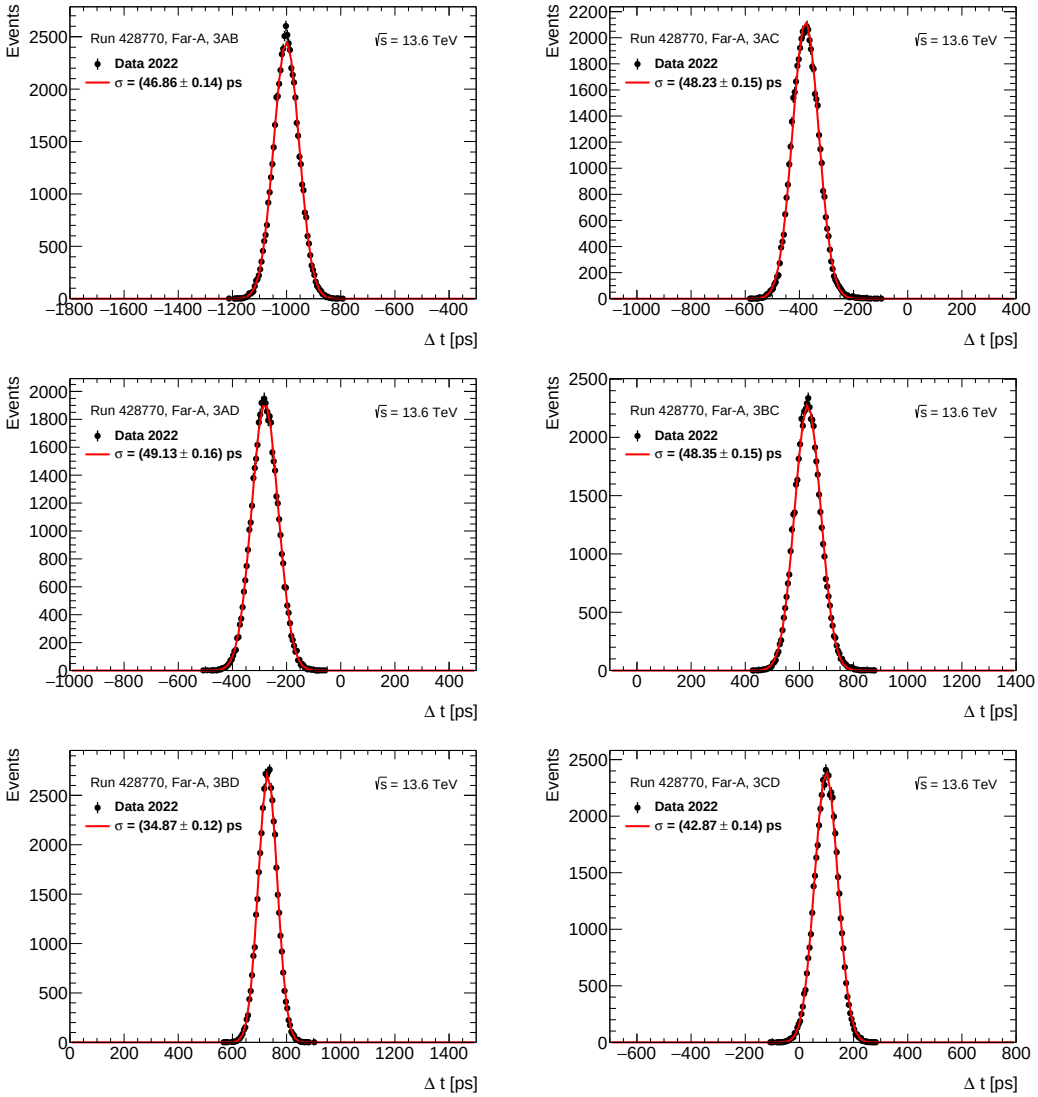

Figure 68: Δt distributions after the likelihood cleanup procedure for the low-μ run 428770 with a Gaussian fitted curve overlaid for all combinations of the ToF channels in train 3 for the A-side.

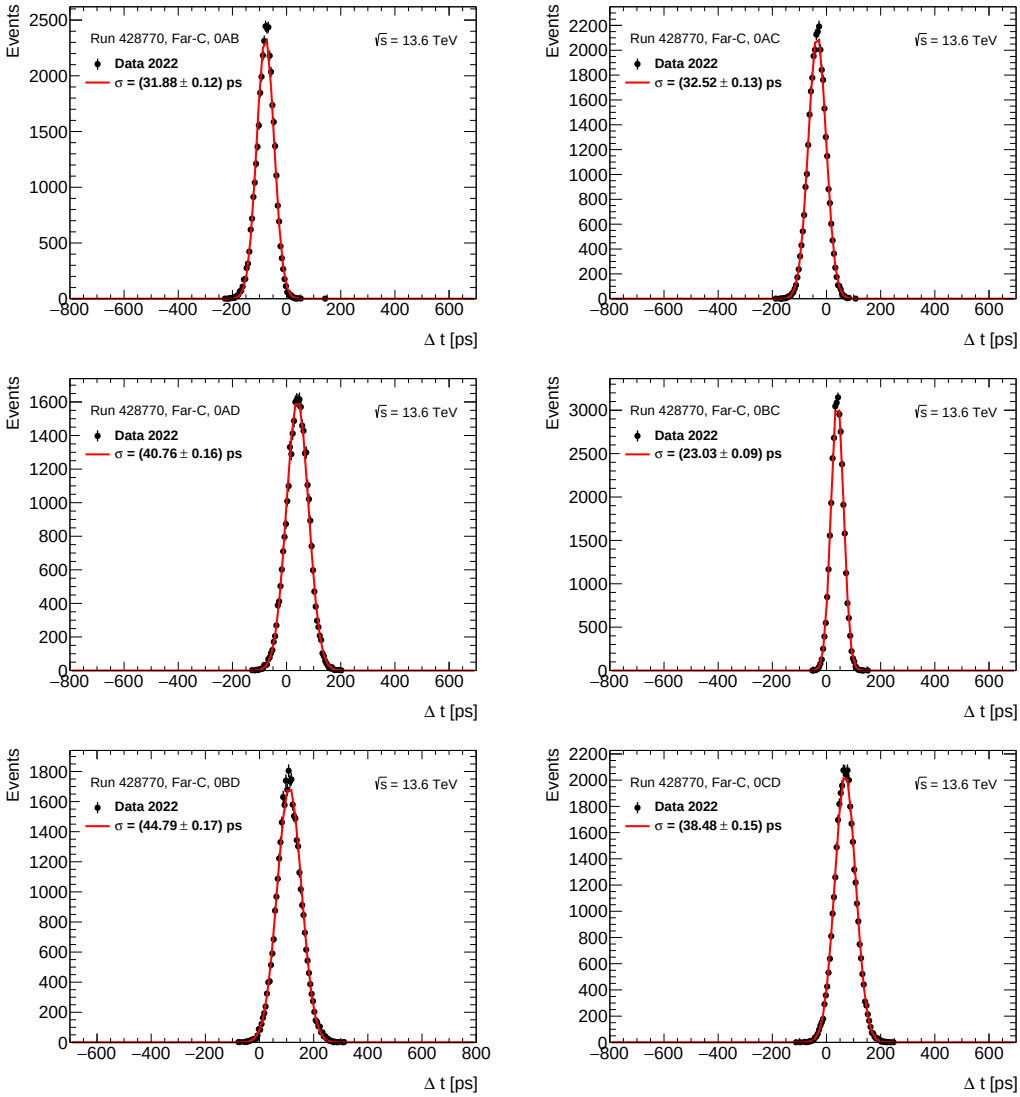

Figure 69: Δt distributions after the likelihood cleanup procedure for the low-μ run 428770 with a Gaussian fitted curve overlaid for all combinations of the ToF channels in train 0 for the C-side.

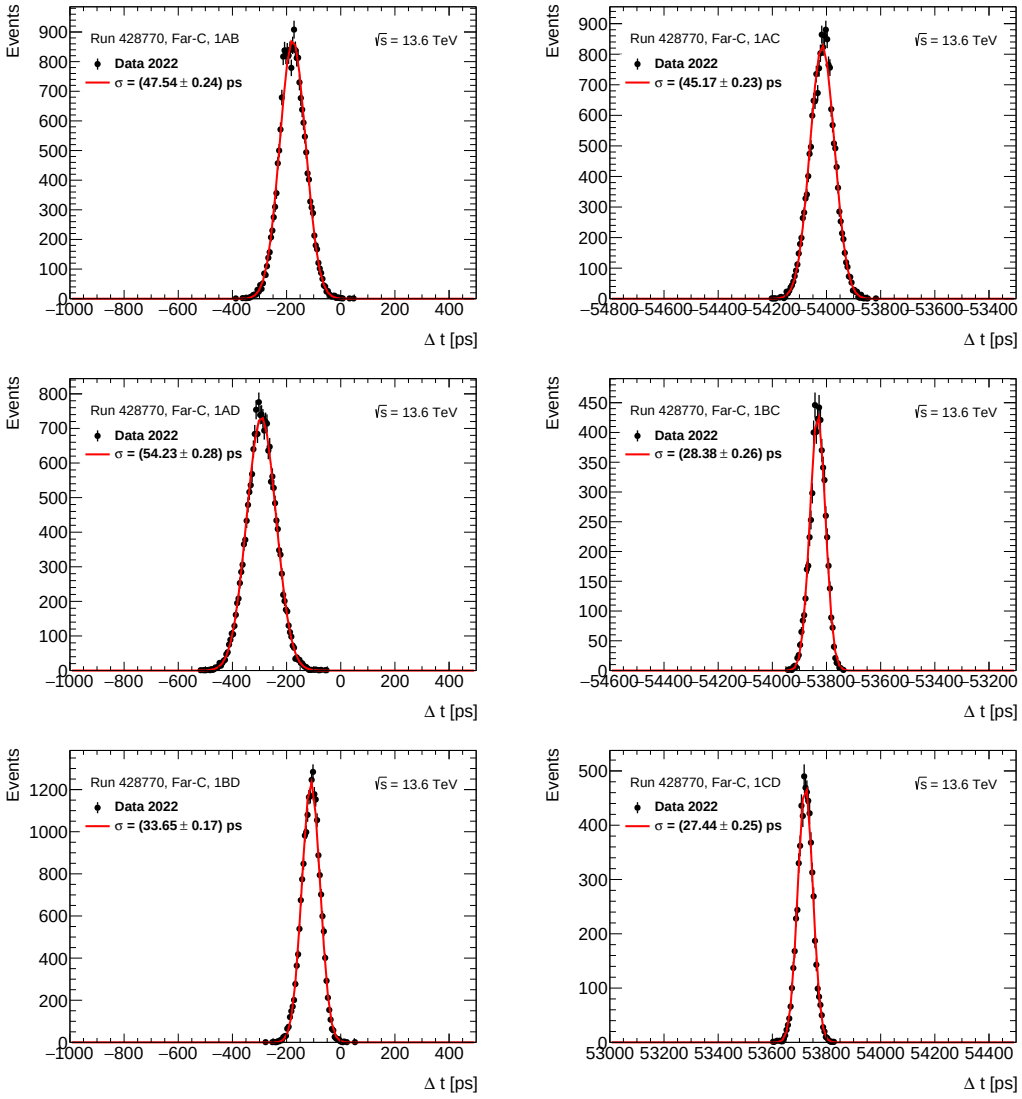

Figure 70: Δt distributions after the likelihood cleanup procedure for the low-μ run 428770 with a Gaussian fitted curve overlaid for all combinations of the ToF channels in train 1 for the C-side.

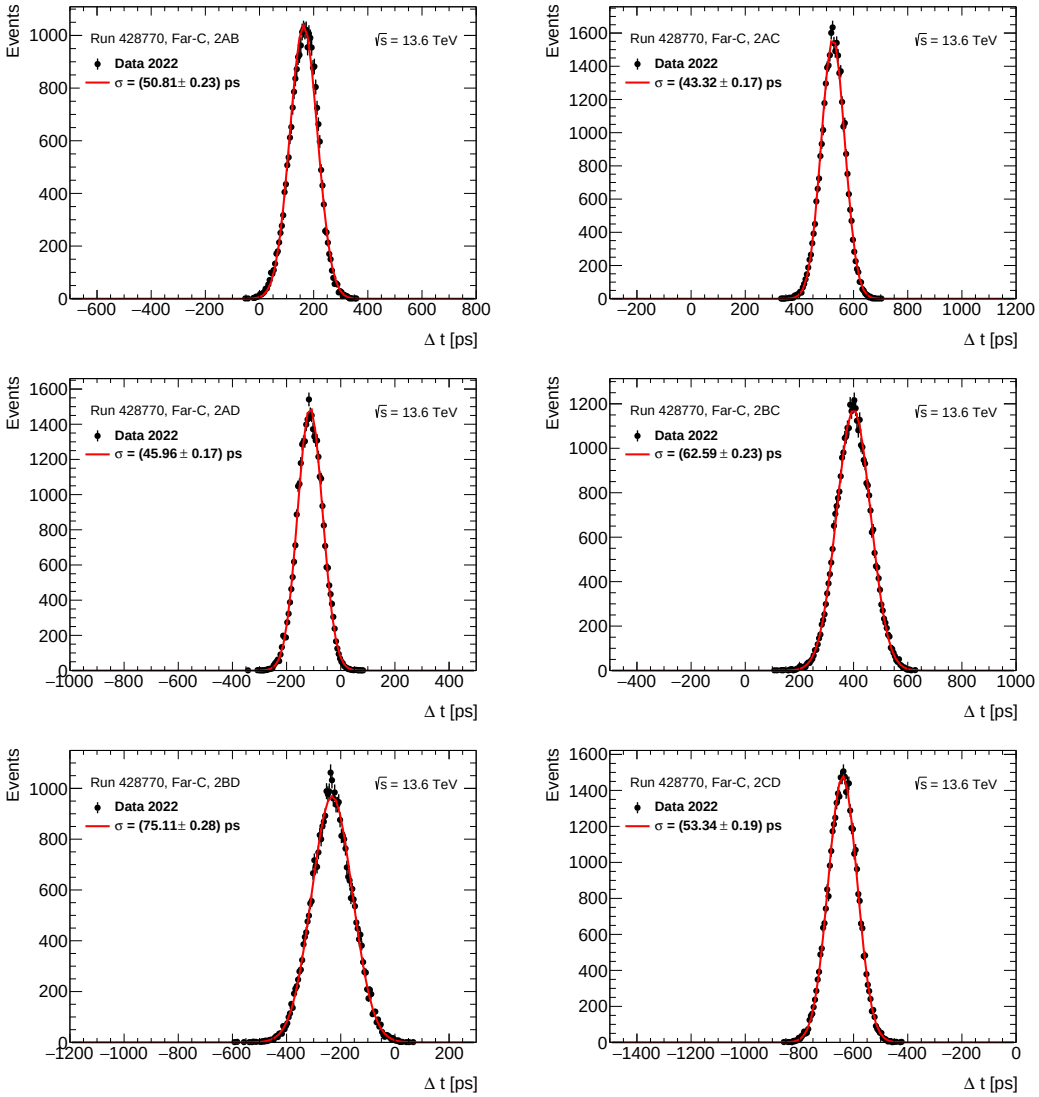

Figure 71: Δt distributions after the likelihood cleanup procedure for the low-μ run 428770 with a Gaussian fitted curve overlaid for all combinations of the ToF channels in train 2 for the C-side.

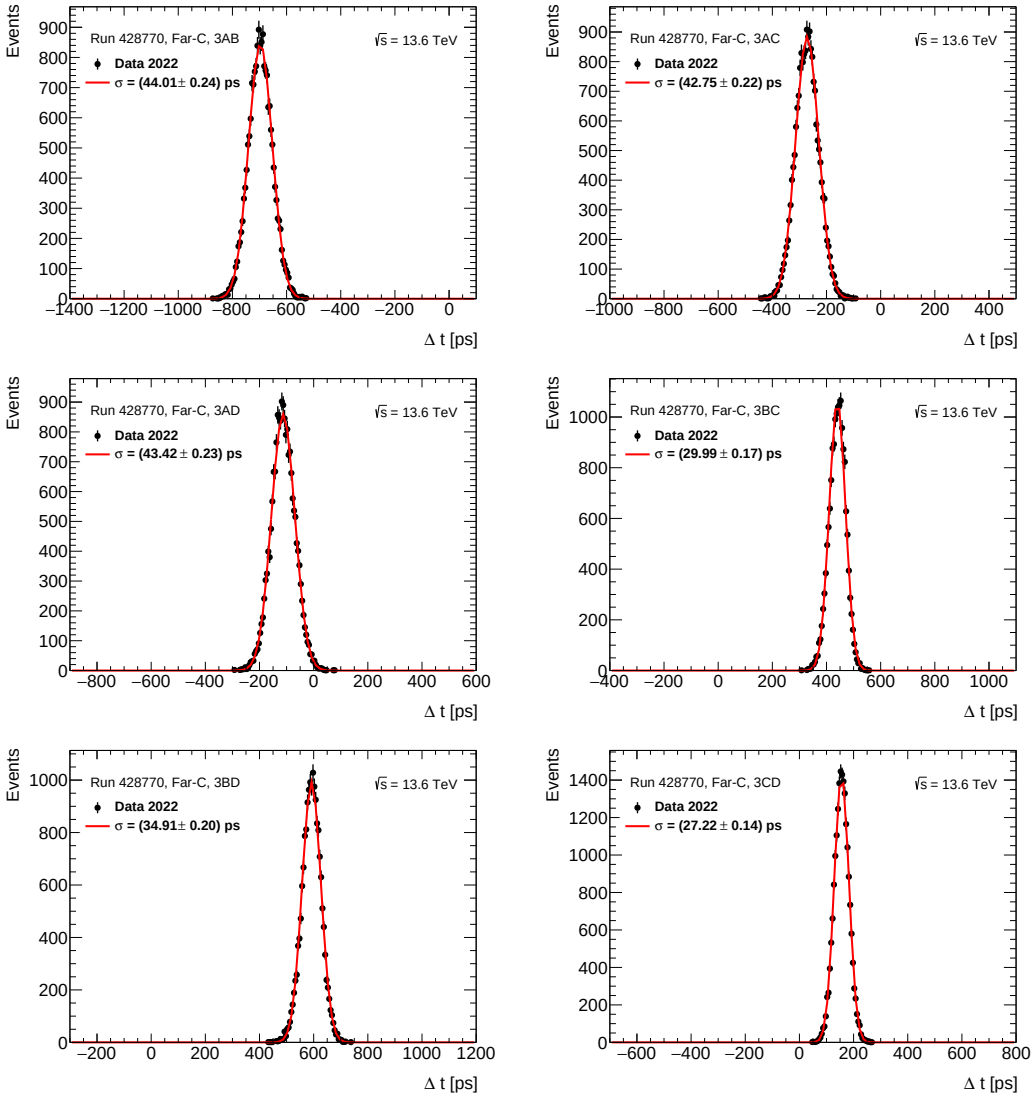

Figure 72: Δt distributions after the likelihood cleanup procedure for the low-μ run 428770 with a Gaussian fitted curve overlaid for all combinations of the ToF channels in train 3 for the C-side.

C ToF efficiency

In Section 3.3.1 efficiencies are calculated in all channels assuming that SiT track points to one of the ToF trains in order to see the full map of ToF activity, both for the train to which the track points, and for other trains.

Efficiencies calculated in such a way for the run 429027 for both cases (ON/OFF) using the method "direct numbers" are shown in Figures 73-76, each Figure corresponds to the ToF train. Empty boxes represents zero response of the corresponding channel.

Efficiencies calculated in such a way for the low-μ run 428770 for both cases (ON/OFF) using the method "direct numbers" are shown in Figures 77-80, each Figure corresponds to the ToF train. Empty boxes represents zero response of the corresponding channel.

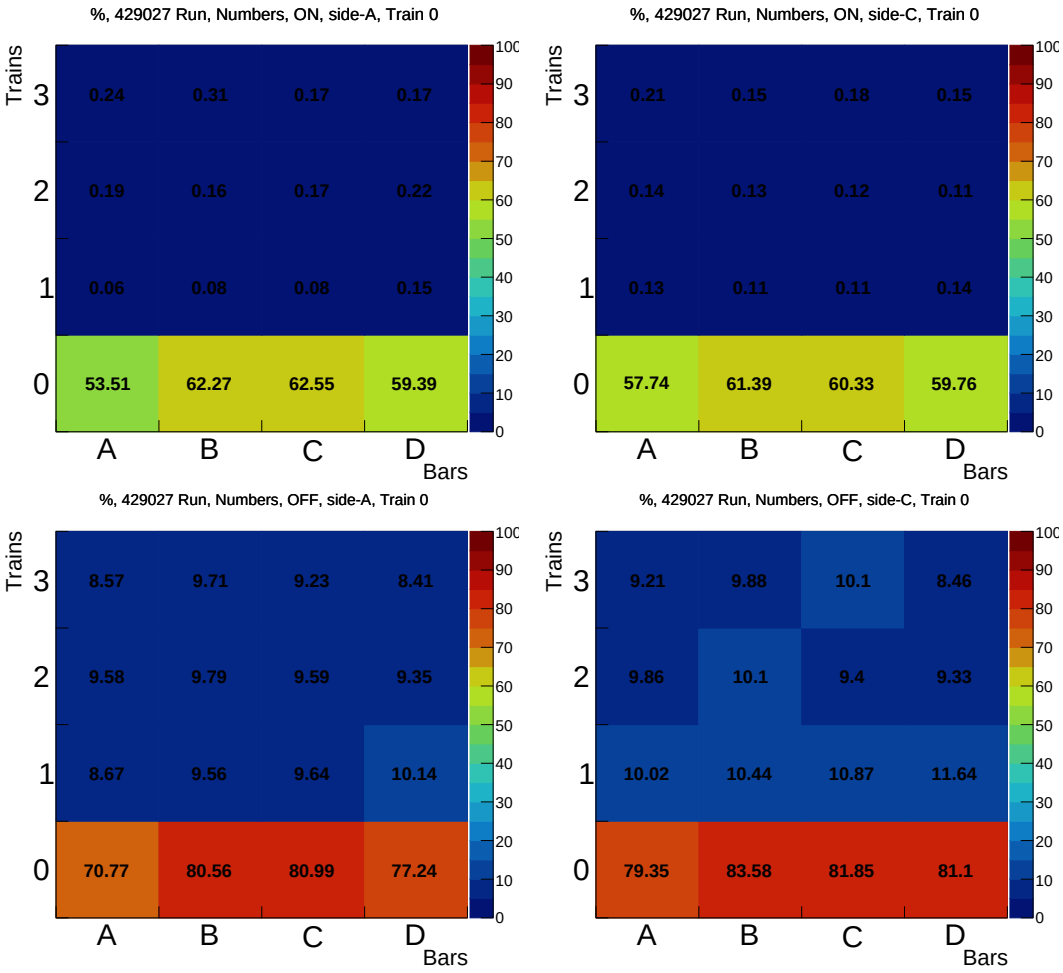

Figure 73: Efficiencies (%) for the run 429027 for each channel of the ToF with track pointing to train 0 for A (left) and C (right) sides with the requirement "one train ON", (top) and OFF, (bottom) for the "direct numbers" method. Empty boxes represents zero response of the corresponding channel.

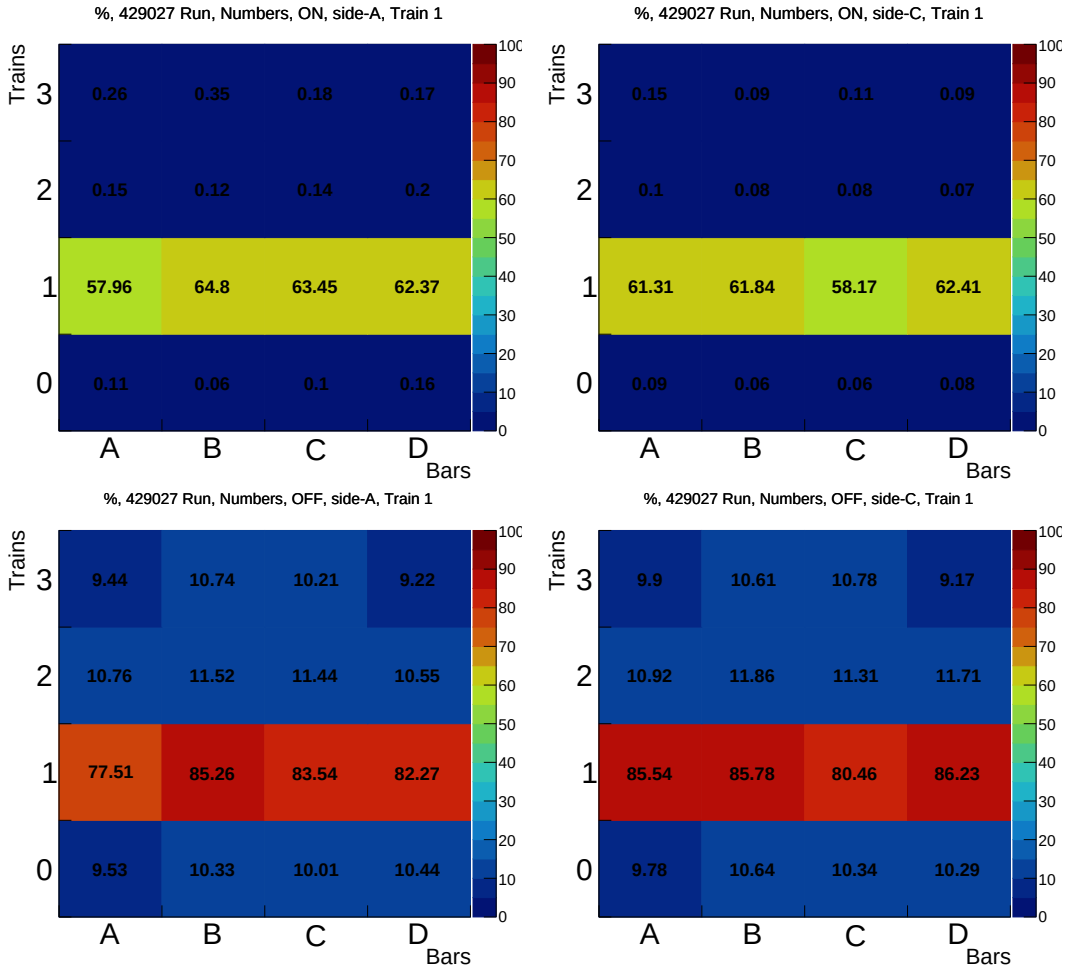

Figure 74: Efficiencies (%) for the run 429027 for each channel of the ToF with track pointing to train 1 for A (left) and C (right) sides with the requirement "one train ON", (top) and OFF, (bottom) for the "direct numbers" method.

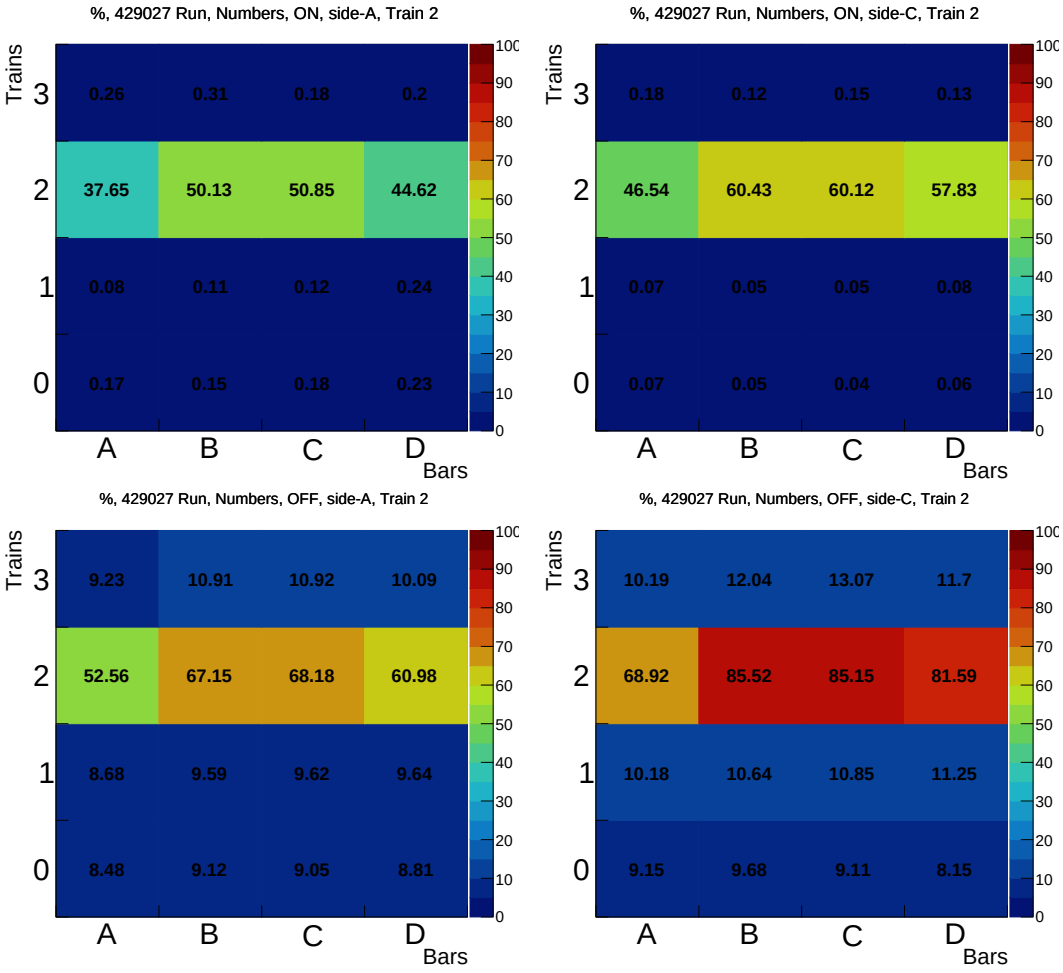

Figure 75: Efficiencies (%) for the run 429027 for each channel of the ToF with track pointing to train 2 for A (left) and C (right) sides with the requirement "one train ON", (top) and OFF, (bottom) for the "direct numbers" method.

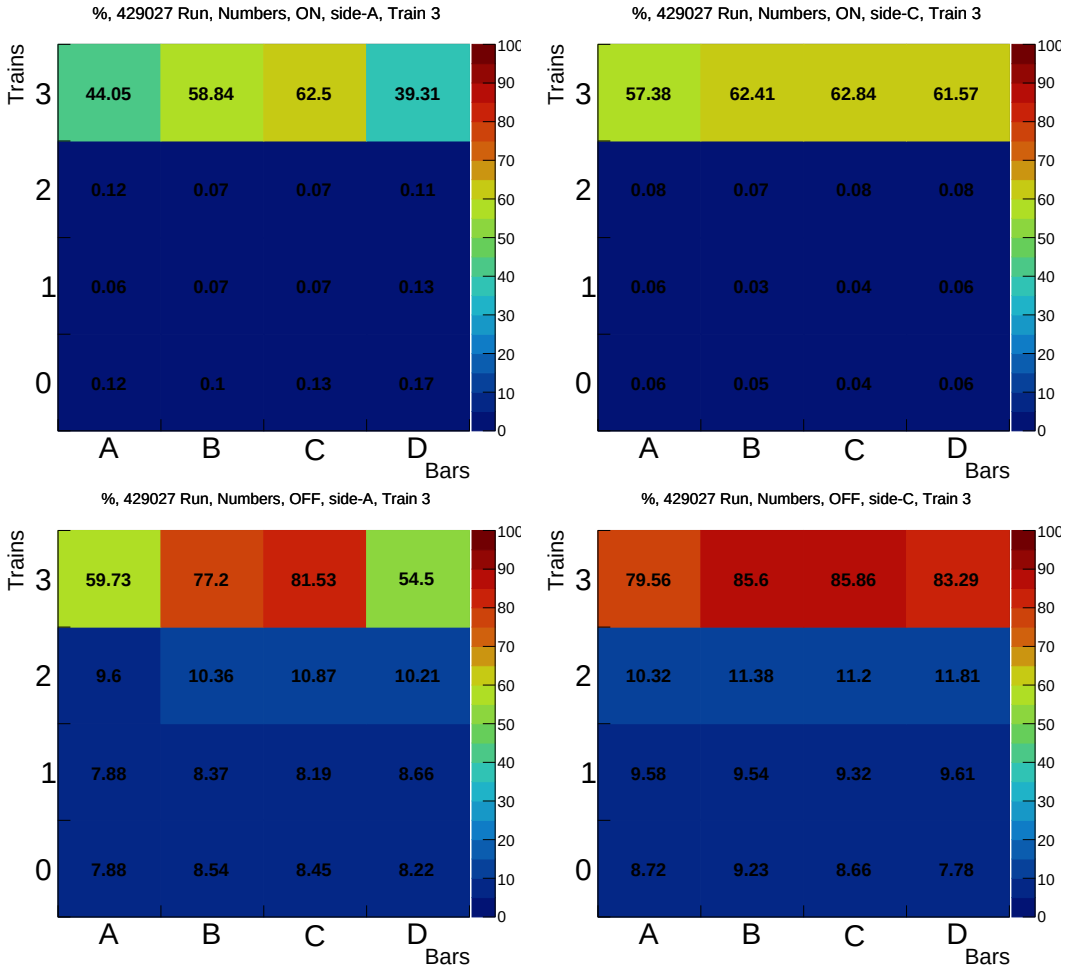

Figure 76: Efficiencies (%) for the run 429027 for each channel of the ToF with track pointing to train 3 for A (left) and C (right) sides with the requirement "one train ON", (top) and OFF, (bottom) for the "direct numbers" method.

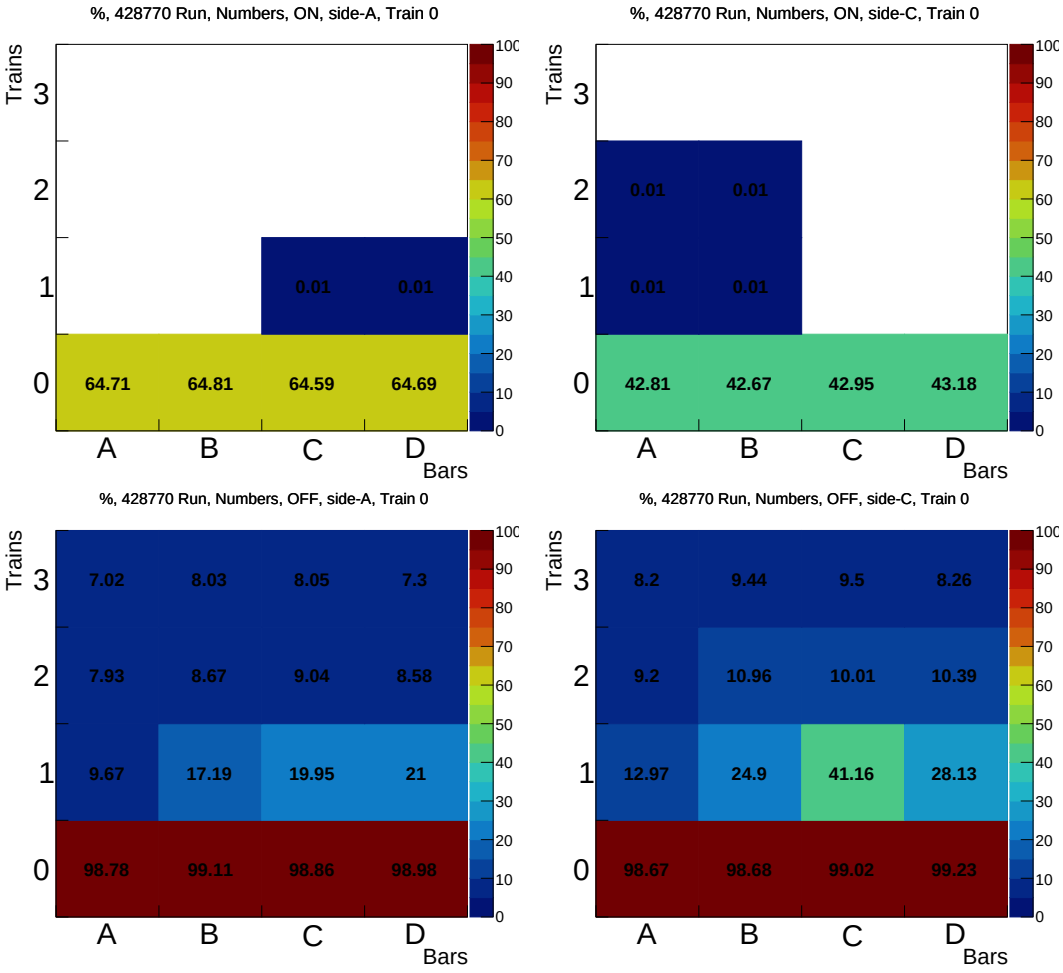

Figure 77: Efficiencies (%) for the low-μ run 428770 for each channel of the ToF with track pointing to train 0 for A (left) and C (right) sides with the requirement "one train ON", (top) and OFF, (bottom) for the "direct numbers" method. Empty boxes represents zero response of the corresponding channel.

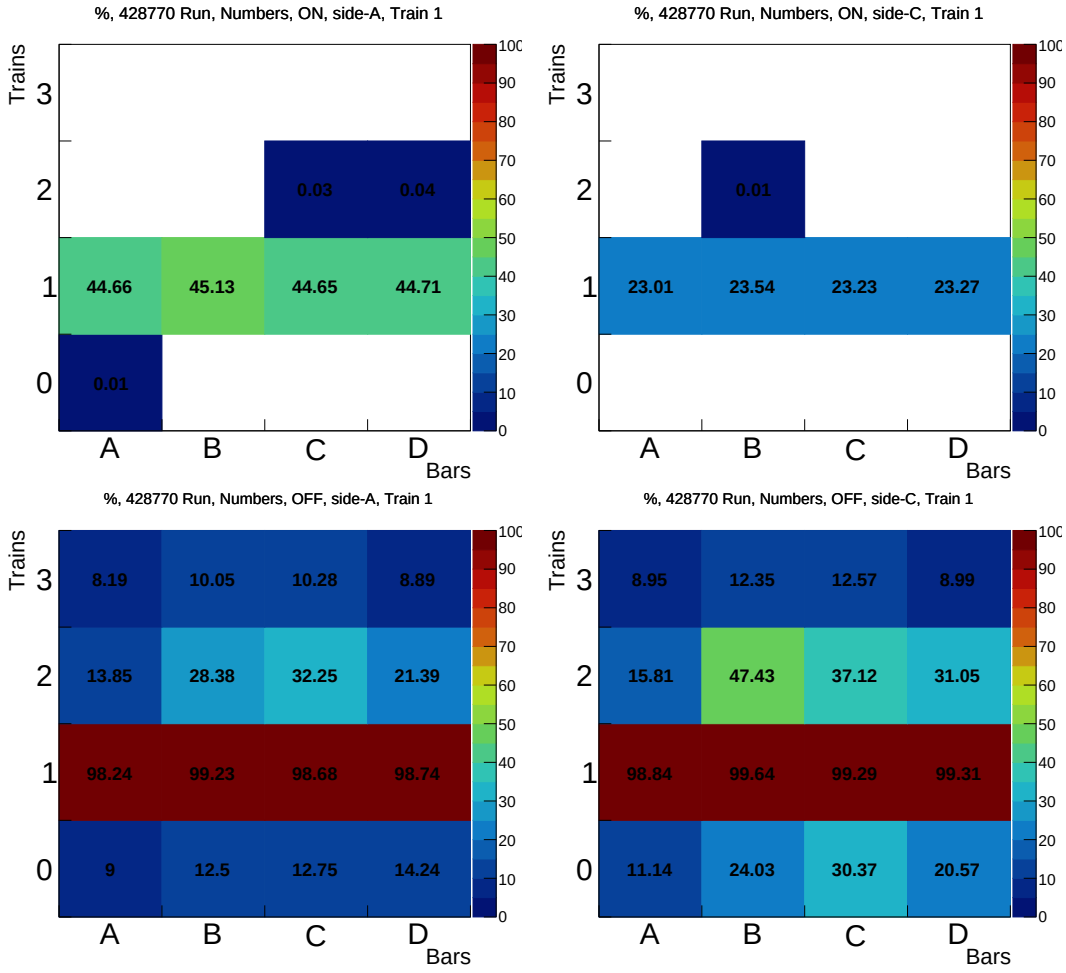

Figure 78: Efficiencies (%) for the low-μ run 428770 for each channel of the ToF with track pointing to train 1 for A (left) and C (right) sides with the requirement "one train ON", (top) and OFF, (bottom) for "direct numbers" method. Empty boxes represents zero response of the corresponding channel.

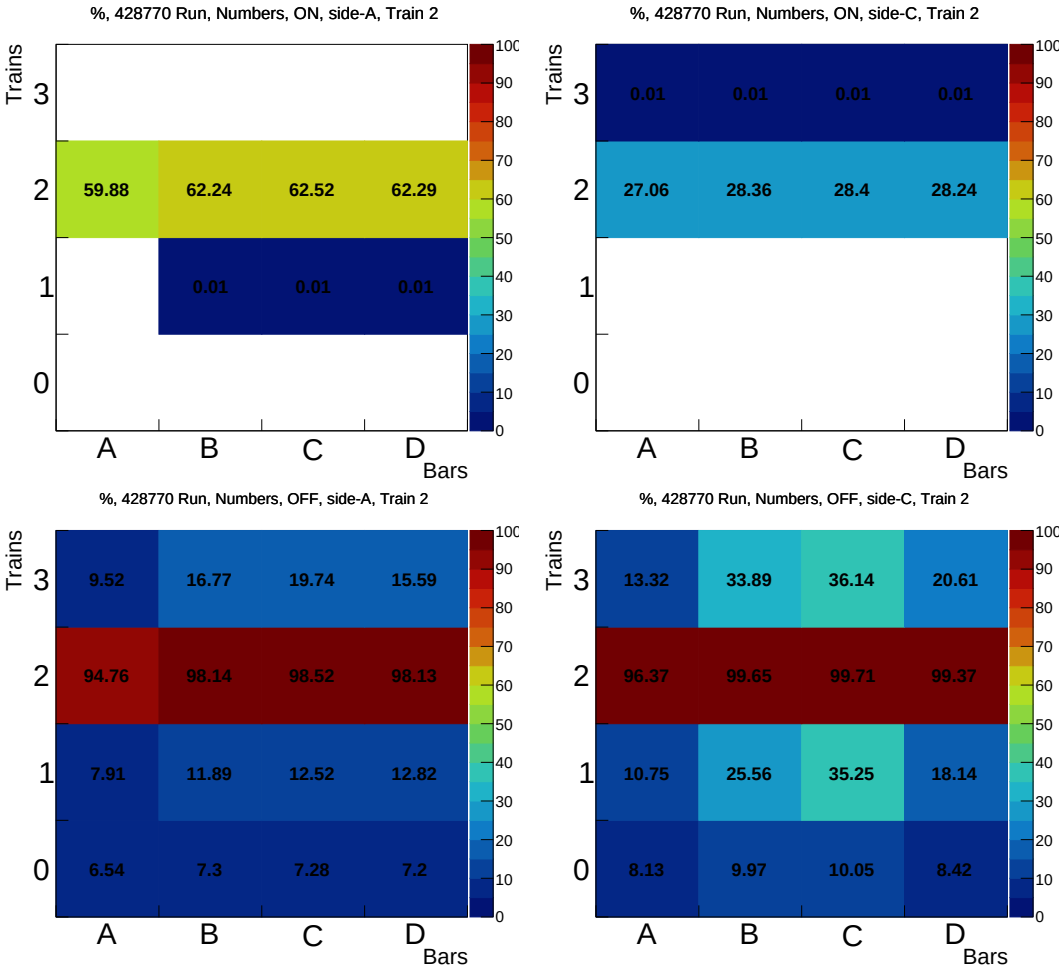

Figure 79: Efficiencies (%) for the low-μ run 428770 for each channel of the ToF with track pointing to train 2 for A (left) and C (right) sides with the requirement "one train ON", (top) and OFF, (bottom) for the "direct numbers" method. Empty boxes represents zero response of the corresponding channel.

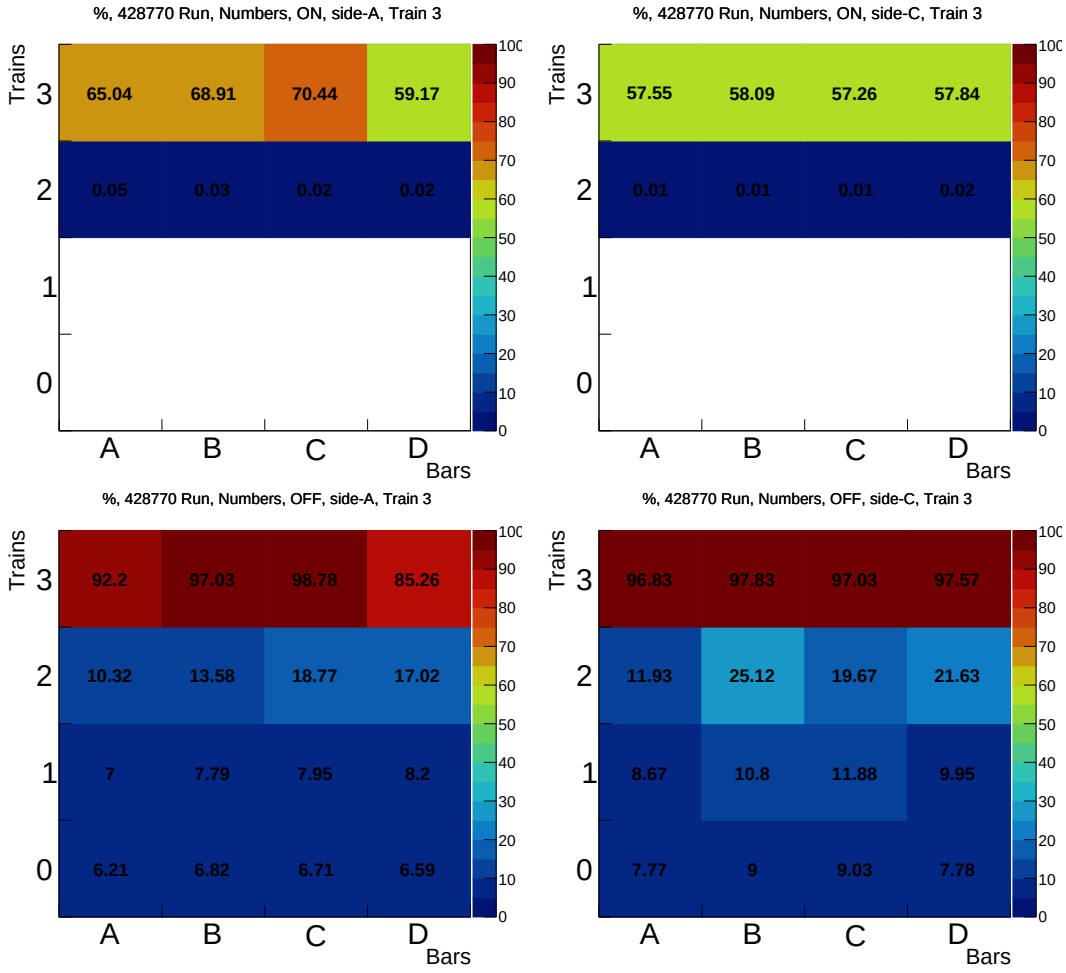

Figure 80: Efficiencies (%) for the low-μ run 428770 for each channel of the ToF with track pointing to train 3 for A (left) and C (right) sides with the requirement "one train ON", (top) and OFF, (bottom) for the "direct numbers" method. Empty boxes represents zero response of the corresponding channel.

Hit correlation map showed in details effect of the activity in trains, neighboring to the one track points on.

Figures 81, 82 shows hit correlation maps for high-μ run 429027 for the A-side and C-side, respectively.

Figures 83, 84 shows hit correlation maps for the low-μ run 428770 for the A-side and C-side, respectively.

Figure 85, 86 shows hit correlation maps for the longest low-μ run in Run-3, 435229, for the A-side and side-C, respectively.

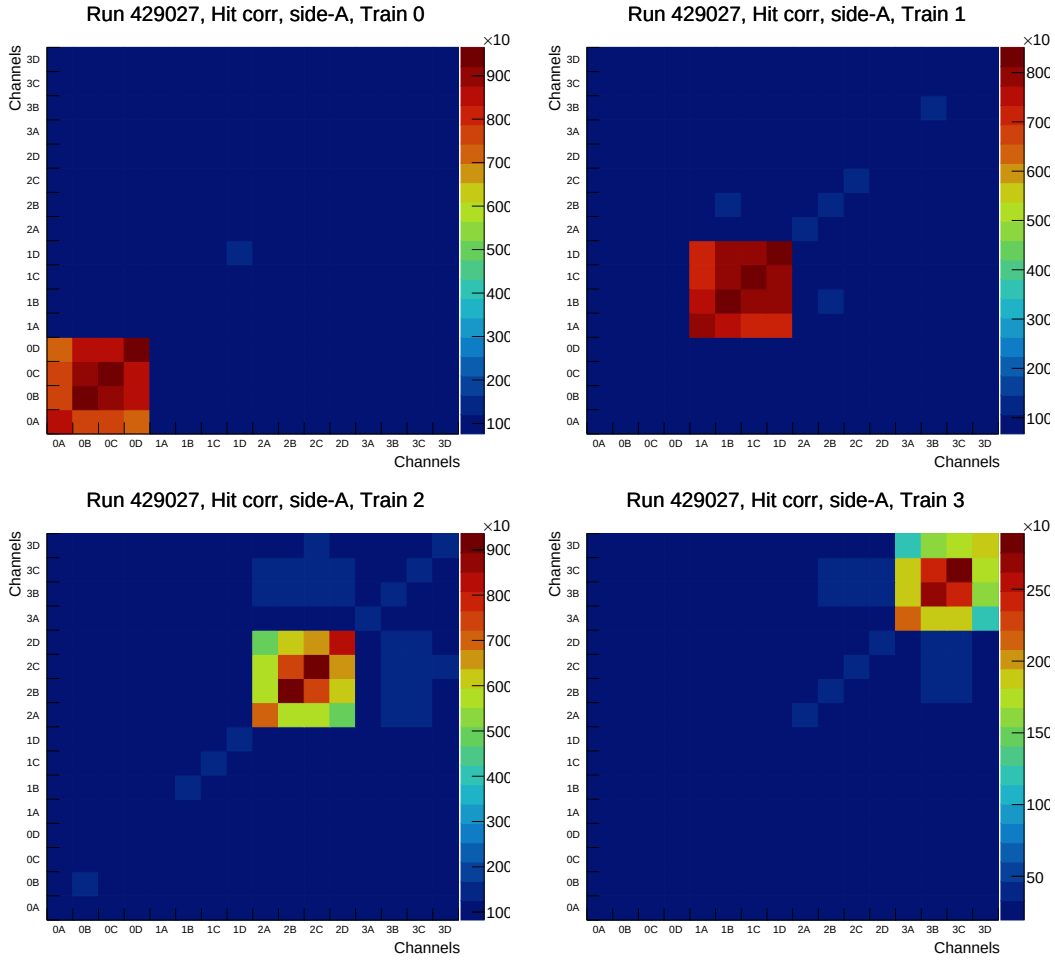

Figure 81: Hit correlation map for the high-μ run 429027 for each channel of the ToF with track pointing to train 0 (top left), train 1 (top right), train 2 (bottom left) and train 3 (bottom right) for the A-side with the requirement "one train OFF".

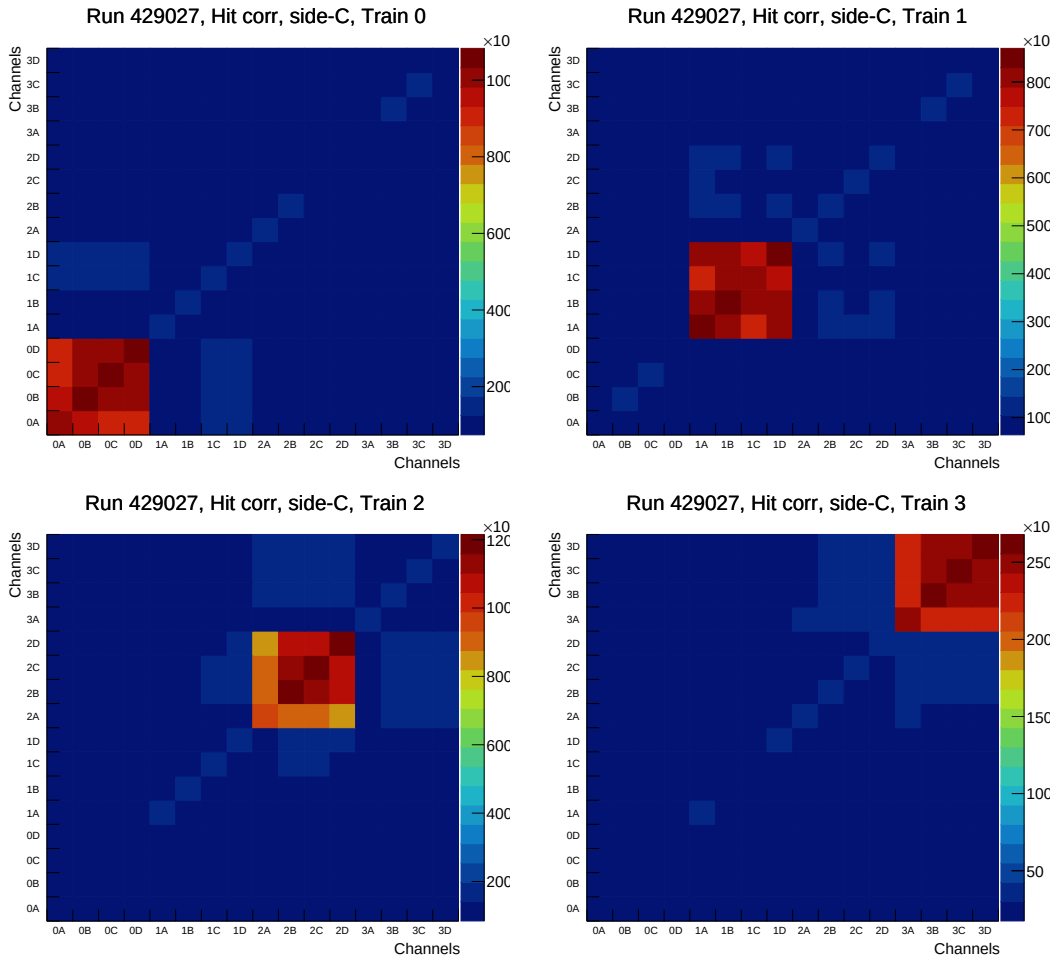

Figure 82: Hit correlation map for the high-μ run 429027 for each channel of the ToF with track pointing to train 0 (top left), train 1 (top right), train 2 (bottom left) and train 3 (bottom right) for the C-side with the requirement "one train OFF".

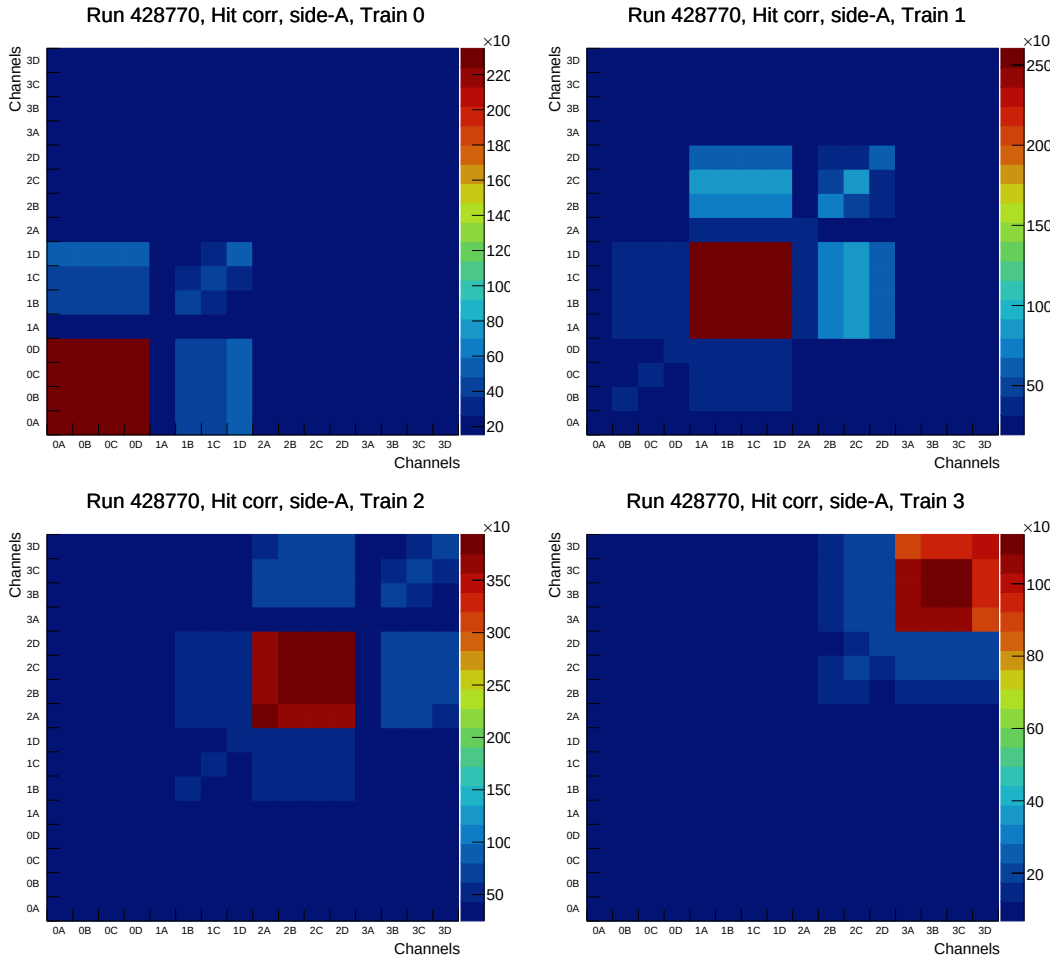

Figure 83: Hit correlation map for the low-μ run 428770 for each channel of the ToF with track pointing to train 0 (top left), train 1 (top right), train 2 (bottom left) and train 3 (bottom right) for the A-side with the requirement "one train OFF".

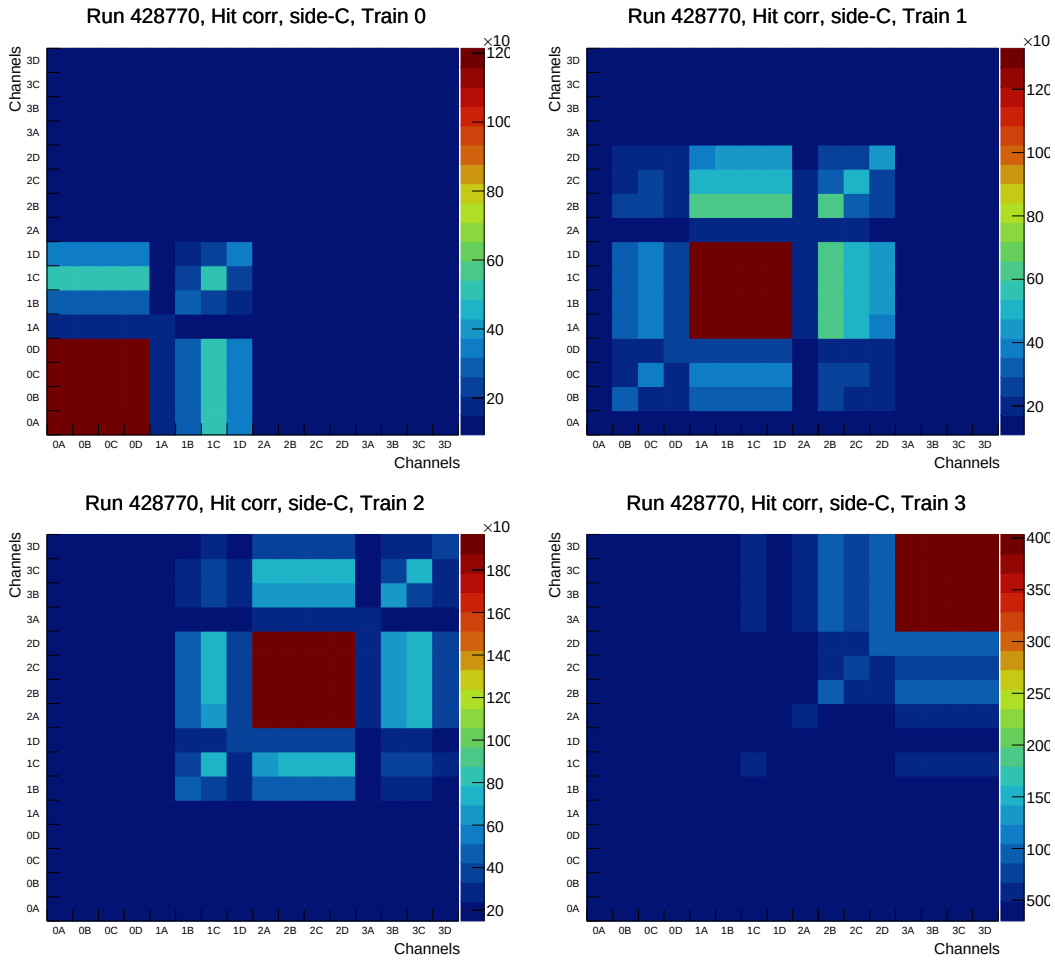

Figure 84: Hit correlation map for the low-μ run 428770 for each channel of the ToF with track pointing to train 0 (top left), train 1 (top right), train 2 (bottom left) and train 3 (bottom right) for the C-side with the requirement "one train OFF".

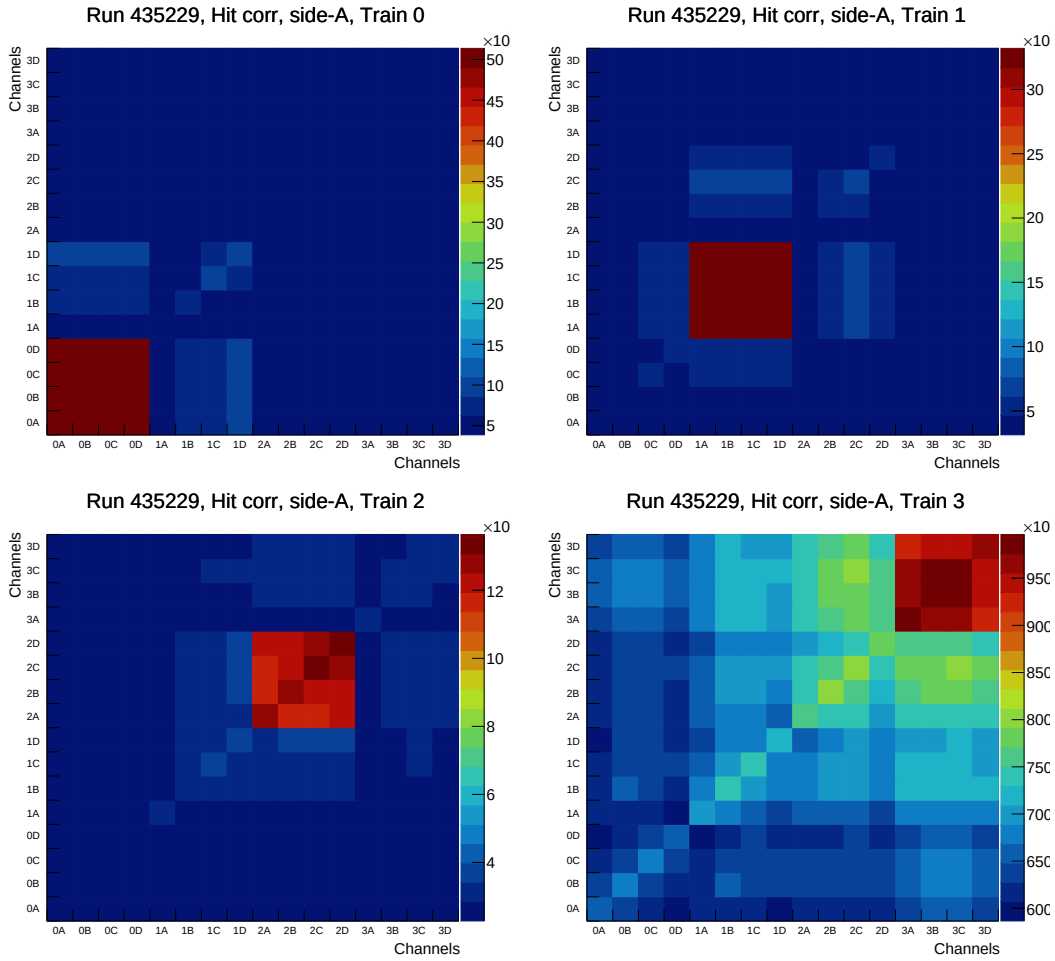

Figure 85: Hit correlation map for the longest low-μ run so far in LHC Run-3, 435229, for each channel of the ToF with track pointing to train 0 (top left), train 1 (top right), train 2 (bottom left) and train 3 (bottom right) for the A-side with the requirement "one train OFF".

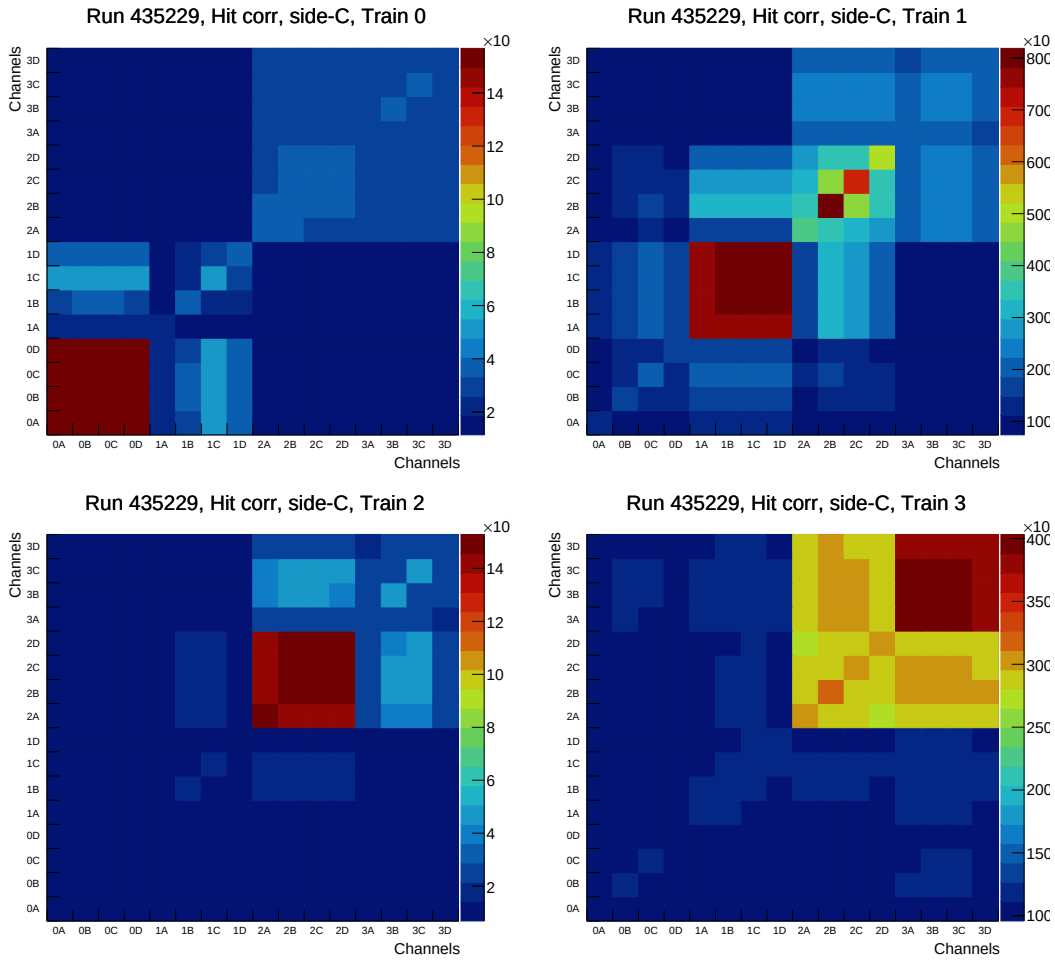

Figure 86: Hit correlation map for the longest low-μ run so far in LHC Run-3, 435229, for each channel of the ToF with track pointing to train 0 (top left), train 1 (top right), train 2 (bottom left) and train 3 (bottom right) for the C-side with the requirement "one train OFF".

Acronyms

AFP	ATLAS Forward Proton. 2, 6, 8, 49, 51, 58, 61–63
ALP	Axion-Like Particle. 2, 61, 62
ALPs	Axion-like particles. 1, 61
AOD	Analysis Object Data. 9
ATLAS	A Toroidal LHC ApparatuS. 5, 6, 9, 49, 50, 58, 59, 61–63
BSM	Beyond the Standard Model. 1, 61
CFD	constant fraction discriminator. 8
CP	Charge conjugation times Parity. 1
HPTDC	high performance time-to-digital converter. 8, 11, 14–19, 22–25, 32, 34, 57, 63, 75, 90, 99–115
LB	lumiblock. 50, 51, 54, 55
LHC	Large Hadron Collider. 1, 2, 5, 8, 11, 50, 62, 63, 143, 144
PMT	Photomultiplier Tube. 8
PV	Primary Vertex. 59
QED	Quantum Electrodynamics. 1
RF	Radiofrequency. 11
RP	Roman Pots. 2
SiT	Silicon pixel Tracker. 2, 6–10, 14, 19–21, 34, 35, 37–39, 41, 44, 45, 49, 131
SM	Standard Model. 1

ToF Time-of-Flight. 2, 6–12, 14–16, 18, 19, 22–30, 32, 34, 35, 37–47, 49–53, 55, 57, 58, 61–63, 70, 75–144